Summer 2023

Study of Non-Covalent Interactions Using Molecular Rotors and Balances

Daniel Onyekachi Madukwe

STUDY OF NON-COVALENT INTERACTIONS USING MOLECULAR ROTORS AND BALANCES

by

Daniel Onyekachi Madukwe

Bachelor of Technology
Federal University of Technology, Owerri, Nigeria, 2007

Submitted in Partial Fulfillment of the Requirements

For the Degree of Doctor of Philosophy in

Chemistry

College of Arts and Sciences

University of South Carolina

2023

Accepted by:

Ken D. Shimizu, Major Professor

Linda Shimizu, Committee Member

Aron Vannucci, Committee Member

Sheri Strickland, Committee Member

Ann Vail, Dean of the Graduate School

DEDICATION

This work is dedicated to God Almighty and to my late parents, Mr. Romanus Madukwe and Mrs. Fidelia Madukwe.

ACKNOWLEDGEMENTS

I am humbled by the tremendous support I received from those who played a crucial role in my journey towards obtaining my PhD degree. I want to begin by expressing my gratitude to God for His unceasing love, guidance, and protection throughout my academic pursuits. My advisor, Dr. Ken Shimizu, deserves my heartfelt appreciation for his exceptional patience, unwavering dedication, and mentorship that guided me through my research. His insightful guidance shaped the direction of my work and helped me navigate the academic world.

I am forever grateful to my late parents, Mr. Romanus Madukwe and Mrs. Fidelia Madukwe, for instilling in me a love for learning and a strong work ethic that have sustained me throughout this academic journey. Their unwavering support and guidance will forever be cherished. To my family, Tobechukwu, Dominic, Mary, and Stella, your emotional and intellectual support sustained me through the trials of graduate school and made me emerge stronger and more resilient. Your love, encouragement, and patience are priceless to me. I cannot forget to extend my gratitude to my committee members, friends, and colleagues for their invaluable support and guidance in my academic journey. Thank you all for playing a part in my success.

ABSTRACT

The main focus of this dissertation is on the quantification of non-covalent interactions using molecular rotors and balances. While molecular rotors were used to measure kinetic effects of weak non-covalent interactions, molecular balances were used to measure their thermodynamic effects. Chapters 1 and 2 focus on the use of molecular rotors in measuring and studying the kinetic effects of the hydrogen bonding interaction on the bond rotation transition states. Chapters 3 and 4 focus on the quantification of lone pair – lone pair and sp^2-CH/π interactions respectively, using molecular balances. These studies were carried out in the ground state.

TABLE OF CONTENTS

LIST OF TABLES

LIST OF FIGURES

LIST OF SCHEMES

LIST OF ABBREVIATIONS

$\Delta\Delta G^{\ddagger}$ ..... Transition State stabilization

$\Delta G^{\ddagger}$ ..... Reaction barriers

$\Delta H^{\ddagger}$ ..... Difference in enthalpy between GS and TS energies

$\Delta S^{\ddagger}$ ..... Difference in entropy between GS and TS energies

DFT ..... Density Functional Theory

FI-SAPT ..... Fragment Intramolecular-Symmetry-Adapted Perturbation Theory

GS ..... Ground State

HB ..... Hydrogen Bond

k_B ..... Boltzmann's Constant

k_c ..... Exchange rate at T_c

NBO ..... Natural Bond Order

R ..... Gas Constant

T ..... Temperature

TS ..... Transition State

CHAPTER 1

INTRODUCTION TO HYDROGEN BONDING

1.1 ABSTRACT

Chapter 1 introduces the concept of hydrogen bonding as a non-covalent interaction and the justifications for studying the interaction. This is followed by a discussion of the methods used in the quantification of the hydrogen bonding interaction strengths. Experimental measurements of rotational barriers are then correlated with empirical parameters to observe trends. Based on the observed trends, inferences can then be made regarding which fundamental forces are important in hydrogen bonding interaction. Finally, fundamental forces such as electrostatics, repulsion, dispersion, and charge transfer (orbital – orbital interaction) shown to contribute to the hydrogen bonding interaction will be introduced.

1.2 OVERVIEW OF HYDROGEN BONDING

Hydrogen bonding is a non-covalent interaction that plays a crucial role in many biological processes, including protein folding, DNA structure, and enzyme activity.[1,2,3,4,5,6] Hydrogen bonds are attractive interactions between a hydrogen atom covalently bonded to a highly electronegative atom, such as oxygen, nitrogen or halogen, and an unshared electron pair of an electronegative atom in the same or another molecule. The interaction results in a strong and directional interaction that can be observed in a wide range of systems, including small molecules, macromolecules, and biological systems. The concept of hydrogen bonding was first introduced by Linus Pauling in the 1930s, who proposed that hydrogen bonds were a major contributing factor in the stability of proteins and other biological molecules.[7] Since then, the study of hydrogen bonding has been a major area of research in the fields of chemistry, biochemistry, and materials science. The

huge interest in hydrogen bonding is due to the importance of hydrogen bonding in a variety of systems such as the formation of water clusters,[8] the stability of DNA[9,10], and the function of enzymes.[11]

1.3 CHARACTERISTICS OF HYDROGEN BONDS

1.3.1 STRENGTH

Hydrogen bonds are one of the stronger non-covalent interactions, leading to relatively short distances between interacting atoms. For example, the hydrogen bond O···O distance in water is typically around 2.82 Å,[12] which is much shorter than the typical van der Waals interaction of around 3.2 Å.[13] This strength is attributed to the highly polar nature of the hydrogen atom, which is capable of forming a strong dipole-dipole interaction with an electronegative atom. Hydrogen bonds can be classified based on their strengths as strong, moderate, and weak. Weak hydrogen bond interactions are the most common with bond energies value between −0.5 and −4.0 kcal/mol. For example, the majority of hydrogen bonds found in catalytic and biological systems fall in the weak category. Moderate hydrogen bonding interactions have a bond energy in the range −4.0 to −15.0 kcal/mol while strong hydrogen bonds have bond energy values in the range of −15.0 to −60.0 kcal/mol.[14] Moderate and strong interactions are usually charge-assisted hydrogen bonds where the heavy atom attached to the proton is positively charged or the acceptor heavy atom is negatively charged (Figure 1.1). Examples are NH_3^+−H•••OH_2 and F^- ••••H−F. The charges enhance the electrostatic component of the hydrogen bonding interaction.

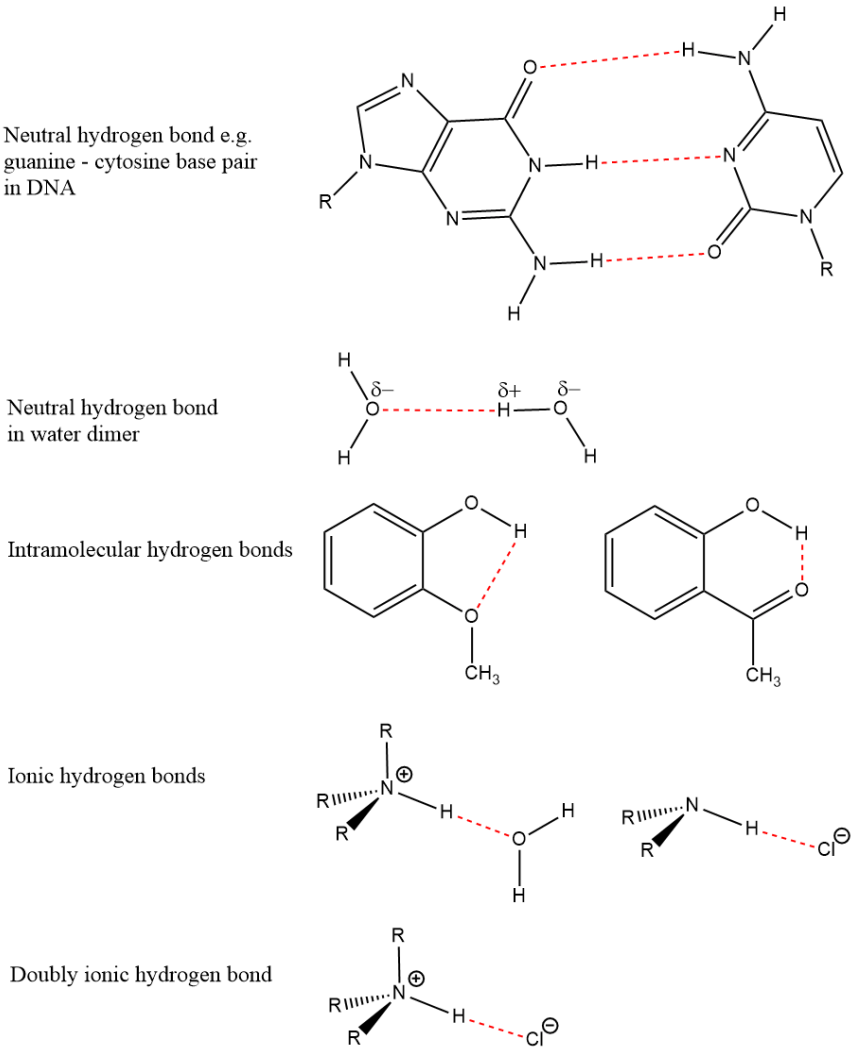

Figure 1.1. Different geometries of hydrogen bond showing how the donor and the lone pair acceptor are aligned.

1.3.2 DIRECTIONALITY

Directionality is another important feature of hydrogen bonds. Unlike van der Waals forces, which are isotropic, hydrogen bonds are highly directional. Hydrogen bonding interactions prefer a geometry where the hydrogen bond donor, hydrogen bond

acceptor, and hydrogen bond donor atoms are linear. The directionality is due to the electrostatic component of hydrogen bonding interaction and the bond strength is maximized when the charges are aligned. A component of the directionality is the minimization of the electrostatic repulsion between the heavy atoms.[15,16,17,18] Strong hydrogen bonds are more directional than the weak ones. For an interaction to be classified as a classical hydrogen bond, the bond angle must be greater than 110°.[19] Directionality is particularly important in the formation of hydrogen-bonded networks, such as those found in water and ice, as well as in the stability of macromolecules, such as proteins and DNA.

1.3.3 JUSTIFICATION FOR STUDYING HYDROGEN BONDING

Since enzymes make use of hydrogen bond in their active sites to speed up reactions by stabilizing transition states, an in-depth understanding of hydrogen bonding can provide insight into the mechanisms of enzymes and into the development of efficient organo-catalysts. Furthermore, due to the fact that hydrogen bonding is a critical component of many protein-ligand interactions, a good understanding of hydrogen bonding could help in drug design. Additionally, a better understanding of hydrogen bonding could help in the design of new materials with improved properties such as durability and thermal stability.[20] Lastly, studying hydrogen bonding is important in predicting and controlling chemical reactions.

1.3.4 FUNDAMENTAL INTERACTIONS GOVERNING HYDROGEN BONDING

Hydrogen bonding is governed by multiple fundamental interactions such as electrostatics, repulsion, orbital-orbital (charge-transfer), and dispersion. Electrostatics are the primary fundamental interaction that govern hydrogen bonding, but orbital-orbital, dispersion, and repulsion also contribute.[21] Understanding the roles and contributions of these fundamental interactions is essential in understanding and predicting the properties and behavior of many chemical and biological systems. Electrostatics is responsible for the attraction between the hydrogen bonding proton and the heavy atom in the hydrogen bond acceptor. The strength of this electrostatic attraction is determined by the distance between the hydrogen bonding proton and the heavy atom as well as their respective charges. Several studies have confirmed that electrostatics is the dominant contributor to hydrogen bonding.[21,22,23]

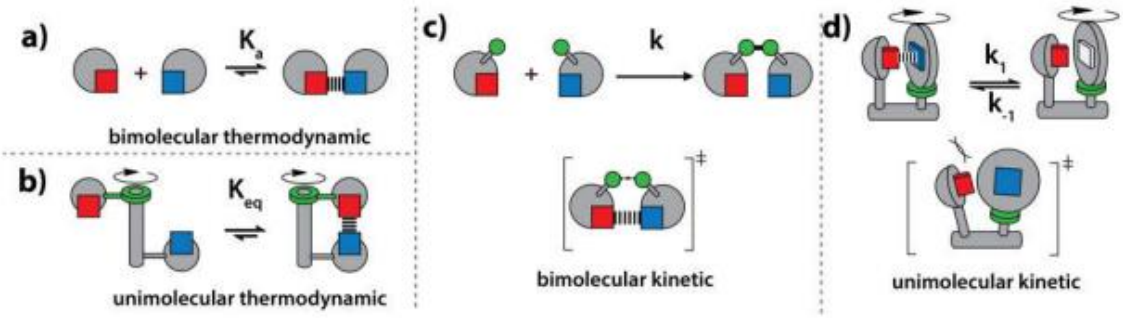

Figure 1.2. Different Schematic representations of the four types of model systems: bimolecular thermodynamic (a), unimolecular thermodynamic (b), bimolecular kinetic (c), and unimolecular kinetic (d).

Several methods can be used to quantify hydrogen bonding interactions. These methods can be grouped into four broad categories based on the types of model systems: (a) thermodynamic bimolecular, (b) thermodynamic unimolecular, (c) kinetic bimolecular,

and (d) kinetic unimolecular (Figure 1.2).[24] However, I will focus on kinetic unimolecular (molecular rotor) and thermodynamic unimolecular (molecular balance) methods. The measurement of hydrogen bonding interactions can be challenging due to the difficulty in separating the contributions of the hydrogen bond from other interactions and biases in a system. A molecular rotor can be used to overcome these difficulties, by separating the hydrogen bonding interactions from the other forces involved. The molecular rotor is designed on the premise that, in a typical chemical process, the transition state must be traversed, even in cases of bond rotation, when transitioning from starting materials to final products.

The molecular rotor method offers a number of advantages over the bimolecular measurement methods. First, bond rotation is a zero-order kinetic process, which allows for easy measurement and analysis of the rate of rotation by dynamic NMR methods. Second, the bond rotation transition states are simple and well defined, and as such, can be easily and accurately modeled using DFT calculations. Third, these rotors are easy to synthesize, and modulation of the hydrogen bond strength can be easily accomplished.

1.3.5 MOLECULAR ROTOR DESIGN

The molecular rotors were designed on the premise that the bond rotation process is similar to a typical chemical reaction going from starting material to product through a transition state (Figure 1.3). The molecular rotors interconvert between a *syn*-conformation and an anti-conformation via a planar transition state, where the ortho-R-group and imide carbonyl oxygen are close together forming stabilizing non-covalent and destabilizing steric interactions (Figure 1.4). The *N*-arylimide based molecular rotors offered a simple and reliable method for quantifying the strength of hydrogen bonding interactions. The *N*-

arylimide rotors were constructed and equipped with hydrogen bond donor (RNH) and acceptor (C=O). These rotors were used to quantify the strength of the TS hydrogen bonds. A control series which only forms the destabilizing steric interactions was also designed to isolate the HB interactions.

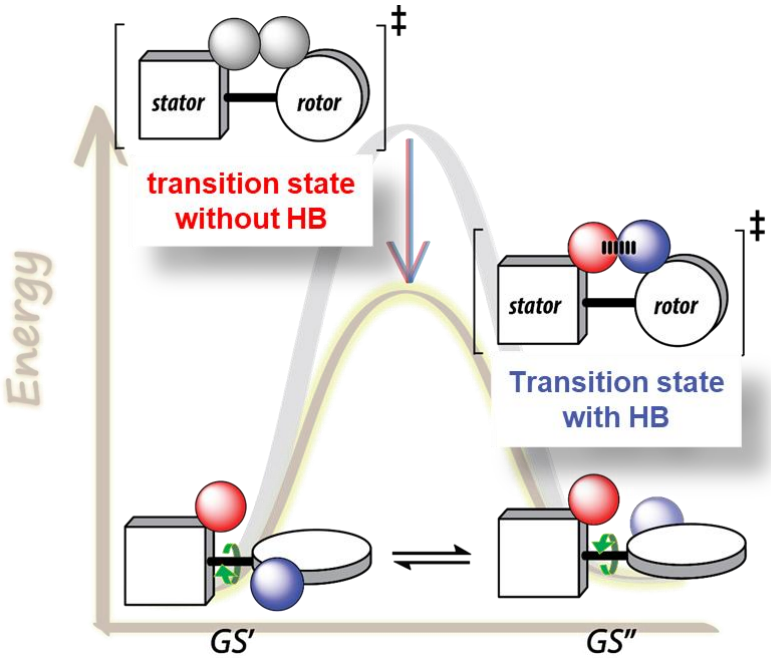

Figure 1.3. Pictorial representation of TS stabilization.

The *N*-phenylimide framework is designed in such a way that a substituted benzene ring is connected to a 5-membered succinimide ring through a C_{aryl}-N_{imide} bond (Figure 1.4). The hydrogen bonding functionally is the R-group attached to the *ortho*-position of the *N*-phenyl unit and the oxygen of the succinimide C=O group. A strong TS hydrogen bond will lower the rotational barrier and lead to faster rotation while a weak interaction will lead to slow rotation. The R′NH•••O=C strengths were modulated by varying the electronic nature of the R′-group attached to the nitrogen.

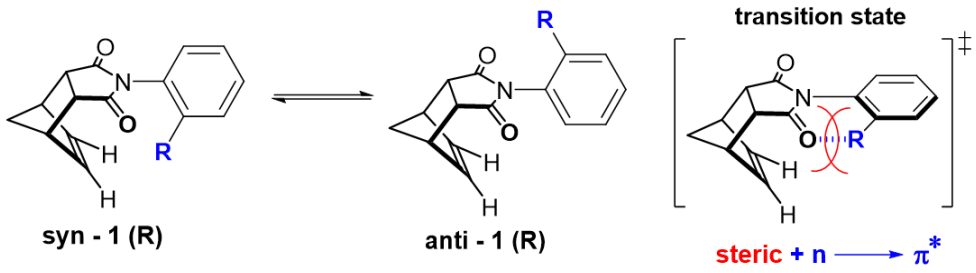

Figure 1.4. Interconversion of molecular rotor from *syn*- to *anti*- conformer

Dynamic NMR (EXSY) experiments were performed to ascertain the rate of interconversion (k_{ex}) from *syn*-to-*anti* and *anti*-to-*syn*. A graph of the exchange rates per temperature vs inverse temperature fitted to Eyring's equation provides the energy parameters, $\Delta H^{\ddagger}$ and $\Delta S^{\ddagger}$ which will ultimately be used in determining $\Delta G^{\ddagger}$ (Figure 1.5).

$$\ln\left(\frac{k_{ex}}{T}\right) = \frac{-\Delta H^{\ddagger}}{R} \times \frac{1}{T} + \ln\left(\frac{k_B}{h}\right) + \frac{-\Delta S^{\ddagger}}{R} \quad \textbf{(Eqn S1)}$$

$$\Delta G^{\ddagger} = \Delta H^{\ddagger} - T \times \Delta S^{\ddagger} \quad \textbf{(Eqn S2)}$$

$\Delta G^{\ddagger}$	= Gibb's free energy of the rotational barrier
R	= gas constant
T	= temperature
k_B	= Boltzmann's constant
k_{ex}	= exchange rate
$\Delta H^{\ddagger}$	= enthalpy change in the rotational barrier
$\Delta S^{\ddagger}$	= entropy change in the rotational barrier

Figure 1.5. Eyring's and Gibb's Free Energy equations.

The difference in $\Delta G^{\ddagger}$ between the hydrogen bonding and non-hydrogen bonding control rotors gives the TS stabilizing effect ($\Delta\Delta G^{\ddagger}$) of the hydrogen bonding interaction. To investigate the fundamental forces governing the hydrogen bonding interaction in the transition state, $\Delta\Delta G^{\ddagger}$ is correlated with parameters such as electrostatics, charge-transfer, dispersion and induction.

1.4 HYDROGEN BOND DESCRIPTORS

Hydrogen bond descriptors are parameters used to quantitatively describe the strength and properties of hydrogen bonds. These descriptors allow us to predict and

analyze the strength of hydrogen bonds and their effects on molecular properties such as reactivity and structure. By correlating these descriptors with experimentally measured data, we can gain insights into the origins of hydrogen bonds. Some common hydrogen bond descriptors used to investigate hydrogen bonding interactions include electrostatic potential (ESP), pKa, α-value, β-value, Hammett sigma parameter (σ).

1.4.1 ELECTROSTATIC POTENTIAL SURFACE (ESP)

ESP values can be measured from quantum chemical calculations of the electrostatic potential (ESP) at various points in space around a molecule.[25] This is typically done by dividing the molecule into small regions, called grid points, and calculating the electrostatic potential at each grid point. The resulting ESP map can be visualized as a surface or contour plot, with regions of positive electrostatic potential (blue) and negative electrostatic potential (red) (Figure 1.6). ESP calculations can be used to probe the contribution of electrostatics in a hydrogen bonding interaction by identifying the regions of positive and negative electrostatic potential around the hydrogen bond acceptor and donor atoms.[26,27] The magnitude of the electrostatic potential (ESP) will be measured at the point on the surface of the R-group nearest to the imide C=O oxygen. This measurement will be correlated to the rotational barrier of the molecular rotor. A good correlation between rotational barrier and ESP suggests that electrostatics is important in the hydrogen bonding interaction.

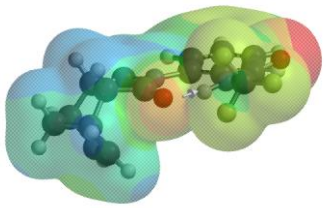

Figure 1.6. ESP map of a molecular rotor **3** ($NHCOCF_3$)

1.4.2 pKa

The pKa of the hydrogen bond donor has been shown to correlate with the strength of the hydrogen bond. This parameter can provide insight into how well a functional group can act as a proton donor in hydrogen bonding. Groups with low pKa are expected to form a stronger hydrogen bond while groups with high pKa are expected to form a weaker hydrogen bond.[28] The strength of hydrogen bond can be modulated by varying the pKa of the hydrogen bond donor group.

1.4.3 α-VALUE

This is an empirical measure of the hydrogen bond donor ability of a functional group in a molecule.[21] α-value is a dimensionless constant that can be used to quantify the donating ability of a hydrogen bond donor group in a molecule. A higher α-value indicates a strong hydrogen bond donor character while a low α-value indicates a weak hydrogen bond donor character.[21]

1.4.4 β-VALUE

The beta value provides an empirical measurement of the hydrogen bond acceptor ability, with higher values indicating a stronger ability to act as an acceptor in hydrogen bonding interactions.

1.4.5 HAMMETT SIGMA PARAMETER (σ)

This parameter is a measure of the electrostatic effects of substituents on a benzene ring. A substituent can alter the phenyl ring's ability to donate or withdraw electrons relative to the benzene when attached to the para- or meta- positions. The Hammett substituent parameters can be used in non-benzene systems such as the R′s of the ortho R′NH groups

in our hydrogen bonding rotors. Hence, Hammett sigma parameter can be correlated with energy barrier to ascertain electrostatic contributions in a hydrogen bonding interaction.

1.5 PAULI REPULSION

Pauli Repulsion is not an electrostatic parameter but rather a steric parameter that derives from the Pauli exclusion principle, which states that no two electrons can have identical quantum numbers.[29] In other words, identical electrons (i.e., electrons with the same spin) cannot be in the same orbital. This forms the fundamental basis for repulsive steric interactions. During a hydrogen bond formation, the filled shells of the hydrogen bond donor and acceptor heavy atoms encroach on each other's space, thereby leading to significant Pauli repulsion. Squeezing a hydrogen bonding proton between the heavy atoms further increases the repulsive effect. This repulsive term must be overcome by attractive terms to form a stable HB. SAPT will be utilized to decompose the total interaction energy into individual components including Pauli repulsion.[30]

1.6 CHARGE TRANSFER (ORBITAL – ORBITAL INTERACTION)

Charge transfer is a stabilizing interaction in which electron density is transferred from one orbital (HOMO) to another (LUMO) in different atoms. In the formation of hydrogen bond, charge is transferred from the bonding orbital of the heavy atom of the hydrogen bond acceptor to the σ*-orbital of the hydrogen bond donor.[31,32] Larger orbitals and smaller differences in orbital energies can enhance orbital – orbital interactions. The former is largely dependent on the orientation or geometry of the hydrogen bond donor and acceptor, while the latter can be modulated by attaching and varying the substituents on the hydrogen bonding system.[25] Natural Bond Order (NBO) can be used to estimate the contribution of charge transfer to hydrogen bonding. A good correlation between rotational barriers and

NBO energies suggests that charge transfer is an important component of the hydrogen bonding interaction.

1.7 DISPERSION

Dispersion forces are caused by the temporary and fluctuating polarization of the electrons within a molecule or atom, which creates a local dipole moment. When two such dipoles approach each other, the attractive forces between the positive and negative ends of the dipoles give rise to dispersion forces. These forces are usually the weakest term in hydrogen bonding interactions.[33] We will not correlate rotational barrier to dispersion parameters because of their minor contribution to hydrogen bonding interactions.

1.8 INDUCTION

Induction occurs when an electron withdrawing group that is connected to a hydrogen bonding system pulls electron density from the hydrogen bonding proton in that system, thereby creating a positive charge on the proton. This positive charge then engenders a temporary attractive interaction with the heavy atom of the hydrogen bond acceptor. Like dispersion, induction is a minor contributing term in hydrogen bonding interactions.[21] Hence, we will not be correlating rotational barrier induction parameter.

CHAPTER 2

STERICALLY COMPRESSED HYDROGEN BOND

2.1 ABSTRACT

Sterically compressed hydrogen bonds are defined as hydrogen bonds where the repulsive component has been reduced as a result of a structural constraint.[34] This study demonstrates that targeting the repulsive term of the hydrogen bonding interaction can lead to substantial enhancements in interaction energies. This method can significantly decrease transition states and enhance reaction rates. The approach involves forming sterically compressed hydrogen bonds by holding the donor and acceptor heavy atoms close together prior to bond formation. We designed a molecular rotor with a rigid framework that enables the formation of short intramolecular hydrogen bonds in the bond rotation transition state (Figure 2.1). The resulting hydrogen bonds strongly stabilized the transition states, leading to remarkable increases in the rotation rate. We synthesized a series of rotors to test whether the observed kinetic effects were due to steric compression. Our findings suggest that steric compression was the primary factor responsible for the larger-than-expected transition state hydrogen bond stabilization. Therefore, we conclude that steric compression is an effective means of enhancing the strength of hydrogen bonds in transition states that is complementary to the traditional strategies of enhancing the attractive components.

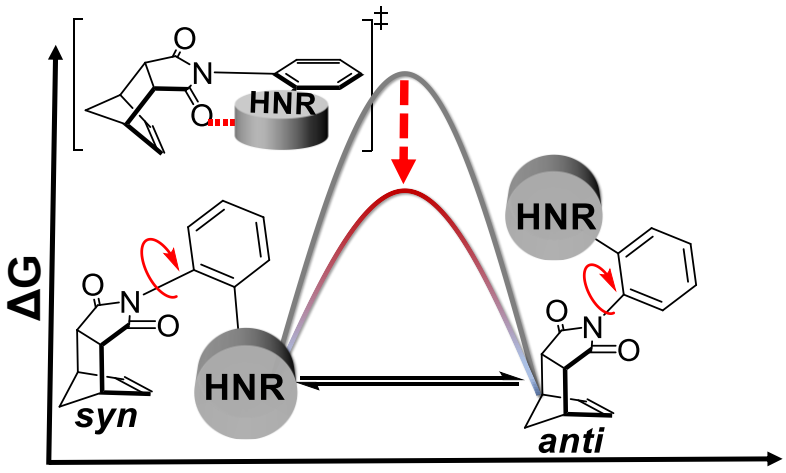

Figure 2.1. Molecular rotor showing TS structure and interconverting *syn*- and *anti*-

2.2 ENHANCING HYDROGEN BOND STRENGTH THROUGH STERIC COMPRESSION

Systems where the heavy atoms are already compressed experience unusually large interaction energies (Figure 2.2).[21,52,53,55] This is because a framework holds the hydrogen bond donor and acceptor atoms closer than the sum of their vdW radii, prestressing the systems and reducing the steric penalty for HB formation (Figure 2.3 B). Hydrogen bonds have received a lot of attention because of the role they play in determining the properties of water and many biological processes.[1,2,3,4,5,6] For example, enzymes use hydrogen bonds in their active sites to stabilize transition states and catalyze biochemical transformations. Similarly, organo-catalysts have been designed to use hydrogen bonds to catalyze synthetic reactions.[35,36,37,38,39,40,41] The traditional strategy for enhancing hydrogen bond strength involves enhancing the attractive component of hydrogen bonds such as electrostatics and orbital-orbital interactions.[42,43,44,45] For example, electron withdrawing groups on the HB donor and electron-donating groups on the hydrogen bond acceptor have been shown to enhance the strength of hydrogen bonds. In this work, we demonstrate that large enhancements of hydrogen bonding interaction energies can be derived from targeting the repulsive component of the hydrogen bonding interaction and demonstrate that this approach can be applied to dramatically lower transition states and increase rates of reactions.

All bonding interactions, including non-covalent interactions, are composed of opposing attractive and repulsive components that are individually much larger than the overall bonding interaction strength. For example, in Figure 2.3, the relative magnitudes of the attractive (green) and repulsive (red) forces are of similar magnitude and so they almost

cancel, leaving a small net interaction energy (blue). The net interaction energy can be increased by either strengthening the attractive component (Figure 2.3B) or reducing the repulsive component (Figure 2.3B). While the former is a common method of enhancing the net interaction energy, we will examine the viability and potential of the second method in this work. Since the repulsive component is large, even a small reduction can lead to large enhancements in the net interaction energies. An example is shown in Figure 2.3B. The energies of the attractive (green) and repulsive (red) components are more than the net interaction energy (blue).[46]

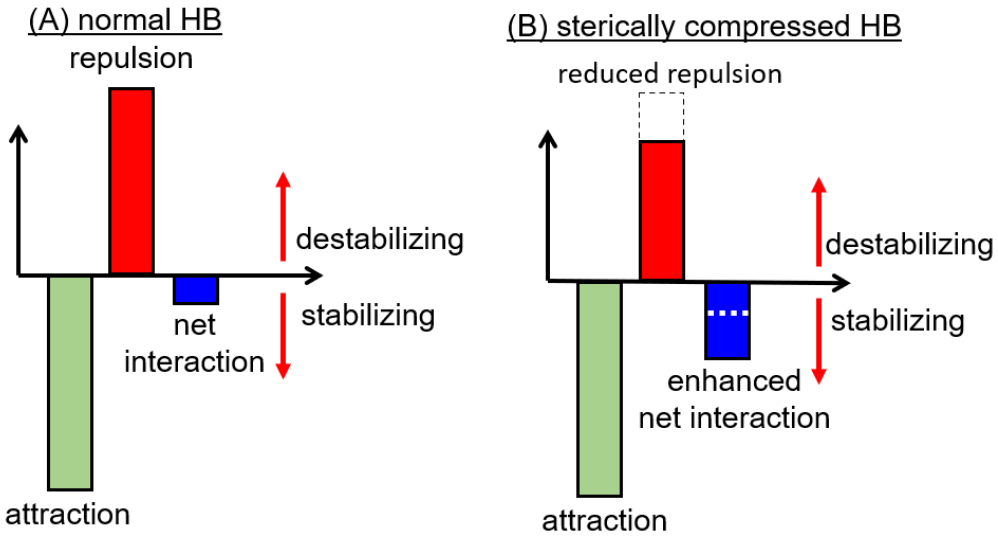

Figure 2.2. Enhancing net interaction by reducing the repulsive components.

To target the repulsive term, a good understanding of the origins of the component in hydrogen bonds is paramount. Hydrogen bonds position the interacting atoms at distances considerably shorter than the sum of their vdW radii.[47,48,49] For example, in crystallography, hydrogen bonds are commonly identified as protons between

electronegative atoms which are closer than the sum distance of their van der Waal radii.[47,48,49] An example is shown in Figure 2.4 of the water dimer. Not only is the hydrogen bonding proton within the vdW radii of the heavy

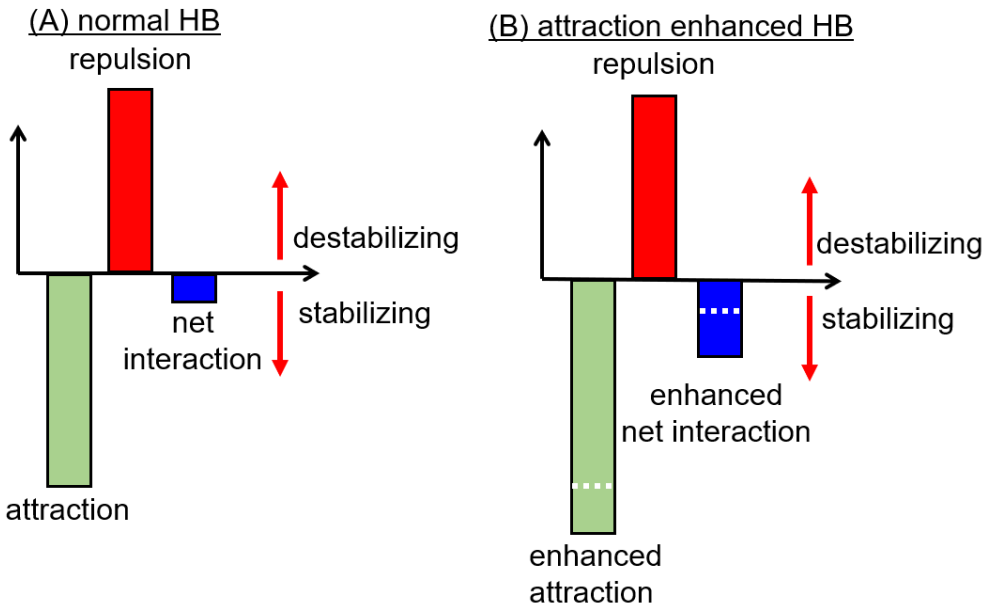

Figure 2.3. Enhancing net interaction energy by enhancing the attractive components.

atom of the hydrogen bond acceptor (< 2.7 Å) but the two oxygen atoms of the HB donor and acceptor are also within each other's vdW radii (< 3.0 Å).[50,51] Thus, there is significant vdW repulsion that must be overcome to form a stabilizing hydrogen bond.

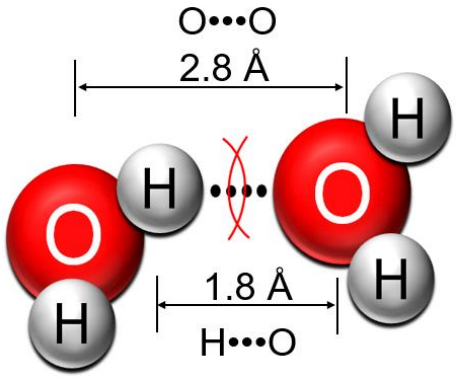

Figure 2.4. Hydrogen bond between two water molecules showing the internuclear distance (1.8 Å) between hydrogen (white, vdW radius 1.2 Å) and oxygen (red, vdW radius 1.5 Å) was less than their summed vdW radii (2.7 Å). Also, the oxygen atoms internuclear distance (red, 2.8 Å) is less than their summed

Examples of the large enhancements in HB strength that are possible from targeting the repulsive component are proton sponge and analogs,[52,53,54,55] which are known for their unusually high predilection for protons. Their proton affinity is due to the strain in the system prior to the hydrogen bond formation from the rigid naphthalene framework holding the diamine groups at a very close proximity. In the proton sponge, the nitrogen heavy atoms are at distances less than the sum of their vdW radii prior to protonation. In Figure 2.5 for instance, the N•••N distance (2.75 Å) for the unprotonated proton sponge is less than the sum of the vdW radii (3.10 Å).[54] This steric compression of the heavy atoms reduces the additional steric interactions needed to form the HB on protonation. This ultimately leads to enhanced basicity for the proton sponge.

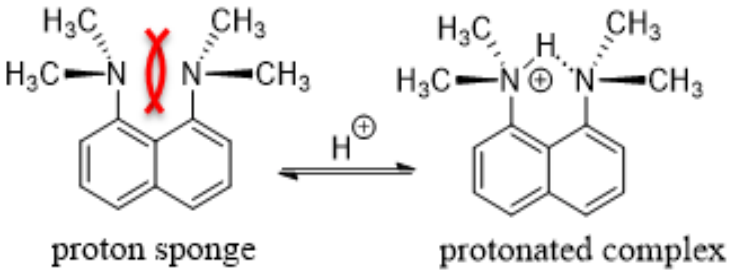

Figure 2.5. Reduction of steric repulsion in proton sponge by the strain in the unprotonated proton sponge.

Hansen used NMR chemical shifts to study and measure intramolecular HB interaction strengths.[34] He observed that hydrogen bond strength can be greatly enhanced when the heavy atoms are forced together within their summed vdW radii. He found out that as the phenolic and aldehyde oxygen atoms distance was reduced, the hydrogen bond strength increased. He was able to systematically push the hydrogen bonding oxygen atoms closer toward each other. By increasing the steric size of the adjacent R-groups, the rigid covalent framework helps overcome the sterics of the system. He confirmed this pre-stressed sterics of the system by monitoring the O•••O distances. Thus, the hydrogen bond does not need to take on the full repulsive component. The shorter the O•••O distance, the greater the reduction in HB repulsive component, and the greater the HB strength. A large enhancement, 9.4 kcal/mol, was observed.

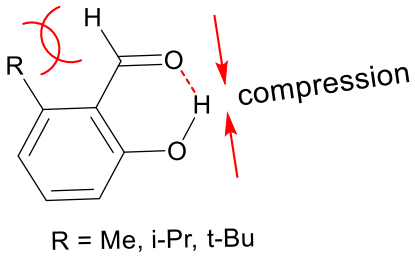

Figure 2.6. Increasing the R-group will lead to compression of the two oxygen atoms thereby resulting in an enhanced hydrogen bond strength.

Similarly, Perrin showed that the high proton affinity of the (±)-α,α′-di-*tert*-butylsuccinate is the result of a reduction in the repulsive component of the strong hydrogen bond formed by protonation of the dianion (Figure 2.7).[56] In the unprotonated form, repulsion of the heavy atoms is pre-formed due to the constraining of the oxygen anions in close proximity to each other, thereby, resulting in an enhanced net interaction.

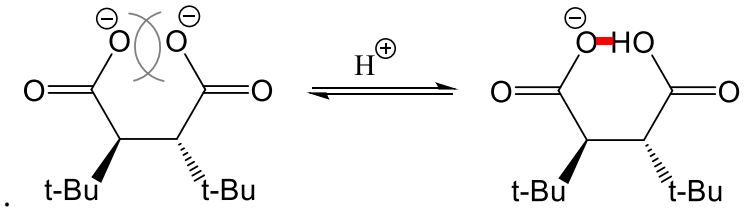

Figure 2.7. The preformed sterics in the dianion is the reason for the high proton affinity.

Whereas all the aforementioned examples measured the thermodynamic effects of sterically compressed HBs, we want to test whether we can use sterically compressed HBs to effect kinetics and reaction rates. Our approach was to examine the kinetic effects of HBs on the bond rotation TS of our molecular rotors. In our earlier publication, we investigated the kinetic effects of HBs (OH•••O=C) using phenolic molecular rotors and observed much larger than expected rate enhancements due to the formation of a HB in the bond rotation TS (Figure 2.8).[46] We hypothesized that these were due to a reduction in the repulsive component of the hydrogen bond.

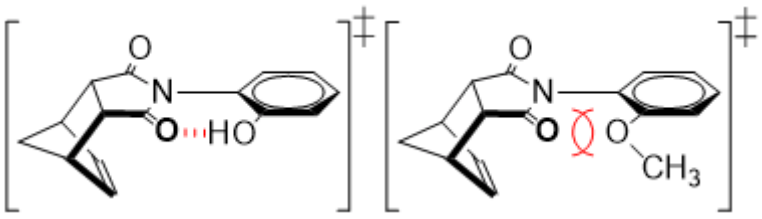

Figure 2.8. TS structures of our hydrogen bonding phenol rotor (left) and control; non-hydrogen bonding rotor (right).

Our goal, therefore, was to confirm that the reason for the larger than expected TS hydrogen bond stabilization in our rotors is due the formation of a sterically compressed hydrogen bond and to demonstrate that steric compression can be used to enhance the strength of hydrogens in TS and affect reaction rates. To test this hypothesis, we first examined the alternative explanation that the unusually strong HB in our rotors was due to an increase in the attractive component. We found that enhancements in the attractive component were insufficient to explain kinetic HB effects in our rotors.

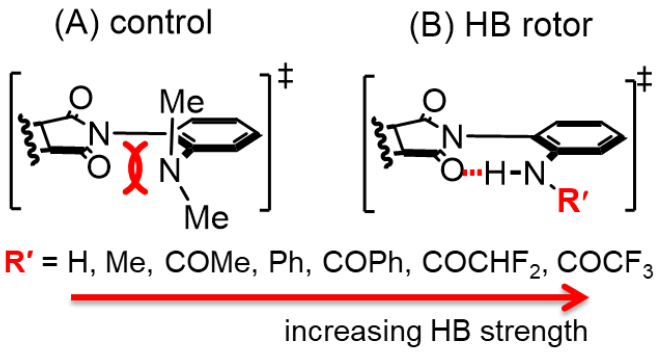

Figure 2.9. Control and HB rotors design to measure the kinetic effects of C=O•••HN.

Our studies began with the design of a new rotor which can modulate the attractive electrostatic component over a wider dynamic range. In our previous OH rotor system, we could not completely rule out electrostatic effects because of the limited range of values for the electrostatic component. In the OH rotors, the electron-withdrawing groups could not be directly connected to the hydrogen bond donor OH group. To address this challenge, we switched to an RNH•••O=C hydrogen bonding system where electron-withdrawing and electron-donating substituents (R) could be attached directly to the hydrogen bond donor nitrogen atom. (Figure 2.9). In control rotor **8**, two methyl groups were attached to the

nitrogen atom. Thus, the rotor lacked a hydrogen bonding proton preventing the formation of HB in the TS. The synthesis of rotors **2** – **5** is a 2-step process (Scheme 1). First, 1,2-Dibromobenzene (**10**) was reacted with norbornene anhydride, **9**, and the resulting aniline rotor **1** was reacted with a variety of acetylating agents to give rotors **2** - **5**. The synthesis of rotors **6** and **7** involves a one-step thermal condensation of norbornene anhydride (**9**) with a corresponding *ortho*-substituted aniline (**10a** and **10b**). Lastly, the synthesis of the control rotor **8** is a one-step thermal condensation of norbornene anhydride (**9**) and aniline (**10c**).

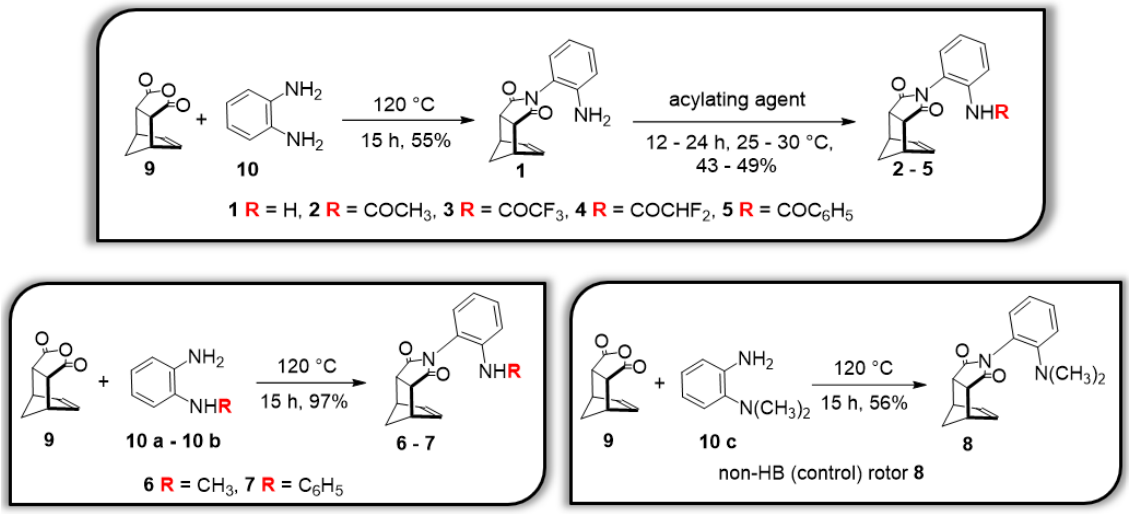

Scheme 2.1 Synthesis of molecular rotors **1 – 7** and control **8**

DFT calculations of the bond rotation TS structures were carried out at B3LYP-D3 level of theory and 6-311G* basis set using the Spartan18 program. The presence of the hydrogen bonding proton between the C=O group and the nitrogen atom suggests that a compressed HB is formed in the TS (Figure 2.10). The OHN bond angle of 163° and O—N internuclear distance of 2.58 Å are consistent with literature reports of similar

compressed hydrogen bonding systems.[45,57,58] Normal hydrogen bonds have O-to-N internuclear distances of 2.6 – 3.2 Å. Additionally, the O•••H distance of 1.61 Å was well within the sum of the van der Waal radii of O and H (1.52 + 1.20 = 2.72 Å).[59,60] This further suggests the formation of a compressed hydrogen bond.

The rotational barriers of the rotors in tetrachloromethane (TCE) and dichloroethane (DCE) were measured (Table 2.1) using EXSY ^{1}H-NMR and showed good correlation with the calculated barriers suggesting that the calculated barriers were accurate. The rotor with the most electron-withdrawing group (R = $COCF_3$) formed the strongest HB, lowering the barrier by 6.4 kcal/mol. These kinetic effects were about 13 to 4 times larger than the 0.5 – 1.5 kcal/mol stabilization observed for similar hydrogen bonds in non-compressed systems.[46,61]

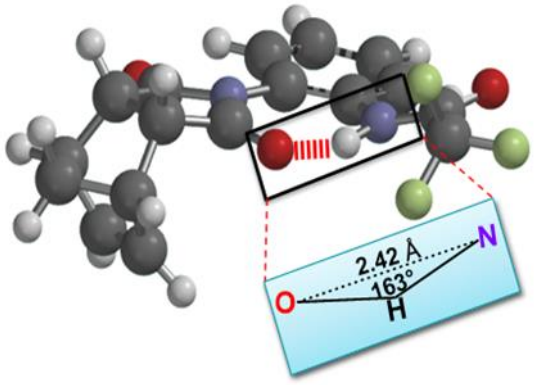

Figure 2.10. 3D model TS structure of rotor **5**

The magnitude of the TS stabilization was correlated with the expected hydrogen bond strengths based on the pKa of the NH groups. Hydrogen bond strengths show good agreement with pKa of HB rotors.[62] The change in rotational barrier (ΔΔG) of each of the rotors was determined by subtracting the rotational barrier of a hydrogen bonding rotor

from that of the non-hydrogen bonding control **8** and plotted against the pKa of the NH group (Figure 2.12B). Although the pKa was varied by 18 orders of magnitude, changes in rotational barriers only varied over a narrow range of less than 2 kcal/mol (Figure 2.12B). Even rotor **1** with R = NH_2, which normally forms a very weak hydrogen bond, showed significant TS stabilization relative to the non-hydrogen bonding control rotor **8**. This suggests that the main source of the TS stabilization is not the strengthening of the electrostatic component as electrostatics have good correlation with pKa.[21]

To show that the large TS stabilization is mainly due to repulsion, we employed Fragment Intramolecular-Symmetry Adaptation Perturbation Theory (FI-SAPT). FI-SAPT is a computational method utilized for examining interactions between different fragments within a molecule. By dividing the molecule into separate fragments and applying perturbation theory, FI-SAPT calculates the interaction energy between these fragments. We applied FI-SAPT to determine the interaction energy of the intramolecular C=O•••HNR interaction in the TS of our rotors.[63,64] To validate that the FI-SAPT calculations were accurately reproducing the intramolecular TS interactions, $FI\text{-}SAPT_{total}$ (jun-cc-pvdz) energies were shown to strongly correlate with the experimentally measured barriers (Figure 2.11, $R^2 = 0.81$). This suggests that the variations in the rotational barriers are due to variations in the TS structures and that we can largely ignore variations in the GS structures.

Table 2.1. Results of experimental and calculated rotational barriers of rotors and pKa of their corresponding R-groups.

Rotor	R-group	Experimental Rotational Barrier (kcal/mol)	Rotational Barrier from Computation (kcal/mol)	pKa of R-group (DMSO)[65]
1	H	16.4	15.3	30.6
2	$COCH_3$	16.5	15.0	21.5
3	$COCF_3$	15.6	16.0	12.6
4	$COCHF_2$	14.9	17.6	13.8
5	COC_6H_6	16.8	17.3	18.8
6	CH_3	17.5	15.8	29.5
7	C_6H_5	17.7	17.1	25.0
8	$N(CH_3)_2$	22.0	21.1	--

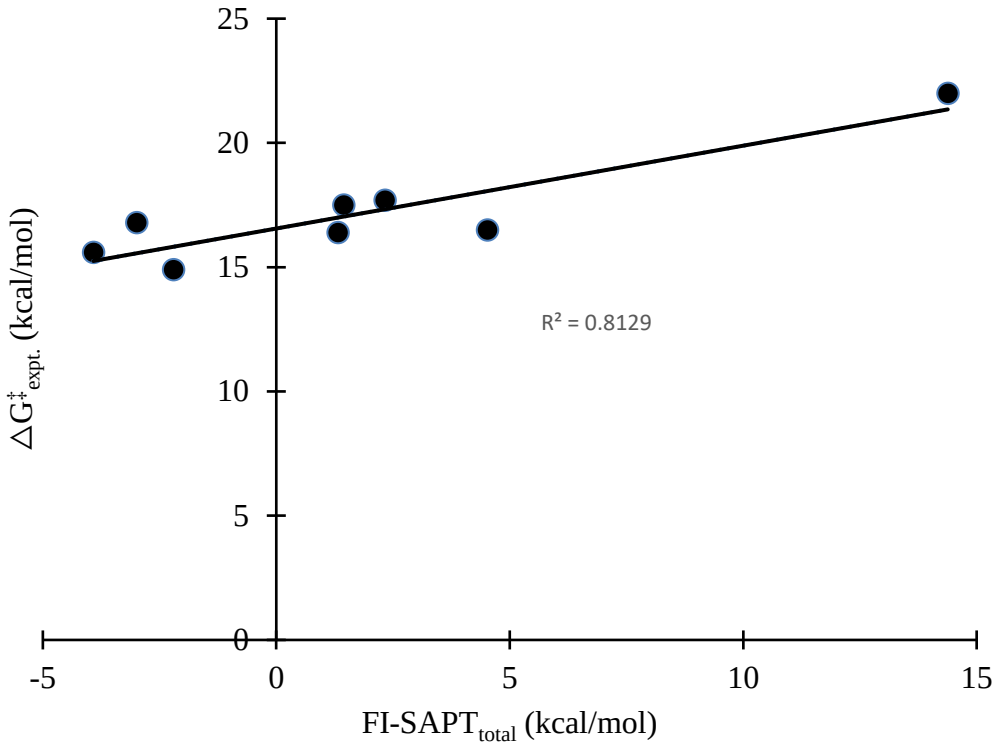

Figure 2.11. Correlation between FI-SAPT$_{total}$ and experimentally measured barriers.

A

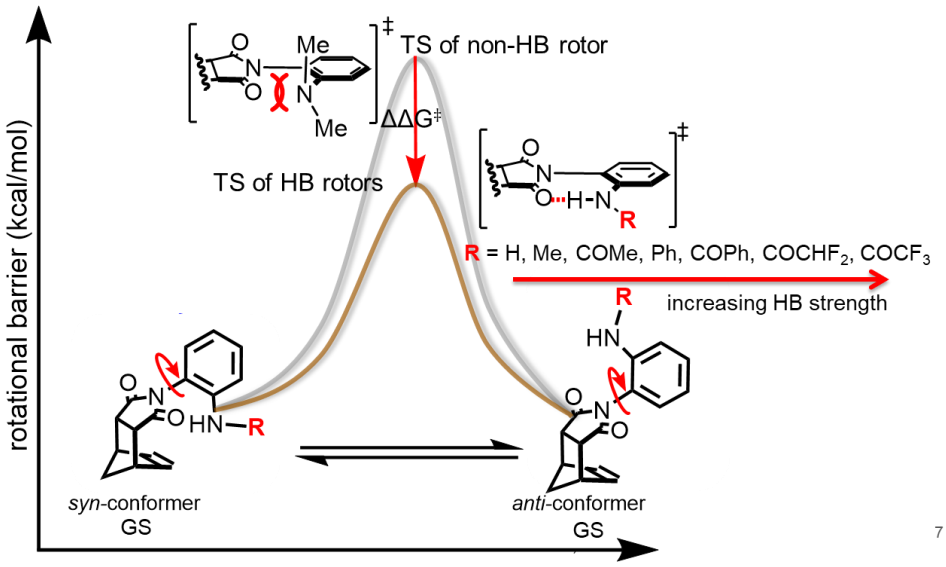

B

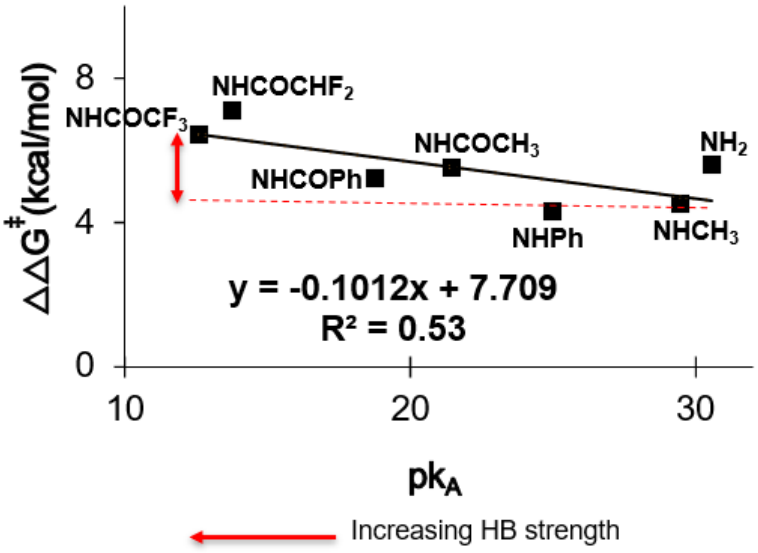

Figure 2.12. Plots showing (A) varying of electrostatic component by electron-withdrawing groups and (B) correlation between HB strength and TS stabilization.

Next, FI-SAPT calculations were conducted on both the non-HB and HB structures of our compressed system and a comparable non-compressed system (Figure 2.13 A). The attractive and repulsive components in both systems were compared against each other to ascertain the source of the large TS stabilization. In order to isolate the effects of HB, the FI-SAPT$_{total}$ energy of the non-HB was subtracted from that of the HB, and the resulting energy difference was compared between the two systems. Furthermore, the energy difference between the attractive components of the non-HB and HB was calculated by subtracting the FI-SAPT energy of the non-HB from that of the HB, and this difference was compared in both systems. Likewise, the energy difference between the repulsive components of the non-HB and HB was determined by subtracting the FI-SAPT energy of the non-HB from that of the HB, and this difference was also compared in both systems. The structures of the non-compressed system depicted in Figure 2.13A (top) represent an equilibrium system in which hydrogen bonding occurs between similar functional groups on separate aniline and *N*-succinimide molecules. When the molecules are positioned close together (O•••N = 2.6 Å) on the right-hand side of the equilibrium, hydrogen bonding interactions are formed, while on the left-hand side, the molecules are too far apart (O•••N = 6.0 Å), and no such interactions occur. Consequently, the difference in FI-SAPT$_{total}$ energies between the two sides of the equilibrium accounts for both attractive and repulsive components of the hydrogen bonding interaction.

In contrast, the structures illustrated in Figure 2.13A (bottom) correspond to the kinetic structures of our molecular rotor, which exemplifies a compressed system. In this rotor, the interacting groups are held closely together by the rigid *N*-phenylimide framework. Although the right structure (HB) of the compressed system (Figure 2.13 A,

bottom) forms similar hydrogen bonding interactions as the top non-compressed system, the left control (non-HB) structure does not. However, because the interacting groups remain in close proximity due to the rigid framework of the rotor, significant repulsive interactions still occur. The carbonyl oxygen and the amine nitrogen are located closer to each other (O•••N = 2.6 Å) than the sum of their vdW radii (3.07 Å). Thus, the △FI-$SAPT_{total}$ includes all the attractive components of the hydrogen bond but only a fraction of the repulsive components. As a result, the energy difference in the compressed system may be substantially greater than that of the non-compressed system.

The FI-SAPT energies of the attractive components were comparable in both the non-compressed and compressed systems, although the non-compressed systems exhibited a slightly higher FI-SAPT energy. This discrepancy can be attributed to the absence of stabilizing dispersion and induction forces within the non-HB component of the non-compressed system, resulting from the large separation between the carbonyl group and nitrogen atom. In contrast, the compressed system benefits from the presence of these dispersion and inductive forces within its non-HB component due to the proximity of the interacting groups. These additional attractive forces in the non-HB component of the compressed system contribute to the slightly reduced attractive component observed in the compressed system.

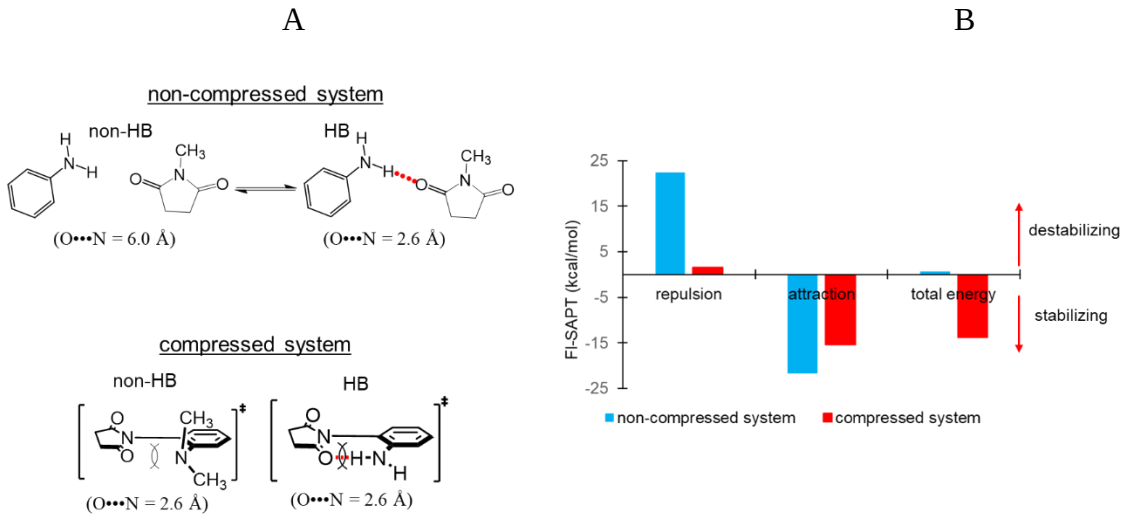

Figure 2.13. (A) Structures of HB and non-HB of non-compressed and compressed systems and (B) FI-SAPT$_{total}$ energies in non-compressed and compreesed systems.

By comparing the FI-SAPT$_{total}$ energies of the non-compressed and compressed systems (Figure 2.13 B), it is evident that the compressed system exhibits a significantly greater stabilization of 13.4 kcal/mol (red bar) in contrast to the non-compressed system of only 0.8 kcal/mol (blue bar). The significant stabilization in the compressed system is mainly due to the considerable reduction in the repulsive term, indicating that repulsion is primarily responsible for the large TS stabilization observed in our molecular rotor system. This is because the large attractive component overcomes minimal repulsion resulting in substantial TS stabilization. Conversely, the FI-SAPT$_{total}$ energy in the non-compressed system is marginal indicating a weak stabilization. This weak stabilization is a consequent of the large repulsive component nearly canceling out the attractive component in the non-compressed system. In conclusion, reduction in repulsion is the reason for the larger than expected TS hydrogen bond stabilization in our molecular rotor system. We have also

demonstrated that steric compression can be used to enhance the strength of hydrogen bonds.

2.3 SUPPLEMENTAL INFORMATION

2.3.1 GENERAL EXPERIMENTAL INFORMATION

NMR spectra were recorded on Bruker 500 MHz and Bruker 400 MHz spectrometers. Chemical shifts are reported in ppm (δ) referenced to the solvent residue. All spectra given for characterization purposes were taken at room temperature. All chemicals and solvents were purchased from commercial suppliers and used as received. Flash chromatography was performed using silica gel from Sorbent Technologies (60 Å, 200 – 400 mesh).

2.3.2 SYNTHESIS

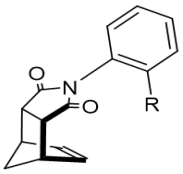

1 R = NH_2, **2** R = $NHCOCH_3$, **3** R = $NHCOCF_3$, **4** R = $NHCOCHF_2$, **5** R = $NHCOC_6H_5$, **6** R = $NHCH_3$, **7** R = NHC_6H_5
8 R = $N(CH_3)_2$

Figure 2.14. Molecular rotors used for the study

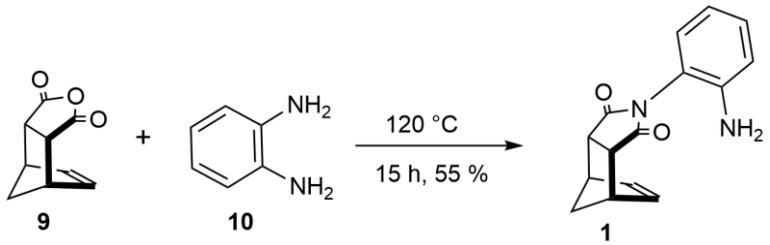

9 **10** **1**

Scheme 2.2. Molecular rotor **1**

cis-5-norbornene-*endo*-2,3-dicarboxylic anhydride **9** (200 mg, 1.22 mmol) and benzene-1,2-diamine **10** (145 mg, 1.34 mmol) were added to a 20-dram vial along with a magnetic stir bar. The vial was then capped and heated to 120 °C in a silicon oil bath for 15 hours while stirring. After letting the vial cool to room temperature, the crude material was purified by column chromatography (ethyl acetate/hexanes = 4:1, v/v) to give a brown solid product **1** (170 mg, 55 %). ^{1}H NMR (400 MHz, $CDCl_3$) δ 7.26 - 7.16 (m, 1 H), 6.91 - 6.77 (m, 3 H), 6.35 (s, 2 H major), 6.27 (s, 2 H minor), 3.76 (br, s, 2 H), 3.50 - 3.42 (m, 4 H), 1.82 (d, *J* = 8.8 Hz, 1 H major), 1.76 (d, *J* = 8.8 Hz, 1 H minor), 1.63 (dd, *J* = 8.8 Hz, 1 H major), 1.57 (dd, *J* = 8.8 Hz, 1 H minor). ^{13}C NMR (101 MHz, $CDCl_3$) δ 177.09, 176.53, 142.68, 135.53, 134.65, 130.31, 130.17, 128.92, 128.44, 119.72, 119.00, 118.26, 117.89, 117.14, 52.69, 52.34, 46.64, 45.89, 45.58, 45.31.

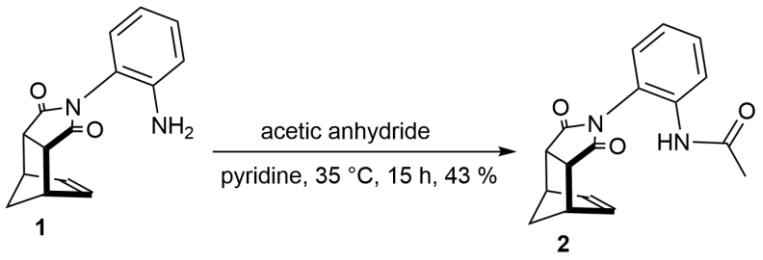

Scheme 2.3. Preparation of rotor **2**

Amine rotor **1** (100 mg, 0.39 mmol), acetic anhydride (7 mL, 74.04 mmol) and pyridine (7 mL, 86.9) were added to a 100 mL round bottom flask along with a magnetic stir bar and refluxed for 15 hours. After letting the round bottom flask cool to room temperature, cold finger technique was then used to remove unreacted acetic anhydride and

the crude material was purified by column chromatography (ethyl acetate/hexanes = 30:1, v/v) to give an off-white solid product **2** (50 mg, 43 %). ^{1}H NMR (300 MHz, $CDCl_3$) δ 8.12 (d, *J* = 8.2 Hz, 1 H major), 7.83 (d, *J* = 8.2 Hz, 1 H minor), 7.40 (dd, *J* = 7.1 and 6.8 Hz, 1 H), 7.20 (dd, *J* = 8.2 and 7.9 Hz, 1 H), 7.06 (d, *J* = 7.4 Hz, 1 H major), 6.99 (d, *J* = 7.4 Hz, 1 H minor), 6.36 (s, 2 H major), 6.28 (s, 2H minor), 5.34 (s, br, 1 H), 3.54 (s, 4 H major), 3.48 (s, 4 H minor), 1.90 - 1.78 (m, 1 H), 1.73 - 1.60 (m, 1 H), 1.58 (s, 3 H). ^{13}C NMR (101 MHz, DMSO) δ 177.27, 168.78, 136.03, 135.34, 135.10, 129.40, 129.12, 124.25, 123.52, 52.29, 46.34, 45.21, 24.38.

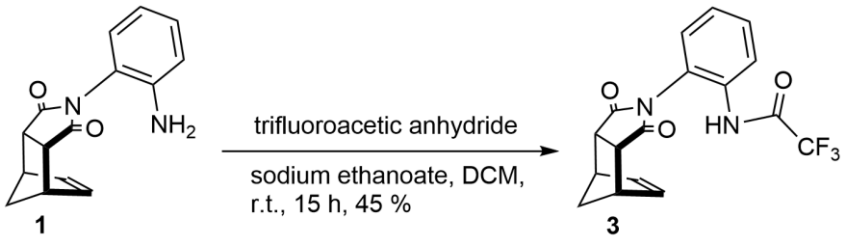

Scheme 2.4. Preparation of rotor **3**

(3aR,4S,7R,7aS)-2-(2-aminophenyl)-3a,4,7,7a-tetrahydro-1H-4,7-methanoisoindole-1,3(2H)-dione, **1** (150 mg, 0.59 mmol), 2,2,2-trifluoroacetic anhydride (7 mL, 0.05 mmol), sodium acetate (200 mg, 2.43 mmol) and dichloromethane (30 mL) were added to a 250 mL round bottom flask vial along with a magnetic stir bar and refluxed for 15 hours. The mixture was washed with deionized water (40 mL) and the solid off-white product **3** (92.8 mg, 45 %) was subsequently extracted and purified by column chromatography (ethyl acetate/hexanes = 2:1, v/v). ^{1}H NMR (500 MHz, CD_2Cl_2) δ 8.34

(br s, 1 H major), 8.22 (br s, 1 H minor), 7.90 (d, *J* = 7.4 Hz, 1 H major), 7.72 (d, *J* = 6.7 Hz, 1 H minor), 7.48 (dd, *J* = 7.7 and 7.7 Hz, 1 H major), 7.35 (dd, *J* = 7.8 and 7.8 Hz, 1 H minor), 7.20 (d, *J* = 7.3 Hz, 1 H major), 7.10 (d, *J* = 6.6 Hz, 1 H minor), 6.25 (s, 2 H), 3.58 - 3.42 (m, 4 H), 1.87 - 1.73 (m, 1 H), 1.69 - 1.59 (m, 1 H), 1.54 (s, 2 H), 1.25 (s, 1 H). ^{13}C NMR (101 MHz, $CDCl_3$) δ 176.90, 135.01, 134.69, 130.74, 130.51, 129.83, 128.54, 128.08, 127.48, 127.20, 125.98, 125.21, 124.56, 120.05, 117.18, 114.31, 52.97, 52.48, 46.73, 45.83, 45.21, 31.60, 14.14, 0.01. ^{19}F NMR (282 MHz, $CDCl_3$) δ -75.49, -75.82.

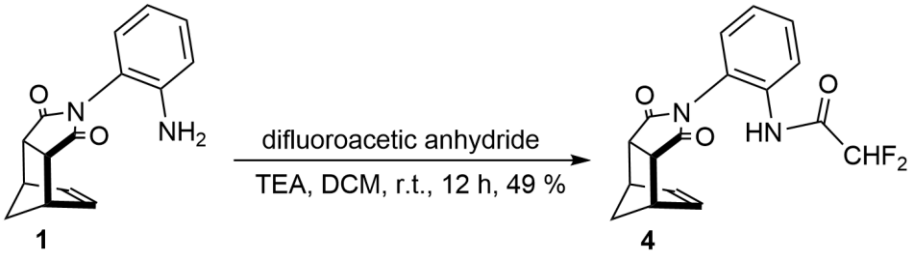

1 4

Scheme 2.5. Preparation of rotor **4**

A 100 mL round bottom flask containing (3aR,4S,7R,7aS)-2-(2-aminophenyl)-3a,4,7,7a-tetrahydro-1H-4,7-methanoisoindole-1,3(2H)-dione, **1** (73.2 mg, 0.29 mmol) was placed in an ice bath followed by the addition of dichloromethane (10 mL). Difluoroacetic anhydride (0.04 mL, 0.32 mmol) was added dropwise, followed by triethylamine (0.05 mL, 0.36 mmol), and the mixture was stirred for 30 minutes with the aid of a magnetic stir bar. The mixture was then removed from the ice bath and allowed to stir continuously at room temperature for 12 hours. The mixture was washed with deionized water (70 mL) and the off-white solid product **4** (47 mg, 49 %) was subsequently

extracted, purified by column chromatography (ethyl acetate/hexanes = 3:2, v/v) and dried under vacuo. ^{1}H NMR (300 MHz, $CDCl_3$) δ 8.23 (br, s, 1 H major), 8.06 (br, s, 1 H minor), 8.02 (d, *J* = 8.33 Hz, 1 H major), 7.81(d, *J* = 8.3 Hz, 1 H minor), 7.43 (t, *J* = 7.9 Hz, 1 H), 7.29 (t, *J* = 7.7 Hz, 1 H), 7.15 (d, *J* = 7.7 Hz, 1 H major), 7.06 (d, *J* = 7.7 Hz, 1 H minor), 6.32 (s, 2 H major), 6.27 (s, 2 H minor), 6.20 - 5.78 (m, 1 H major & minor), 3.51 (s, 4H major), 3.45 (s, 4H minor), 1.82 (dd, *J* = 9.1 and 9.0 Hz, 1 H), 1.62 (dd, *J* = 9.1 and 9.0 Hz, 1 H). ^{13}C NMR (100 MHz, chloroform-d) δ 176.85, 135.12, 134.68, 131.56, 131.19, 129.84, 128.60, 128.08, 126.98, 126.65, 125.72, 124.78, 124.11, 74.20, 73.84, 52.90, 52.46, 46.74, 45.82, 45.21.

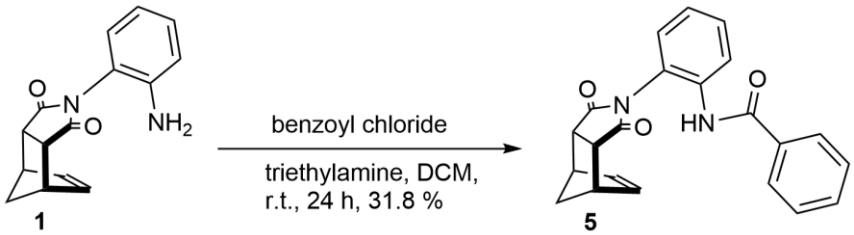

Scheme 2.6. Preparation of rotor **5**

Triethylamine (0.028 mL, 0.20 mmol) was added to a 100 mL round bottom flask containing **1** (0.046 g, 0.18 mmol), followed by the addition of dichloromethane (10 mL) and benzoyl chloride (0.030 mL, 0.26 mmol). The mixture was then mixed with the aid of a magnetic stir bar for 24 hours and subsequently washed three times with saturated $NaHCO_3$ (40 mL), dichloromethane (50 mL) and saturated NaCl (50 mL) respectively. The organic layer was then dried over anhydrous $MgSO_4$, filtered and concentrated, first, under nitrogen line, then, under vacuo. Purification via column chromatography (ethyl

acetate/hexanes = 3:2, v/v) gives a brown solid product **5** (20.6 mg, 31.8 %). ^{1}H NMR (300 MHz, $CDCl_3$) δ 8.10 (s, 1 H minor), 8.01 (d, *J* = 7.84 Hz, 1 H major), 7.95 (d, *J* = 7.84, 1 H minor), 7.85 (s, 1 H major), 7.82 (d, *J* = 7.23, 2 H), 7.62 - 7.59 (m, 1 H), 7.56 - 7.48 (m, 3 H), 7.31 (dd, *J* = 7.66 & 7.61 Hz, 1 H), 7.19 (d, *J* = 7.66 Hz, 1 H major), 7.07 (d, *J* = 7.66 Hz, 1 H minor), 6.30 (s, 2 H, minor), 5.69 (s, 2 H major), 3.49 (dd, *J* = 19.79 & 19.04 Hz, 3 H), 3.38 (s, 1 H), 1.69 - 1.68 (m, 1 H), 1.29 (dd, *J* = 4.49 & 8.34 Hz, 1 H).

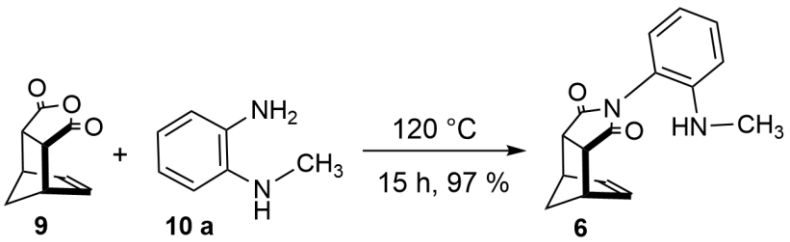

Scheme 2.7. Preparation of rotor **6**

cis-5-norbornene-*endo*-2,3-dicarboxylic anhydride **9** (103.5 mg, 0.63 mmol) and N1-methylbenzene-1,2-diamine **10 a** (107.5 mg, 0.88 mmol) and were added to a 20-dram vial along with a magnetic stir bar. The vial was then capped and heated to 120 °C in a silicon oil bath for 15 hours while stirring. After letting the vial cool to room temperature, the crude material was purified by column chromatography (ethyl acetate/hexanes = 1:1, v/v) to give a brown solid **6** (268.3 mg, 97 %). ^{1}H NMR (400 MHz, $CDCl_3$) δ 7.29 (d, *J* = 6.1, 1 H), 6.78 - 6.71 (m, 3 H), 6.37 (s, 2 H major), 6.27 (s, 2 H minor), 3.50 (s, 4 H minor), 3.47 (s, 4 H major), 3.40 (s, 1 H), 2.94 (s, 3 H minor), 2.79 (s, 3 H major), 1.79 (dd, *J* = 26.8 & 9.4 Hz, 1 H), 1.60 (dd, J = 27.3 & 8.8 Hz, 1 H) ^{13}C NMR (100 MHz, chloroform-

d) δ 177.44, 176.77, 144.93, 135.62, 134.73, 130.74, 130.64, 128.80, 128.49, 118.42, 117.74, 117.45, 117.10, 112.47, 111.38, 52.83, 52.37, 46.76, 45.96, 45.64, 45.46, 30.81, 30.43.

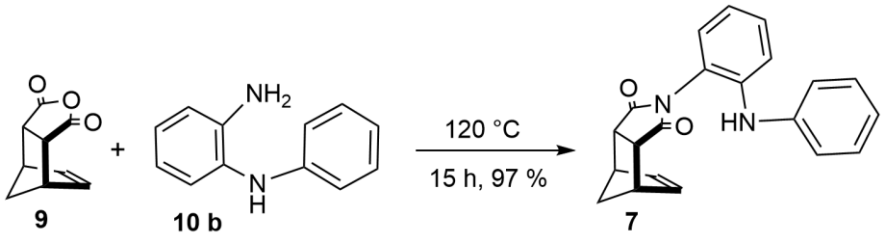

9 10 b 7

Scheme 2.8. Preparation of rotor **7** via thermal condensation.

cis-5-norbornene-*endo*-2,3-dicarboxylic anhydride **9** (112.3 mg, 0.68 mmol) and *N*-phenyl-*o*-phenylenediamine **10 b** (113.4 mg, 0.62 mmol) were added to a 20-dram vial along with a magnetic stir bar. The vial was then capped and heated to 120 °C in a silicon oil bath for 15 hours while stirring. After letting the vial cool to room temperature, the crude material was purified by column chromatography (ethyl acetate/hexanes = 1:1, v/v) to give a brown solid **7** (198.3 mg, 97 %). ^{1}H NMR (500 MHz, 1,1,2,2-tetrachloroethane-d_2) δ 7.41 (dd, *J* = 7.5 and 7.6 Hz, 1 H), 7.34 (dd, *J* = 7.5 and 8.0 Hz, 1 H), 7.29 - 7.23 (m, 2 H), 7.09 - 6.91 (m, 5 H), 6.28 (s, 2 H major), 6.20 (s, 2 H minor), 5.60 (s, br, 1 H major), 5.38 (s, 1 H minor), 3.50 - 3.48 (m, 3 H), 3.35 - 3.34 (m, 1 H), 1.80 (dd, *J* = 9.3 and 9.2 Hz, 1 H), 1.60 - 1.58 (m, 1 H). ^{13}C NMR (100 MHz, $CDCl_3$) δ 177.10, 176.89, 143.20, 142.75, 139.98, 139.75, 135.23, 134.66, 130.11, 129.92, 129.51, 129.33, 129.26, 128.85, 123.55, 122.61, 122.39, 121.94, 121.43, 121.26, 121.11, 119.68, 118.17, 117.91, 77.53, 52.64, 52.35, 46.62, 45.86, 45.48, 45.37.

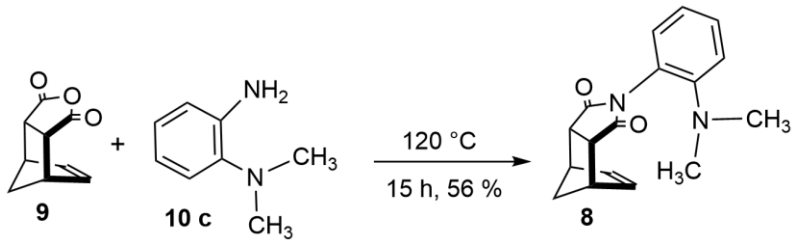

Scheme 2.9. Preparation of rotor **8**

cis-5-norbornene-*endo*-2,3-dicarboxylic anhydride **9** (100 mg, 0.61 mmol) and N1,N1-dimethylbenzene-1,2-diamine **10 c** (126.2 mg, 0.93 mmol) were added to a 20-dram vial along with a magnetic stir bar. The vial was then capped and heated to 120 ºC in a silicon oil bath for 15 hours with mild stirring. After letting the vial cool to room temperature, the crude material was purified by column chromatography (ethyl acetate/hexanes = 3:1, v/v) to give a brown liquid **8** (96 mg, 56 %). ^{1}H NMR (500 MHz, TCE) δ 7.43 – 7.32 (m, 1H), 7.19 - 7.13 (m, 1 H), 7.02 (dd, *J* = 15.2 & 7.51 Hz, 1 H), 6.82 (d, *J* = 7.7 Hz, 1 H), 6.30 (s, 2 H major), 6.26 (s, 2 H minor), 3.49 – 3.42 (m, 4 H), 2.68 (s, 6 H major), 2.56 (s, 6 H minor), 1.83 (d, *J* = 8.7 Hz, 1 H), 1.63 (d, *J* = 8.7 Hz, 1 H). ^{13}C NMR (101 MHz, $CDCl_3$) δ 177.15, 176.81, 151.13, 134.70, 134.60, 130.32, 130.18, 129.37, 129.27, 125.52, 124.97, 122.60, 122.54, 120.19, 52.69, 52.34, 46.88, 45.98, 45.70, 45.35, 45.19, 43.87, 0.01.

2.3.3 1H and 13C NMR spectra

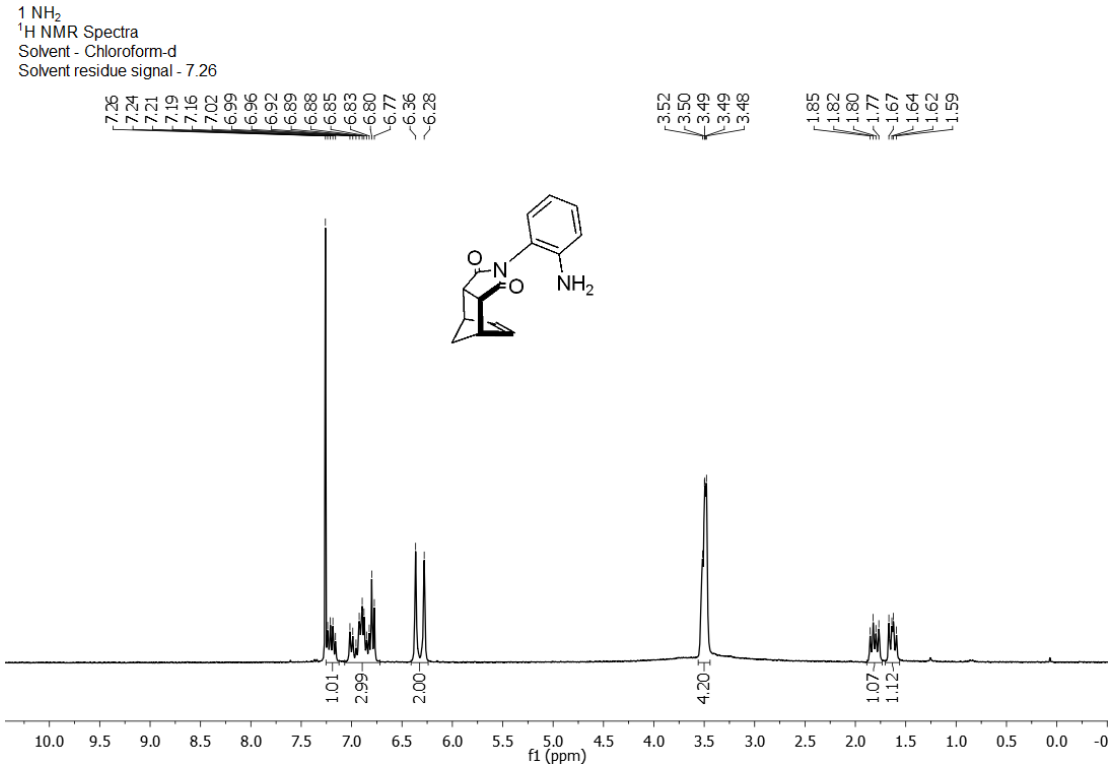

Figure 2.15. ^{1}H NMR spectra of rotor **1**(NH_2) (400 MHz, chloroform-d)

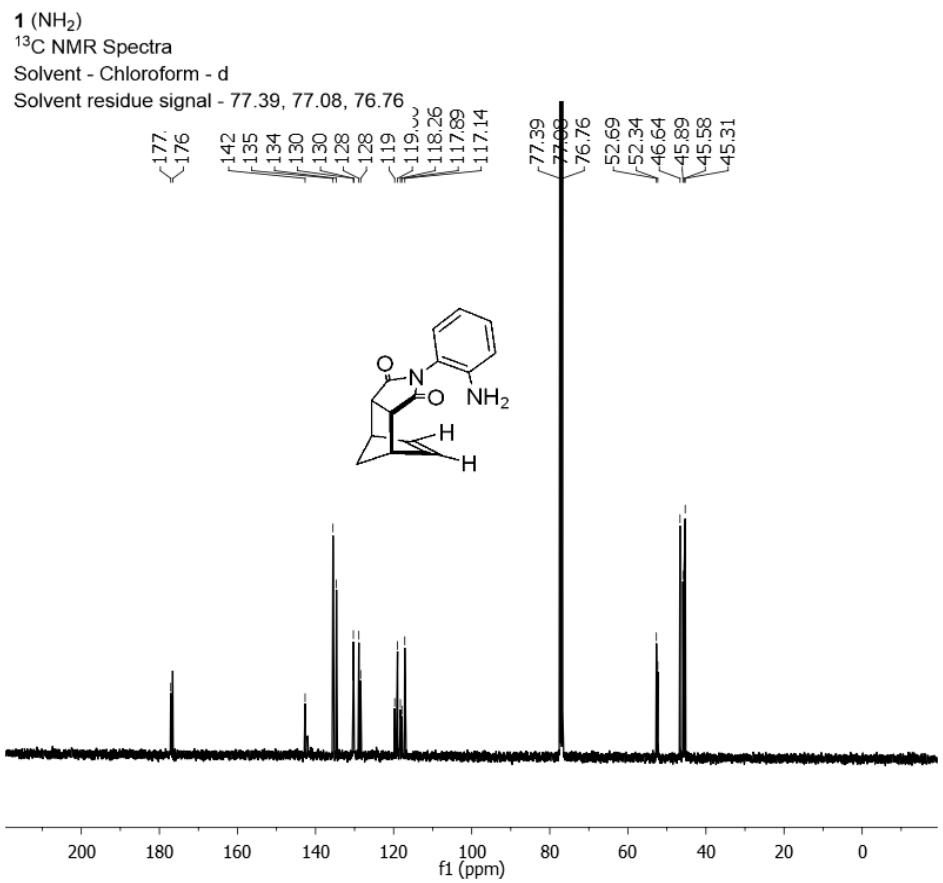

Figure 2.16. ^{13}C NMR spectra of rotor **1**(NH_2) (100 MHz, chloroform-d)

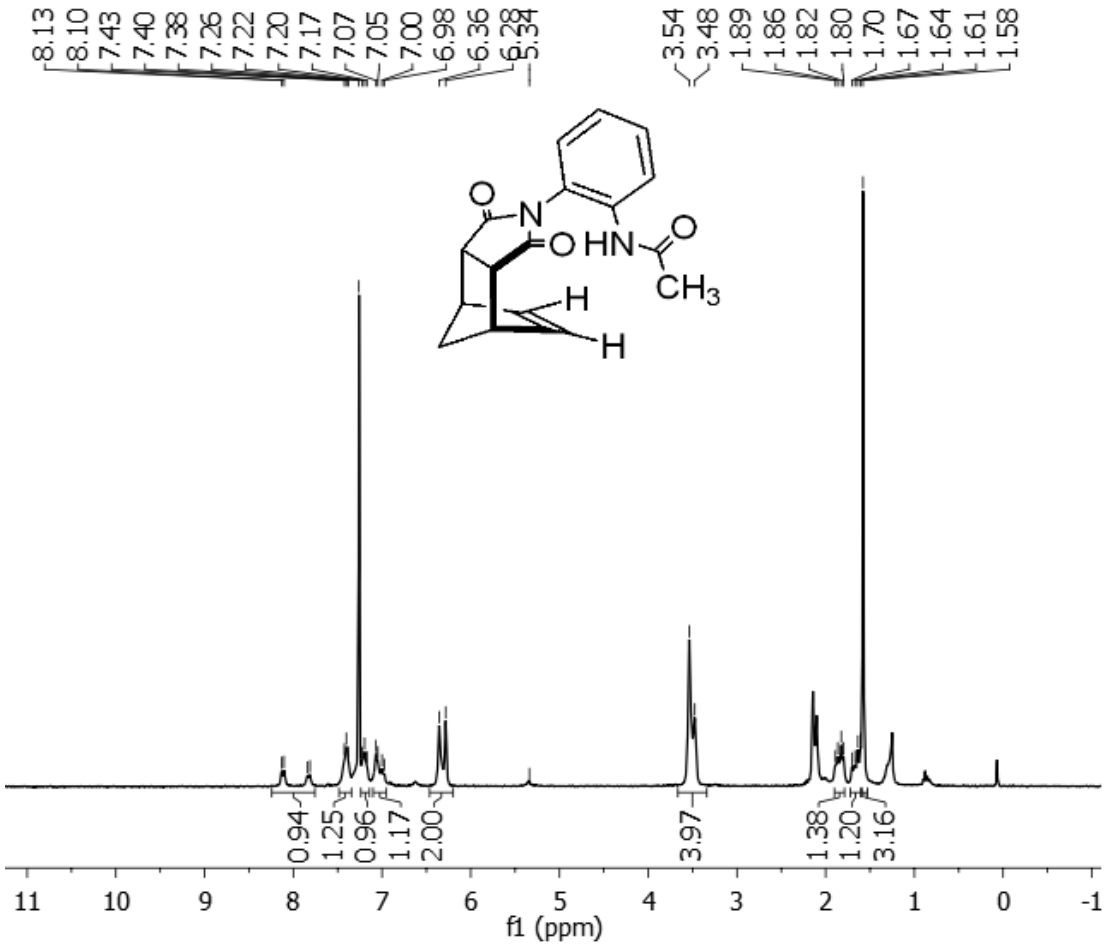

Figure 2.17. ^{1}H spectra of rotor **2**(NHCOCH$_3$) (300 MHz, chloroform-d)

2 ($NHCOCH_3$)
^{13}C NMR Spectra
Solvent - DMSO - d6
Solvent residue signal - 40.61, 40.40, 40.20, 39.99, 39.78, 39.57, 39.36

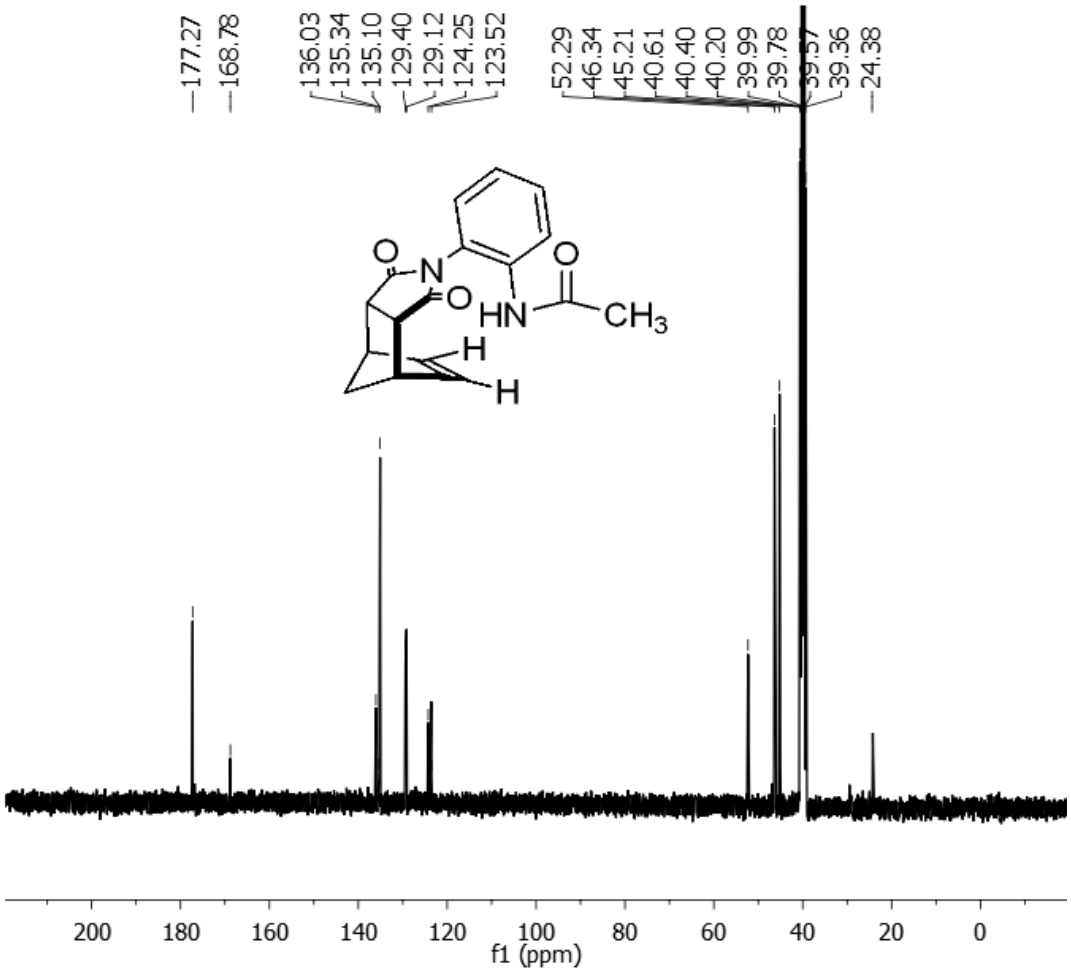

Figure 2.18. ^{13}C spectra of rotor **2**($NHCOCH_3$) (100 MHz, dimethyl sulfoxide-d6)

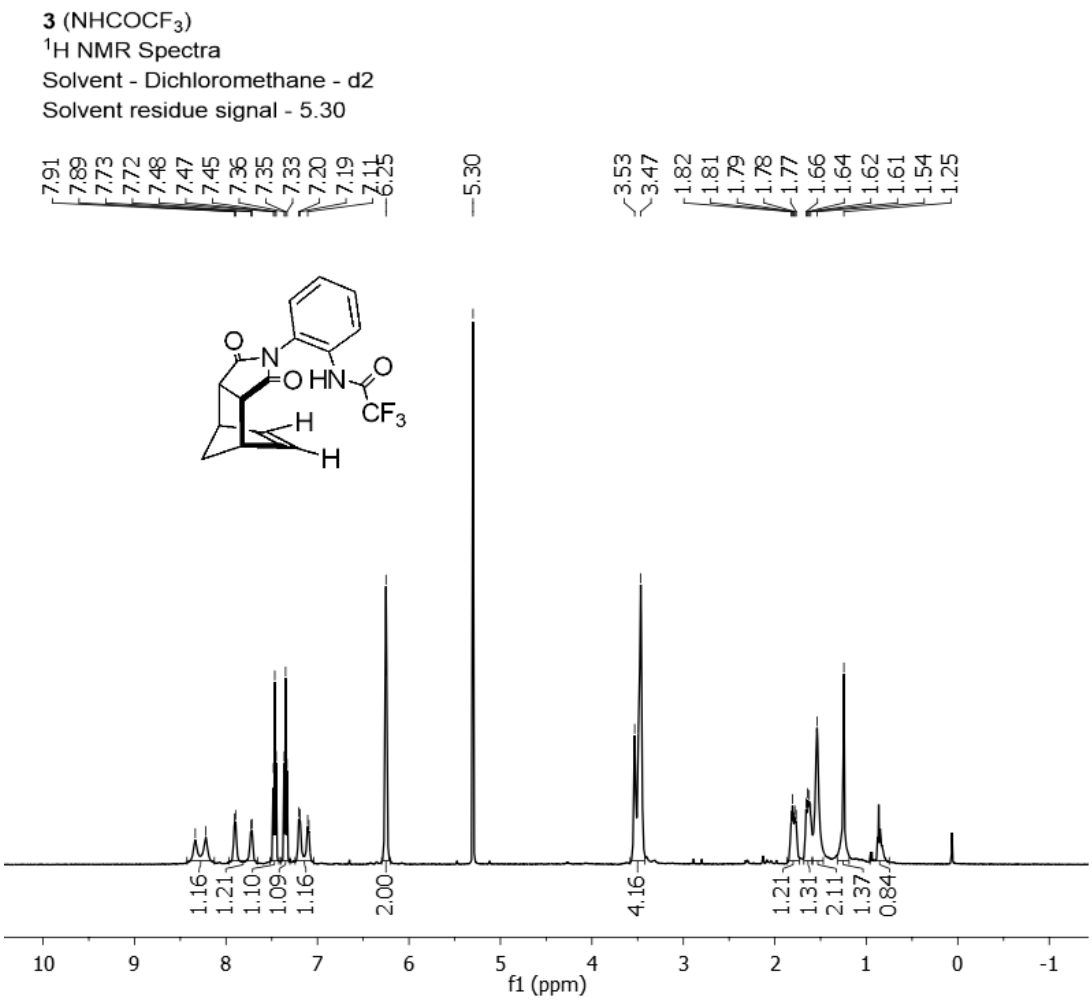

Figure 2.19. ^{1}H spectra of rotor **3** ($NHCOCF_3$) (500 MHz, dichloromethane-d2)

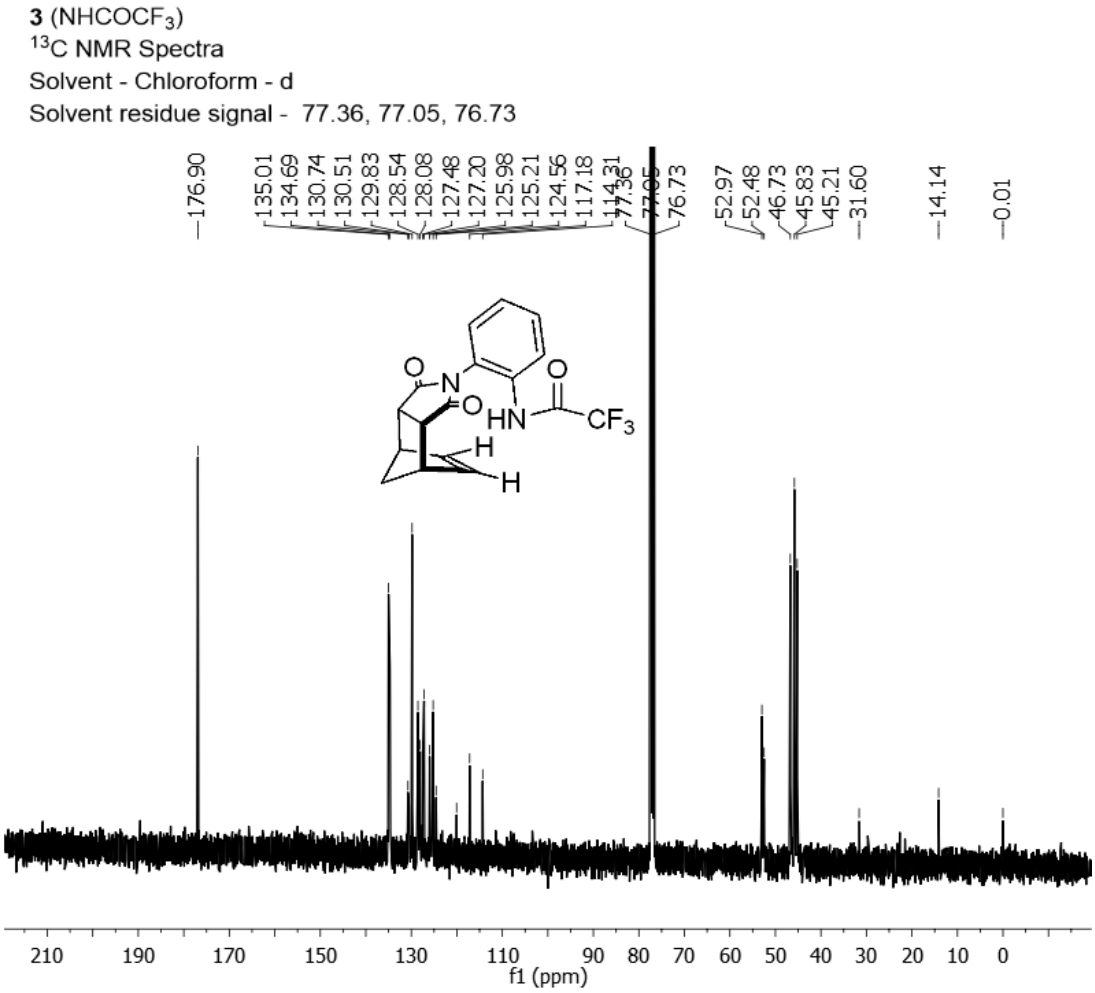

Figure 2.20. ^{13}C NMR spectra of rotor **3** ($NHCOCF_3$) (100 MHz, chloroform-d)

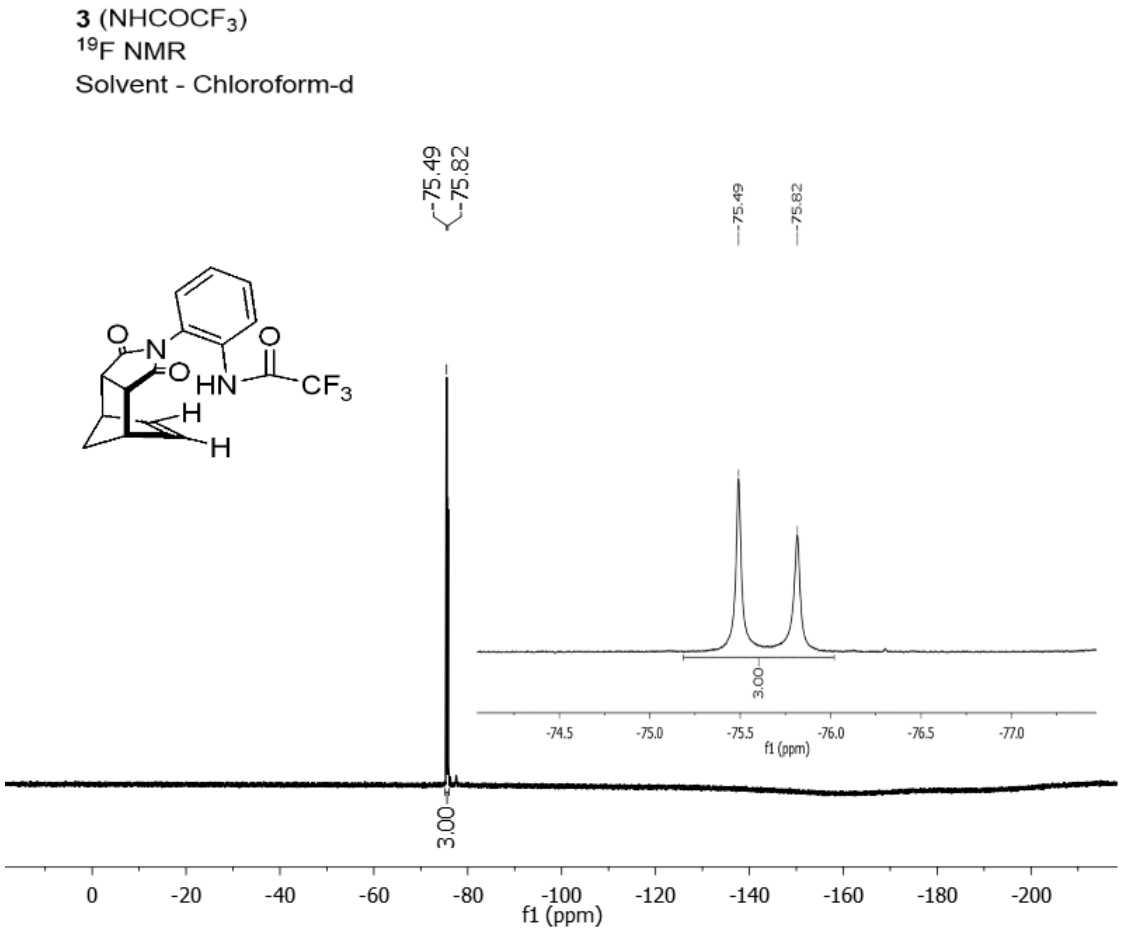

Figure 2.21. ^{19}F NMR spectra of rotor **3** ($NHCOCF_3$) (282 HMz, chloroform-d)

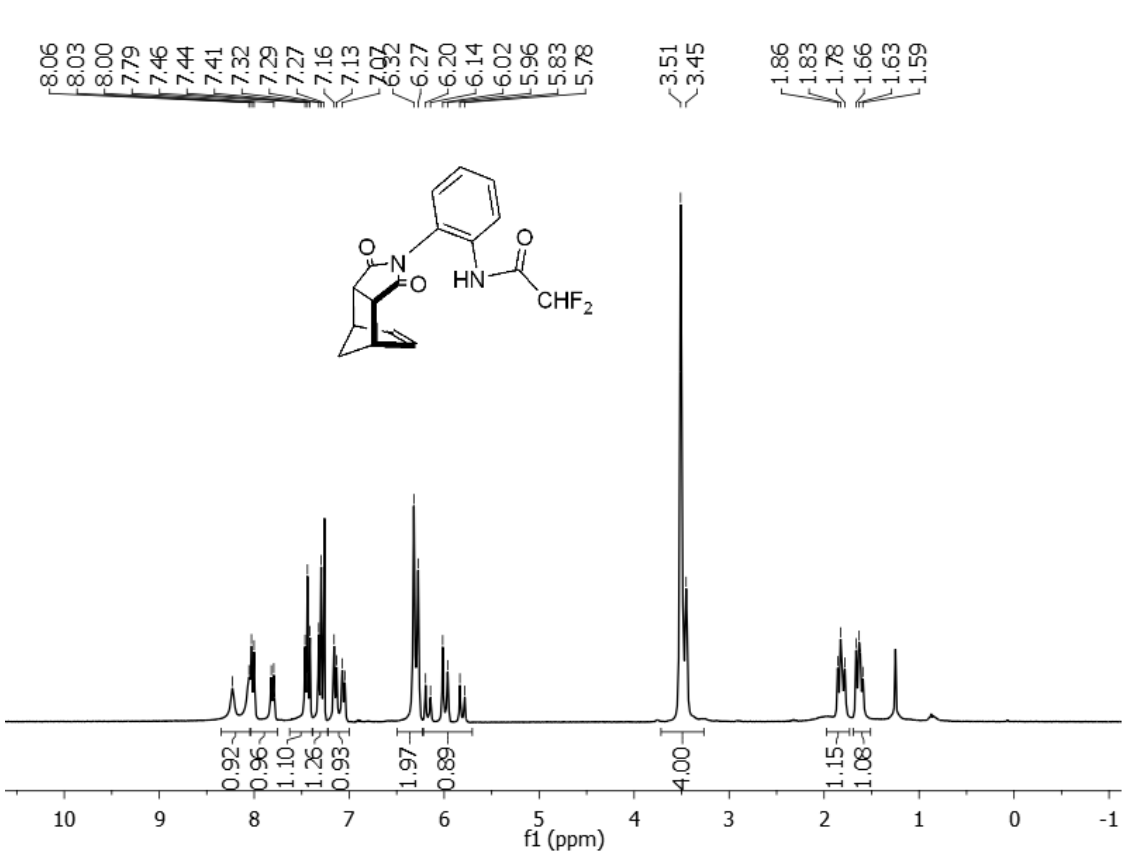

Figure 2.22. ^{1}H NMR spectra of rotor **4**(NHCOCHF$_2$) (300 MHz, chloroform-d)

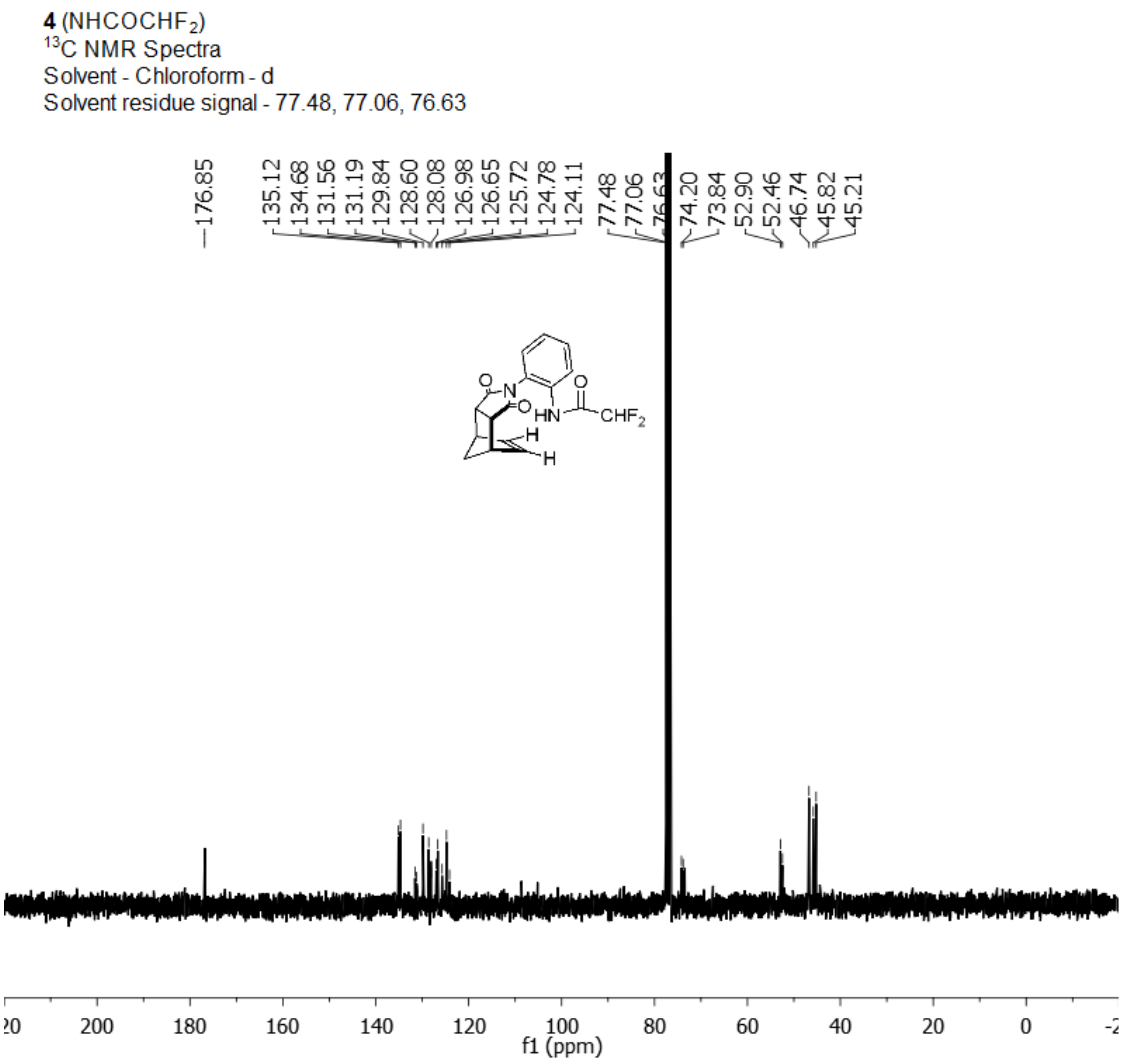

Figure 2.23. ^{13}C NMR spectra of rotor **4**(NHCOCHF**2**) (100 MHz, chloroform-d)

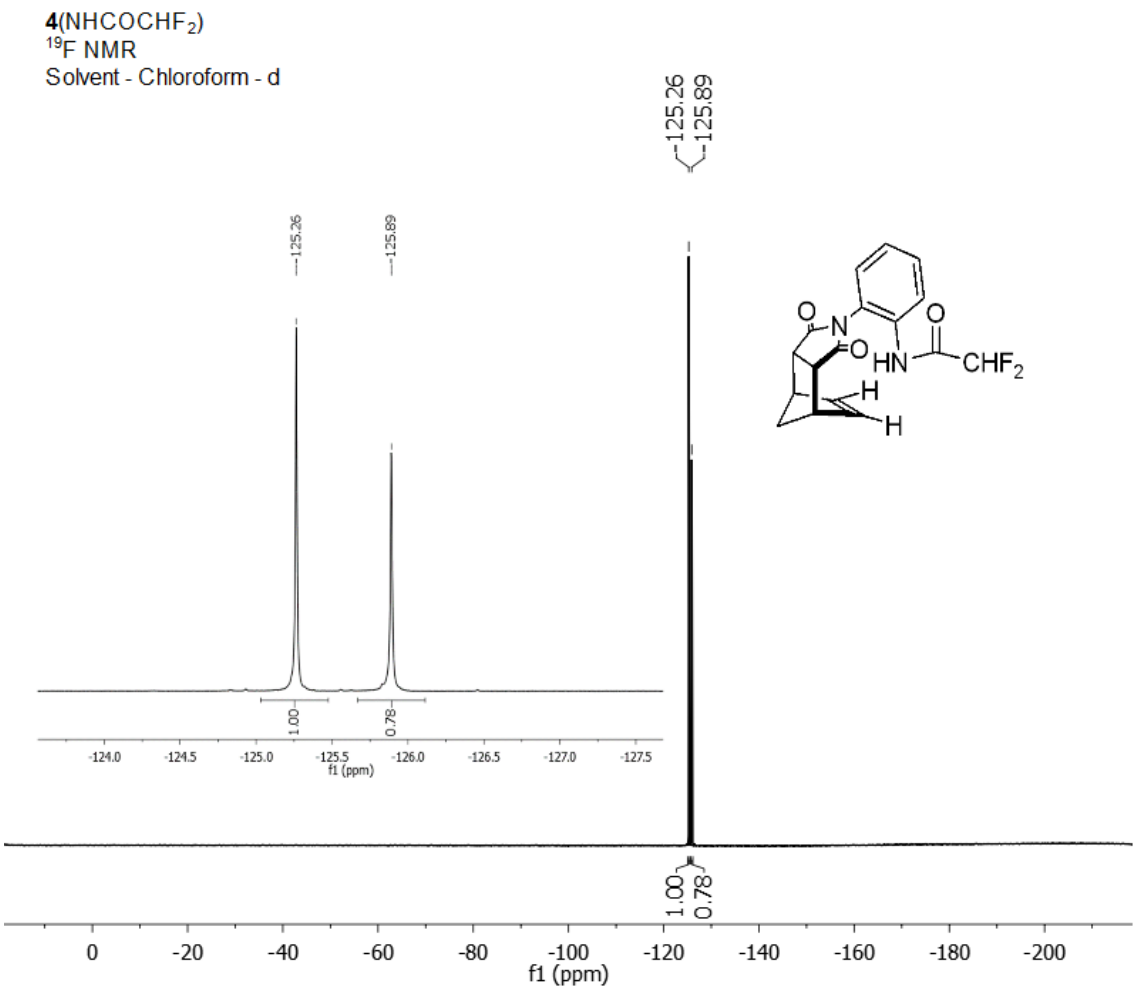

Figure 2.24. ^{19}F NMR spectra of rotor **4**($NHCOCHF_2$) (282 MHz, chloroform-d)

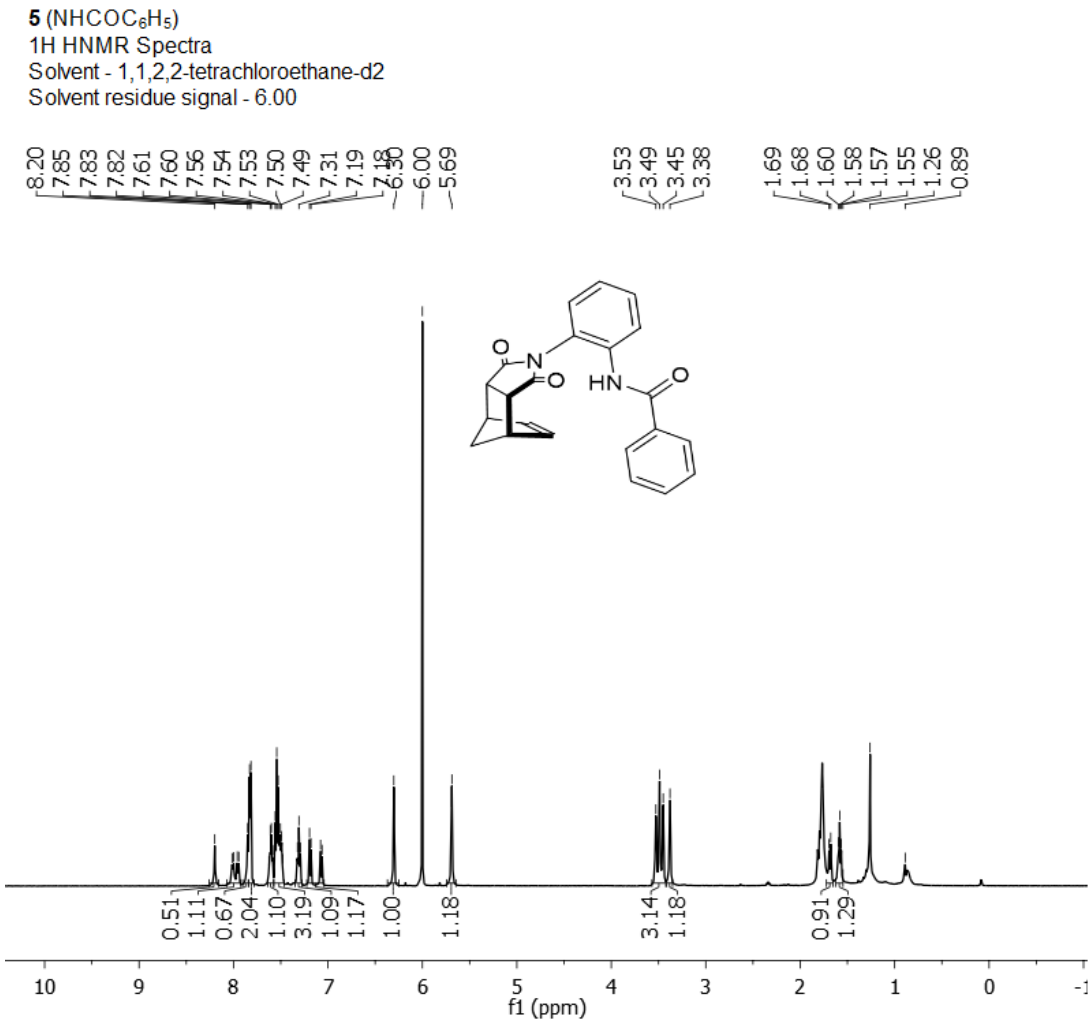

Figure 2.25. ^{1}H NMR spectra of rotor **5**($NHCOC_6H_6$) (300 MHz, chloroform-d)

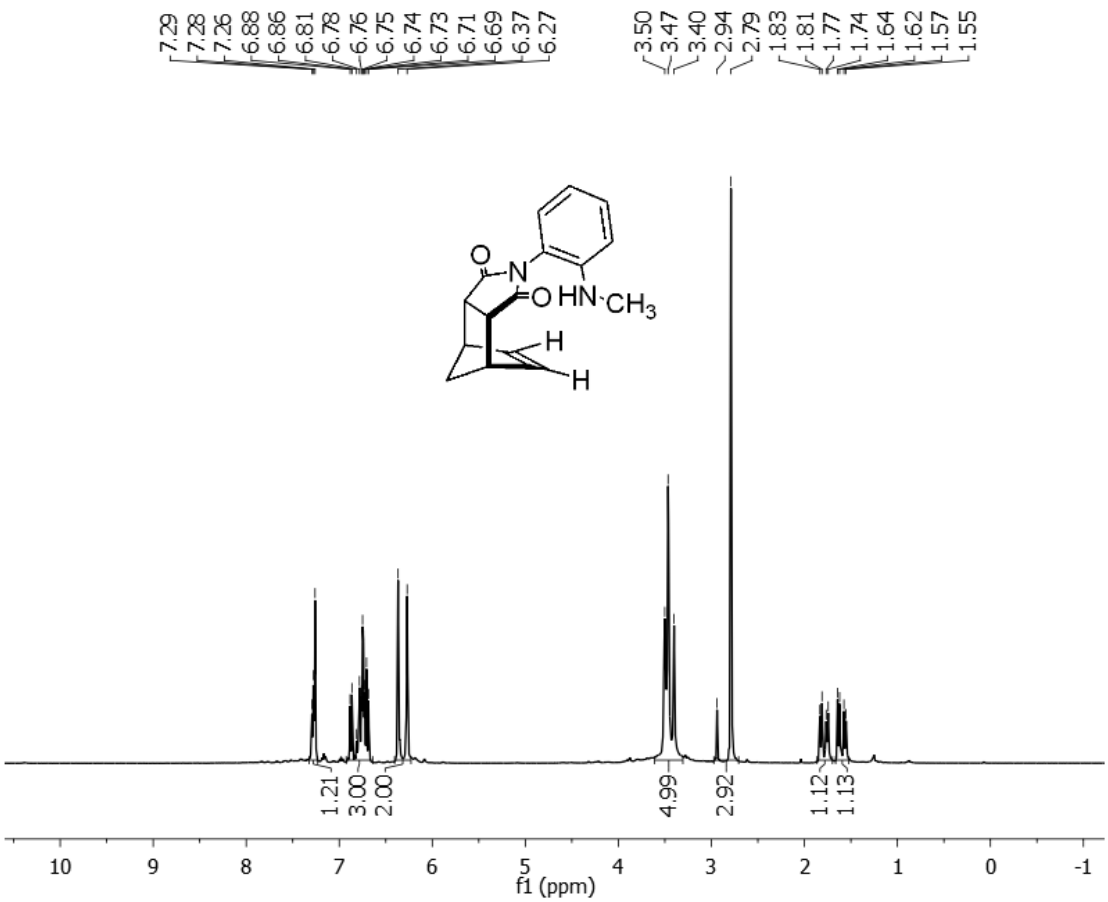

Figure 2.26. ^{1}H NMR spectra of rotor **6**($NHCH_3$) (400 MHz, chloroform-d)

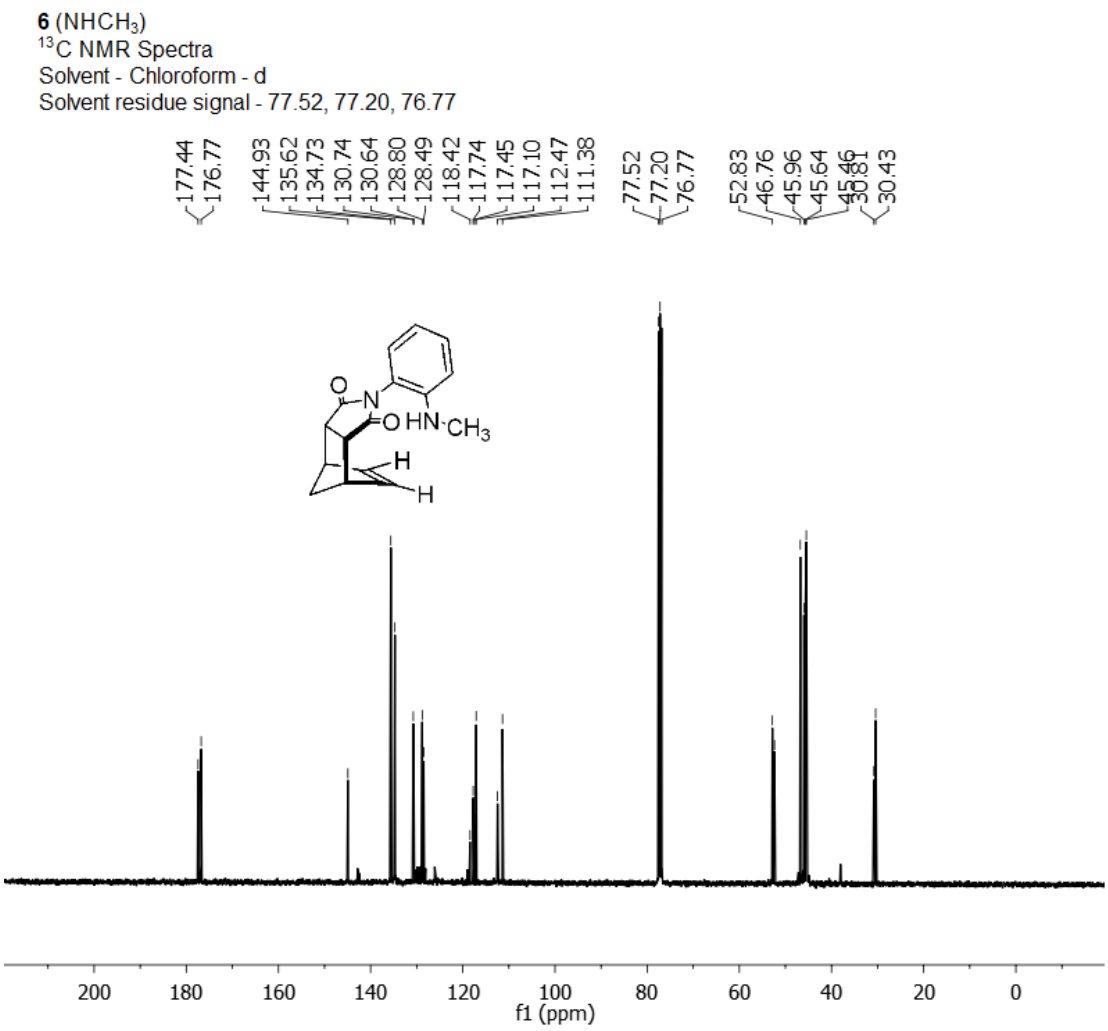

Figure 2.27. ^{13}C NMR spectra of rotor **6**($NHCH_3$) (100 MHz, chloroform-d)

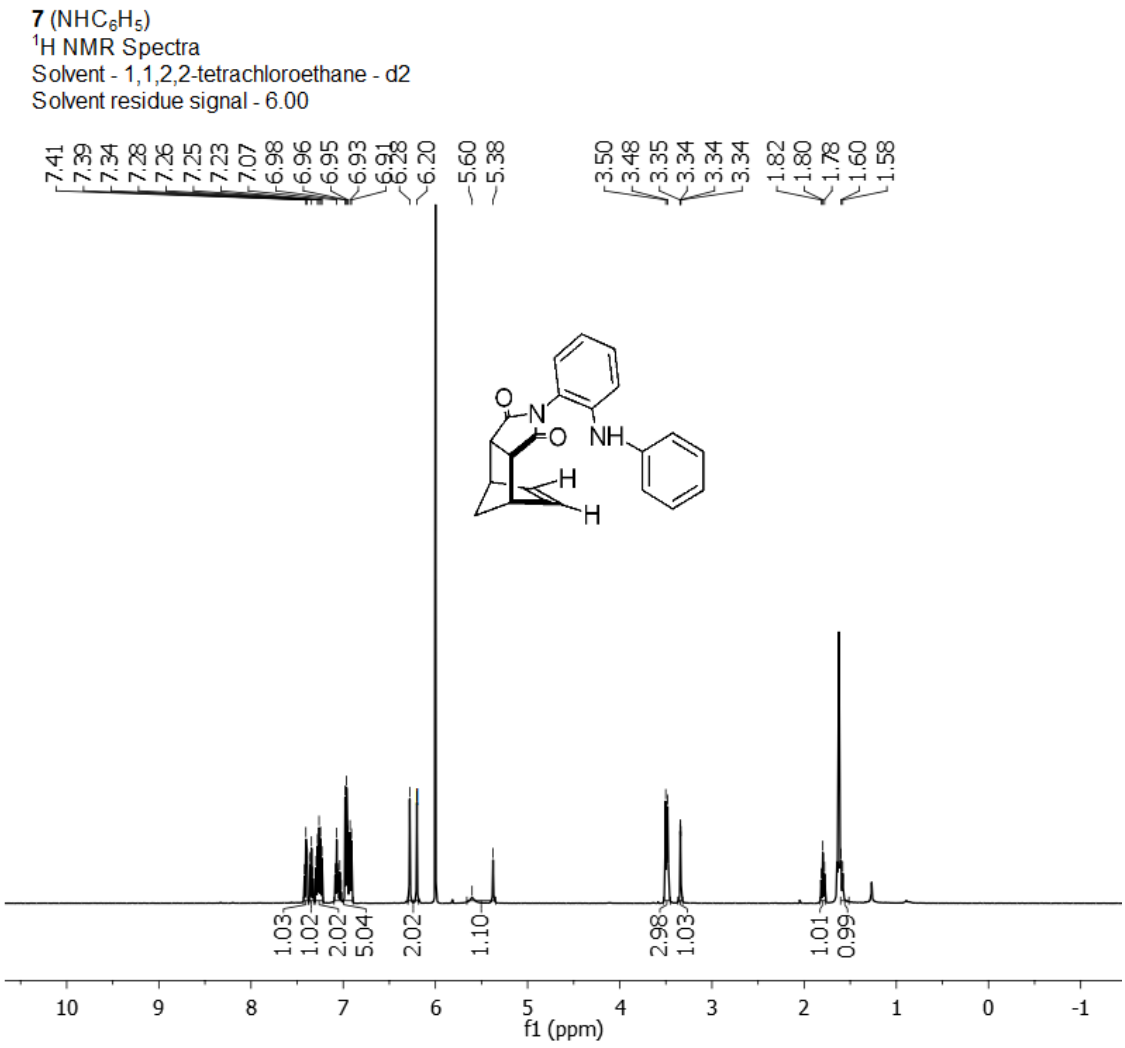

Figure 2.28. ^{1}H spectra of rotor **7(**NHC_6H_5) (500 MHz, chloroform-d)

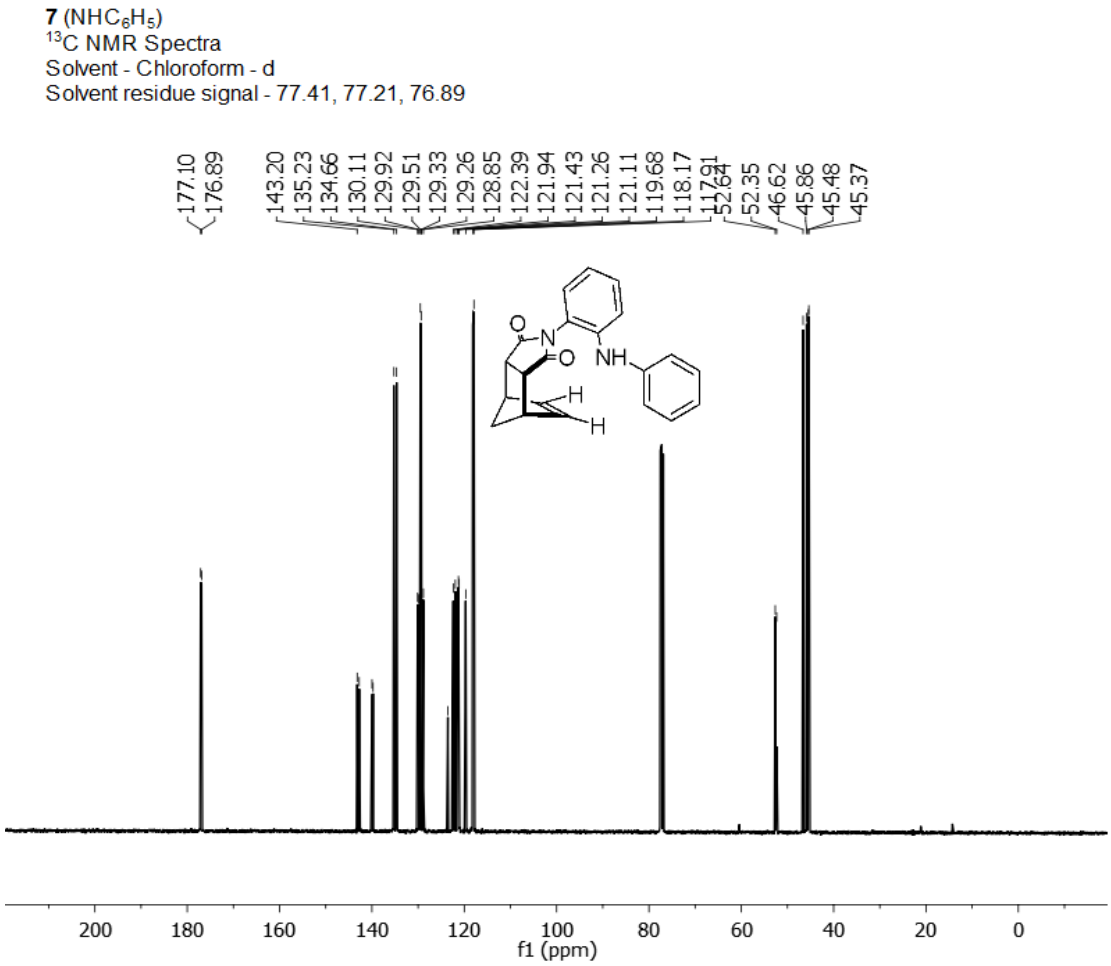

Figure 2.29. ^{13}C spectra of rotor **7(**NHC_6H_5) (100 MHz, chloroform-d)

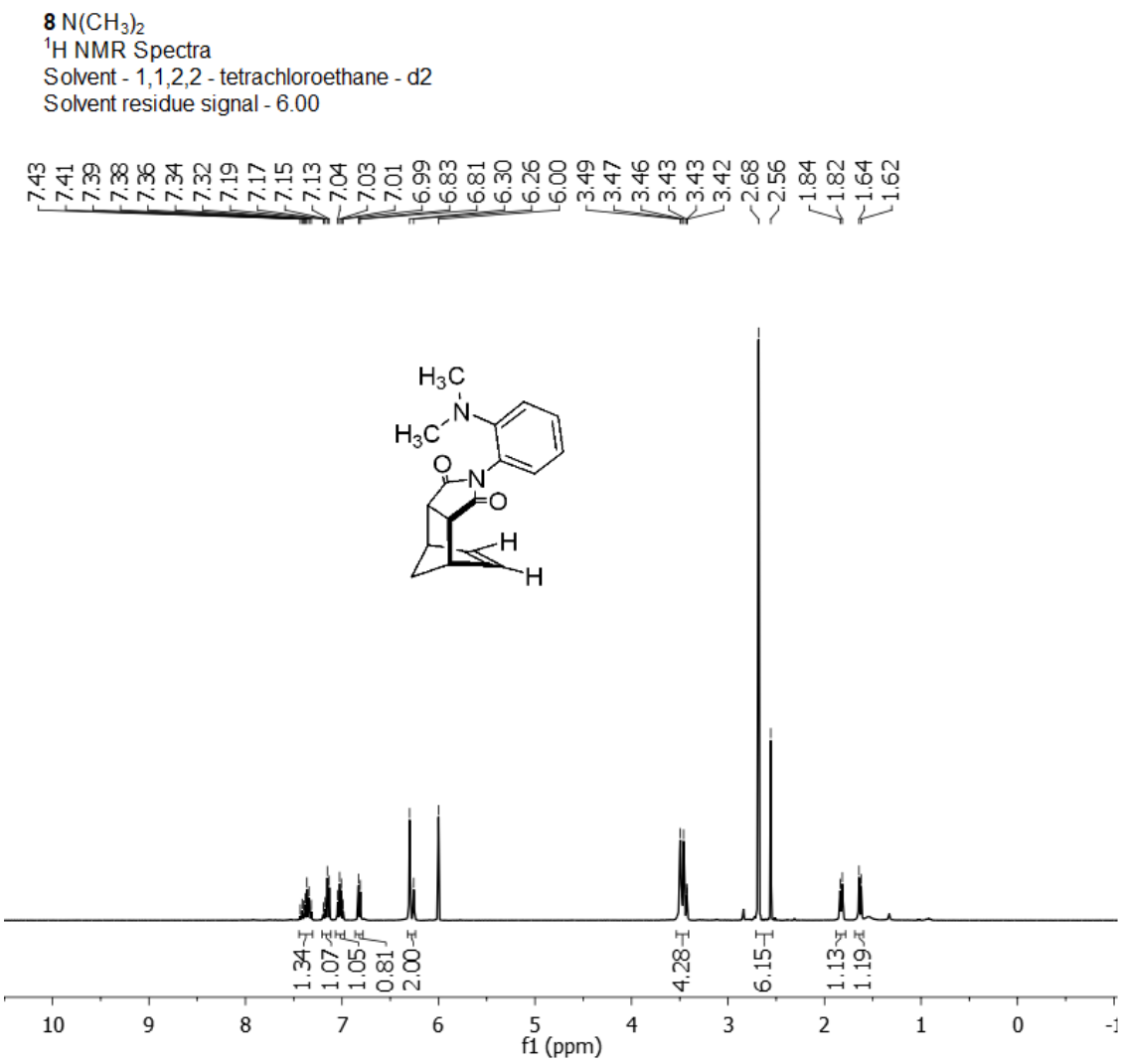

Figure 2.30. ^{1}H NMR spectra of rotor **8** $N(CH_3)_2$ (500 MHz, 1,1,2,2 - tetrachloroethane-d2)

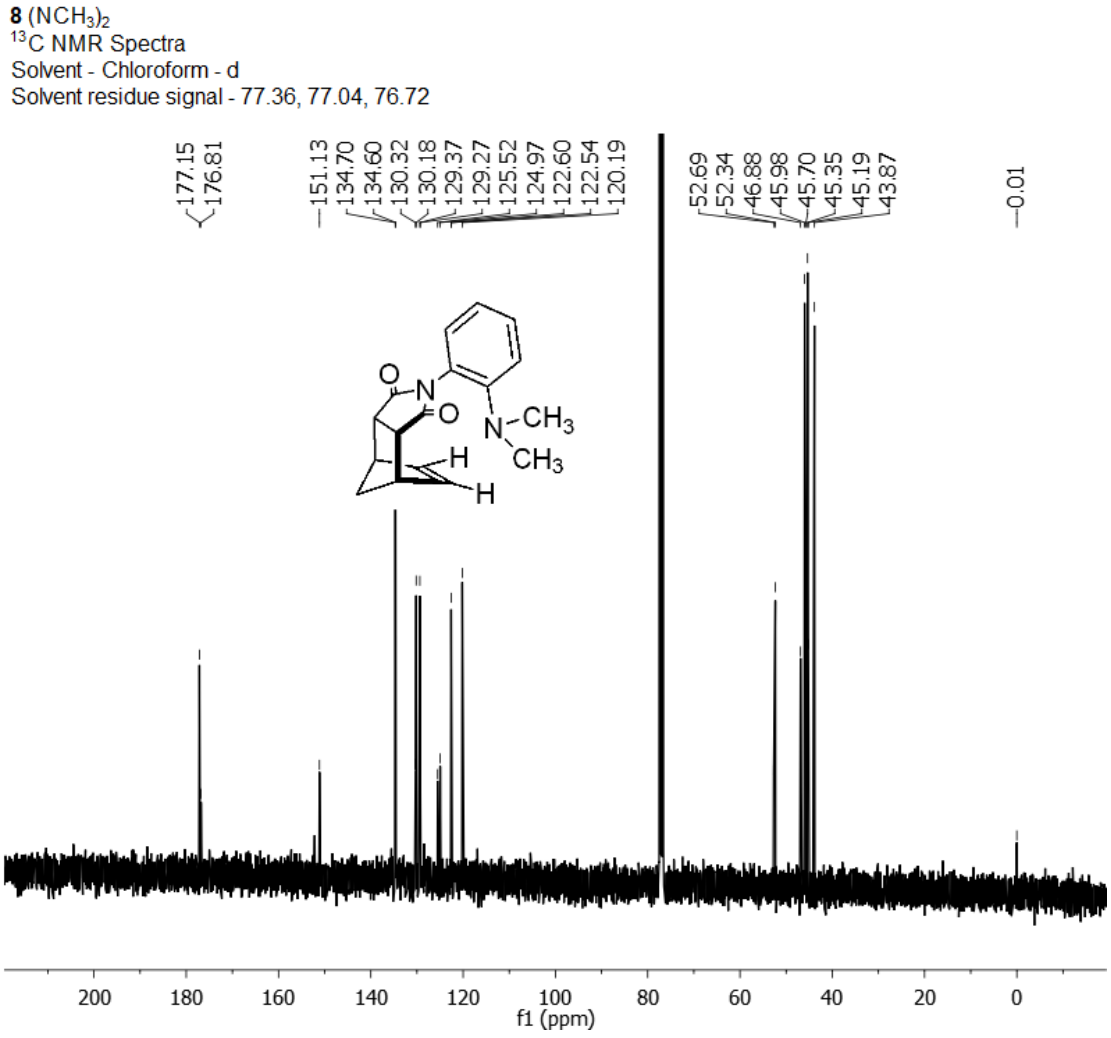

Figure 2.31. ^{13}C NMR spectra of rotor **8** $N(CH_3)_2$ (100 MHz, chloroform-d)

2.3.4 HIGH RESOLUTION MASS SPEC.

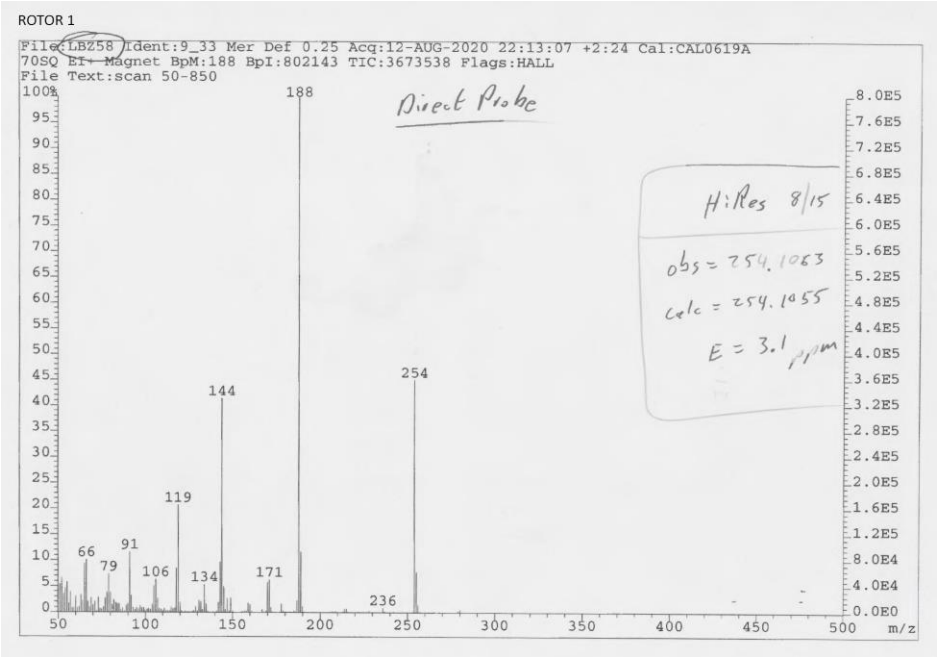

Figure 2.32. High resolution mass spec of rotor **1** (NH2)

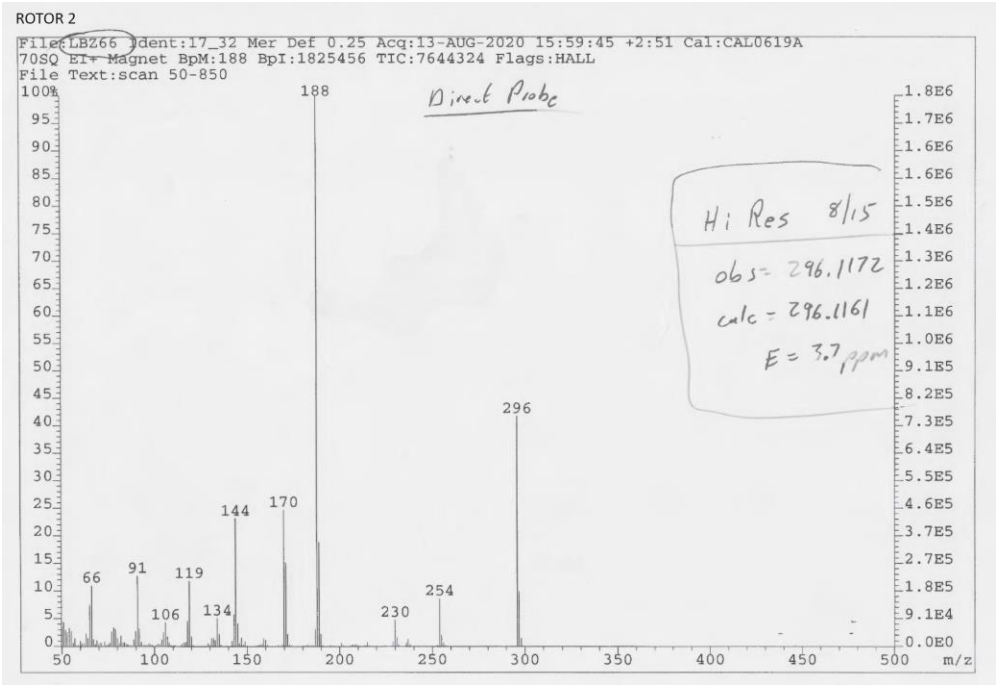

Figure 2.33. High resolution mass spec of rotor **2** ($NHCOCH_3$)

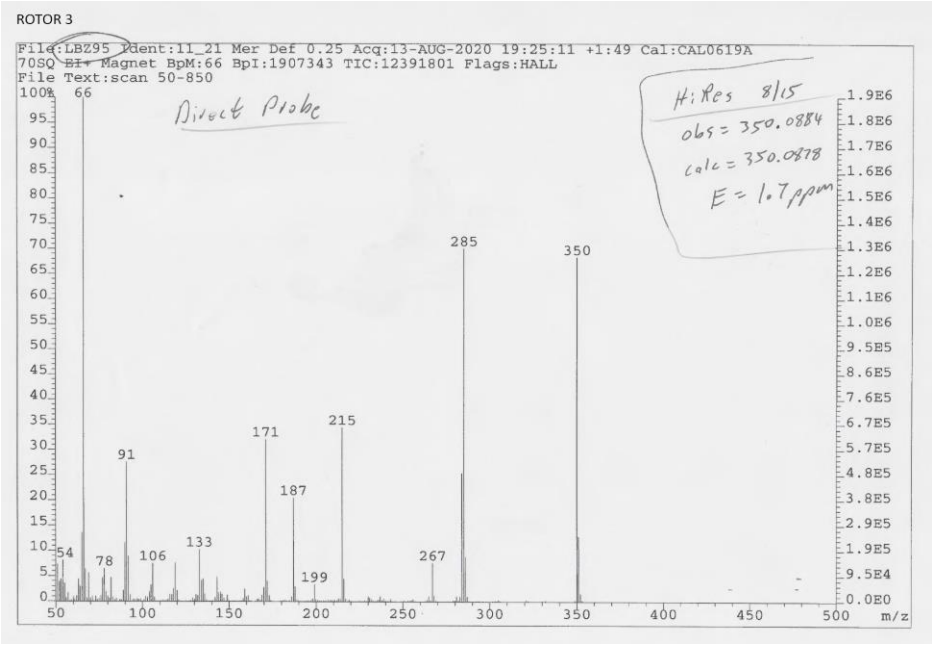

Figure 2.34. High resolution mass spec of rotor **3** ($NHCOCF_3$)

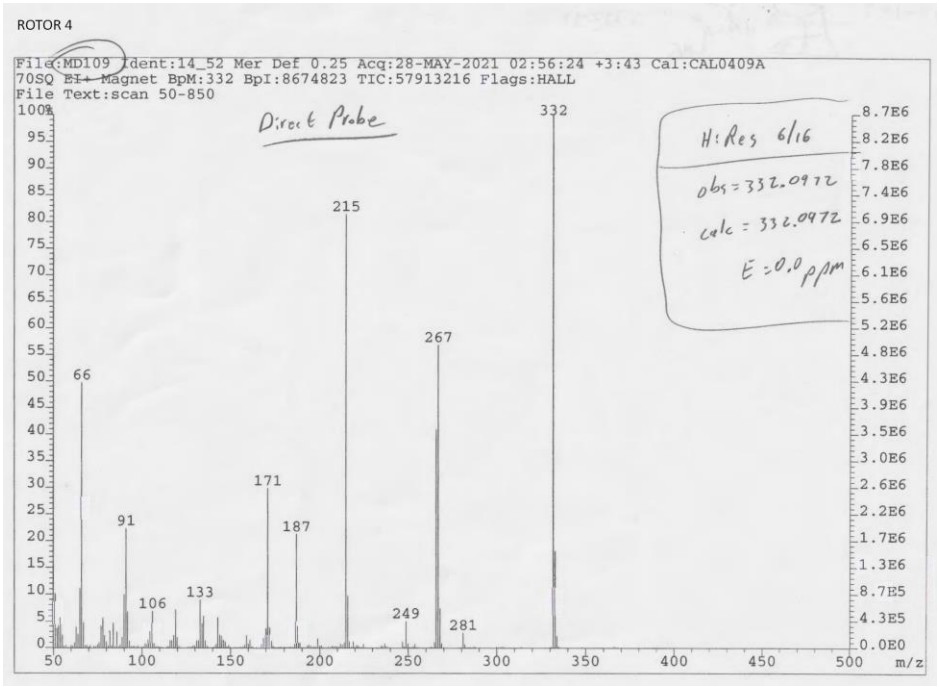

Figure 2.35. High resolution mass spec of rotor **4** ($NHCOCF_2$)

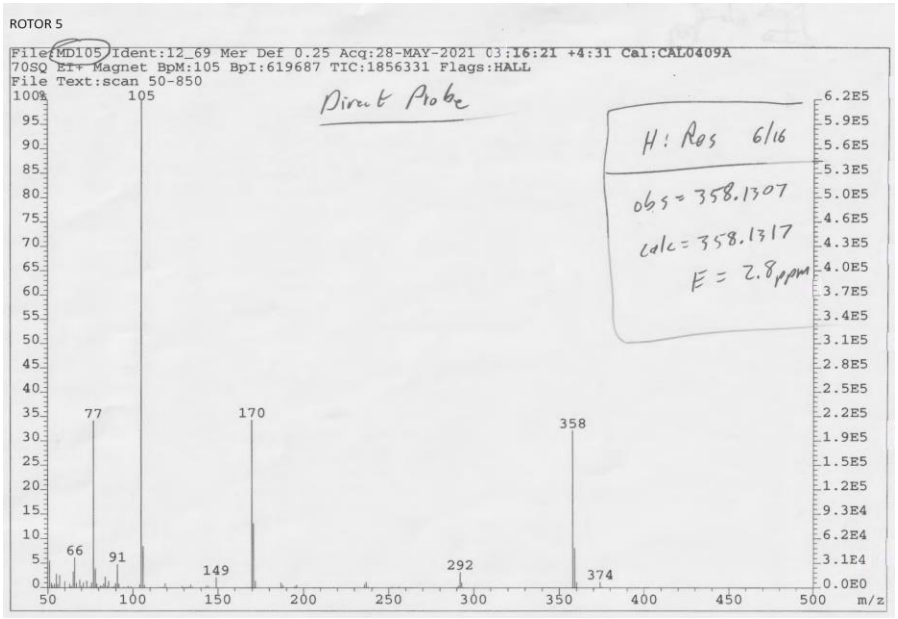

Figure 2.36. High resolution mass spec of rotor **5** ($NHCOC_6H_6$)

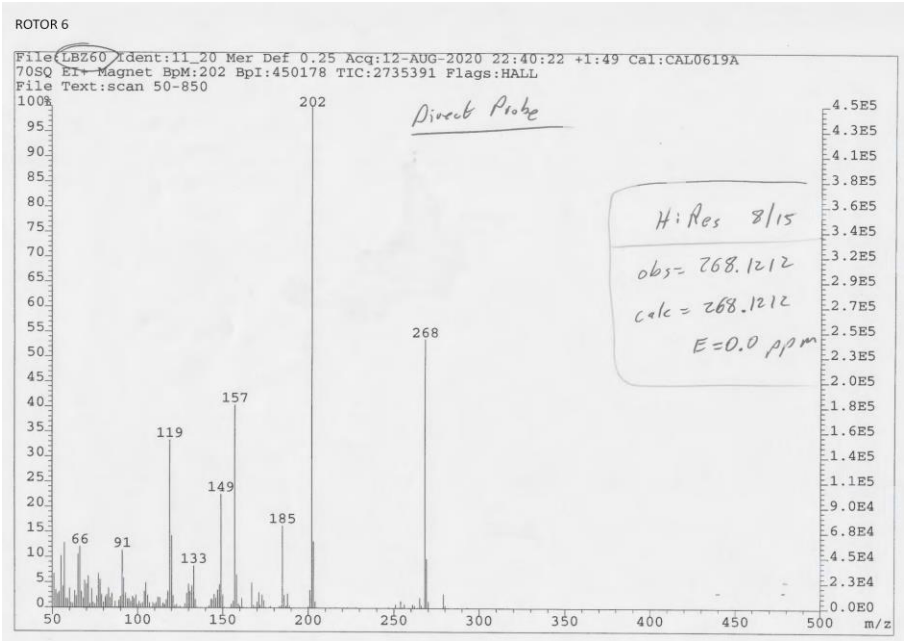

Figure 2.37. High resolution mass spec of rotor **6** ($NHCH_3$)

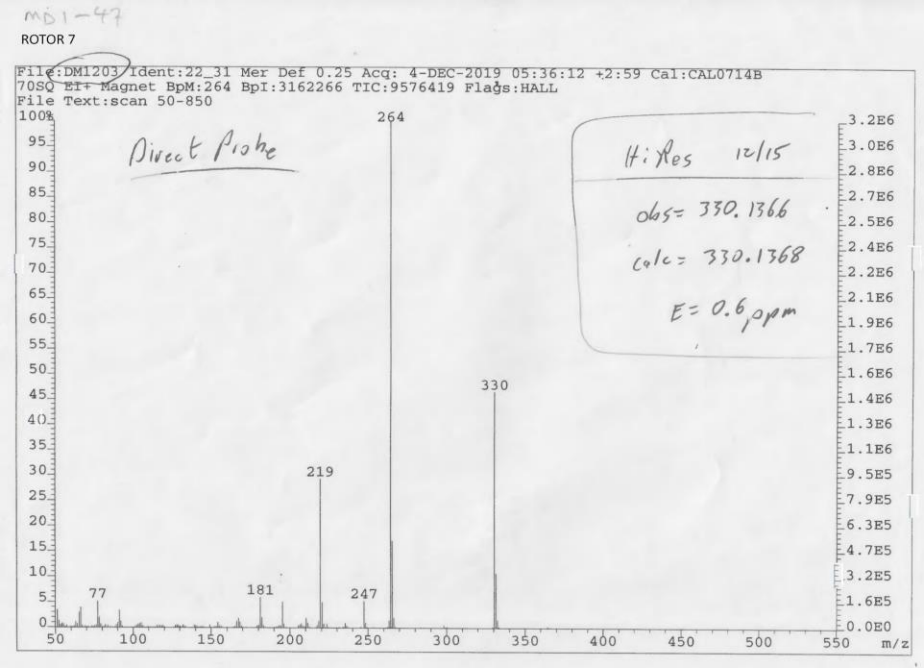

Figure 2.38. High resolution mass spec of rotor **7** (NHC_6H_5)

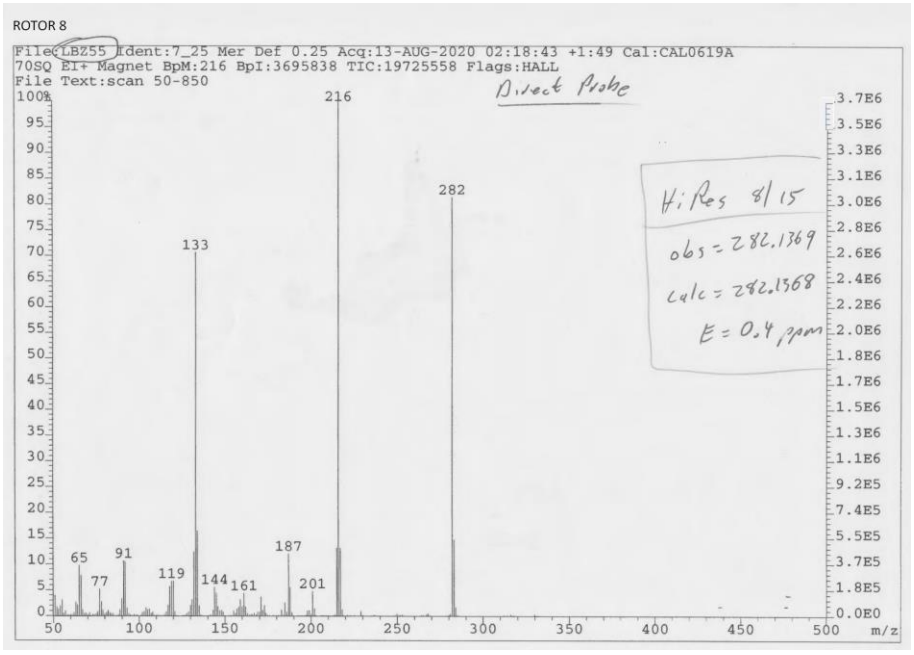

Figure 2.39. High resolution mass spec of rotor **8** ($N(CH_3)_2$)

2.3.5 ADDITIONAL TABLES AND FIGURES

Table 2.2. Experimentally measured ($\Delta G^{\ddagger}_{Expt.}$, kcal/mol), calculated ($\Delta G^{\ddagger}_{Calc.}$, kcal/mol) rotational barriers for rotors **1 - 6 (R)** with various R-groups at 25 °C, experimentally quantified TS stabilization ($\Delta\Delta G^{\ddagger}_{Expt.}$, kcal/mol).

Rotor	$\Delta G^{\ddagger}_{Expt.}$ (kcal/mol)	$\Delta G^{\ddagger}_{Calc.}$ (kcal/mol)	$\Delta\Delta G^{\ddagger}_{Expt.}$ (kcal/mol)	pKa (in DMSO) of Corresponding Amine/Amide
1 NH_2	16.4	15.3	5.6	30.6
2 $NHCOCH_3$	16.5	15.0	5.5	21.5
3 $NHCOCF_3$	15.6	16.0	6.4	12.6
4 $NHCOCHF_2$	14.9	17.6	7.1	13.8
5 $NHCOC_6H_5$	16.8	17.3	5.2	18.8
6 $NHCH_3$	17.5	15.8	4.5	29.5
7 NHC_6H_5	17.7	17.1	4.3	25.0
8 $N(CH_3)_2$	22.0	21.1	0.0	--

Error in the EXSY rotational barriers was ± 0.1 kcal/mol; B3LYP-D3/6-311G*

2.3.6 EXPERIMENTAL DETERMINATION OF ROTATIONAL BARRIERS

The rotational barriers (Table 2) were determined via exchange spectroscopy (EXSY) NMR experiments. (EXSY) NMR is observable by running nuclear Overhauser effect spectroscopy (NOESY) NMR experiments. In the spectra obtained from the NOESY experiments, out-of-phase signals off the diagonal of the 2D spectra originate from the nuclear Overhauser effect, while in-phase signals off the diagonal originate from exchange dynamics.[66] Integration of the signals were performed using Topspin software, and rate constants were obtained using the EXSYCalc software. The rotational barrier for each rotor were extrapolated to the room temperature for consistency. The TS enthalpy ($\Delta H^{\ddagger}$) and TS entropy ($\Delta S^{\ddagger}$) were obtained from the Eyring plots (Figure S1) following Equation S1. The rotation barriers were determined by plugging the TS enthalpy and entropy along with a temperature into Equation S2.

$$\ln\left(\frac{k_{ex}}{T}\right) = \frac{-\Delta H^{\ddagger}}{R} \times \frac{1}{T} + \ln\left(\frac{k_B}{h}\right) + \frac{-\Delta S^{\ddagger}}{R} \quad \textbf{(Eqn S1)}$$

$$\Delta G^{\ddagger} = \Delta H^{\ddagger} - T \times \Delta S^{\ddagger} \quad \textbf{(Eqn S2)}$$

$\Delta G^{\ddagger}$	= Gibb's free energy of the rotational barrier
R	= gas constant
T	= temperature
k_B	= Boltzmann's constant
k_{ex}	= exchange rate
$\Delta H^{\ddagger}$	= enthalpy change in the rotational barrier
$\Delta S^{\ddagger}$	= entropy change in the rotational barrier

Figure 2.40. Eyring and Gibb's Free Energy equations

Due to the wide temperature range needed for rotational barrier determination *two* solvents (dichloromethane and tetrachloroethane) with similar chemical properties but different melting/boiling temperatures were chosen. Dichloromethane-d2 (melting point = -95 °C, boiling point = 40 °C) is an appropriate choice for the rotors that requires a temperature range below 25 °C. Meanwhile, tetrachloroethane-d2 (melting point = -45 °C, boiling point = 145 °C) was an appropriate choice for the rotors that requires a temperature range above 25 °C.

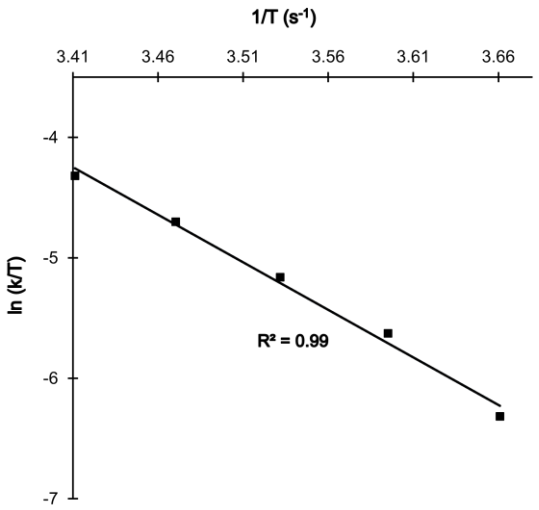

Figure 2.41. Eyring's plot for **3**($NHCOCF_3$)

Table 2.3. Experimental rotational barriers for rotors **1 - 8** via EXSY NMR

	rotational barrier (kcal/mol)							*Temperature range* (ºC)
	syn → *anti*			*anti* → *syn*			*average* $\Delta G^{\ddagger}$	
Rotor	$\Delta G^{\ddagger}$	$\Delta H^{\ddagger}$	$T\Delta S^{\ddagger}$	$\Delta G^{\ddagger}$	$\Delta H^{\ddagger}$	$T\Delta S^{\ddagger}$		
1	16.43	18.79	2.36	16.33	16.99	0.66	16.38	-5 - 20
2	16.45	11.50	-4.95	16.46	11.51	-4.95	16.46	0 - 20
3	15.6	16.66	1.07	15.71	16.17	0.48	15.65	0 - 20
4	14.91	11.63	-3.28	14.90	11.02	-3.88	14.91	0 - 20
5	16.65	13.58	-3.07	16.93	13.92	-3.01	16.79	0 - 20
6	17.49	12.65	-4.84	17.55	12.45	-5.10	17.52	30 - 55
7	17.67	12.33	-5.34	17.71	12.55	-5.16	17.69	30 - 55
8	21.47	20.16	-1.31	22.55	21.83	-0.72	22.01	30 - 55

2.3.7 CALCULATION OF ROTATIONAL BARRIERS, TS AND GS GEOMETRIES

Following instructions from a benchmark study on the accuracy of different levels of theory for rotational barrier calculation, we optimized the ground state (GS) and transition state (TS) for our rotors using B3LYP-D3(0)/6-311G* and corrected for thermodynamic contributions[66]. All calculations were performed using *Spartan'18.* Convergence criteria were 10^{-4} Hartree and 10^{-4} atomic units as the maximum norm of the cartesian gradient. Vibrational analysis was also carried out at B3LYP-D3(0)/6-311G* and at 25 °C. To reduce error, the calculated GS energies for the *syn*- and *anti*- conformers were averaged. With thermodynamic corrections, the calculated barriers ($\Delta G^{\ddagger}$calc) reproduced the experimental barriers ($\Delta G^{\ddagger}$exp) with an accuracy of ±1.15 kcal/mol (Table S1 and Figure S29), suggesting that the calculated TS and GS geometries (Tables S4-33) were also accurate.

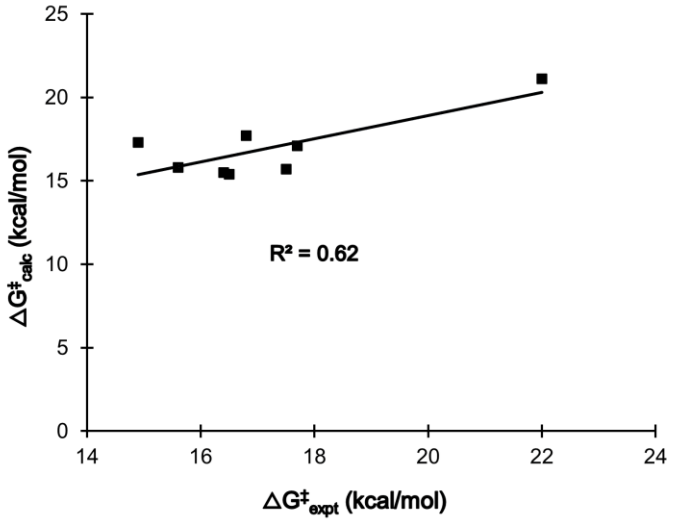

Figure 2.42. Correlation of the calculated ($\Delta G^{\ddagger}_{calc}$) and experimental ($\Delta G^{\ddagger}_{exp}$) rotational barriers for **1(R)**. Structures were calculated at the B3LYP-D3(0)/6-311G* level of theory with thermodynamic corrections.

2.3.8 TS XYZ COORDINATES OF ROTORS

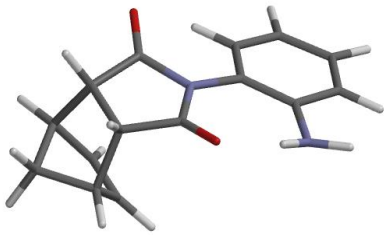

ROTOR **1** TS XYZ COORDINATES

1	0.996425000	-3.617472000	-2.377931000
6	1.205503000	-3.342876000	-1.339019000
6	1.928679000	-1.981349000	-1.190297000
6	1.778529000	-1.757073000	0.305755000
6	0.608061000	-2.285575000	0.678712000
6	-0.046412000	-2.878769000	-0.557624000
1	1.734988000	-4.159629000	-0.844941000
1	2.930779000	-1.881638000	-1.602781000
1	2.448042000	-1.158491000	0.910786000
1	0.132922000	-2.207097000	1.648753000
1	-0.846172000	-3.598309000	-0.393125000
6	-0.473767000	-1.678372000	-1.503877000
1	-1.084352000	-2.050920000	-2.326490000
6	0.859138000	-1.065337000	-1.919465000
1	1.042045000	-1.056130000	-2.994298000
6	-1.215557000	-0.566636000	-0.811974000
6	0.806157000	0.352394000	-1.413466000
8	1.602109000	1.202614000	-1.718803000
8	-2.405952000	-0.629641000	-0.589320000
7	-0.331540000	0.503542000	-0.544030000
6	-0.468979000	1.620151000	0.401124000
6	-0.430289000	3.832709000	2.179952000
6	-1.611048000	1.898430000	1.214922000
6	0.666104000	2.436867000	0.574067000
6	0.702205000	3.519668000	1.436038000
6	-1.545667000	3.032973000	2.059349000
1	1.546887000	2.239714000	-0.008020000
1	1.607970000	4.110679000	1.510468000
1	-2.423541000	3.249006000	2.662740000
1	-0.443574000	4.684592000	2.852465000
7	-2.751474000	1.133636000	1.340012000
1	-3.533463000	1.604666000	1.765814000
1	-2.984756000	0.493673000	0.594505000

ROTOR **2** TS XYZ COORDINATES

1	1.378946000	-3.839265000	-2.709487000
6	1.613066000	-3.516140000	-1.690182000

6	2.333161000	-2.147200000	-1.621168000
6	2.220802000	-1.857685000	-0.132429000
6	1.062207000	-2.372358000	0.293116000
6	0.378731000	-3.022292000	-0.898399000
1	2.159044000	-4.307234000	-1.173031000
1	3.323870000	-2.062448000	-2.063176000
1	2.908232000	-1.238168000	0.430002000
1	0.614696000	-2.260398000	1.272968000
1	-0.413130000	-3.736336000	-0.681416000
6	-0.079745000	-1.871702000	-1.890729000
1	-0.700340000	-2.291066000	-2.682421000
6	1.241319000	-1.267103000	-2.362552000
1	1.398240000	-1.300762000	-3.440982000
6	-0.824718000	-0.732536000	-1.249507000
6	1.196741000	0.168713000	-1.909675000

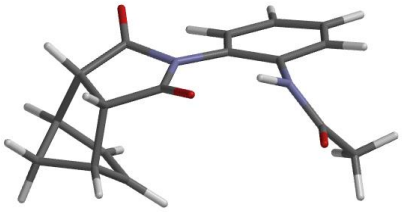

8	1.978946000	1.016400000	-2.251734000
8	-2.014220000	-0.760362000	-1.043128000
7	0.075269000	0.345730000	-1.023926000
6	-0.038647000	1.487704000	-0.126477000
6	0.021061000	3.813934000	1.506931000
6	-1.193137000	1.877624000	0.614571000
6	1.132254000	2.243013000	0.073204000
6	1.176512000	3.370109000	0.879237000
6	-1.135047000	3.071458000	1.354621000
1	2.036521000	1.958659000	-0.433085000
1	2.113914000	3.904649000	0.986318000
1	-2.054052000	3.401480000	1.821748000
1	0.013327000	4.721419000	2.100714000
7	-2.400344000	1.164523000	0.698392000
1	-2.679742000	0.622496000	-0.110869000
6	-3.074589000	0.747599000	1.839614000
8	-4.094056000	0.094950000	1.727876000
6	-2.505705000	1.083544000	3.208269000
1	-1.418427000	1.165163000	3.224094000
1	-2.832732000	0.297110000	3.887328000
1	-2.918227000	2.026778000	3.575368000

ROTOR **3** TS XYZ COORDINATES

1	0.968458000	-3.445317000	-3.256198000
6	1.549198000	-3.332060000	-2.334794000

6	2.301732000	-1.981894000	-2.235581000
6	2.715607000	-2.007240000	-0.770498000
6	1.755726000	-2.642534000	-0.088580000
6	0.679282000	-3.056648000	-1.083098000
1	2.207291000	-4.193730000	-2.211864000
1	3.083688000	-1.773595000	-2.962315000
1	3.579940000	-1.494029000	-0.368809000
1	1.675902000	-2.757153000	0.984947000
1	-0.017147000	-3.826326000	-0.757863000
6	-0.025081000	-1.733416000	-1.569040000
1	-0.919296000	-1.964209000	-2.152070000
6	1.066775000	-1.006558000	-2.339787000
1	0.823595000	-0.797698000	-3.383806000
6	-0.412539000	-0.802038000	-0.454272000

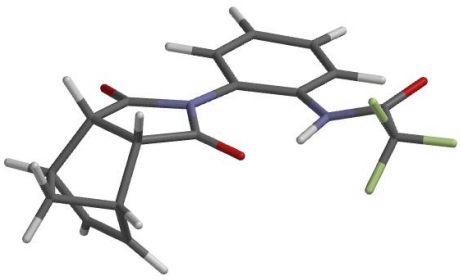

6	1.249822000	0.304773000	-1.621141000
8	2.142358000	1.069194000	-1.870513000
8	-1.143433000	-1.173279000	0.440846000
7	0.225406000	0.449540000	-0.598022000
6	0.053598000	1.686710000	0.190270000
6	0.012548000	4.189805000	1.544902000
6	-0.810698000	1.896436000	1.314169000
6	0.802675000	2.797560000	-0.238045000
6	0.787163000	4.023033000	0.409443000
6	-0.772435000	3.136417000	1.975640000
1	1.442346000	2.702117000	-1.093071000
1	1.396141000	4.830599000	0.018338000
1	-1.413657000	3.264875000	2.832627000
1	0.000976000	5.127754000	2.089037000
7	-1.729762000	0.944283000	1.796420000
1	-1.579243000	-0.011653000	1.471477000
6	-2.863495000	1.166272000	2.513800000
6	-3.690145000	-0.142620000	2.680114000
8	-3.296555000	2.198877000	2.975105000
9	-2.906534000	-1.215581000	2.932873000
9	-4.372998000	-0.403304000	1.543467000
9	-4.567212000	-0.027363000	3.675892000

ROTOR **4** TS XYZ COORDINATES

1	1.093336000	-3.622344000	-3.031018000
6	1.566564000	-3.512455000	-2.049768000

6	2.391140000	-2.210391000	-1.899214000
6	2.625218000	-2.207907000	-0.394626000
6	1.550735000	-2.755401000	0.184176000
6	0.575489000	-3.136622000	-0.921586000
1	2.146046000	-4.409302000	-1.823922000
1	3.267251000	-2.080526000	-2.530750000
1	3.467209000	-1.734831000	0.094407000
1	1.334245000	-2.822806000	1.242680000
1	-0.205910000	-3.847391000	-0.662200000
6	0.023216000	-1.788324000	-1.528022000
1	-0.809992000	-1.983800000	-2.206103000
6	1.245349000	-1.164444000	-2.183705000
1	1.144853000	-0.983361000	-3.255978000
6	-0.429713000	-0.788803000	-0.499688000

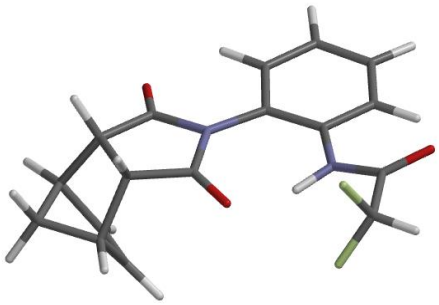

6	1.431739000	0.161240000	-1.492807000
8	2.393995000	0.858066000	-1.675062000
8	-1.302623000	-1.066825000	0.295042000
7	0.318747000	0.406458000	-0.591801000
6	0.146652000	1.678763000	0.142654000
6	0.133309000	4.228683000	1.408591000
6	-0.832706000	1.992176000	1.143074000
6	1.032352000	2.712675000	-0.211832000
6	1.034260000	3.959722000	0.392611000
6	-0.780257000	3.254106000	1.763702000
1	1.765779000	2.536103000	-0.973098000
1	1.753044000	4.701947000	0.062902000
1	-1.515875000	3.464051000	2.522940000
1	0.123702000	5.186067000	1.918145000
7	-1.871350000	1.130263000	1.541116000
1	-1.780170000	0.159946000	1.238779000
6	-3.030303000	1.436739000	2.185790000
8	-3.409577000	2.507292000	2.624429000
6	-3.973569000	0.226370000	2.320384000
1	-4.714477000	0.416925000	3.098030000
9	-4.617503000	0.018347000	1.131563000
9	-3.290204000	-0.920406000	2.620162000

ROTOR **5** TS XYZ COORDINATES

1	-1.663208336	0.280230011	4.518676136
6	-0.722666119	0.229827203	3.960258565

6	-0.488177008	-1.131500663	3.259383709
6	0.682720281	-0.769984253	2.355593839
6	0.537450471	0.507866955	1.990342252
6	-0.740248285	1.027053047	2.633728646
1	0.104566303	0.514679350	4.612438986
1	-0.368172172	-2.015479983	3.882759846
1	1.423374215	-1.473881484	1.997240795
1	1.140202524	1.060889960	1.281872965
1	-0.855756636	2.107811811	2.685567066
6	-1.950749122	0.299246446	1.925998706
1	-2.896258772	0.750483571	2.233580246
6	-1.784517250	-1.169211274	2.362882324
1	-2.626865133	-1.562651168	2.935143956
6	-1.887166071	0.274971182	0.416238775
6	-1.656972223	-1.960290017	1.080152330

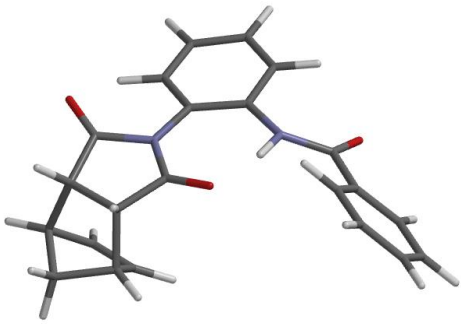

8	-1.514695918	-3.147227818	0.964608445
8	-1.914846137	1.241649179	-0.319758321
7	-1.739338158	-1.045901861	-0.006434248
6	-1.649146521	-1.493210623	-1.368251721
6	-1.405971505	-2.583496021	-3.918869431
6	-0.668056777	-0.999025985	-2.246622258
6	-2.515141446	-2.503335403	-1.786509922
6	-2.397861886	-3.049201608	-3.057945610
6	-0.552955926	-1.562602424	-3.521382090
1	-3.260935288	-2.877818347	-1.096598498
1	-3.071526185	-3.839640694	-3.370374437
1	0.220167139	-1.196330923	-4.182059645
1	-1.300281817	-3.010607144	-4.910699610
7	0.157804988	0.060208567	-1.832140995
1	-0.312410544	0.768397244	-1.288069132
6	1.504412976	0.186417527	-2.074473446
8	2.153817445	-0.619793487	-2.717871885
6	2.142323118	1.382093636	-1.417758857
6	3.464711224	3.480944794	-0.121995825
6	1.435671055	2.522140360	-1.013910975
6	3.519636042	1.315838101	-1.186162649
6	4.175417366	2.353954830	-0.533679871
6	2.096452384	3.566533397	-0.372482225
1	0.371702701	2.619391672	-1.202152329
1	4.054403627	0.435396779	-1.522406687

1	5.242028521	2.284956916	-0.346255782
1	1.539660963	4.447325766	-0.069704530
1	3.976047196	4.292276661	0.386104614

ROTOR **6** TS XYZ COORDINATES

1	1.215254000	-3.673090000	-2.739322000
6	1.540365000	-3.369780000	-1.738870000
6	2.196958000	-1.967270000	-1.695743000
6	2.231514000	-1.732152000	-0.194305000
6	1.150814000	-2.318067000	0.332458000
6	0.374053000	-2.961946000	-0.804479000
1	2.173534000	-4.147404000	-1.308421000
1	3.128568000	-1.816685000	-2.237721000
1	2.942393000	-1.092790000	0.313933000
1	0.803978000	-2.252894000	1.356246000
1	-0.355286000	-3.722466000	-0.531584000
6	-0.239342000	-1.806166000	-1.697900000
1	-0.921908000	-2.230134000	-2.434450000
6	0.990071000	-1.120370000	-2.279072000
1	1.030834000	-1.103292000	-3.368611000
6	-0.957419000	-0.731600000	-0.928749000

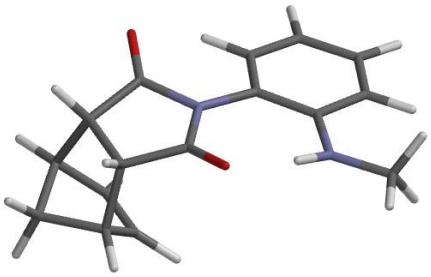

6	0.919576000	0.294485000	-1.765732000
8	1.623101000	1.184916000	-2.167818000
8	-2.111478000	-0.863022000	-0.574626000
7	-0.110285000	0.387530000	-0.760502000
6	-0.179756000	1.494056000	0.209859000
6	0.007653000	3.673464000	2.016558000
6	-1.209038000	1.692419000	1.196371000
6	0.912879000	2.376275000	0.223952000
6	1.024367000	3.445010000	1.101431000
6	-1.074639000	2.815713000	2.049144000
1	1.701662000	2.245002000	-0.492600000
1	1.896184000	4.087225000	1.048973000
1	-1.854803000	2.999214000	2.774536000
1	0.050088000	4.510860000	2.706046000
7	-2.271303000	0.854466000	1.415482000
1	-2.498074000	0.203311000	0.678245000
6	-3.315086000	1.121738000	2.377906000
1	-2.924705000	1.157279000	3.401079000
1	-4.035880000	0.304539000	2.328249000

1 -3.854845000 2.061624000 2.190035000

ROTOR **7** TS XYZ COORDINATES

1	1.661660000	-3.590035000	-3.456440000
6	1.911129000	-3.361735000	-2.415497000
6	2.729304000	-2.058834000	-2.244219000
6	2.627273000	-1.870282000	-0.739330000
6	1.431345000	-2.327673000	-0.353603000
6	0.710867000	-2.837201000	-1.591116000
1	2.393042000	-4.227101000	-1.957017000
1	3.726607000	-2.015518000	-2.677429000
1	3.351879000	-1.340589000	-0.133688000
1	0.983113000	-2.246400000	0.628964000
1	-0.132630000	-3.505153000	-1.427620000
6	0.345856000	-1.583468000	-2.493474000
1	-0.305464000	-1.891358000	-3.311474000
6	1.709457000	-1.049827000	-2.923228000
1	1.868901000	-1.020817000	-4.001355000
6	-0.303394000	-0.444901000	-1.755462000

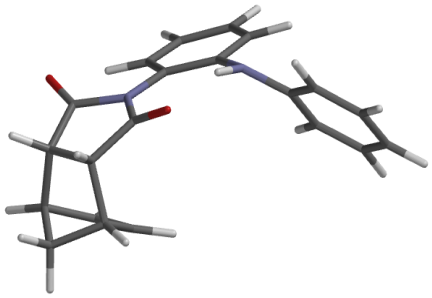

6	1.767549000	0.350299000	-2.371521000
8	2.605360000	1.161591000	-2.668499000
8	-1.493599000	-0.414230000	-1.530448000
7	0.669754000	0.542833000	-1.458398000
6	0.677582000	1.581846000	-0.424139000
6	1.016138000	3.558550000	1.588083000
6	-0.401057000	1.907802000	0.450736000
6	1.899268000	2.253564000	-0.221102000
6	2.080260000	3.210085000	0.763643000
6	-0.193195000	2.919241000	1.411772000
1	2.734693000	2.034863000	-0.860025000
1	3.049629000	3.685151000	0.866258000
1	-1.042894000	3.184705000	2.029103000
1	1.120075000	4.327434000	2.346457000
7	-1.668271000	1.329653000	0.434944000
1	-1.917856000	0.848747000	-0.419118000
6	-2.365248000	0.861483000	1.561195000
6	-3.867475000	-0.162296000	3.712232000
6	-1.764027000	0.629758000	2.807810000
6	-3.729942000	0.565685000	1.409830000
6	-4.465854000	0.052968000	2.470874000
6	-2.514178000	0.129773000	3.868019000

1	-0.707637000	0.828811000	2.938939000
1	-4.204203000	0.747959000	0.450422000
1	-5.519097000	-0.169277000	2.328949000
1	-2.028241000	-0.043264000	4.823610000
1	-4.446478000	-0.552843000	4.542361000

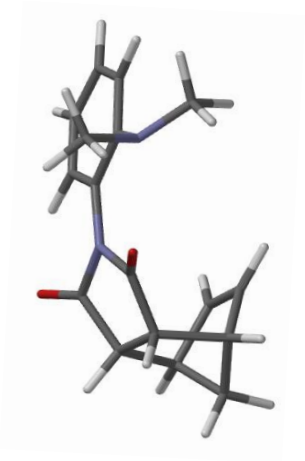

ROTOR **8** TS XYZ COORDINATES

1	1.402246000	-3.492534000	-2.981051000
6	1.808543000	-3.107486000	-2.040221000
6	2.274151000	-1.634625000	-2.120817000
6	2.468212000	-1.331300000	-0.643268000
6	1.547465000	-2.024673000	0.034999000
6	0.727552000	-2.814010000	-0.972544000
1	2.590017000	-3.778565000	-1.678672000
1	3.101424000	-1.390487000	-2.784265000
1	3.137579000	-0.576546000	-0.250075000
1	1.323225000	-1.954311000	1.092160000
1	0.147165000	-3.649914000	-0.585918000
6	-0.145579000	-1.788939000	-1.811717000
1	-0.839370000	-2.335097000	-2.450970000
6	0.902162000	-0.967825000	-2.558539000
1	0.801937000	-0.977592000	-3.644266000
6	-0.930269000	-0.783250000	-1.005158000
6	0.740271000	0.439622000	-2.041593000
8	1.308460000	1.393466000	-2.516286000
8	-2.041028000	-0.982167000	-0.604663000
7	-0.153170000	0.437583000	-0.928093000
6	-0.074115000	1.435364000	0.133102000
6	0.520274000	3.228867000	2.258155000
6	-0.857878000	1.428718000	1.322359000
6	0.943202000	2.402844000	0.038391000
6	1.243151000	3.276223000	1.076105000
6	-0.525303000	2.323626000	2.350584000
1	1.524035000	2.472655000	-0.863231000
1	2.053630000	3.985386000	0.944685000
1	-1.133518000	2.306906000	3.247322000
1	0.743732000	3.897604000	3.083032000
7	-1.962311000	0.565733000	1.507146000

6	-2.175550000	0.008564000	2.827300000
1	-1.224380000	-0.306540000	3.259511000
1	-2.815190000	-0.874527000	2.733948000
1	-2.668080000	0.696688000	3.537833000
6	-3.196793000	1.030632000	0.886281000
1	-3.659461000	1.851100000	1.462194000
1	-3.905421000	0.204186000	0.810572000
1	-3.001017000	1.384621000	-0.124336000

2.3.9 TRANSITION STATE AND GROUND STATE STRUCTURES OF ROTORS

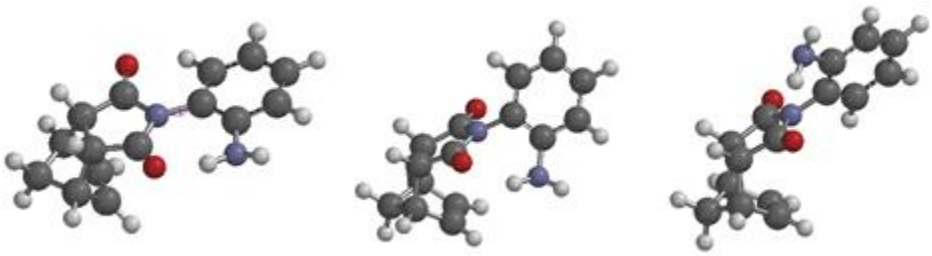

TS GS *syn*-conformer GS *anti*-conformer

Figure 2.43. 3D model of rotor **1**

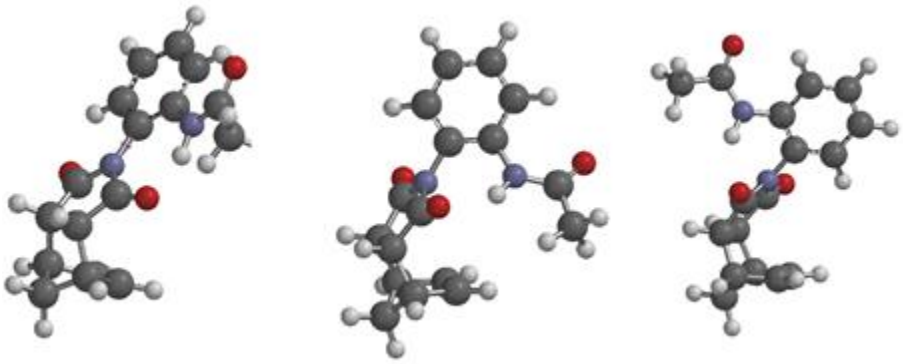

TS GS *syn*-conformer GS *anti*-conformer

Figure 2.44. 3D model of rotor **2**

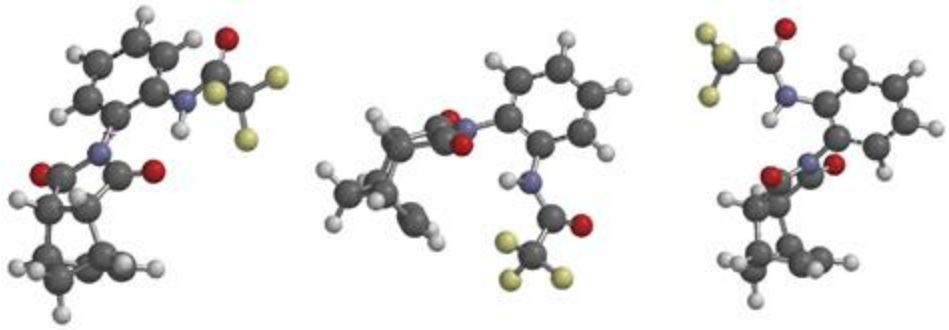

TS GS *syn*-conformer GS *anti*-conformer

Figure 2.45. 3D model of rotor **3**

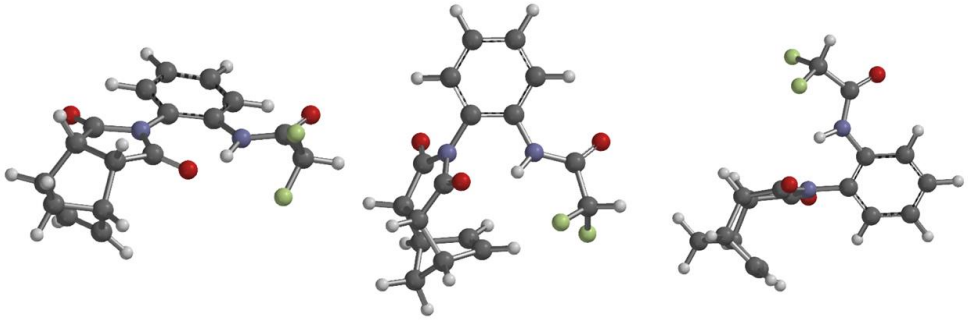

TS GS *syn*-conformer GS *anti*-conformer

Figure 2.46. 3D model of rotor **4**

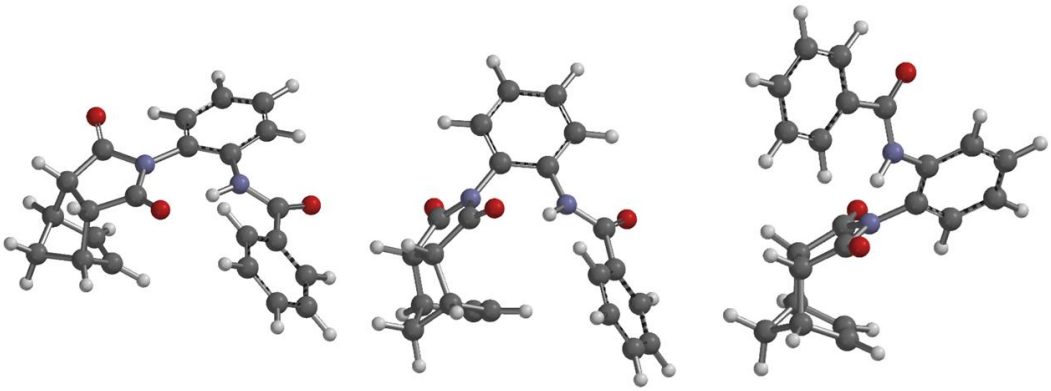

TS GS *syn*-conformer GS *anti*-conformer

Figure 2.47. 3D model of rotor **5**

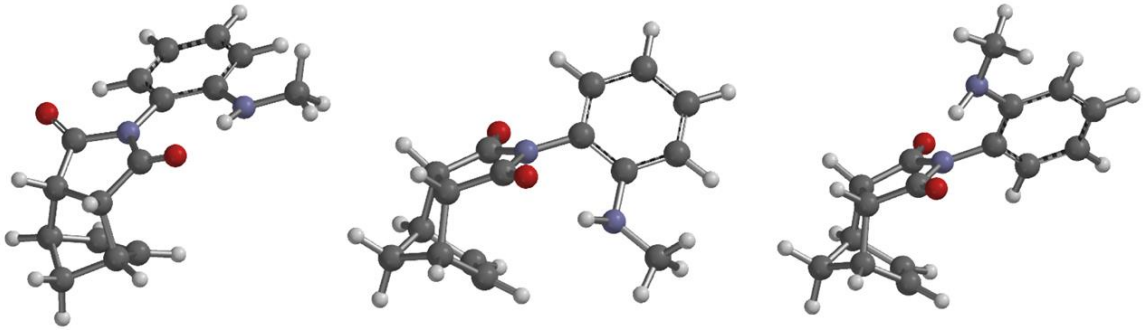

TS GS *syn*-conformer GS *anti*-conformer

Figure 2.48. 3D model of rotor **6**

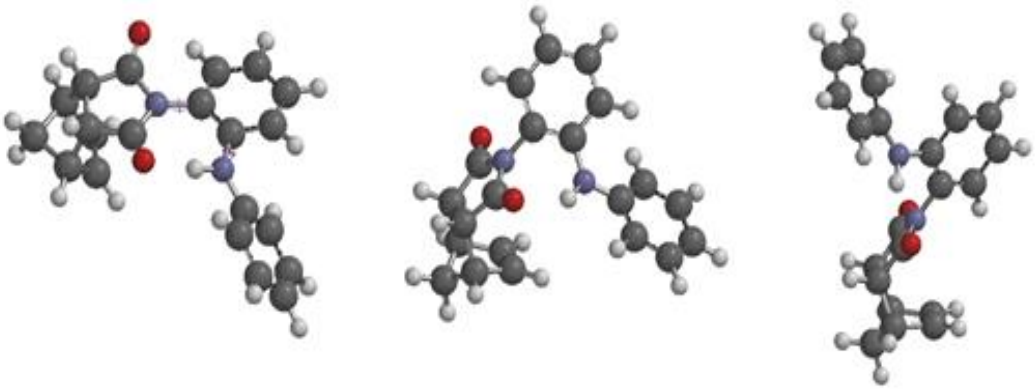

TS GS *syn*-conformer GS *anti*-conformer

Figure 2.49. 3D model of rotor **7**

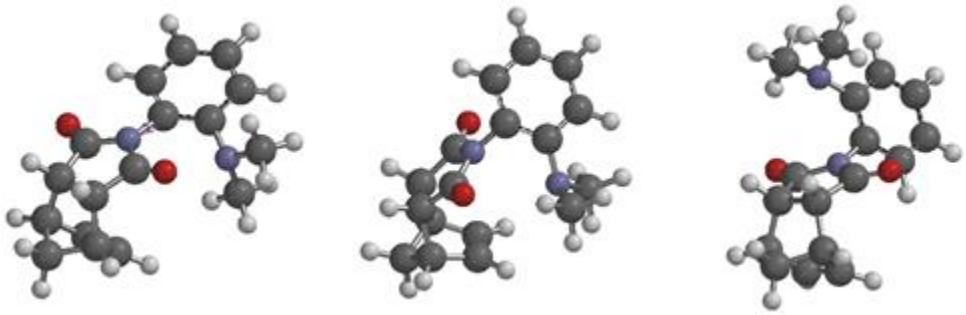

TS GS *syn*-conformer GS *anti*-conformer

Figure 2.50. 3D model of rotor **8**

2.3.10 EXSY Spectra of Rotor 4

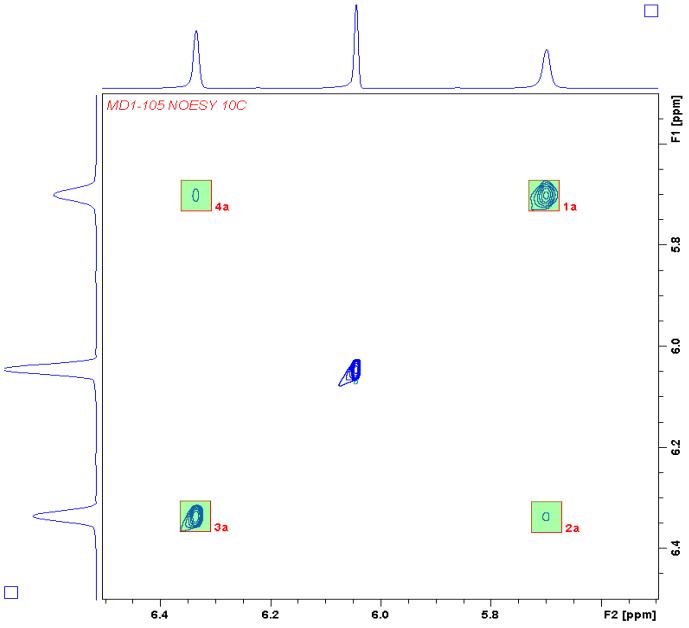

Figure 2.51. EXSY spectra of rotor **4** at 10°

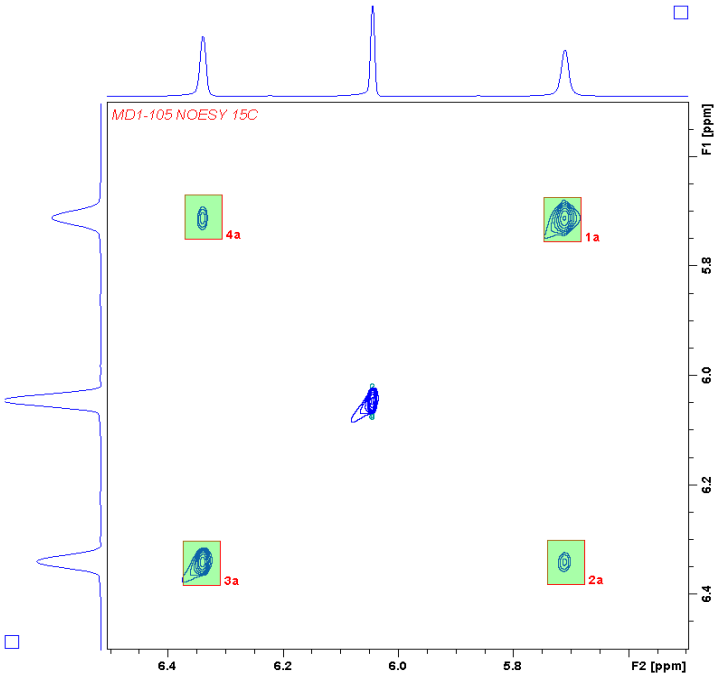

Figure 2.52. EXSY spectra of rotor **4** at 15°

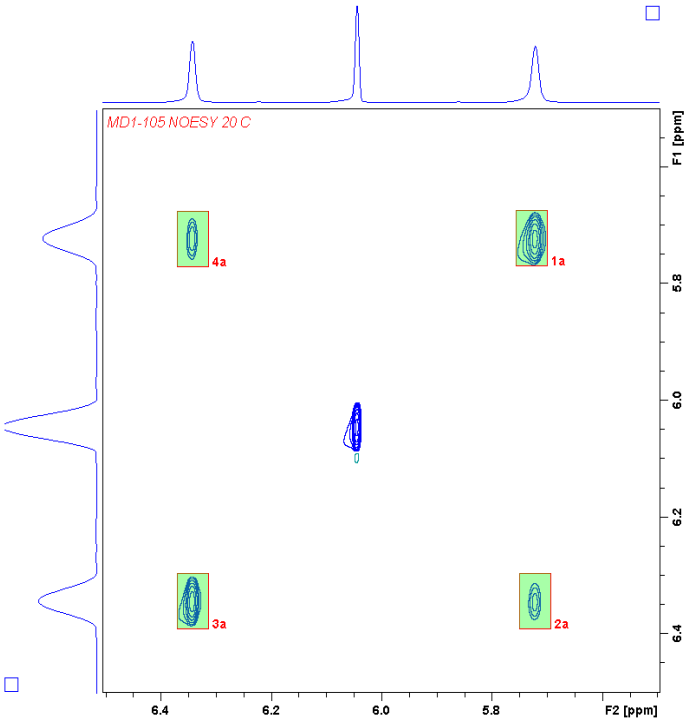

Figure 2.53. EXSY spectra of rotor **4** at 20°

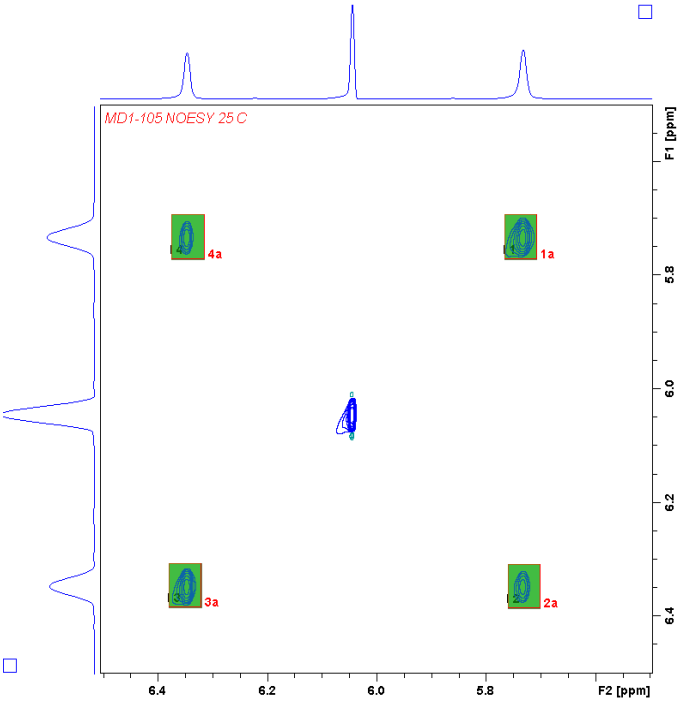

Figure 2.54. EXSY spectra of rotor **4** at 25°

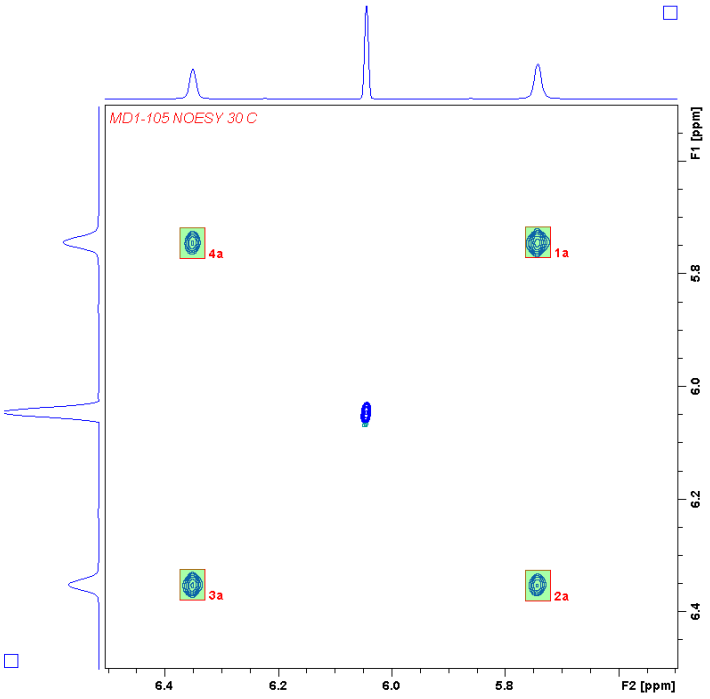

Figure 2.55. EXSY spectra of rotor **4** at 30°

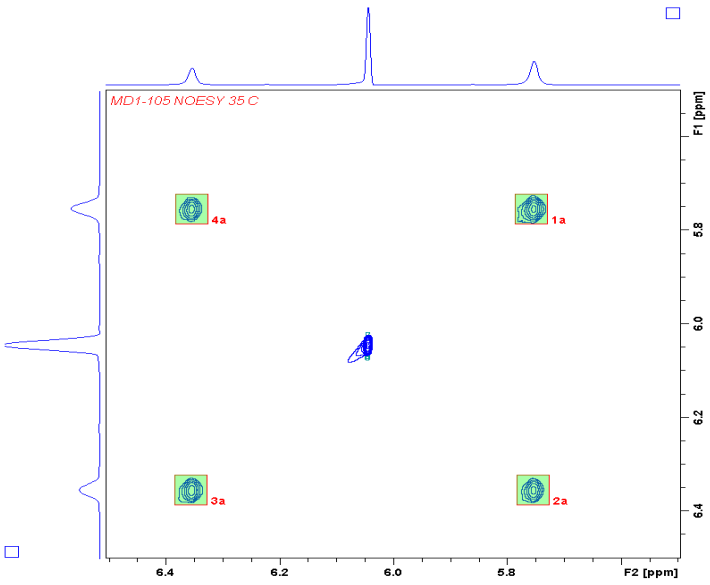

Figure 2.56. EXSY spectra of rotor **4** at 35°

CHAPTER 3

SP^2-CH/Π INTERACTION

3.1 ABSTRACT

The sp^2-CH/π interaction is a crucial factor influencing the structures and properties of biopolymers, molecular crystals, and liquids. Despite extensive research on the sp^3-CH/π interaction, limited information is available on the sp^2-CH/π interaction. Therefore, the aim of this study was to investigate the extent to which electrostatics govern the *sp2*-CH/π interaction. To achieve this objective, a molecular balance was designed based on a N-biphenylimide framework with one of the phenyl rings capable of forming an intramolecular CH/π interaction. Subsequently, electron-withdrawing and electron-donating substituents (X) were attached to the para-position of the phenyl ring that can form the CH/π interaction to modulate its π-system (Figure 3.1). The folding ratio was measured in $CDCl_3$ and varied with the Hammett parameter, sigma-meta (σ_m). Our findings suggest that electrostatics play a relatively minor role in the sp^2-CH/π interaction.

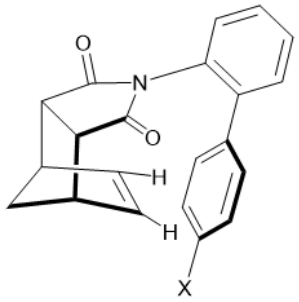

Figure 3.1. Molecular balance structure showing the alkene hydrogen atoms in a *syn*-conformation with the para-substituted benzene ring.

3.2 ELECTROSTATIC CONTRIBUTIONS IN SP^2-CH/Π INTERACTIONS

Liquids, molecular crystals, and biopolymers have structures and properties that are largely governed by inter- and intramolecular non-covalent interactions.[67,68,69] One such interaction is the CH/π interaction. This interaction involves the attraction between a hydrogen bonded to a carbon and aromatic surface.[70,71] CH/π interactions have garnered significant attention because of the role they play in regulating crystal packing,[72,73,74,75,76] biological molecule architectures[77,78,79] and molecular recognition processes.[80,81,82,83,84,85] Experimental[73,79,80,84,85] and theoretical studies[86,87,88,89] have been carried out to characterize and study the origins of CH/π interactions. While most of these studies focused on the sp^3 – CH/π interaction, few have focused on sp^2-CH/π interactions.

Experimental observation of electrostatic trends in a CH/π interactions is extremely difficult because the CH/π interaction is a very weak non-covalent interaction. In the gas phase at MP2/cc-pVTZ level and CCSD(T) basis set, the estimated strength of the sp^2-CH/π interaction is around 1.4 kcal/mol, while in solution it is generally less than this value.[90,91,92,93] While the electrostatic component has been found to be insignificant in the sp^3 – CH/π interaction, it remains unclear whether this holds true for the sp^2-CH/π interaction, given the higher polarizability of the sp^2-CH bond compared to the sp^3-CH bond. The goal of this study, therefore, is to examine whether sp^2-CH/π interaction is primarily driven by electrostatics. Answering this question is significant because understanding the fundamental force governing this interaction could aid in developing an accurate predictive model.

Our strategy for studying the sp^2-CH/π interactions was to systematically attach electron-withdrawing and electron-donating substituents to the *para*-position of the phenyl

ring that contains the π-system that can form an intramolecular CH/π interaction (Figure 3.2 A). We opted for the para-position as the optimal point of attachment of these substituents. While allowing for modulation of the electrostatics of the π-system, the substituents cannot directly form interactions with the CH groups.

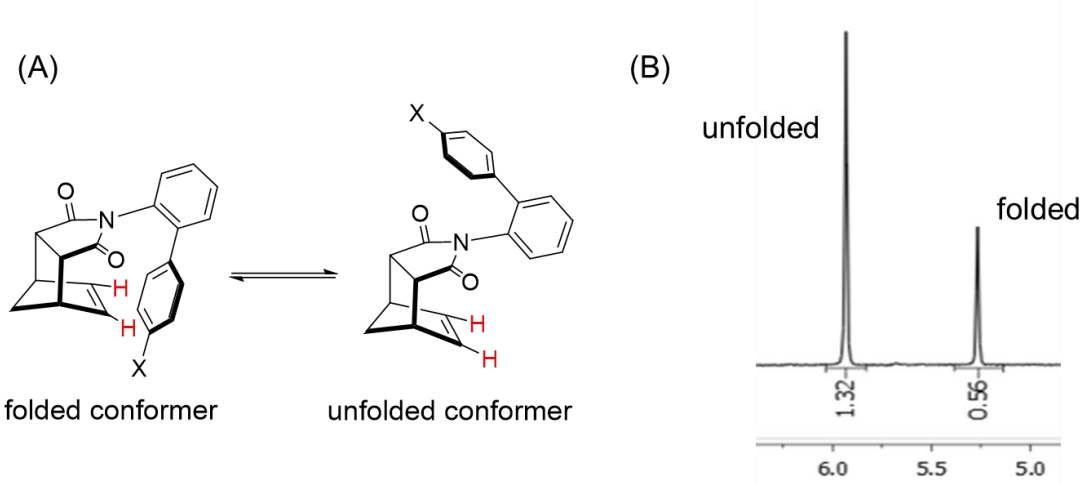

Figure 3.2 Quantifying the ration of conformational isomers. (A) folded and unfolded conformers with EDGs X = **1** H, **2** OMe, **3** t-Bu, **4** Ph and EWGs X = **5** F, **6** CF3, **7** CN, **8** NO2 (B) ^{1}H-NMR spectra of alkene region of **5** in $CDCl_3$

Our model system offers a number of advantages over the previous bimolecular systems. Having both interacting groups attached to the same framework increases the effective molarity of the groups forming the CH/π interaction, thus enabling the balance to overcome the complexation entropy. Furthermore, our system offers better control of the geometry of the interaction due to the rigid N-phenyl imide framework. Lastly, the molecular balances are easy to make. The synthesis of the molecular balances was a two-step process. The first step involved an air-sensitive Suzuki coupling reaction of 2-aminophenylboronic ester with a *para*-substituted bromobenzene to form the 2-amino-biphenyl product (Scheme 3.1). In the second step, the 2-amino-biphenyl product was thermally condensed with norbornene anhydride to form the desired *N*-phenylimide

molecular balance. A series of 8 sp^2-CH/π balances with varying X-substituents were synthesized and used for this study.

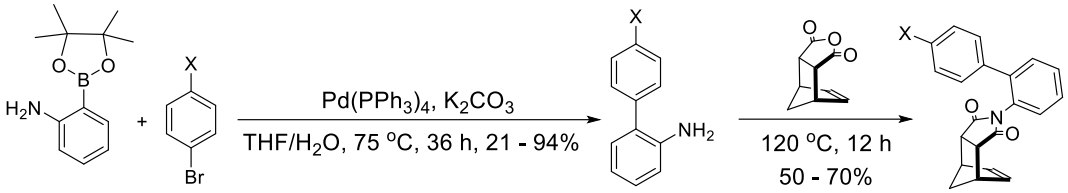

X = **1** H, **2** OMe, **3** *t*-Bu, **4** Ph, **5** F, **6** CF_3, **7** CN, **8** NO_2

Scheme 3.1 General synthesis of the molecular balances

The molecular balance was designed such that the system forms discrete *unfolded* and *folded* conformers as a result of restricted rotation of the $C_{(phenyl)}$-$N_{(imide)}$ single bond. The proximity of the sp^2-hydrogens to the π-surface of the benzene ring at the ortho position of the *N*-phenyl balance in the *folded* conformation is expected to form an attractive intramolecular interaction between the two groups. The rigid bicyclic framework keeps the interacting species apart in the *unfolded* conformer, The conformers reached equilibrium after 60 minutes and the interconversion was slow on the NMR timescale, allowing measurement of the folding equilibrium ratio by integration. The equilibration time was determined using 2-D TLC (Figure 3.3). A sample of the molecular balance was spotted onto one corner of a squared two-dimensional thin-layer chromatography (2-D TLC) plate. An ethyl acetate/hexanes (1/4) solvent system was used to develop the plate in one direction, which facilitated the separation of the sample spot into two distinct conformers. Subsequently, the TLC plate was removed from the developing chamber and left dry at ambient temperature for varying length of time. Then, the dry TLC plate was reintroduced into the same solvent mixture and developed perpendicularly to the first

development direction. This procedure was repeated at various time intervals, and the spot positions and intensities of the two conformers were analyzed and compared to establish the equilibrium time of the molecular system.

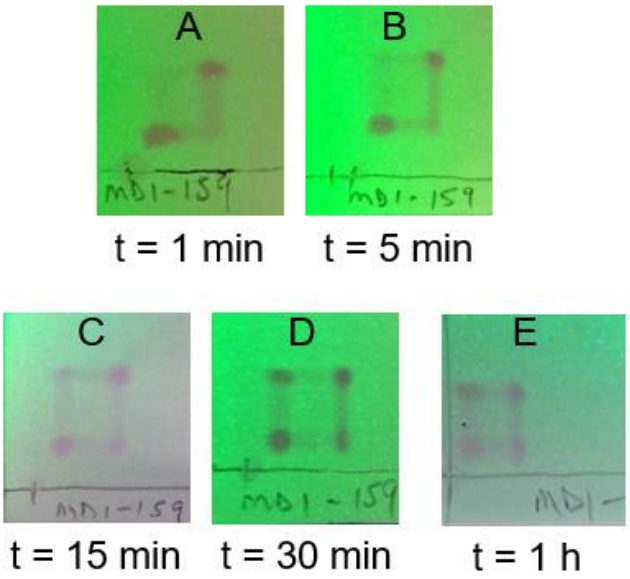

Figure 3.3. 2-D TLC of equilibrating conformers of *t*-Bu balance **3** in ethyl acetate/hexanes (1/4) solvent system at different times.

To confirm the time needed to reach equilibrium, ^{1}H-NMR spectroscopy was employed. The folding ratios of the molecular balance were measured at different times, and a comparison was made. The folding ratios remained constant after 60 minutes, signifying the establishment of equilibrium. The folding ratio is the ratio of the folded conformer to the unfolded conformer and is an indicator of CH/π interaction strength. Subsequently, the folding ratios were correlated with the Hammett parameter, sigma-meta (σ_m), to probe if electrostatics is the driving force in a CH/π interaction. The Hammett

parameter (σ_m) is an electrostatic parameter utilized to quantify the electron-donating or electron-withdrawing nature of substituents present on an aromatic ring.[42]

Table 3.1. Hammett parameters, ESP values, folded (F), unfolded (U) and folding ratio (F/U) values of balances **1** – **8**

Balance	σ_m	ESP (KJ/mol)	U/ $CDCl_3$	F/ $CDCl_3$	ln(F/U) $CDCl_3$	U/ (C_6D_6)	F/ (C_6D_6)	ln(F/U) (C_6D_6)
1(H)	0	-84.2	1.27	0.79	-0.47	1.28	0.65	-0.68
2(OMe)	0.12	-90.1	1.37	0.55	-0.91	1.42	0.52	-1.00
3(*t*-Bu)	-0.1	-88.9	1.07	0.85	-0.23	1.1	0.77	-0.36
4(Ph)	0.06	-77.2	1.29	0.66	-0.67	1.25	0.62	-0.70
(F)	0.34	-52.1	1.22	0.6	-0.71	1.32	0.56	-0.86
6($CF_{3)}$	0.43	-37.5	1.29	0.66	-0.67	1.27	0.66	-0.65
7(CN)	0.56	-15	1.34	0.6	-0.80	1.33	0.64	-0.73
8($NO_{2)}$	0.71	-3.5	1.43	0.53	-0.99	1.4	0.52	-0.99

NMR spectroscopy was used to identify the two conformers in chloroform solution. The highlighted protons (Figure 3.2 A) were used to assign the folded and unfolded conformers in the ^{1}H-NMR spectra. In the folded conformer, the highlighted protons experienced a shielding effect from the proximity of the benzene ring relative to the *unfolded* conformer. This shielding effect is due to anisotropy effects of the benzene π-system. Consequently, the alkene ^{1}H-NMR peak at 5.25 ppm (Figure 3.2 B) was assigned the *folded* conformer while the peak at 5.9 ppm was assigned the unfolded conformer. Both peaks were integrated and the natural log of the *folded* to *unfolded* conformer ratio [ln(F/U) or ln(K)], was plotted against sigma-meta (σ_m) (Figure 3.4, left).

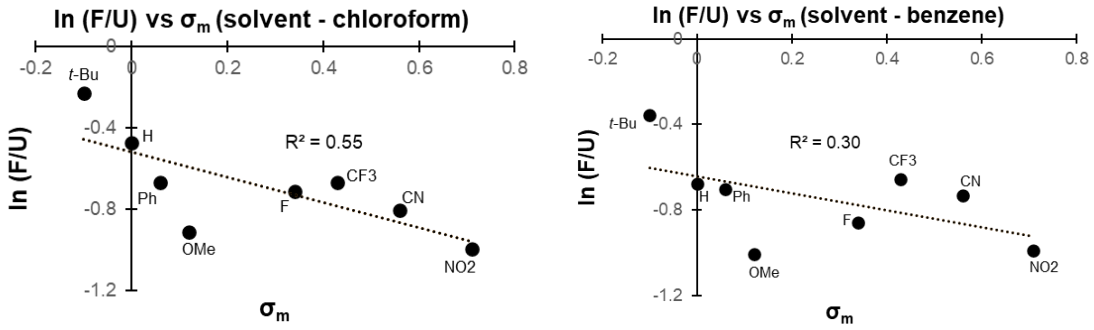

Figure 3.4. Plots of folding ratio (K) vs sigma meta (σ_m) in chloroform and benzene.

A weak correlation (0.55) was observed between ln(K) and sigma meta (σ_m). To probe this observation, a graph of folding ratio versus sigma meta (σ_m) in benzene was also measured (Figure 3.4, right), and a similar trend was observed. The folding ratios in chloroform and benzene showed good agreement ($R^2 = 0.9$, Figure 3.5, left) suggesting the accuracy and consistencies of our experimental measurements. The poor correlation with sigma meta (σ_m) suggests that electrostatics is not a primary component of the alkene CH/π interaction. To further test the importance of electrostatics in CH/π interaction, the folding ratio was correlated with the electrostatic potential (ESP) of the benzene π-system (Figure 3.5, right).[21,94] The ESP was determined by first optimizing the geometry of the folded conformation using the B3LYP-D3-6-311G** functional and basis set, followed by generating electrostatic potential surfaces of the optimized structures. Subsequently, we identified the most positive value (kcal/mol) of the electrostatic potential surface at the center of the benzene ring. However, our findings revealed only a weak correlation (R^2 = 0.34) between the folding ratio and the ESP of the benzene π-system, further suggesting that electrostatics may not be a significant contributing term in CH/π interactions.

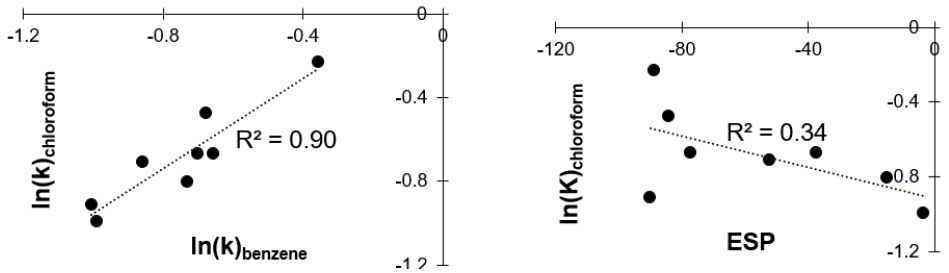

Figure 3.5. Folding ratios in chloroform vs benzene (left) and folding ratio vs ESP (right).

However, on a closer look at the folding ratio vs σ_m plot (Figure 3.6), the EWG and EDG each appear to have separate trendlines with the EDGs having a better correlation (R^2

Table 3.2. Total and individual FI-SAPT energies

balances	electrostatics (kcal/mol)	exchange (kcal/mol)	induction (kcal/mol)	dispersion (kcal/mol)	total (kcal/mol)
1(H)	-0.3	12.2	-2.1	-4.3	5.5
2(OMe)	0.1	12.2	-2.1	-4.7	5.4
3(*t*-Bu)	-1.3	2.6	-0.6	-1.5	-0.8
4(Ph)	-0.8	14.1	-2.4	-5.7	5.1
5(F)	1.8	8.5	-1.5	-4.0	4.9
6(CF_3)	-0.7	12.0	-1.9	-4.6	4.8
7(CN)	-1.5	11.6	-1.9	-4.3	8.2
8(NO_2)	0.2	8.8	-1.4	-4.3	3.3

= 0.99) than the EWGs (R^2 = 0.86) (Figure 3.6). We posit that there may be other equally influential energy components at play, such as dispersion of the substituent with the CH group. To confirm that electrostatics were only a minor component of the alkene CH/π interaction, we turned to FI-SAPT as implemented in psi4.[95] FI-SAPT is a computational tool, which offers valuable insights into the interactions between various fragments within a molecule. By separating the molecule into distinct fragments and employing perturbation theory, FI-SAPT can accurately compute the interaction energy between them.[64] The energy deconvolution analysis (JUN-CC-PVDZ) was performed on the C=O and substituted phenyl group fragments of molecular balances **1** through **8.** The FI-SAPT total interaction energies show poor correlation with the experimental folding ratios (Figure 3.6, right), further suggesting the weak contribution of electrostatics in sp^2-CH/π interactions.

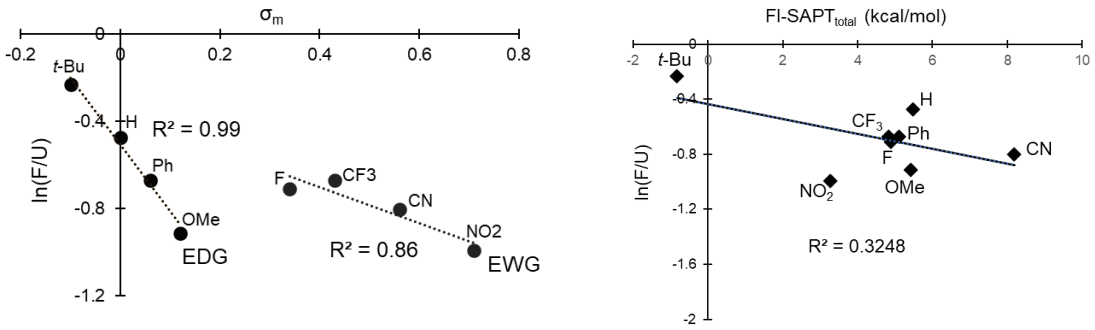

Figure 3.6. EDG- and EWG-trends in $CDCl_3$ (left) and FI-SAPT total energy ln(F/U) in $CDCl_3$ vs (right).

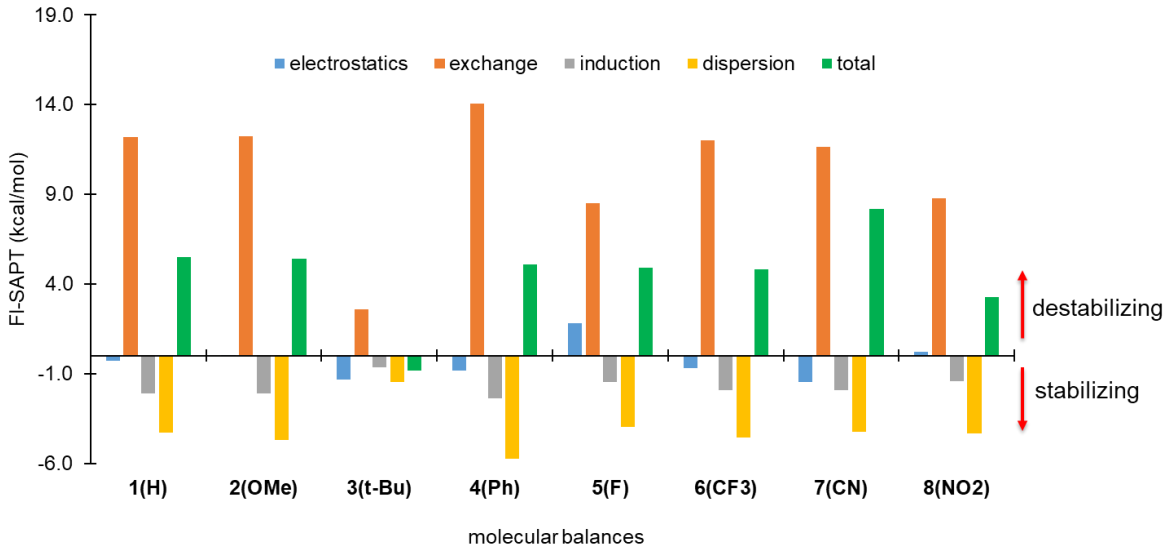

Figure 3.7. FI-SAPT showing total and individual interaction energies in balances **1 – 8.**

The total interaction energies within the transition state (TS) interactions of the balances were then decomposed into distinct physical components, namely electrostatics, repulsion, induction, and dispersion (Figure 3.7). Among the attractive components, electrostatics appeared to have the least contribution (blue bar) across all molecular balances, while dispersion was found to be more influential than electrostatics and induction. Notably, even when we introduced strong electron-withdrawing group **8**(NO_2) and electron-donating group **3**(*t*-Bu) at the para-position, the electrostatic term only changed marginally (Figure 3.8).

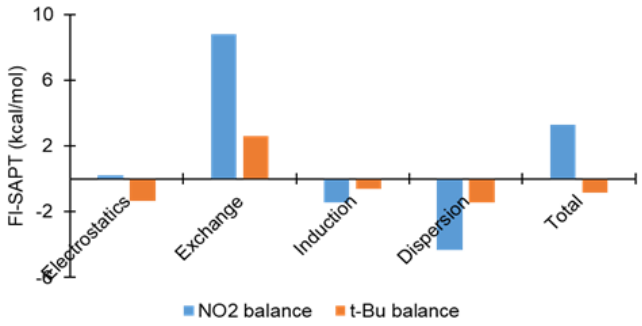

Figure 3.8. Comparison of total and individual components of FI-SAPT energies in **3** *t*-Bu (orange) and **10** NO_2 (blue). The net interaction is stabilizing in **3** *t*-bu but destabilizing in **10** NO_2.

In contrast, repulsion (red bar) emerged as the major contributing term in all the balances, resulting in a predominantly destabilizing net interaction (green bar, Figure 3.7). Only balance **3** (*t*-Bu) displayed a stabilizing interaction. We hypothesize that the *tert*-butyl group in balance **3** makes the *para*-substituted benzene ring more electron-rich by donating electron via positive inductive effect. This leads to the formation of a stabilizing interaction with the alkene sp^2-hydrogen (Figure 3.9). Conversely, the NO_2-group in balance **8** makes the benzene ring more electron-poor, leading to a destabilizing interaction with the alkene sp^2-hydrogen. This explains the high folding ratio observed in balance **3**(*t*-Bu) and the low folding ratio in balance **8**(NO_2) (Figure 3.4). Despite balance **3**(*t*-Bu) exhibiting the highest folding ratio, the stabilizing interaction was relatively weak (< -1.0 kcal/mol, Figure 3.8).

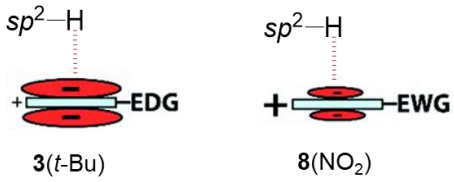

Figure 3.9. Comparison of FI-SAPT energies in **3** *t*-bu (red) versus **10** NO_2

To further test the hypothesis that repulsion is the major contributing term in sp^2-CH/π interactions, crystallography was utilized to examine the crystal structures of balances **2**(OMe), **3**(*t*-Bu), **6**(CF_3) and **8**(NO_2). Balances **2**(OMe), **3**(*t*-Bu), and **6**(CF_3) crystalized in the *unfolded* conformation, suggesting that repulsion plays a dominant role in governing sp^2-CH/π interactions. **8**(NO_2), on the other hand, crystallized in the *folded* conformation. To eliminate the possibility that repulsion is a minor contributing term relative to the attractive forces in balance **8**(NO_2), the internuclear distance of the alkene sp^2-hydrogen (H8) and the closest point on the benzene ring (C18) was measured (Figure 3.10C). The internuclear distance between H8 and C18 was found to be 2.92 Å, which falls outside the sum of the vdW radii of H8 and C19 (2.90 Å). This suggests that the crystallization of **8**(NO_2) in the folded conformation could be due to other factors like crystal packing but not repulsion.

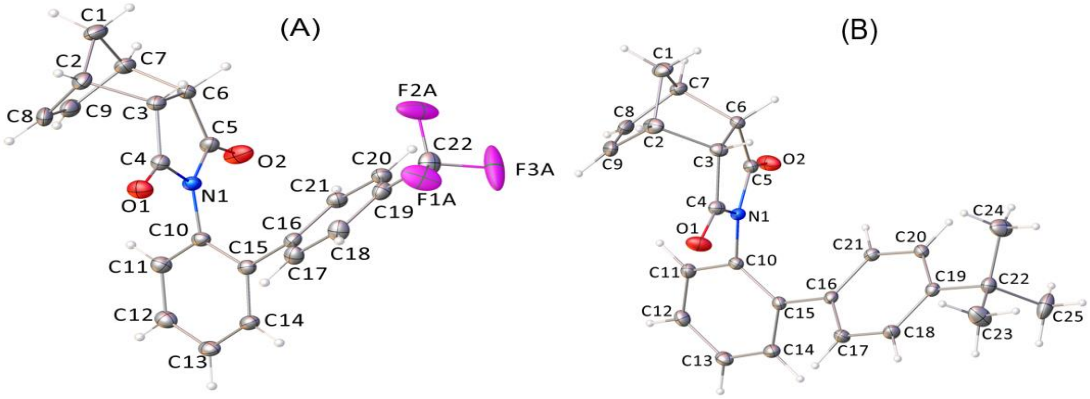

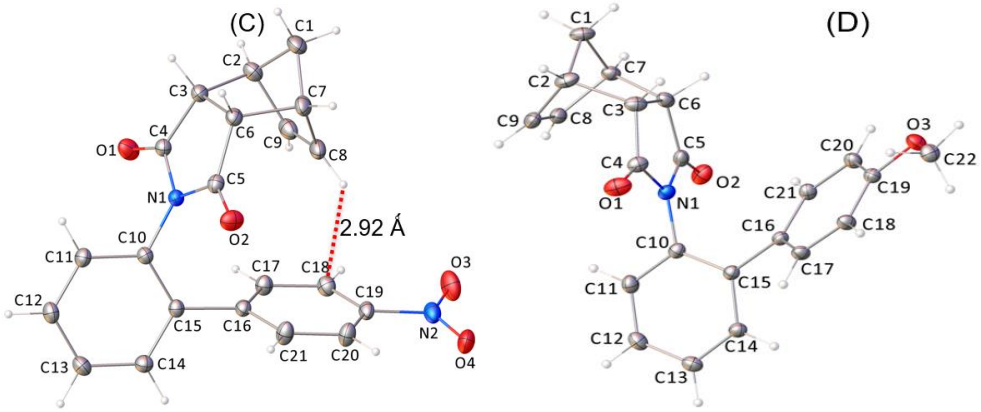

Figure 3.10. Crystal structures of balances **6**(CF_3) A, **3**(*t*-Bu) B, **8**(NO_2) C and **2**(OMe) D

Comparing the attractive forces in all the balances revealed that dispersion was the most stabilizing, followed by induction and electrostatics, in that order (Figure 3.7). This trend was consistent across all the balances. Despite the inability of these balances to form a stabilizing interaction, we were able to establish that dispersion, rather than electrostatics, is the fundamental attractive force governing CH/π interactions, while repulsion stands as the most significant contributing term in alkene sp^2-CH/π interactions.

3.3 SUPPORTING INFORMATION

3.3.1 GENERAL EXPERIMENTAL INFORMATION

NMR spectra were recorded on Bruker 300 MHz spectrometer. Chemical shifts are reported in ppm (δ) referenced to the solvent residue. All spectra given for characterization purposes were taken at 25 ºC. All chemicals and solvents were purchased from commercial

suppliers and used as received. Flash chromatography was performed using silica gel from Sorbent Technologies (60 Å, 200 – 400 mesh).

3.3.2 SYNTHESIS OF COMPOUNDS

[1,1'-Biphenyl]-2-amine (154.6 mg, 0.91 mmol) and *cis*-5-norbornene-*endo*-2,3-dicarboxylic anhydride (101 mg, 0.61 mmol) were added to a 20-dram vial along with a magnetic stir bar. The vial was then capped and heated to 120 ºC in a silicon oil bath for 12 hours with mild stirring. After letting the vial cool to room temperature, the crude material was purified by column chromatography (ethyl acetate/hexanes = 1:4, v/v) to give a brown crystalline solid **1** (17.2 mg, 90 %). ^{1}H NMR (300 MHz, $CDCl_3$) δ 7.49 – 7.30 (m, 6 H), 7.24 - 7.18 (m, 2 H), 7.07 – 6.99 (m, 1 H), 6.27 (s, 2 H major), 5.28 (s, 2 H minor), 3.40 – 3.14 (m, 4 H), 1.73 (d, J = 8.7 Hz, 1 H major), 1.58 (d, J = 8.7 Hz, 1 H minor), 1.50 (d, J = 8.7 Hz, 1 H major), 1.45 (d, J = 8.7 Hz 1 H minor). ^{13}C NMR (100 MHz, chloroform-d) δ 176.95, 176.72, 141.96, 141.12, 138.90, 138.58, 134.64, 134.41, 131.31, 130.73, 130.38, 130.01, 129.59, 129.38, 129.10, 128.71, 128.63, 128.48, 128.44, 128.32, 128.23, 127.77, 127.66, 127.62, 52.50, 52.28, 46.67, 45.66, 45.22, 44.72.

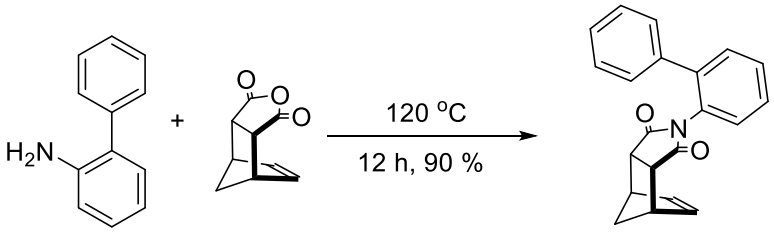

Scheme 3.2. Synthesis of balance **1**

2-Aminophenylboronic acid pinacol (101.0 mg, 0.46 mmol), 1-bromo-4-methoxybenzene (256.0 mg, 1.37 mmol), tetrakis(triphenylphosphine) palladium (0) (51.8 mg, 0.02 mmol), and potassium carbonate (340.6 mg, 2.46 mmol) were added to a round-bottom flask, which was then connected to a dual manifold Schlenk line. The round-bottom flask was evacuated and purged with N_2 gas three times by manipulating the manifold valve. Deionized H_2O, which had been bubbled with N_2 gas, was mixed with THF in a 2:1 ratio, and 4 mL of the THF/H_2O mixture was added to the purged round-bottom flask. The mixture was then heated at 75 °C for 36 hours under a nitrogen atmosphere. After cooling the flask to room temperature, the product was isolated by liquid-liquid extraction using 50 mL of brine and 10 mL of ethyl acetate, which was carried out three times. The organic layer was dried over anhydrous magnesium sulfate, and the solvent was removed using a rotary evaporator. The crude material was purified by column chromatography (ethyl acetate/hexanes = 1:6, v/v) to give an off-white powder 4'-methoxy-[1,1'-biphenyl]-2-amine (41.6 mg, 45%). ^{1}H NMR (300 MHz, $CDCl_3$) δ 7.39 (d, 8.7, 2 H), 7.18 – 7.11 (m, 2 H), 6.99 (d, J = 8.7 Hz, 2 H), 6.87 – 6.78 (m, 2 H), 3.85 (s, 3 H), 3.85 (s, br, 2 H).

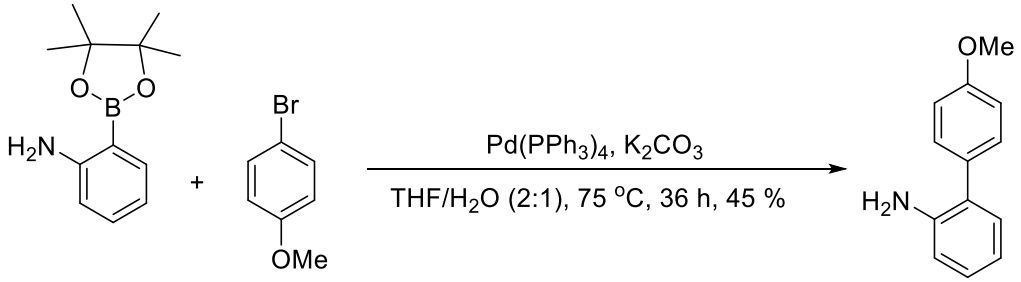

Scheme 3.3. Synthesis of precursor for balance **2**

4'-Methoxy-[1,1'-biphenyl]-2-amine (29.9 mg, 0.2 mmol) and *cis*-5-norbornene-*endo*-2,3-dicarboxylic anhydride (17.0 mg, 0.1 mmol) were added to a 20-dram vial along

with a magnetic stir bar. The vial was then capped and heated to 120 ºC in a silicon oil bath for 25 hours with mild stirring. After letting the vial cool to room temperature, the crude material was purified by column chromatography (ethyl acetate/hexanes = 1:4, v/v) to give a white crystalline solid **2** (23.2 mg, 64.83 %). ^{1}H NMR (300 MHz, $CDCl_3$) δ 7.44 – 7.29 (m, 3 H), 7.15 (d, J = 8.4, 2 H major), 7.10 (d, 8.4, 2 H minor), 7.05 – 6.96 (m, 1 H), 6.88 (t, J = 8.5 Hz, 2 H), 6.27 (s, 2 H major), 5.38 (s, 2 H), 3.83 (s, 3 H minor), 3.81 (s, 3 H major), 3.40 – 3.16 (m, 4 H), 1.74 – 1.61 (m, 1 H), 1.52 – 1.45 (m, 1 H). ^{13}C NMR (100 MHz, chloroform-d) δ 177.01, 176.74, 159.33, 159.10, 140.81, 134.62, 134.38, 131.67, 131.34, 130.96, 130.81, 130.46, 130.07, 129.55, 129.09, 128.63, 128.45, 128.40, 128.10 113.65, 113.18, 55.41, 55.22, 52.50, 52.28, 46.68, 45.68, 45.21, 44.72.

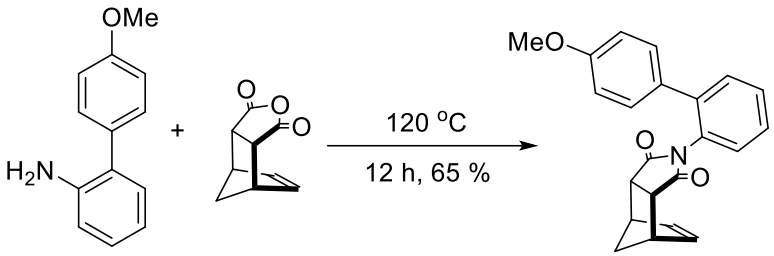

Scheme 3.4. Synthesis of balance **2**

2-Aminophenylboronic acid pinacol (105.2 mg, 0.48 mmol), 1-bromo-4-(*tert*-butyl) benzene (295 mg, 1.38 mmol), tetrakis(triphenylphosphine) palladium (0) (28 mg, 0.02 mmol), and potassium carbonate (342.9 mg, 2.48 mmol) were added to a round-bottom flask, which was then connected to a dual manifold Schlenk line. The round-bottom flask was evacuated and purged with N_2 gas three times by manipulating the manifold valve. Deionized H_2O, which had been bubbled with N_2 gas, was mixed with THF in a 2:1 ratio, and 4 mL of the THF/H_2O mixture was added to the purged round-bottom flask. The

mixture was then heated at 75 °C for 36 hours under a nitrogen atmosphere. After cooling the flask to room temperature, the product was isolated by liquid-liquid extraction using 50 mL of brine and 10 mL of ethyl acetate, which was carried out three times. The organic layer was dried over anhydrous magnesium sulfate, and the solvent was removed using a rotary evaporator. The crude material was purified by column chromatography (ethyl acetate/hexanes = 1:6, v/v) to give a brown solid 4'-(*tert*-butyl)-[1,1'-biphenyl]-2-amine (101.2 mg, 93 %). ^{1}H NMR (300 MHz, $CDCl_3$) δ 7.50 (d, J = 8.3 Hz, 2 H), 7.42 (d, J = 8.3 Hz, 2 H), 7.20 – 7.15 (m, 2 H), 6.87 – 6.77 (m, 2 H), 3.80 (s, br, 2 H), 1.40 (s, 9 H).

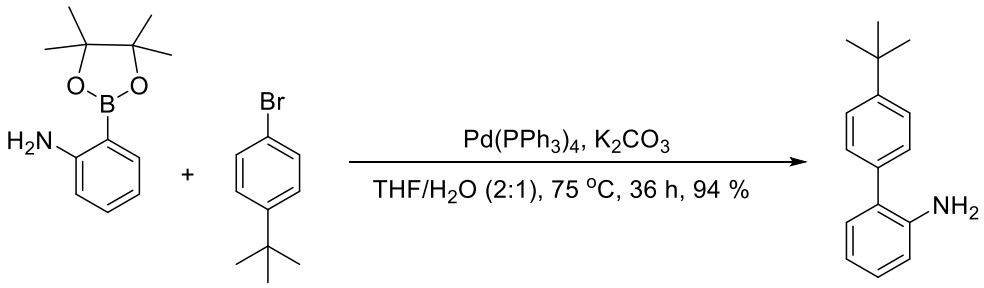

Scheme 3.5. Synthesis of precursor for balance **3**

4'-(*tert*-Butyl)-[1,1'-biphenyl]-2-amine (50.5 mg, 0.2 mmol) and *cis*-5-norbornene-*endo*-2,3-dicarboxylic anhydride (25.2 mg, 0.2 mmol) were added to a 20-dram vial along with a magnetic stir bar. The vial was then capped and heated to 120 ºC in a silicon oil bath for 25 hours with mild stirring. After letting the vial cool to room temperature, the crude material was purified by column chromatography (ethyl acetate/hexanes = 1:4, v/v) to give a brown crystalline solid **3** (39.4 mg, 71 %). ^{1}H NMR (300 MHz, $CDCl_3$) δ 7.47 – 7.28 (m, 5 H), 7.16 (d, J = 8.4 Hz, 2 H major), 7.11 (d, J = 8.4 Hz, 2 H minor), 7.06 – 6.97 (m, 1 H), 6.27 (s, 2 H major), 5.26 (s, 2 H minor), 3.40 – 3.15 (m, 4 H), 1.73 (d, J = 8.9 Hz, 1 H

minor), 1.57 (d, J = 8.9 Hz, 1 H major), 1.52 (d, J = 8.9 Hz, 1 H minor), 1.44 (d, J = 8.9 Hz, 1 H major), 1.35 (s, 9 H minor), 1.32 (s, 9 H major). ^{13}C NMR (100 MHz, chloroform-d) δ 177.04, 176.76, 150.53, 150.44, 142.06, 141.06, 135.89, 135.53, 134.65, 134.30, 131.35, 130.88, 130.52, 129.96, 129.56, 129.09, 128.97, 128.59, 128.49, 128.42, 128.18, 127.92, 125.13, 124.64, 52.44, 52.26, 46.67, 45.68, 45.19, 44.70, 34.58, 31.40, 31.36, 29.72.

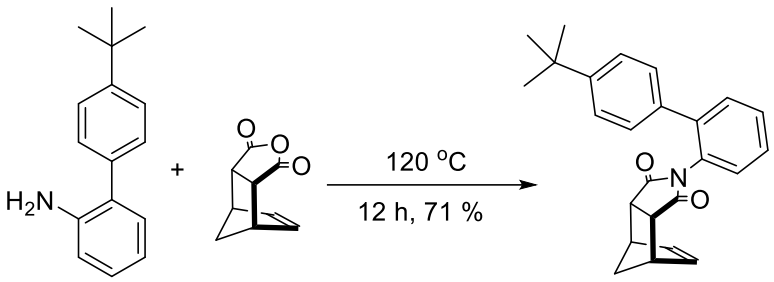

Scheme 3.6. Synthesis of balance **3**

2-Aminophenylboronic acid pinacol (103.9 mg, 0.47 mmol), 4-bromo-1,1'-biphenyl (326.0 mg, 1.40 mmol), tetrakis(triphenylphosphine) palladium (0) (27.5 mg, 0.02 mmol), and potassium carbonate (393.2 mg, 2.84 mmol) were added to a round-bottom flask, which was then connected to a dual manifold Schlenk line. The round-bottom flask was evacuated and purged with N_2 gas three times by manipulating the manifold valve. Deionized H_2O, which had been bubbled with N_2 gas, was mixed with THF in a 2:1 ratio, and 4 mL of the THF/H_2O mixture was added to the purged round-bottom flask. The mixture was then heated at 75 °C for 36 hours under a nitrogen atmosphere. After cooling the flask to room temperature, the product was isolated by liquid-liquid extraction using 50 mL of brine and 10 mL of ethyl acetate, which was carried out three times. The organic

layer was dried over anhydrous magnesium sulfate, and the solvent was removed using a rotary evaporator. The crude material was purified by column chromatography (ethyl acetate/hexanes = 1:6, v/v) to give a brown solid [1,1':4',1"-terphenyl]-2-amine (43.9 mg, 38 %). ^{1}H NMR (300 MHz, $CDCl_3$) δ 7.71 – 7.65 (m, 4 H), 7.56 (d, J = 8.1 Hz, 2 H), 7.49 (t, J = 7.2 Hz, 2 H), 7.38 (t, J = 7.2 Hz, 1 H), 7.19 (t, J = 7.4 Hz, 2 H), 6.90 – 6.80 (m, 2 H), 3.76 (s, br, 2 H)

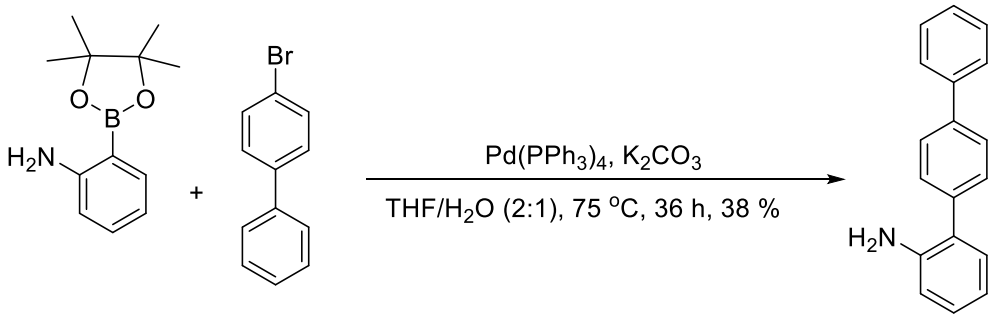

Scheme 3.7. Synthesis of precursor for balance **4**

[1,1':4',1"-terphenyl]-2-amine (45.6 mg, 0.2 mmol) and *cis*-5-norbornene-*endo*-2,3-dicarboxylic anhydride (21.9 mg, 0.1 mmol) were added to a 20-dram vial along with a magnetic stir bar. The vial was then capped and heated to 120 ºC in a silicon oil bath for 12 hours with mild stirring. After letting the vial cool to room temperature, the crude material was purified by column chromatography (ethyl acetate/hexanes = 1:4, v/v) to give a brown solid **4** (44.2 mg, 91.36 %). ^{1}H NMR (300 MHz, $CDCl_3$) δ 7.64 - 7.58 (m, 4 H), 7.50 – 7.26 (m, 8 H), 7.10 – 7.01 (m, 1 H), 6.29 (s, 2 H major), 5.37 (s, 2 H minor), 3.42 – 3.18 (m, 4 H), 1.74 (d, J = 8.9 Hz, 1 H major), 1.58 (d, J = 8.9 Hz, 1 H minor), 1.51 (d, J = 8.9 Hz, 1 H major), 1.46 (d, J = 8.9 Hz, 1 H minor). ^{13}C NMR (100 MHz, chloroform-d) δ

177.05, 176.74, 141.61, 140.84, 140.77, 140.71, 140.52, 140.32, 137.87, 137.56, 134.65, 134.43, 131.27, 130.76, 130.45, 130.00, 129.83, 129.65, 129.18, 128.89, 128.85, 128.74, 128.53, 128.51, 127.47, 127.12, 127.04, 126.92, 126.50, 52.55, 52.30, 46.72, 45.71, 45.24, 44.76.

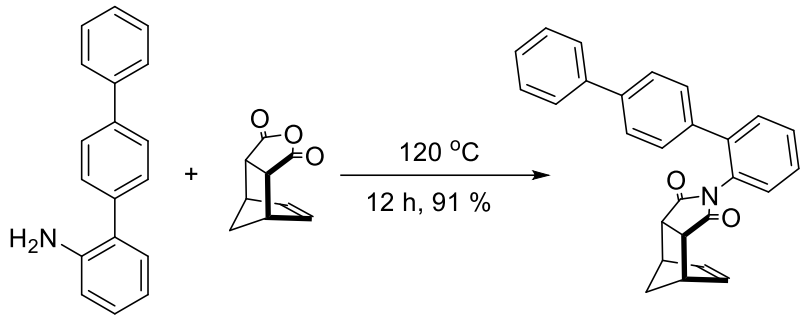

Scheme 3.8. Synthesis of balance **4**

2-Aminophenylboronic acid pinacol (106.2 mg, 0.48 mmol), 1-bromo-4-fluorobenzene (239.4 mg, 1.37 mmol), tetrakis(triphenylphosphine) palladium (0) (30.4 mg, 0.02 mmol), and potassium carbonate (341.2 mg, 2.47 mmol) were added to a round-bottom flask, which was then connected to a dual manifold Schlenk line. The round-bottom flask was evacuated and purged with N_2 gas three times by manipulating the manifold valve. Deionized H_2O, which had been bubbled with N_2 gas, was mixed with THF in a 2:1 ratio, and 4 mL of the THF/H_2O mixture was added to the purged round-bottom flask. The mixture was then heated at 75 °C for 36 hours under a nitrogen atmosphere. After cooling the flask to room temperature, the product was isolated by liquid-liquid extraction using 50 mL of brine and 10 mL of ethyl acetate, which was carried out three times. The organic layer was dried over anhydrous magnesium sulfate, and the solvent was removed using a

rotary evaporator. The crude material was purified by column chromatography (ethyl acetate/hexanes = 1:6, v/v) to give a brown solid 4'-fluoro-[1,1'-biphenyl]-2-amine (29.9 mg, 33 %). ^{1}H NMR (300 MHz, $CDCl_3$) δ 7.43 (dd, J = 8.1 & 5.6 Hz, 2 H), 7.20 – 7.10 (m, 4 H), 6.86 – 6.76 (m, 2 H), 3.69 (s, br, 2 H).

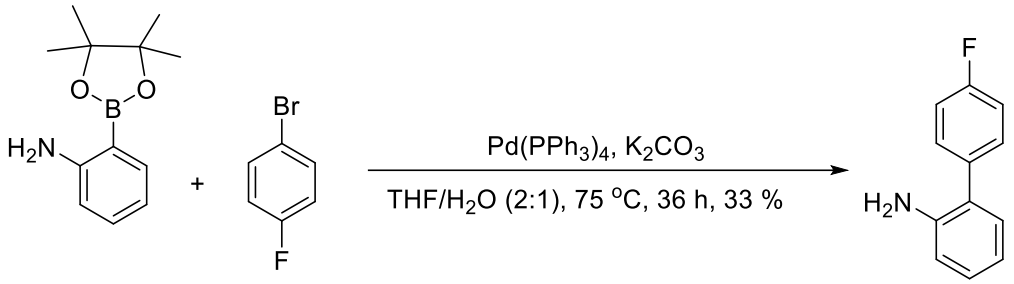

Scheme 3.9. Synthesis of balance **5** precursor

4'-Fluoro-[1,1'-biphenyl]-2-amine (25.4 mg, 0.1 mmol) and *cis*-5-norbornene-*endo*-2,3-dicarboxylic anhydride (17.5 mg, 0.1 mmol) were added to a 20-dram vial along with a magnetic stir bar. The vial was then capped and heated to 120 ºC in a silicon oil bath for 12 hours with mild stirring. After letting the vial cool to room temperature, the crude material was purified by column chromatography (ethyl acetate/hexanes = 1:4, v/v) to give a light brown solid **5** (25.4 mg, 73 %). ^{1}H NMR (300 MHz, $CDCl_3$) δ 7.49 – 7.36 (m, 3 H), 7.22 – 7.14 (m, 2 H), 7.08 – 6.97 (m, 3 H), 6.27 (s, 2 H major), 5.36 (s, 2 H minor), 3.41 – 3.15 (m, 4 H), 1.74 (d, J = 8.9 Hz, 1 H major), 1.62 (d, J = 8.9 Hz, 1 H minor), 1.53 – 1.46 (m, 1 H).

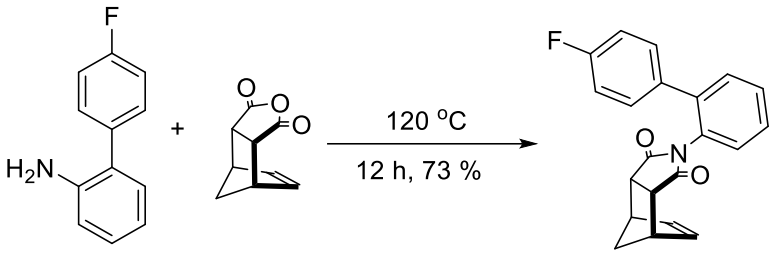

Scheme 3.10. Synthesis of balance **5**

2-Aminophenylboronic acid pinacol (100.3 mg, 0.48 mmol), 1-bromo-4-(trifluoromethyl) benzene (305 mg, 1.36 mmol), tetrakis(triphenylphosphine) palladium (0) (27 mg, 0.02 mmol), and potassium carbonate (316.4 mg, 2.29 mmol) were added to a round-bottom flask, which was then connected to a dual manifold Schlenk line. The round-bottom flask was evacuated and purged with N_2 gas three times by manipulating the manifold valve. Deionized H_2O, which had been bubbled with N_2 gas, was mixed with THF in a 2:1 ratio, and 4 mL of the THF/H_2O mixture was added to the purged round-bottom flask. The mixture was then heated at 75 °C for 36 hours under a nitrogen atmosphere. After cooling the flask to room temperature, the product was isolated by liquid-liquid extraction using 50 mL of brine and 10 mL of ethyl acetate, which was carried out three times. The organic layer was dried over anhydrous magnesium sulfate, and the solvent was removed using a rotary evaporator. The crude material was purified by column chromatography (ethyl acetate/hexanes = 1:6, v/v) to give an off-white solid 4'-(trifluoromethyl)-[1,1'-biphenyl]-2-amine (49.0 mg, 45 %). ^{1}H NMR (300 MHz, $CDCl_3$) δ 7.74 (d, J = 8.3 Hz, 2 H), 7.63 (d, J = 8.3 Hz, 2 H), 7.27 – 7.21 (m, 1 H), 7.16 (d, J = 7.6 Hz, 1 H), 6.90 (t, J = 7.7 Hz, 1 H), 6.83 (d, J = 7.8 Hz, 1 H), 3.86 (s, br, 2 H)

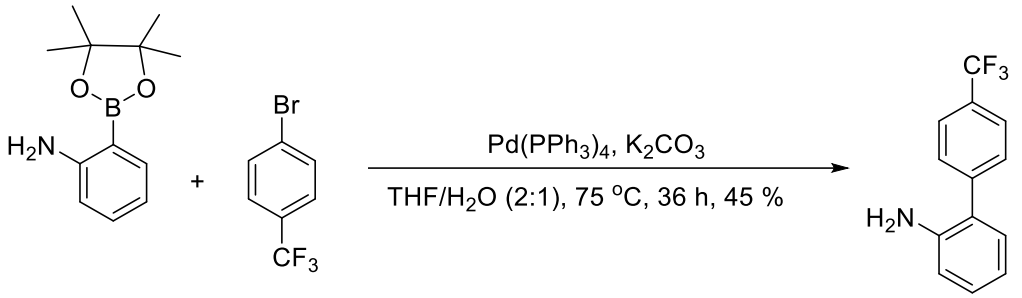

Scheme 3.11. Synthesis of precursor for balance **6**

4'-(Trifluoromethyl)-[1,1'-biphenyl]-2-amine (47.9 mg, 0.2 mmol) and *cis*-5-norbornene-*endo*-2,3-dicarboxylic anhydride (22.3 mg, 0.1 mmol) were added to a 20-dram vial along with a magnetic stir bar. The vial was then capped and heated to 120 ºC in a silicon oil bath for 12 hours with mild stirring. After letting the vial cool to room temperature, the crude material was purified by column chromatography (ethyl acetate/hexanes = 1:4, v/v) to give a white crystalline solid **6** (31.8 mg, 62 %). ^{1}H NMR (300 MHz, $CDCl_3$) δ 7.65 – 7.59 (t, J = 8.8 Hz, 2 H), 7.52 – 7.28 (m, 5 H), 7.10 – 7.01 (m, 1 H), 6.28 (s, 2 H major), 5.25 (s, 2 H minor), 3.42 – 3.17 (m, 4 H), 1.74 (d, J = 8.9 Hz, 1 H major), 1.62 (d, J = 8.9 Hz, 1 H minor), 1.52 (d, J = 8.9 Hz, 1 H major), 1.47 (d, J = 8.9 Hz, 1 H minor). ^{13}C NMR (100 MHz, chloroform-d) δ 176.89, 176.58, 142.55, 142.26, 140.46, 139.74, 134.64, 134.32, 130.83, 130.54, 129.88, 129.74, 129.29, 129.19, 128.89, 128.75, 128.66, 125.27, 125.23, 125.19, 125.16, 124.70, 124.67, 124.63, 52.74, 52.31, 46.73, 45.64, 45.32, 44.72.

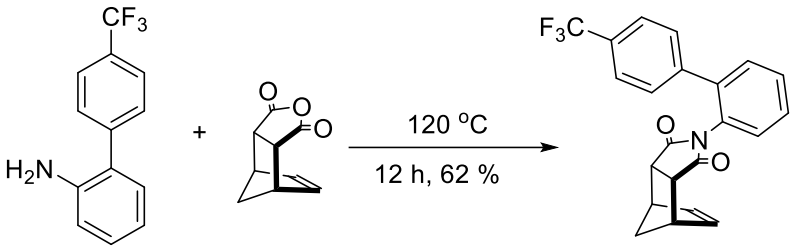

Scheme 3.12. Synthesis of balance **6**

2-Aminophenylboronic acid pinicol (102.3 mg, 0.47 mmol), 4-bromobenzonitrile (249.3 mg, 1.37 mmol), tetrakis(triphenylphosphine) palladium (0) (51.8 mg, 0.02 mmol), and potassium carbonate (343.7 mg, 2.49 mmol) were added to a round-bottom flask, which was then connected to a dual manifold Schlenk line. The round-bottom flask was evacuated and purged with N_2 gas three times by manipulating the manifold valve. Deionized H_2O, which had been bubbled with N_2 gas, was mixed with THF in a 2:1 ratio, and 4 mL of the THF/H_2O mixture was added to the purged round-bottom flask. The mixture was then heated at 75 °C for 36 hours under a nitrogen atmosphere. After cooling the flask to room temperature, the product was isolated by liquid-liquid extraction using 50 mL of brine and 10 mL of ethyl acetate, which was carried out three times. The organic layer was dried over anhydrous magnesium sulfate, and the solvent was removed using a rotary evaporator. The crude material was purified by column chromatography (ethyl acetate/hexanes = 1:5, v/v) to give a brown solid 2'-amino-[1,1'-biphenyl]-4-carbonitrile (18.8 mg, 21 %). ^{1}H NMR (300 MHz, $CDCl_3$) δ 7.73 (d, J = 8.3 Hz, 2 H), 7.60 (d, J = 8.3 Hz, 2 H), 7.21 (t, J = 8.1 Hz, 1 H), 7.10 (d, J = 7.6 Hz, 1 H), 6.88 – 6.78 (m, 2 H), 3.75 (s, br, 2 H).

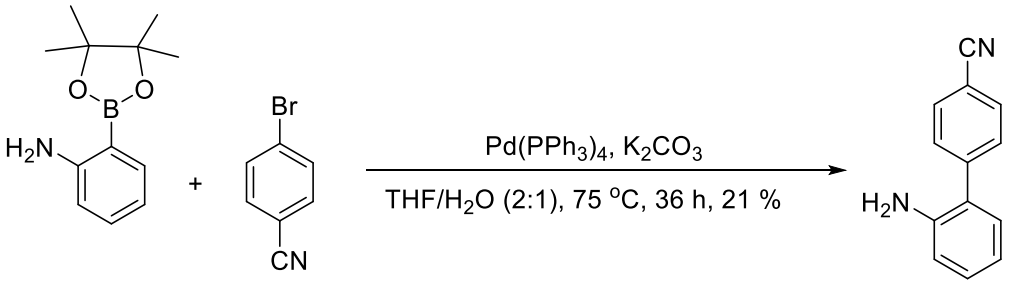

Scheme 3.13. Synthesis of precursor for balance **7**

2'-amino-[1,1'-biphenyl]-4-carbonitrile (15.9 mg, 0.1 mmol) and *cis*-5-norbornene-*endo*-2,3-dicarboxylic anhydride (10.9 mg, 0.1 mmol) were added to a 20-dram vial along with a magnetic stir bar. The vial was then capped and heated to 120 ºC in a silicon oil bath for 12 hours with mild stirring. After letting the vial cool to room temperature, the crude material was purified by column chromatography (ethyl acetate/hexanes = 1:2, v/v) to give a white powder **7** (15.4 mg, 72 %). ^{1}H NMR (300 MHz, $CDCl_3$) δ 7.65 (t, J = 8.9 Hz, 2 H), 7.53 – 7.44 (m, 2 H), 7.39 – 7.31 (m, 3 H), 7.11 – 7.01 (m, 1 H), 6.27 (s, 2 H major), 5.29 (s, 2 H minor), 3.43 – 3.16 (m, 4 H), 1.75 (d, J = 8.9 Hz, 1 H major), 1.65 (d, J = 8.9 Hz, 1 H minor), 1.54 – 1.48 (m, 1 H). ^{13}C NMR (100 MHz, chloroform-d) δ 176.83, 176.53, 143.75, 143.40, 139.89, 139.25, 134.64, 134.52, 132.08, 131.57, 130.69, 130.37, 130.29, 130.02, 129.82, 129.80, 129.59, 129.55, 129.40, 129.18, 129.03, 128.74, 118.63, 111.66, 111.65, 52.78, 52.35, 46.74, 45.64, 45.38, 44.76, 29.72.

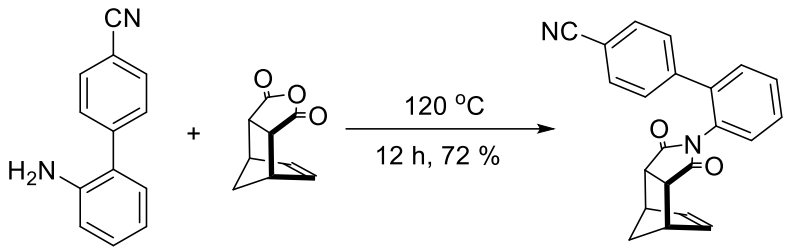

Scheme 3.14. Synthesis of balance **7**

2-Aminophenylboronic acid pinacol (114.8 mg, 0.52 mmol), 1-bromo-4-nitrobenzene (295.1 mg, 1.46 mmol), tetrakis(triphenylphosphine) palladium (0) (27 mg, 0.02 mmol), and potassium carbonate (332.8 mg, 2.41 mmol) were added to a round-bottom flask, which was then connected to a dual manifold Schlenk line. The round-bottom flask was evacuated and purged with N_2 gas three times by manipulating the manifold valve. Deionized H_2O, which had been bubbled with N_2 gas, was mixed with THF in a 2:1 ratio, and 4 mL of the THF/H_2O mixture was added to the purged round-bottom flask. The mixture was then heated at 75 °C for 36 hours under a nitrogen atmosphere. After cooling the flask to room temperature, the product was isolated by liquid-liquid extraction using 50 mL of brine and 10 mL of ethyl acetate, which was carried out three times. The organic layer was dried over anhydrous magnesium sulfate, and the solvent was removed using a rotary evaporator. The crude material was purified by column chromatography (ethyl acetate/hexanes = 1:6, v/v) to give a brown solid 4'-nitro-[1,1'-biphenyl]-2-amine (47.1 mg, 42 %). ^{1}H NMR (300 MHz, $CDCl_3$) δ 8.30 (d, J = 8.7 Hz, 2 H), 7.67 (d, J = 8.6 Hz, 2 H),

7.22 (t, J = 7.7 Hz, 1 H), 7.13 (d, J = 7.7 Hz, 1 H), 6.87 (t, J = 7.7 Hz, 1 H), 6.80 (d, J = 7.8 Hz, 1 H), 3.79 (s, br, 2 H).

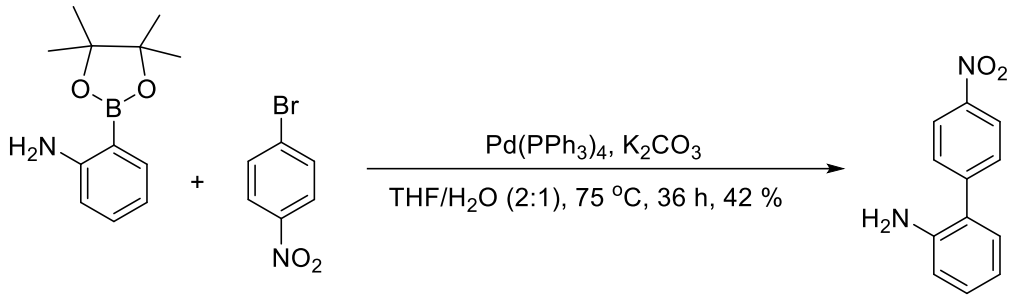

Scheme 3.15. Synthesis of precursor for balance **8**

4'-nitro-[1,1'-biphenyl]-2-amine (38.0 mg, 0.2 mmol) and *cis*-5-norbornene-*endo*-2,3-dicarboxylic anhydride (19.7 mg, 0.1 mmol) were added to a 20-dram vial along with a magnetic stir bar. The vial was then capped and heated to 120 ºC in a silicon oil bath for 12 hours with mild stirring. After letting the vial cool to room temperature, the crude material was purified by column chromatography (ethyl acetate/hexanes = 1:4, v/v) to give a light brown powder **10** (38 mg, 88 %). ^{1}H NMR (300 MHz, $CDCl_3$) δ 8.22 (t, J = 7.8 Hz, 2 H), 7.52 – 7.27 (m, 5 H), 7.13 – 7.03 (m, 1 H), 6.27 (s, 2 H major), 5.31 (s, 2 H minor), 3.43 – 3.17 (m, 4 H), 1.74 (d, J = 8.9 Hz, 1 H major), 1.63 (d, J = 8.9 Hz, 1 H minor), 1.53 – 1.47 (m, 1 H major). δ 176.80, 176.49, 147.57, 147.40, 145.65, 145.36, 139.51, 138.86, 134.65, 134.56, 130.64, 130.56, 130.29, 129.82, 129.70, 129.41, 129.36, 129.09, 128.79, 123.54, 122.94, 52.81, 52.34, 46.75, 45.65, 45.40, 44.76,

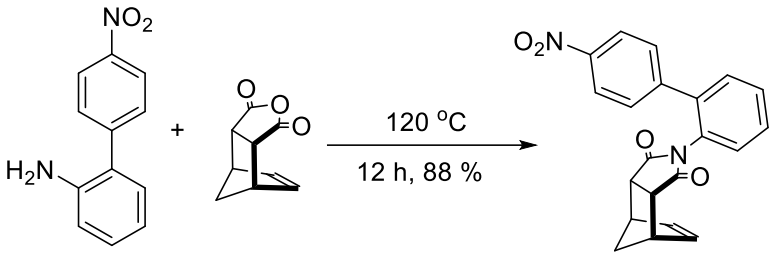

Scheme 3.16. Synthesis of balance **8**

3.3.3. ^{1}H NMR and ^{13}C NMR Spectra

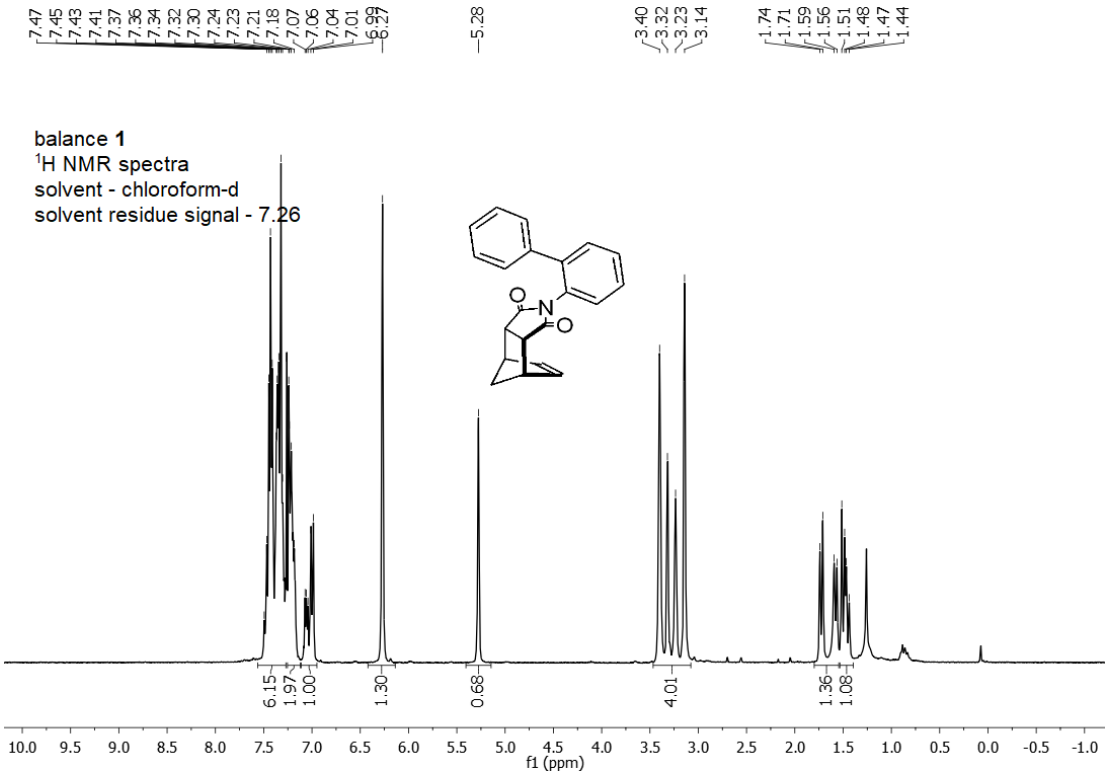

Figure 3.11. ^{1}H NMR spectra of balance **1** (300 MHz, $CDCl_3$)

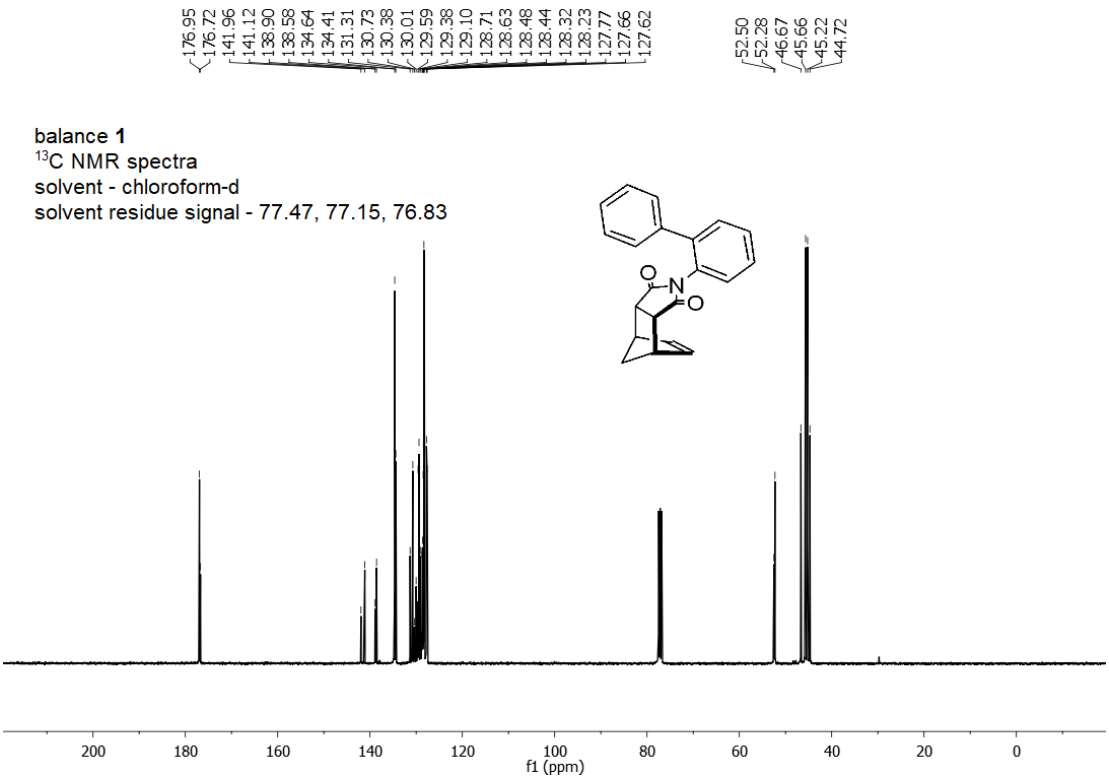

Figure 3.12. ^{13}C NMR spectra of balance **1** (100 MHz, $CDCl_3$)

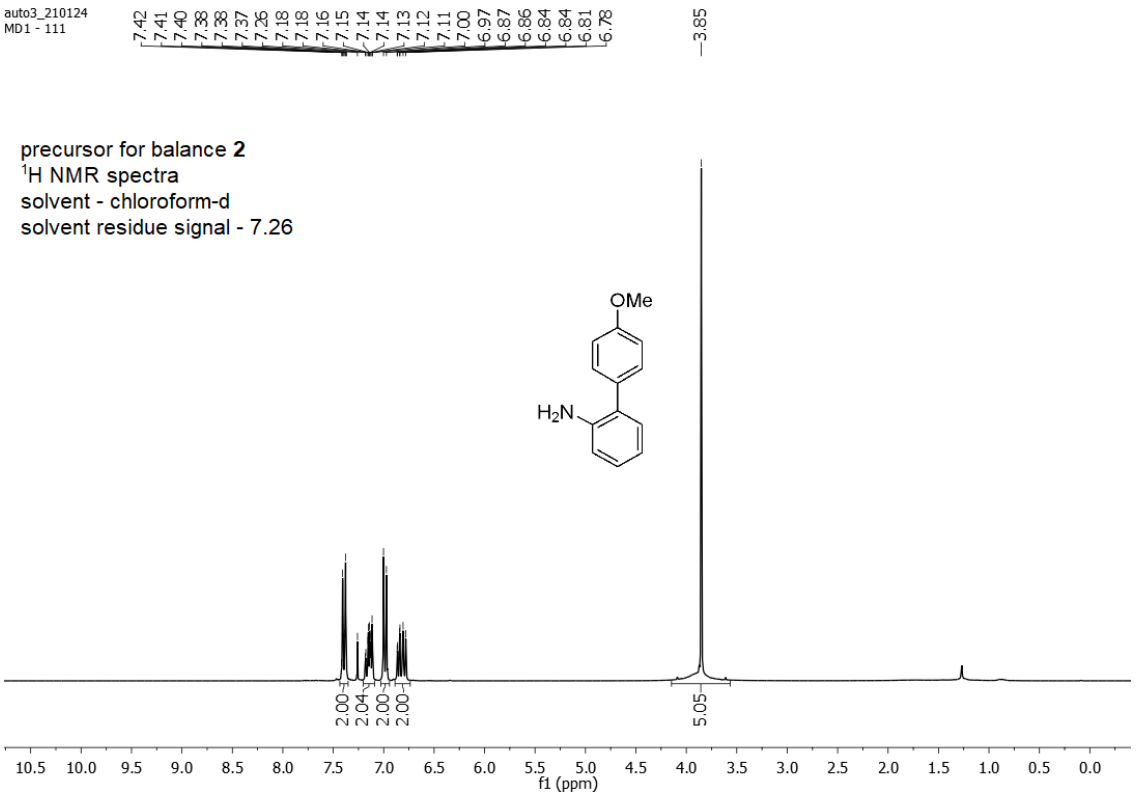

Figure 3.13. ^{1}H NMR spectra of precursor for balance **2** (300 MHz, chloroform-d)

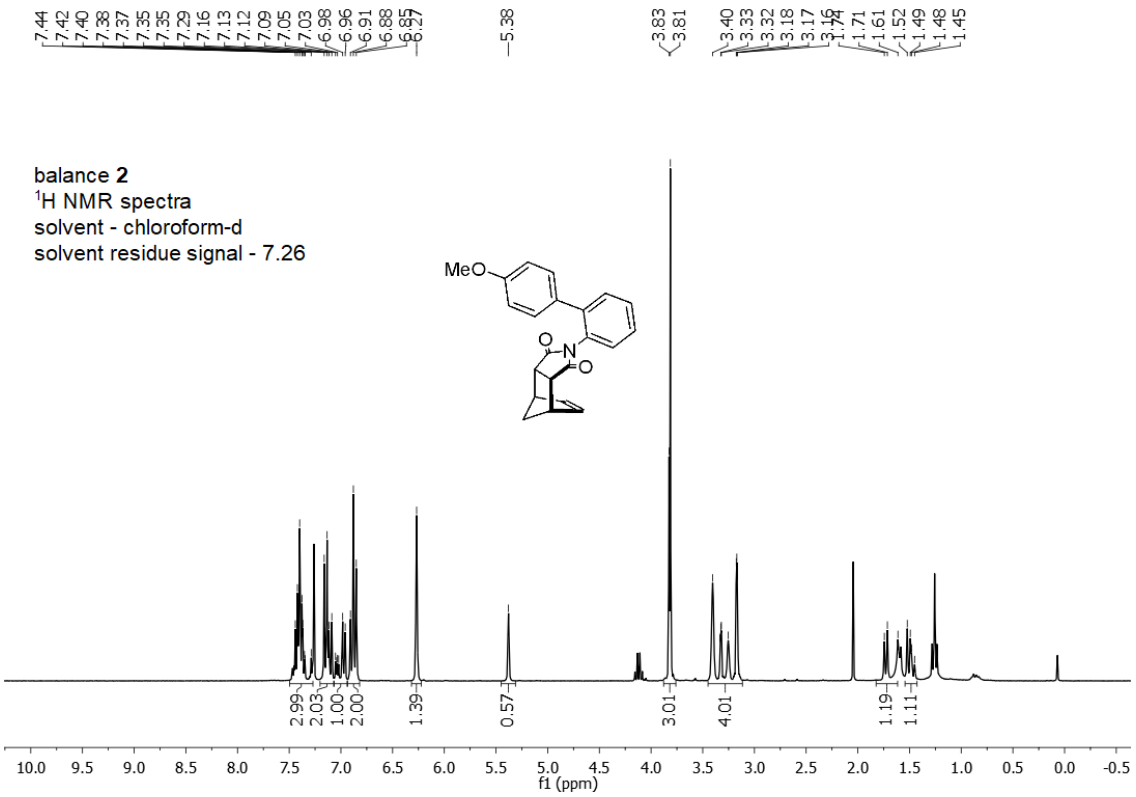

Figure 3.14. ^{1}H NMR spectra of balance **2** (300 MHz, $CDCl_3$)

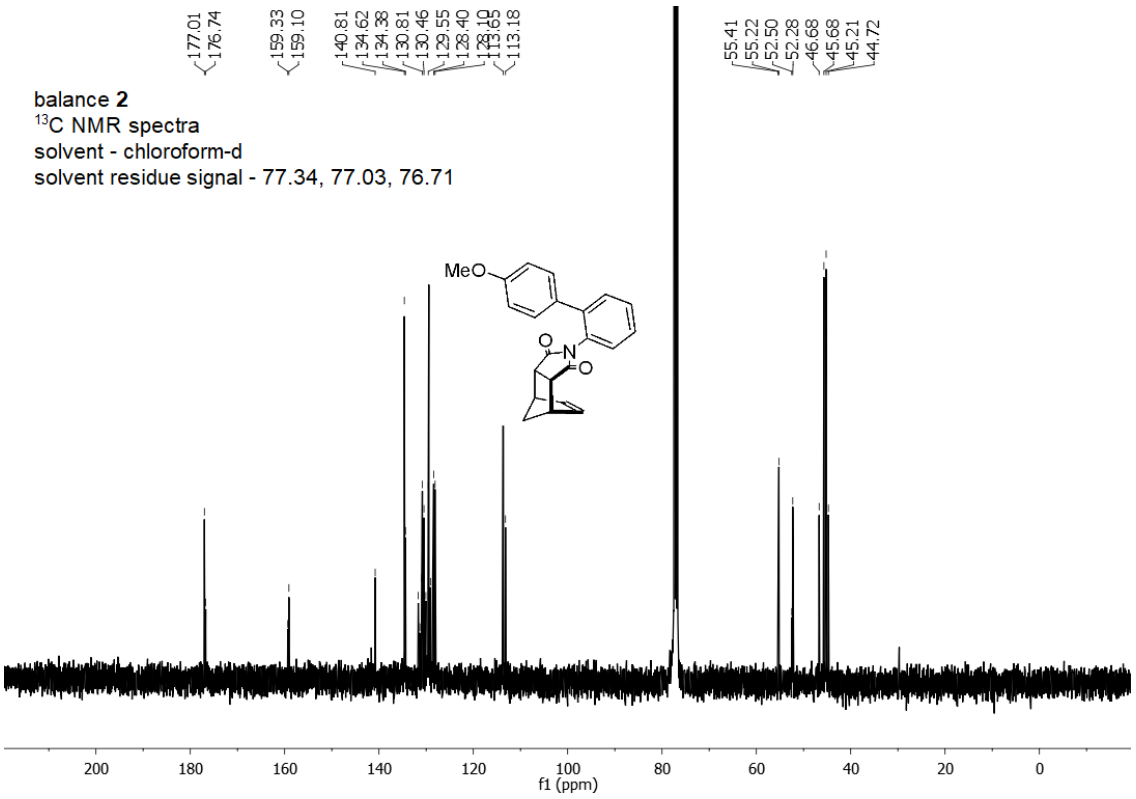

Figure 3.15. ^{13}C NMR spectra of balance **2** (100 MHz, $CDCl_3$)

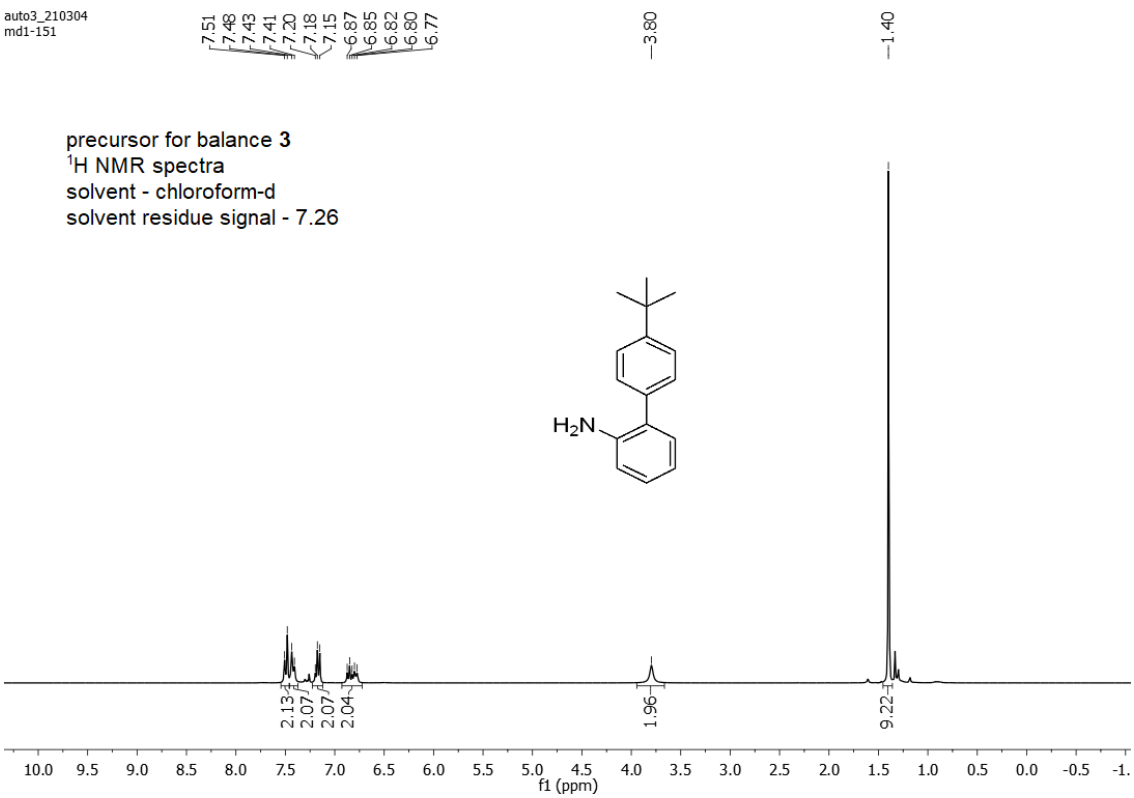

Figure 3.16. ^{1}H NMR spectra of precursor for balance **3** (300 MHz, chloroform-d)

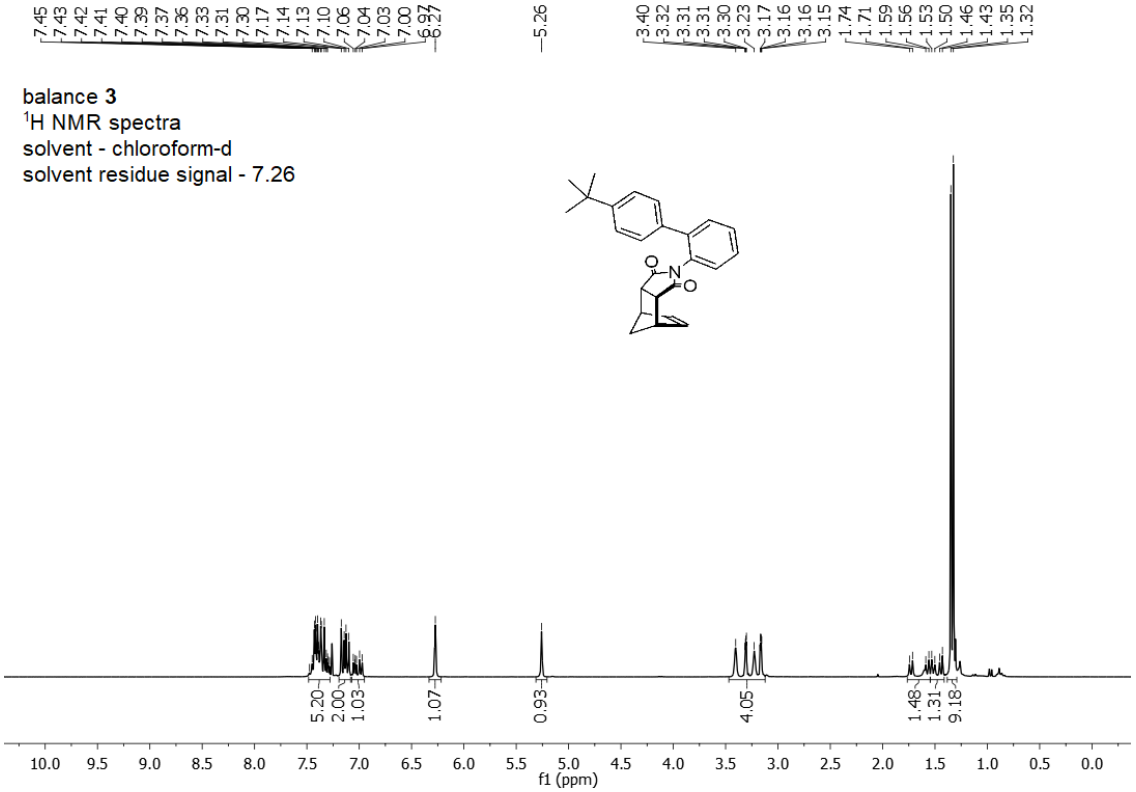

Figure 3.17. ^{1}H NMR spectra of balance **3** (300 MHz, $CDCl_3$)

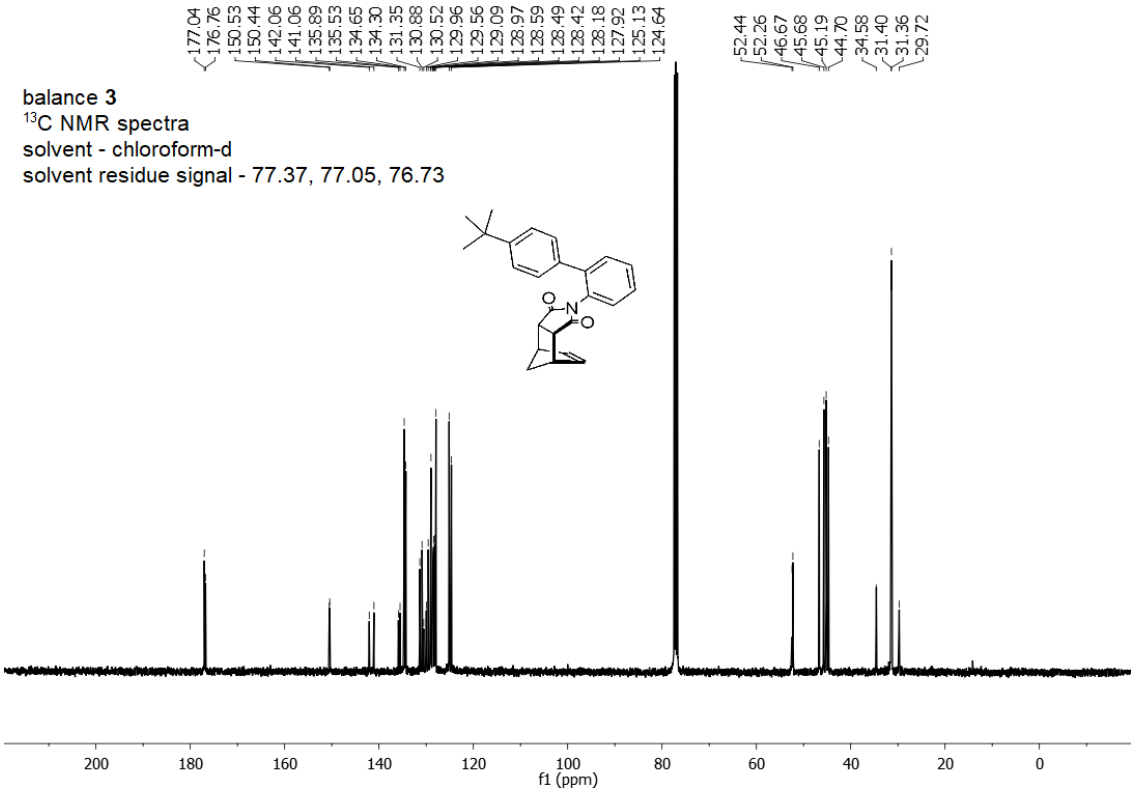

Figure 3.18. ^{13}C NMR spectra of balance **3** (100 MHz, $CDCl_3$)

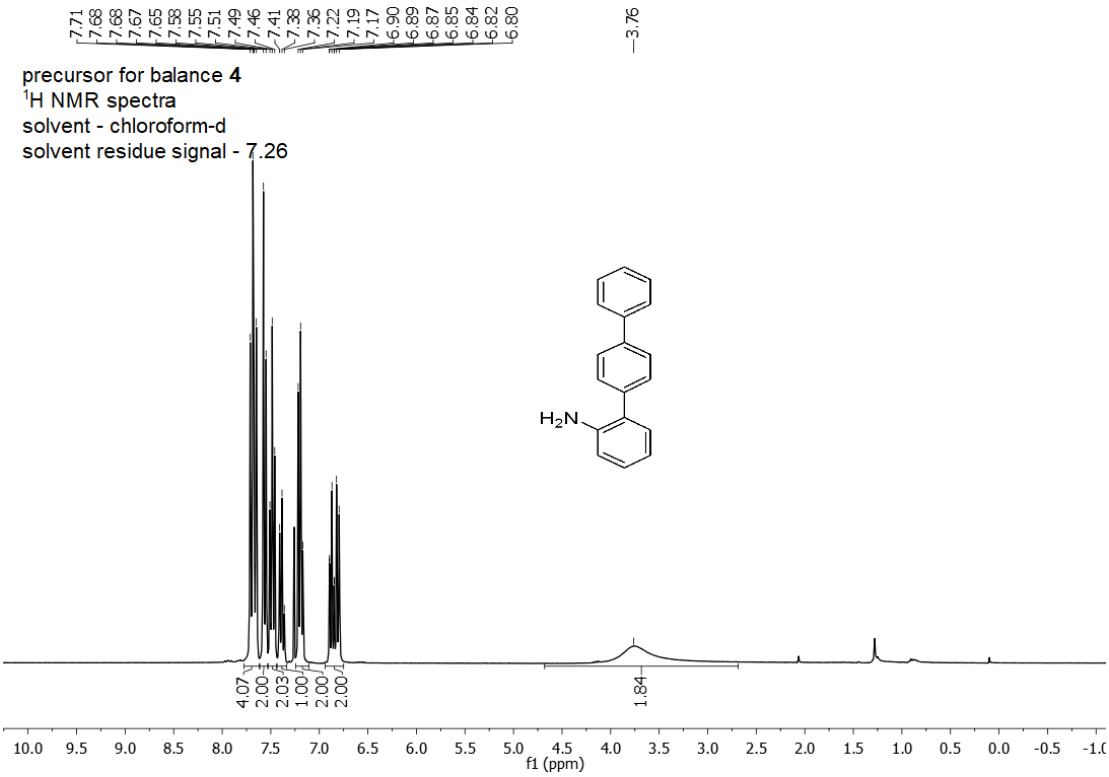

Figure 3.19. ^{1}H NMR spectra of precursor for balance **4** (300 MHz, chloroform-d)

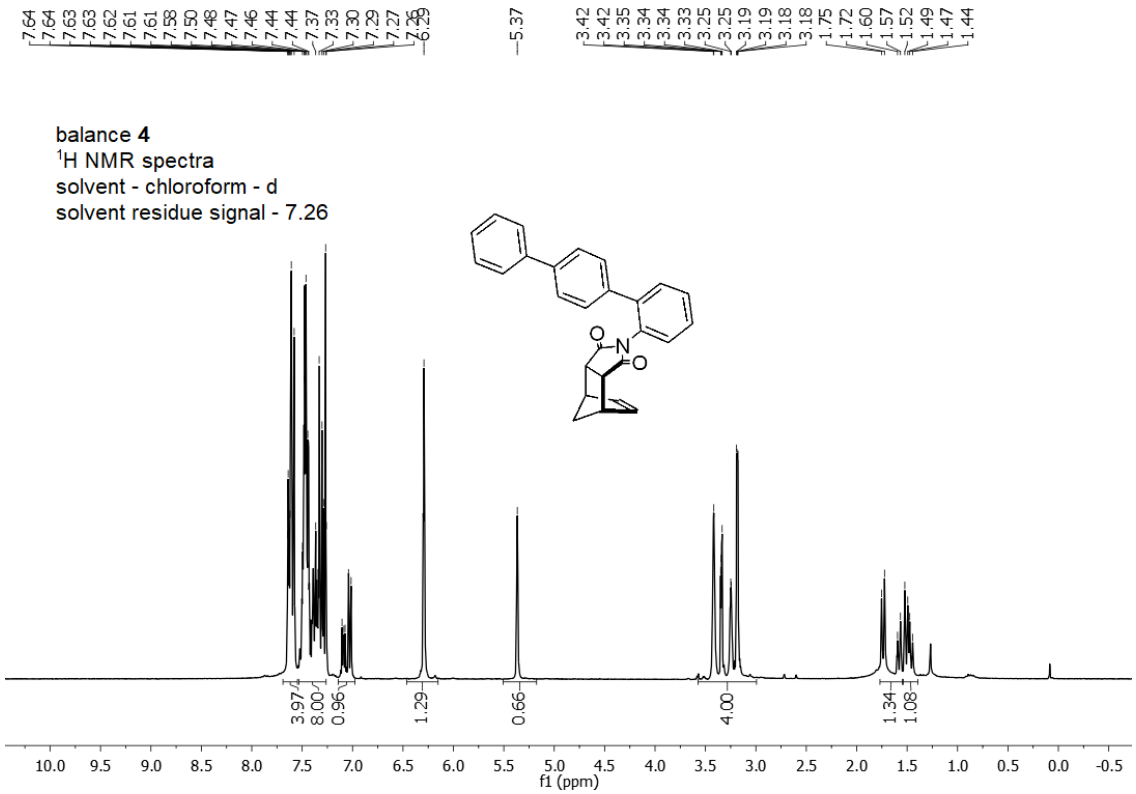

Figure 3.20. ^{1}H NMR spectra of balance **4** (300 MHz, $CDCl_3$)

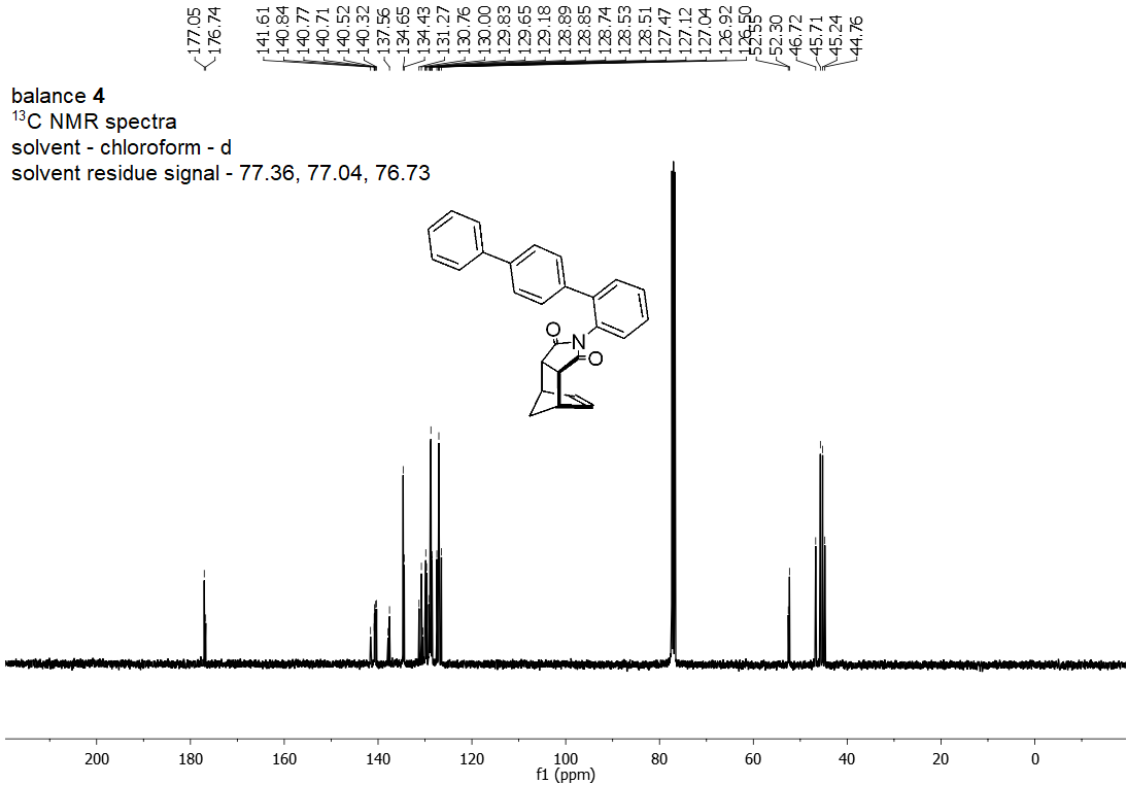

Figure 3.21. ^{13}C NMR spectra of balance **4** (100 MHz, $CDCl_3$)

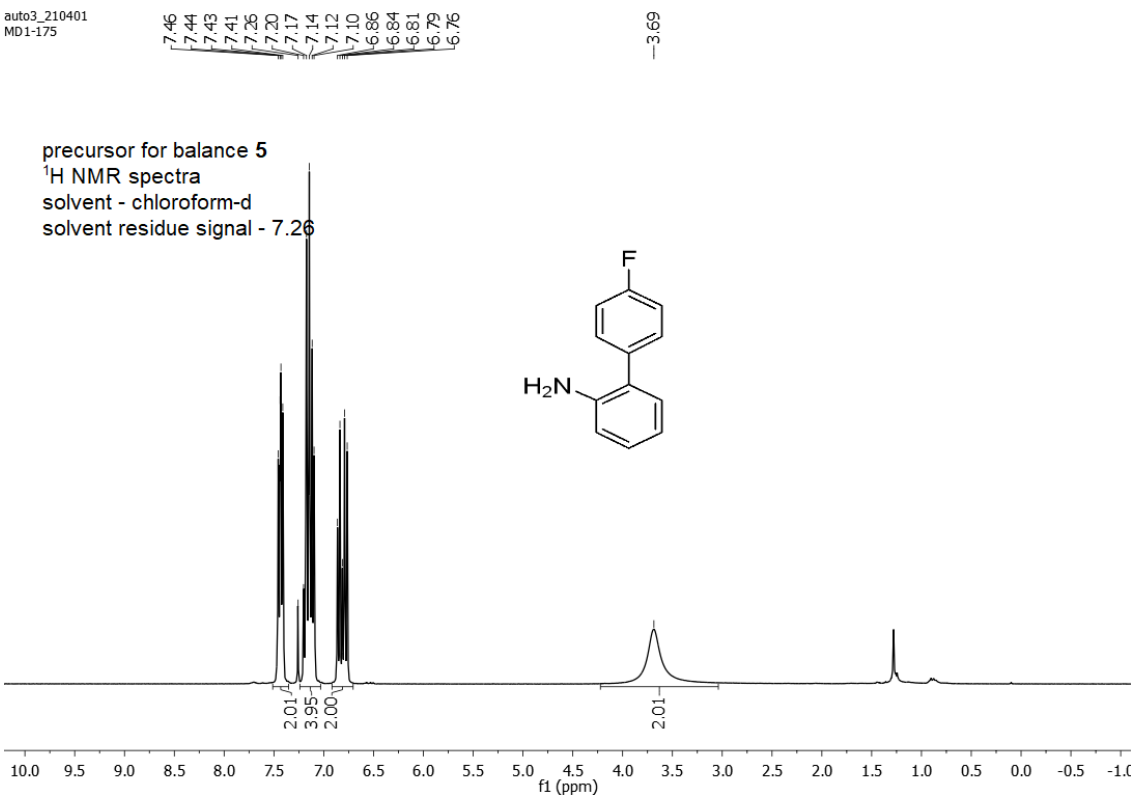

Figure 3.22. ^{1}H NMR spectra of precursor for balance **5** (300 MHz, chloroform-d)

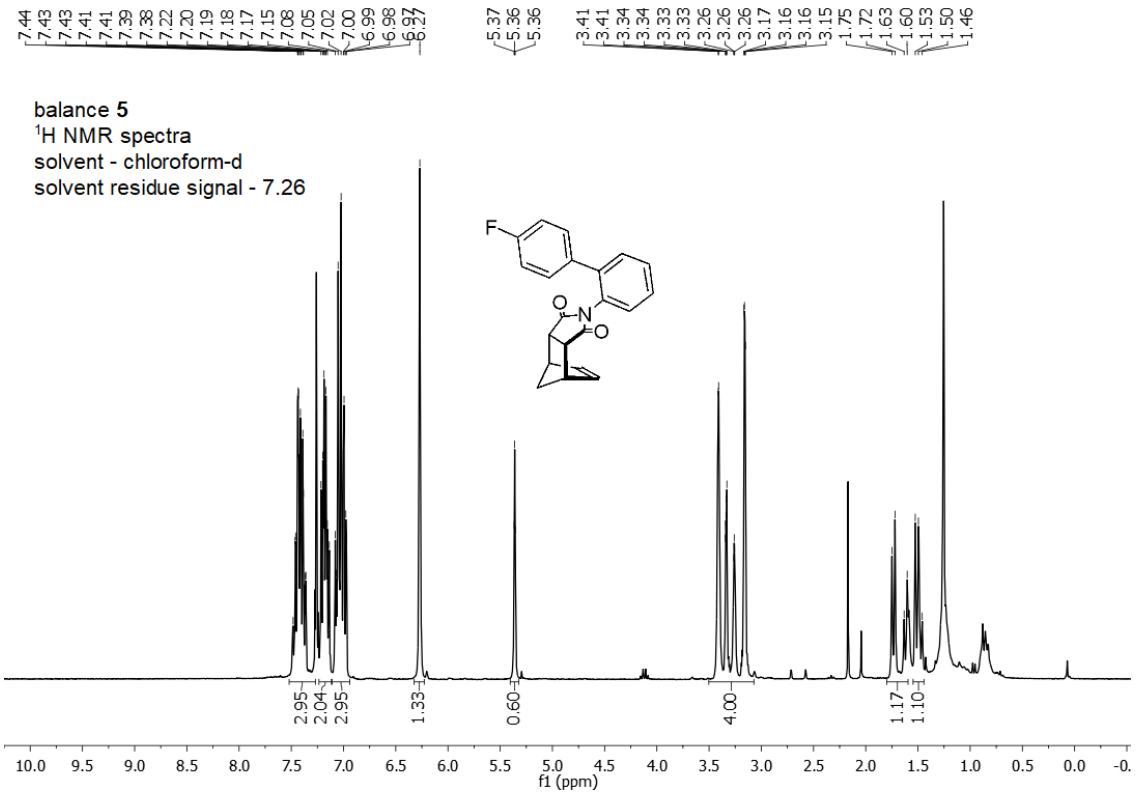

Figure 3.23. ^{1}H NMR spectra of balance **5** (300 MHz, chloroform-d)

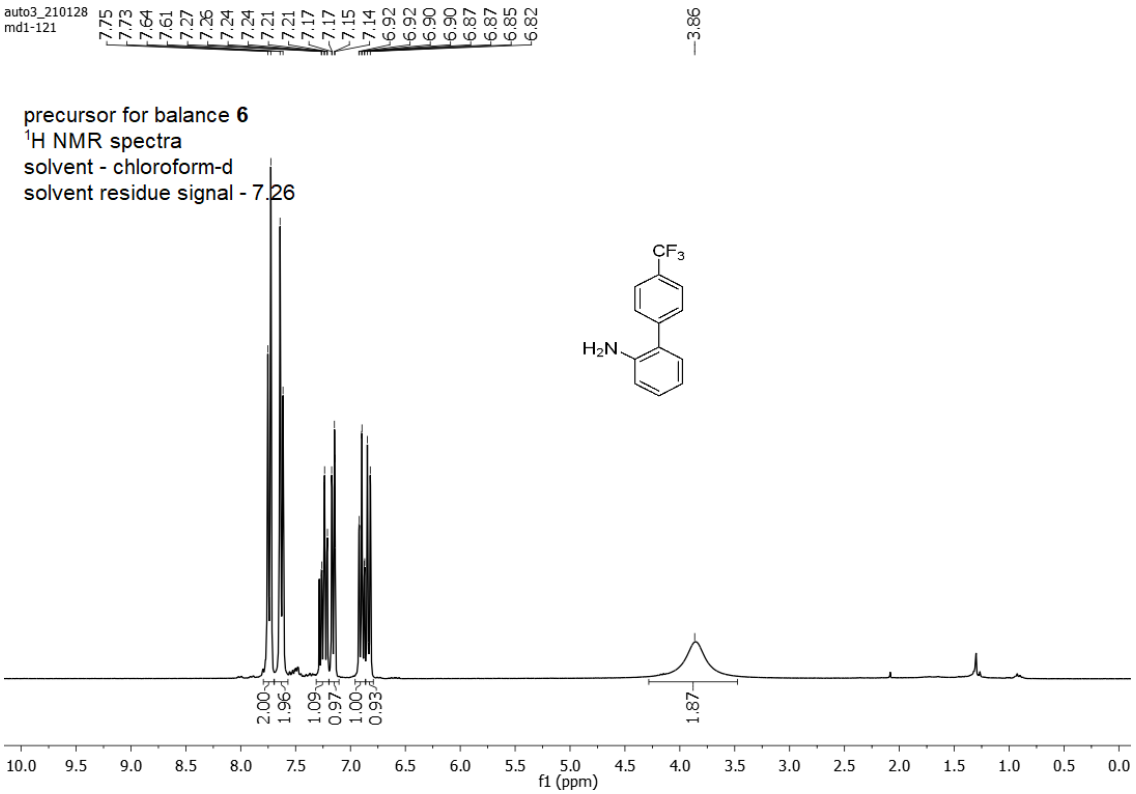

Figure 3.24. ^{1}H NMR spectra of precursor for balance **6** (300 MHz, chloroform-d)

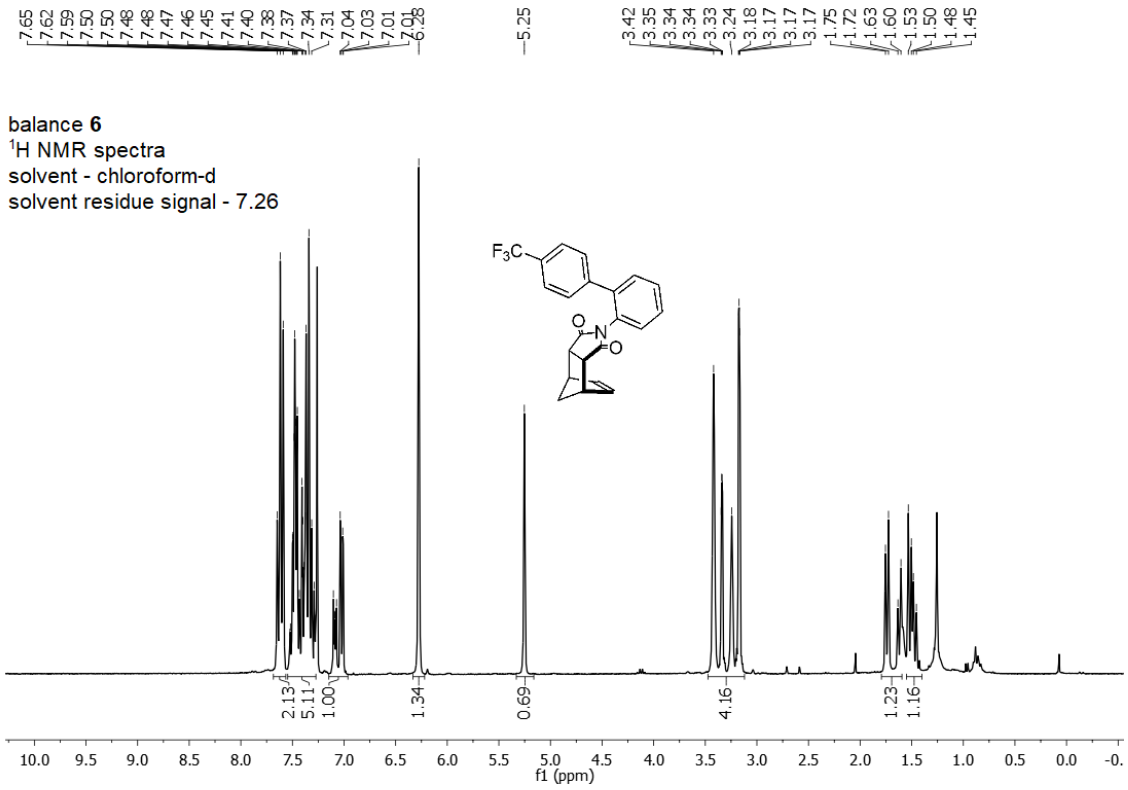

Figure 3.25. ^{1}H NMR spectra of balance **6** (300 MHz, $CDCl_3$)

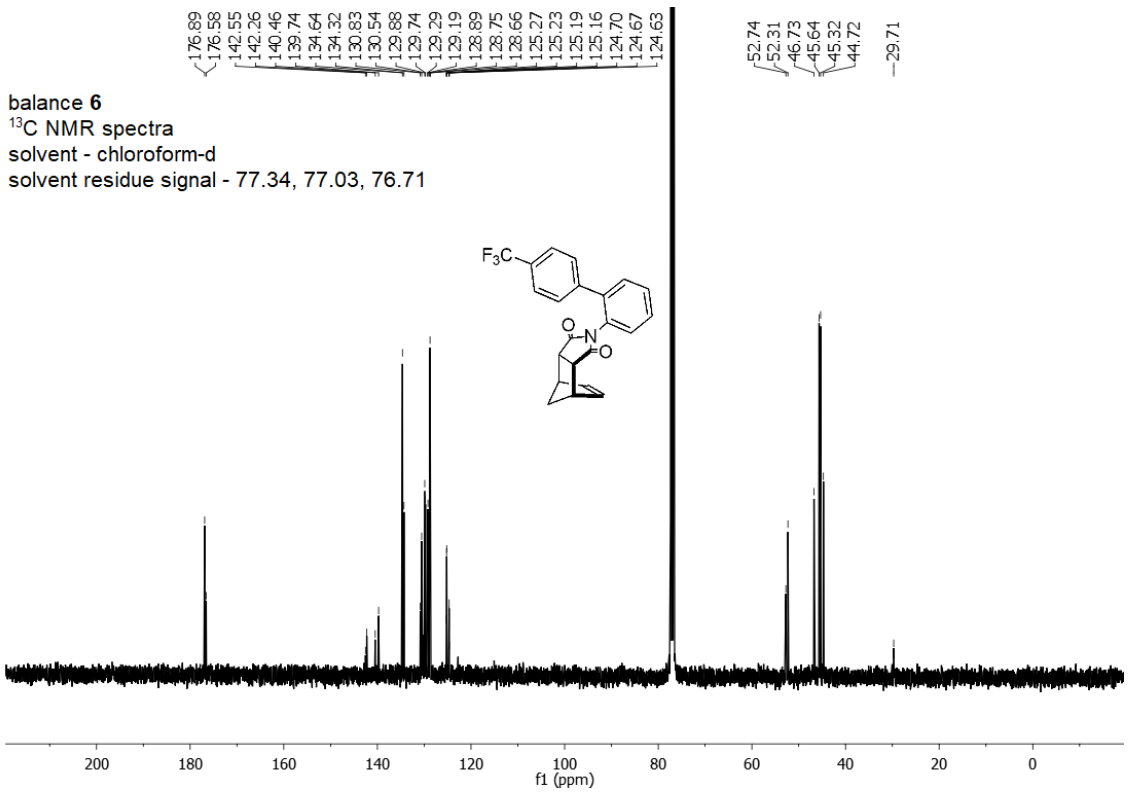

Figure 3.26. ^{13}C NMR spectra of balance **6** (100 MHz, $CDCl_3$)

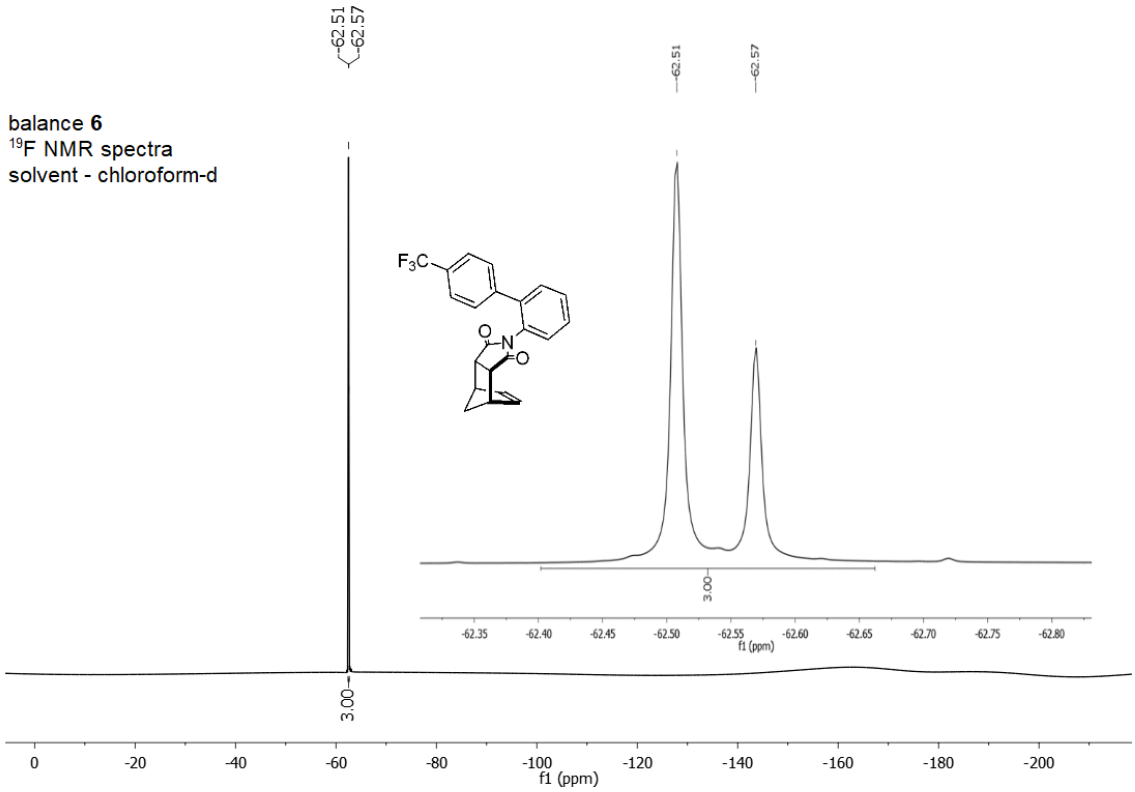

Figure 3.27. ^{19}F NMR spectra of balance **6** (300 MHz, $CDCl_3$)

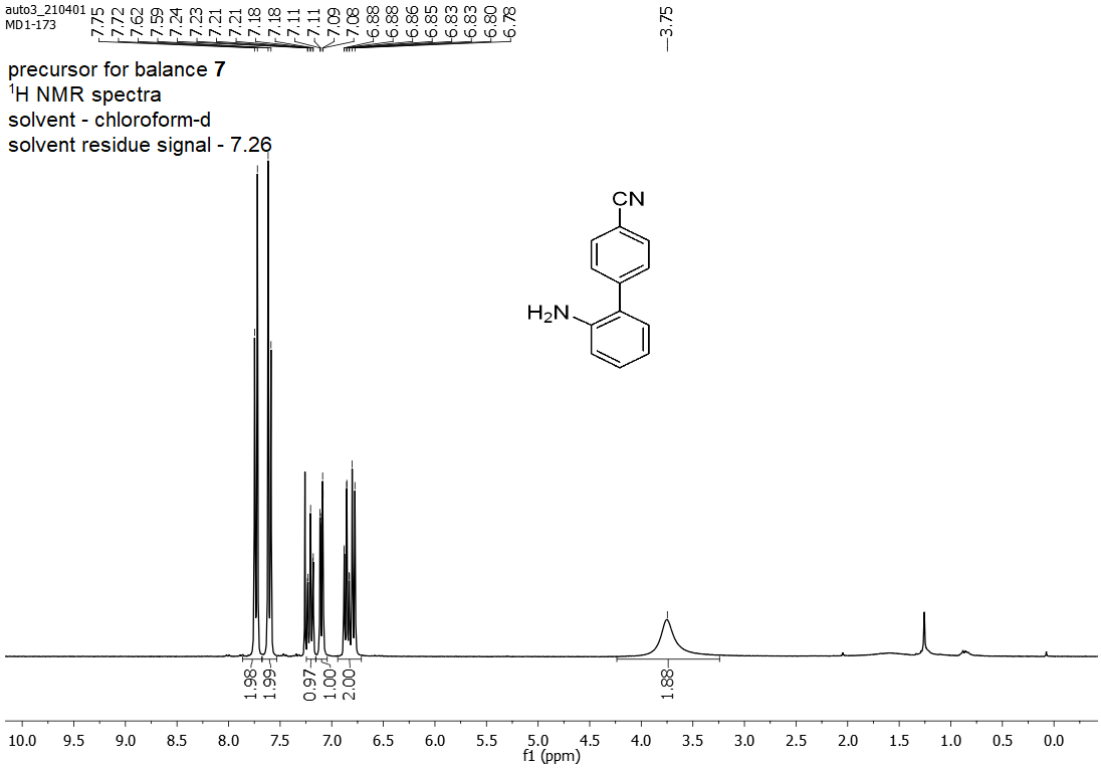

Figure 3.28. ^{1}H NMR spectra of precursor for balance **7** (300 MHz, $CDCl_3$)

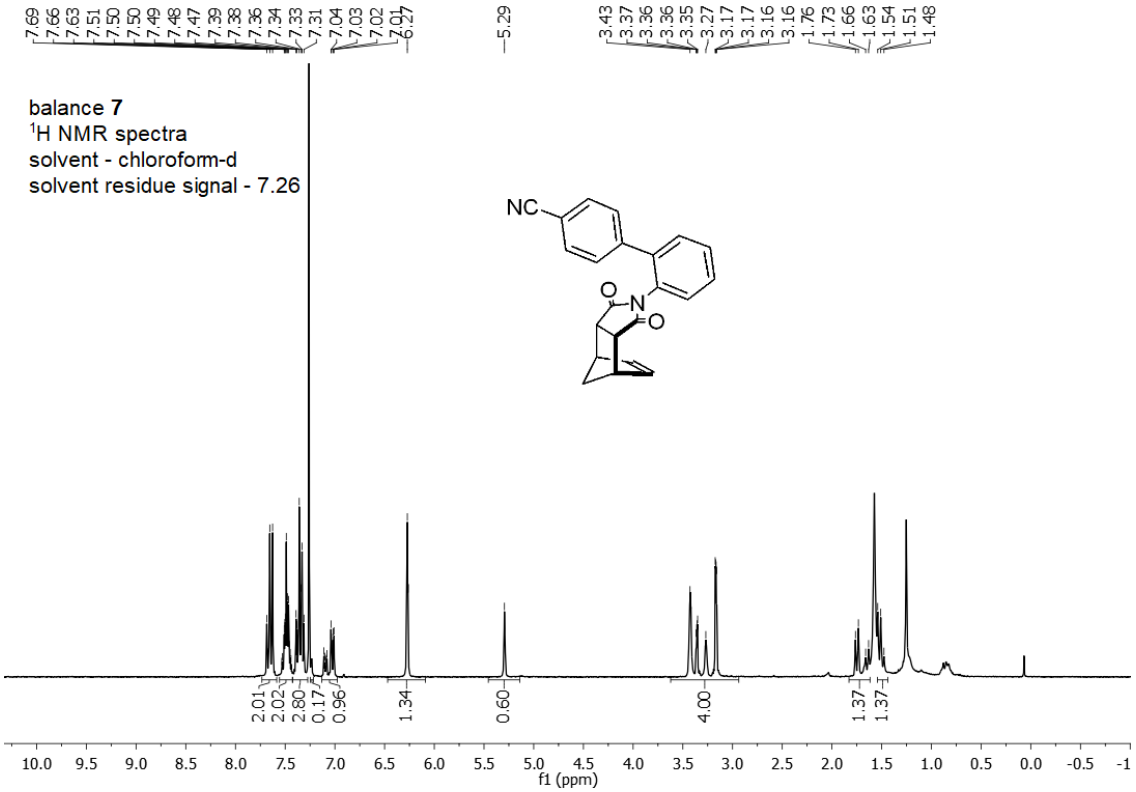

Figure 3.29. ^{1}H NMR spectra of balance **7** (300 MHz, chloroform-d)

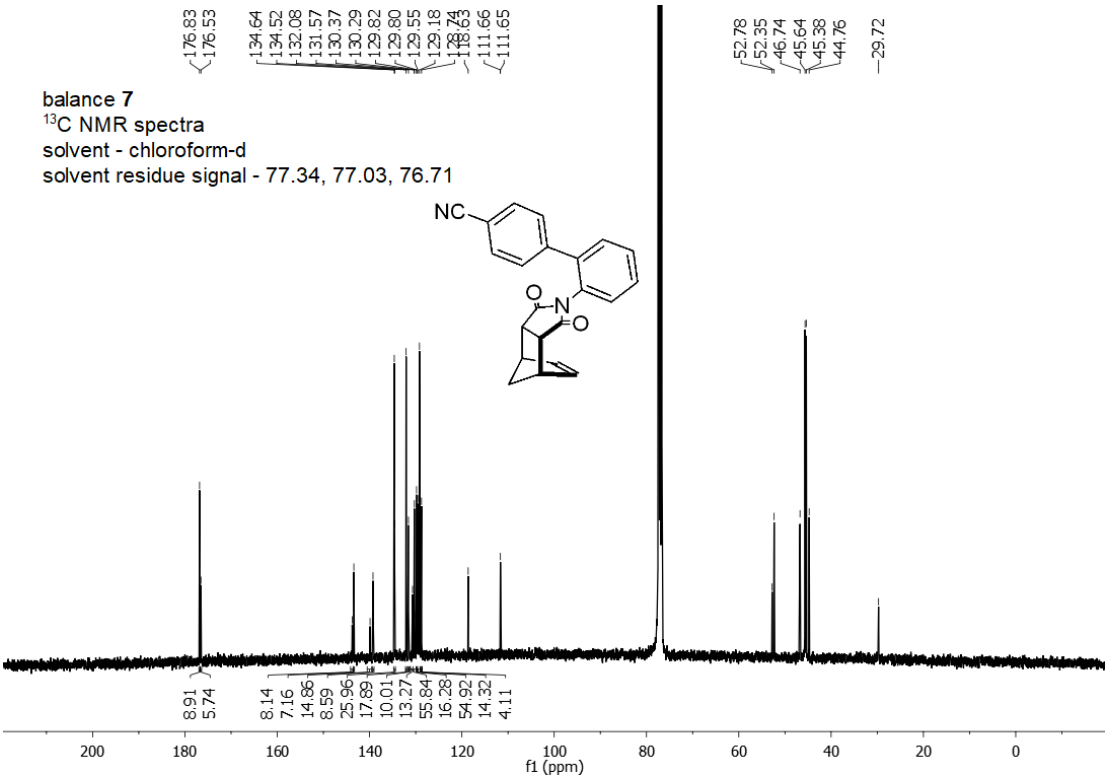

Figure 3.30. ^{1}H NMR spectra of balance **7** (100 MHz, chloroform-d)

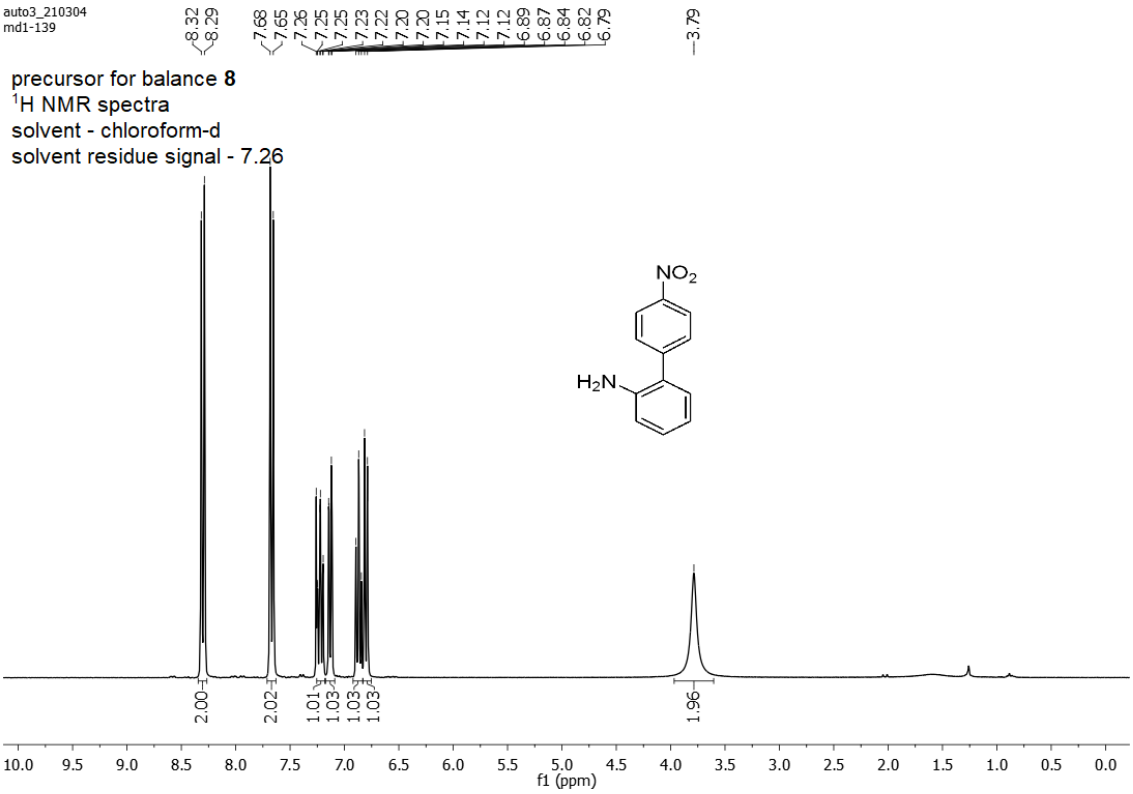

Figure 3.31. ^{1}H NMR spectra of precursor for balance **8** (300 MHz, chloroform-d)

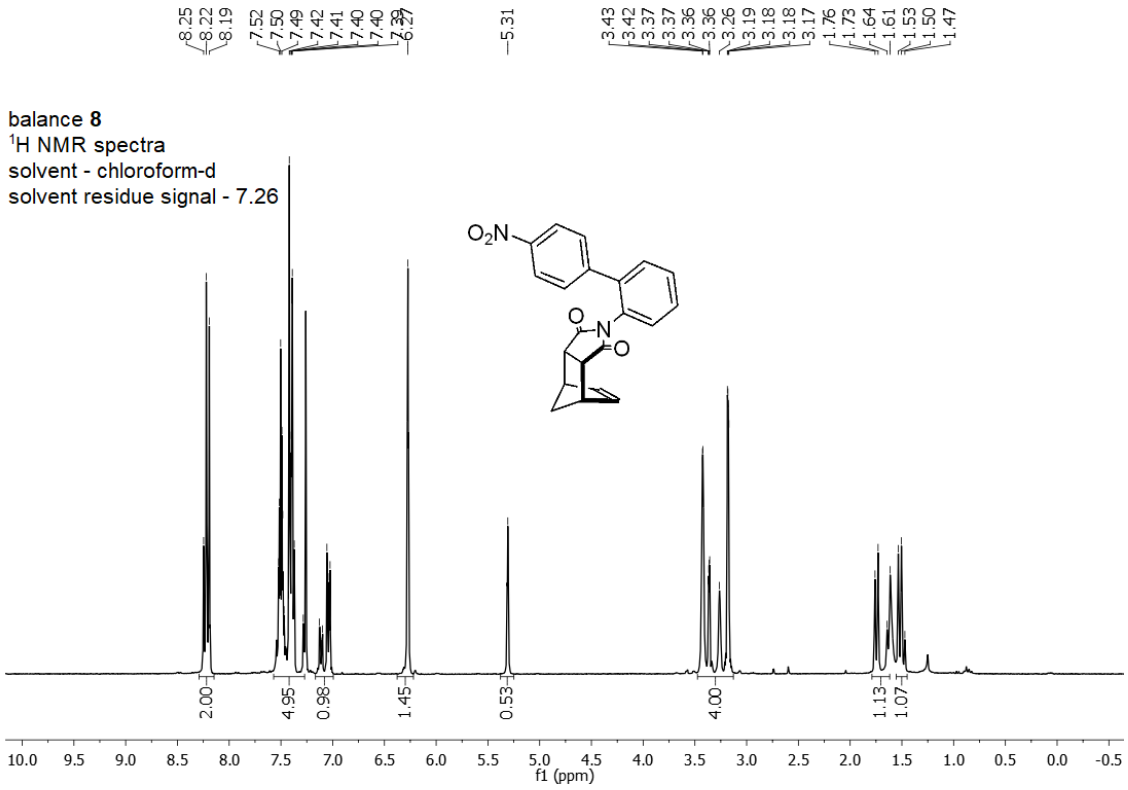

Figure 3.32. ^{1}H NMR spectra of balance **8** (300 MHz, $CDCl_3$)

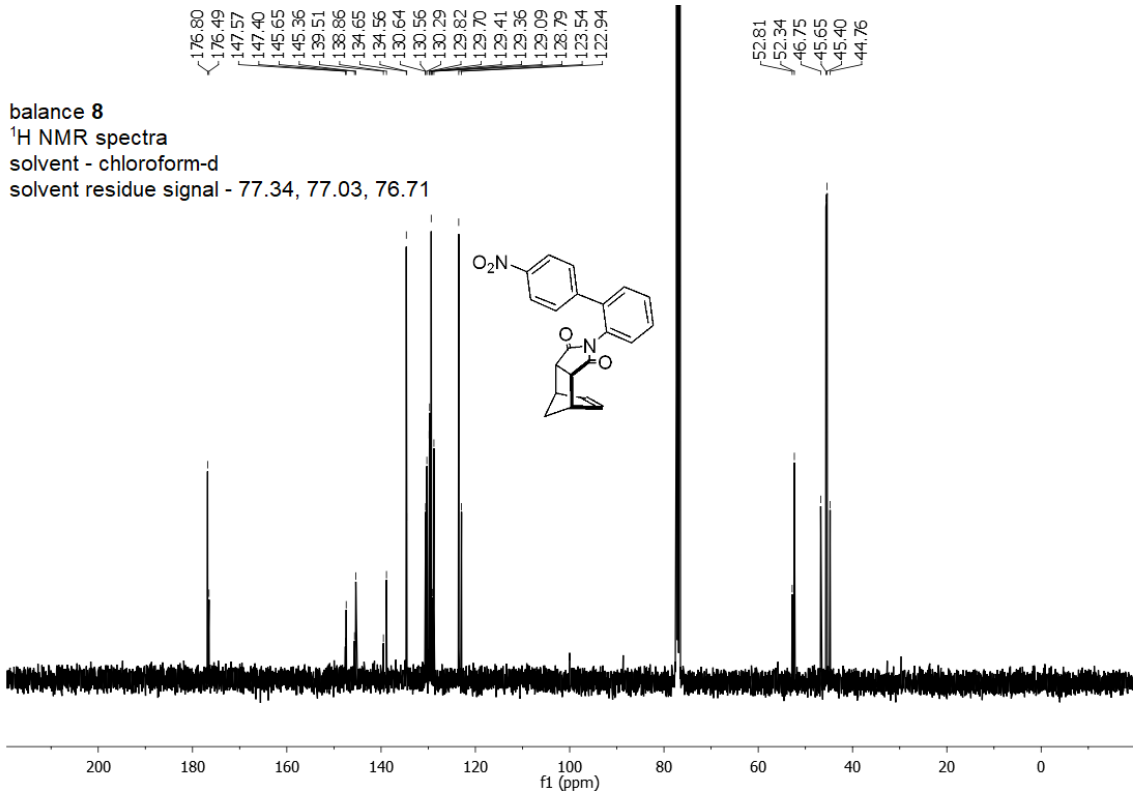

Figure 3.33. ^{13}C NMR spectra of balance **8** (100 MHz, , $CDCl_3$)

CHAPTER 4

LONE PAIR – LONE PAIR (LP-LP) INTERACTION

4.1 ABSTRACT

This study aims to quantify the strength of through-space lone pair-lone pair (lp-lp) interactions and compare their strength to the geminal lp-lp interaction. Through-space lp-lp interaction is crucial in determining a molecule's properties, reactivity, and shape. To achieve our objectives, we designed two sets of molecular rotors: one capable of forming repulsive lp-lp interactions in the bond rotation transition state, and another acting as a control, which cannot form lp-lp interactions. We measured the rotational barriers of both rotor sets in TCE-d2 using EXSY ^{1}H NMR and plotted the data against Mazzanti's steric parameter, B-values, to isolate the steric component in the rotor system. Our findings reveal that through-space lp-lp interaction has a strength of approximately +1.1 kcal/mol, indicating that this type of interaction is relatively weak.

4.2 QUANTIFICATION OF LONE PAIR – LONE PAIR INTERACTION

A lone pair are defined as two valence electrons that are localized on an atom and do not participate in chemical bonding.[96] The presence of a lone pair on an atom can influence the shape, reactivity, and properties of a molecule.[97] For example, strong repulsive geminal lp-lp interactions are used in VSEPR theory to predict bond angles,[98,99,100] providing the rationale for why the water molecule has a bond angle of 104.5°, which is smaller than the ideal tetrahedral bond angle of 109.5° (Figure 4.1A). Furthermore, repulsive through-space lp-lp interactions have been cited to explain the enhanced acidity and structure of proton sponge (Figure 4.1B).[55]

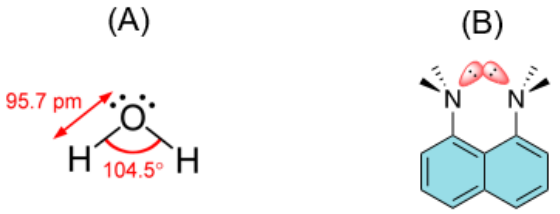

Figure 4.1. Lp-lp interaction influencing (A) the shape of the water molecule and (B) basicity of proton sponge.

Because of the significant role lp-lp interactions play in describing the structure and reactivity of molecules, we must address the following questions: (a) Is the through-space lp-lp interaction a strong repulsive interaction comparable to the geminal lp-lp interaction? (b) Can we measure the magnitude of the lp-lp interaction? Quantifying the interaction between lone pairs is crucial to obtaining a better understanding of the behavior and properties of molecules. Knowledge of the magnitude and direction of the lone pair-lone pair interaction can help in designing new molecules and materials. For instance, in

developing new drugs, it is essential to understand how the lone pairs in various functional groups will interact with each other and with the target molecule. Despite the crucial role that lone pair-lone pair interactions play, only a few studies have focused on investigating these interactions. This scarcity of research can be attributed to the challenges associated with measuring through-space lone pair-lone pair interactions in solution, primarily due to their inherently weak nature.

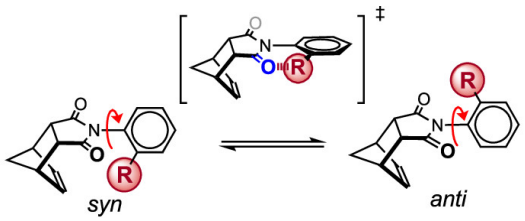

Figure 4.2. (A) lp rotor: **12**(F), **13**(OCF_3), **14**(OMe), **15**(NMe_2), **16**(Cl), **17**(Br), **18**(SMe), **19**(I), **20**(CF_3)

(B) control: **1**(2-fluorenyl), **2**(-CH_2)$_3$-, **3**(C=CH_2)Me, **4**(Me), **5**(Ph), **6**(2-propyl), **7**(Et), **8**(2,3-diMe), **9**-(CH_2)$_4$-, **10**(*i*-Pr), **11**(1-naphthyl)

To address this issue, we designed a molecular rotor based on a rigid *N*-phenylimide framework (Figure 4.2). The rotor interconverts between *folded* and *unfolded* conformations through a bond rotation transition state. We incorporated an R-group onto the framework, which can form a lone pair-lone pair interaction with the carbonyl oxygen of the succinimide. The first atom of the R-group possesses a lone pair, enabling the formation of the desired lone pair-lone pair interaction (Figure 4.2A). In the transition state, the rigid framework brings the carbonyl oxygen and the R-group into close proximity, forming a destabilizing intramolecular lone pair-lone pair interaction. Our model system presents a simple and reliable method for quantifying the strength of lone pair – lone pair

interactions. By connecting both the R-group and carbonyl group to the same framework, our rotor provides precise control over interaction distances and geometries, due to the rigid N-phenylimide framework. Additionally, the synthesis of our rotors is straightforward.

Exchange spectroscopy was then utilized to measure the rotational barriers of the rotors in TCE-d2 using EXSY 1H NMR.[66] These measurements were performed in the slow exchange regime (0 – 90 °C), resulting in two separate peaks for the *folded* and *unfolded* conformers. The Eyring plot was used to generate the enthalpy and entropy of the rotational barriers, which were then employed to calculate the Gibb's free energy ($\Delta G^{\ddagger}_{exp}$) at 25 °C for all the rotors. Since the rotational barrier of the rotors is primarily governed by sterics, a control rotor set was introduced to examine the lone pair-lone pair interaction in the transition state (Figure 4.2B). The control rotor set consists of R-groups that lack lone pairs, preventing the formation of lone pair-lone pair interactions. In contrast, the first rotor set is designed to form repulsive lp-lp interactions during bond rotation transition states. By selecting R-groups without lone pairs for the control set, we can compare the rotational barriers between the two sets and assess the strength of lone pair-lone pair interactions.

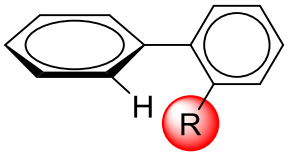

Figure 4.3. Mazzanti's biphenyl system

We measured the rotational barriers of both rotor sets and plotted the data against Mazzanti's steric parameter, B-values (Figure 4.3).[101] We chose Mazzanti's B-values

because they are based on the rotational barriers of similar biaryl rotors.[101] This parameter quantifies the steric hindrance exhibited by the R-group during the aryl-aryl bond rotation within the biphenyl framework. Mazzanti's biaryls cannot form lp-lp interactions with the R-groups, providing a direct measure of the steric component of the rotational barriers. We verified the ability of B-value to accurately predict the steric interactions in our *N*-phenylimide rotor system by analyzing the rotational barrier trends for a series of rotors.[102] Excellent agreement was observed between $\Delta G^{\ddagger}_{expt}$ and B-values for the control rotors (Figure 4.4), indicating that the B-values accurately predict the energy barriers in our rotor system.[102] We determined the strength of the lp-lp interaction by examining the barrier difference between the control and lone pair rotor trend lines on the plot (Figure 4.4).

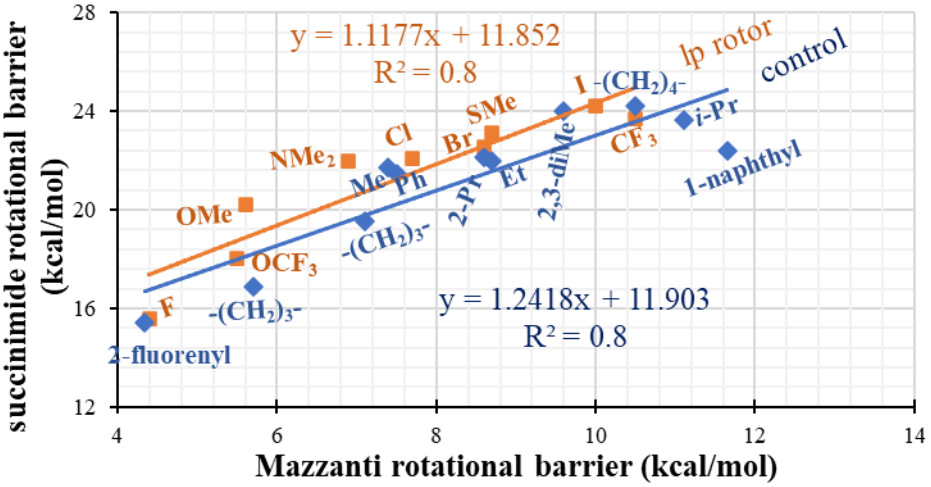

control**:** **1**(2-fluorenyl), **2**(-CH_2)$_3$-, **3**(C=CH_2)Me, **4**(Me), **5**(Ph), **6**(2-propyl), **7**(Et), **8**(2,3-diMe), **9**-(CH_2)4-, **10**(iPr), **11**(1-naphthyl)

lp rotor**:** **12**(F), **13**(OCF_3), **14**(OMe), **15**(NMe_2), **16**(Cl), **17**(Br), **18**(SMe), **19**(I), **20**(CF_3)

Figure 4.4. Energy barrier comparison of lone pair (lp) rotor series and control rotor series as a function of B-value

To obtain this barrier difference, we extended the uppermost and lowermost regions of the lone pair (lp) and control trend lines horizontally to the vertical axis of the linear free energy relationship plots. The resulting barrier difference on the vertical axis provides valuable insights into the strength of the lone pair-lone pair interaction, spanning a range of values from 0.8 to 2.8 kcal/mol. Additionally, we validated the accuracy of the experimentally measured barriers by establishing a correlation with the calculated barriers. DFT calculations of the transition state structures of the molecular rotor system were performed using the Spartan 18 program at the B3LYP-D3 level of theory and 6-311G* basis set. The correlation demonstrated a high level of agreement between the measured and calculated barriers (Figure 4.5).

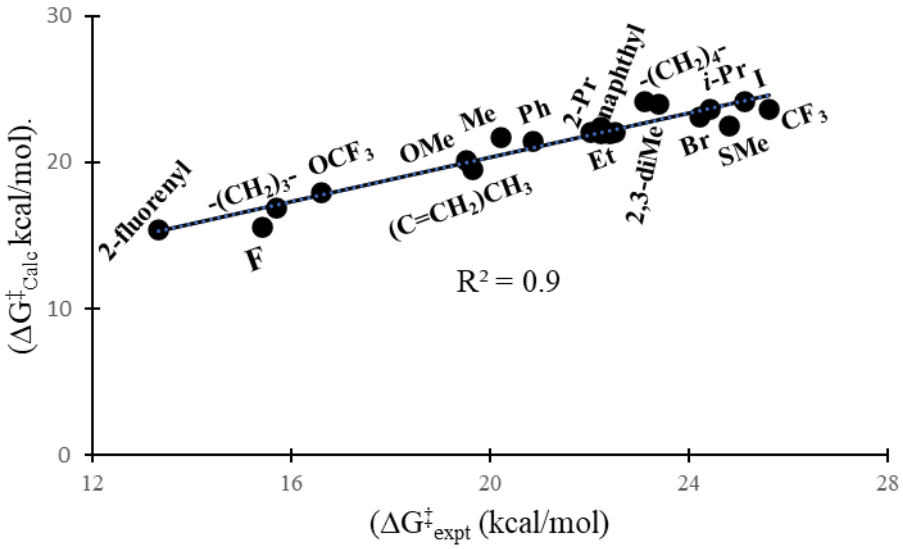

Figure 4.5. Correlation between experimental and calculated barriers

The synthesis of the rotors was achieved through a simple one-step thermal condensation process involving norbornene anhydride and the corresponding aniline (Scheme 4.1). Detailed information on the syntheses of the individual rotors can be found in the experimental section.

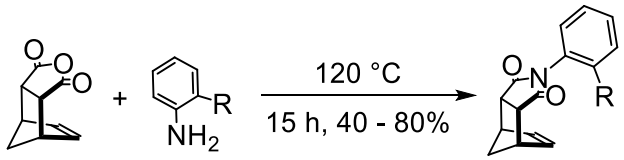

Scheme 4.1. General synthesis of molecular rotors.

To test whether through-space lone pair-lone pair (lp-lp) interactions could form in our rotor system, we monitored the energy barriers of lp rotors with varying R-groups. We hypothesized that lp rotors with R-groups having low electron density would exhibit low barriers, while those with high electron density would display higher barriers. This assumption was based on the idea that R-groups with high electron density would experience stronger repulsive interactions with the carbonyl oxygen of the succinimide, resulting in higher barriers. On the other hand, R-groups with low electron density would encounter weaker repulsive interactions with the carbonyl oxygen of the succinimide, leading to relatively lower barriers. Figure 4.4 illustrates that the observed trends were consistent with our hypothesis, suggesting that through-space lp-lp interactions could form in the lp rotors. In summary, we have successfully determined the strength of the through-space lp-lp interaction to be approximately 0.8 - 2.8 kcal/mol. However, it is important to note that the barriers considered in this study range from 15 to 24 kcal/mol. To validate the accuracy of the measured lp-lp interaction strength, further investigation is required with barriers below 15 kcal/mol.

4.3 SUPPORTING INFORMATION

4.3.1 GENERAL EXPERIMENTAL INFORMATION

NMR spectra were recorded on Bruker 300 MHz spectrometer. Chemical shifts are reported in ppm (δ) referenced to the solvent residue. All spectra given for characterization purposes were taken at 25 ºC. All chemicals and solvents were purchased from commercial suppliers and used as received. Flash chromatography was performed using silica gel from Sorbent Technologies (60 Å, 200 – 400 mesh).

4.3.2 SYNTHESIS OF COMPOUNDS

Rotors **2, 3, 4, 5, 7, 9, 10, 12 – 14** and **16 – 20** will not be reported here as they have been previously reported.[103]

1-Aminonofluorene (45.2 mg, 0.25 mmol) and *cis*-5-norbornene-*endo*-2,3-dicarboxylic anhydride (36.8 mg, 0.22 mmol) were added to a 20-dram vial along with a magnetic stir bar. The vial was then capped and heated to 120 ºC in a silicon oil bath for 12 hours with mild stirring. After letting the vial cool to room temperature, the crude material was purified by column chromatography (ethyl acetate/hexanes = 1:3, v/v) to give a brown powder **1** (53.1 mg, 72 %). ^{1}H NMR (300 MHz, $CDCl_3$) δ 7.80 (t, d = 8.4 Hz, 2 H), 7.52 – 7.29 (m, 4 H), 7.04 – 6.94 (m, 1 H), 6.41 (s, 2 H), 3.73 – 3.65 (m, 2 H), 3.54 – 3.50 (m, 4 H), 1.84 (d, J = 8.3 Hz, 1 H), 1.64 (d, J = 8.6 Hz, 1 H). ^{13}C NMR (100 MHz, chloroform-d) δ 176.31, 143.74, 142.60, 140.99, 140.37, 135.07, 134.84, 129.00, 127.97, 127.34, 126.87, 125.83, 124.96, 120.63, 120.18, 52.50, 46.49, 46.08, 45.41, 36.30, 35.48, 29.74.

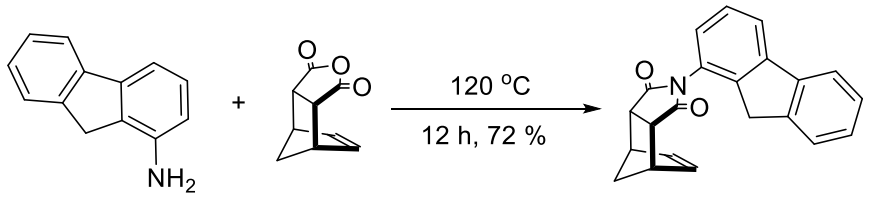

Scheme 4.6. Synthesis of rotor **1**

1-Aminonaphthalene (97.8 mg, 0.68 mmol) and *cis*-5-norbornene-*endo*-2,3-dicarboxylic anhydride (101.1 mg, 0.62 mmol) were added to a 20-dram vial along with a magnetic stir bar. The vial was then capped and heated to 120 ºC in a silicon oil bath for 12 hours with mild stirring. After letting the vial cool to room temperature, the crude material was purified by column chromatography (ethyl acetate/hexanes = 1:3, v/v) to give a light brown crystalline solid **5** (0.1604 mg, 90 %). ^{1}H NMR (300 MHz, $CDCl_3$) δ 7.9 (t, d = 8.5 Hz, 2 H), 7.63 – 7.48 (m, 4 H), 7.24 - 7.12 (m, 1 H), 6.55 (s, 2 H minor), 6.38 (s, 2 H major), 3.58 – 3.57 (m, 4 H), 1.89 (d, J = 8.8 Hz, 1 H minor), 1.83 (d, J = 8.8 Hz, 1 H major), 1.70 – 1.64 (m, 1 H). ^{13}C NMR (100 MHz, chloroform-d) δ 176.22, 175.91, 134.66, 133.70, 133.30, 128.85, 128.82, 128.48, 128.09, 127.83, 127.53, 127.50, 126.03, 125.81, 125.48, 121.67, 121.01, 51.89, 51.33, 45.92, 44.92, 44.55, 44.26.

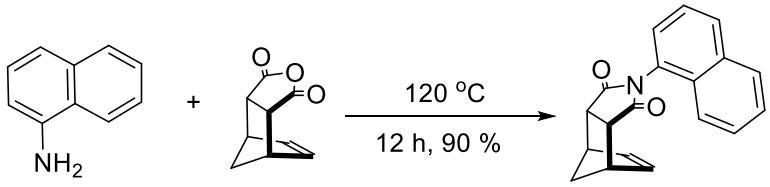

Scheme 4.5. Synthesis of rotor **5**

2-Propylaniline (115.2 mg, 0.85 mmol) and *cis*-5-norbornene-*endo*-2,3-dicarboxylic anhydride (118.7 mg, 0.72 mmol) were added to a 20-dram vial along with a magnetic stir bar. The vial was then capped and heated to 120 ºC in a silicon oil bath for 12 hours with mild stirring. After letting the vial cool to room temperature, the crude material was purified by column chromatography (ethyl acetate/hexanes = 1:3, v/v) to give a brown film **6** (143.4 mg, 70 %). ^{1}H NMR (300 MHz, $CDCl_3$) δ 7.42 – 7.26 (m, 3 H), 7.01 (d, J = 7.8 Hz, 1 H major), 6.9 (d, J = 7.9 Hz, 1 H minor), 6.37 (s, 2 H), 3.54 – 3.50 (m, 4 H), 2.46 – 2.36 (m, 2 H), 1.84 (t, J = 8.5 Hz, 1 H), 1.67 – 1.49 (m, 3 H), 1.03 – 0.94 (m, 3 H). ^{13}C NMR (100 MHz, chloroform-d) δ 176.63, 178.34, 141.99, 141.69, 136.54, 136.01, 132.29, 131.37, 131.30, 130.90, 130.82, 130.07, 129.70, 128.28, 128.21, 79.05, 78.98, 78.73, 78.66, 78.41, 78.34, 54.36, 53.71, 48.21, 47.13, 46.84, 46.55, 34.87, 34.55, 24.97, 24.42, 15.58.

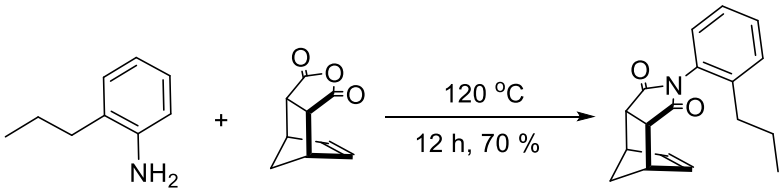

Scheme 4.2. synthesis of rotor **6**

2,3-Dimethylaniline (99.3 mg, 0.82 mmol) and *cis*-5-norbornene-*endo*-2,3-dicarboxylic anhydride (103.2 mg, 0.63 mmol) were added to a 20-dram vial along with a magnetic stir bar. The vial was then capped and heated to 120 ºC in a silicon oil bath for 12 hours with mild stirring. After letting the vial cool to room temperature, the crude material was purified by column chromatography (ethyl acetate/hexanes = 1:3, v/v) to give

an off-white powder **8** (0.0664 mg, 40 %). ^{1}H NMR (300 MHz, $CDCl_3$) δ 7.20 – 7.10 (m, 2 H), 6.82 (d, J = 7.4 Hz, 1 H minor), 6.7 (d, J = 7.4 Hz, 1 H major), 6.32 (s, 2 H minor), 6.30 (s, 2 H major), 3.51 – 3.46 (m, 4 H), 2.29 (s, 3 H), 1.99 (s, 3 H major), 1.98 (s, 3 H minor), 1.83 – 1.78 (m, 1 H), 1.65 – 1.60 (m, 1 H). ^{13}C NMR (100 MHz, chloroform-d) δ 177.32, 177.08, 176.14, 176.07, 140.49, 140.15, 135.20, 134.67, 130.90, 130.84, 130.18, 130.04, 129.92, 129.81, 129.49, 129.45, 128.56, 128.19, 127.78, 127.06, 126.96, 126.85, 52.98, 52.34, 48.32, 47.75, 47.31, 46.86, 45.79, 45.46, 45.18, 39.61, 39.29, 33.52, 33.25, 29.61, 23.68, 23.06, 14.12, 14.10.

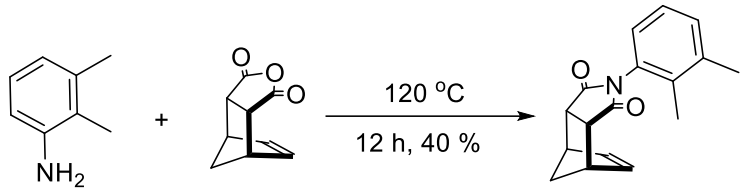

Scheme 4.3. Synthesis of rotor **8**

1-Methylnaphthalen-2-amine (100.0 mg, 0.52 mmol) and *cis*-5-norbornene-*endo*-2,3-dicarboxylic anhydride (56.5 mg, 0.34 mmol) were added to a 20-dram vial along with a magnetic stir bar. The vial was then capped and heated to 120 ºC in a silicon oil bath for 12 hours with mild stirring. After letting the vial cool to room temperature, the crude material was purified by column chromatography (ethyl acetate/hexanes = 1:3, v/v) to give a light brown powder **11** (48.3 mg, 46 %). ^{1}H NMR (300 MHz, $CDCl_3$) δ 8.04 – 8.03 (m, 1 H), 7.63 – 7.48 (m, 3 H), 7.37 – 7.33 (m, 1 H) 7.14 (d, J = 7.5 Hz, 1 H minor), 7.02 (d, J = 7.4 Hz, 1 H major), 6.55 (s, 2 H minor), 6.37 (s, 2 H major), 3.58 – 3.57 (m, 4 H), 2.71 (s, 3 H), 1.89 (d, J = 8.9 Hz, 1 H minor), 1.83 (d, J = 8.9 Hz, 1 H major), 1.70 – 1.65 (m, 1 H). ^{13}C NMR (100 MHz, chloroform-d) δ 177.42, 177.12, 136.69, 135.74, 134.74, 133.37,

129.40, 127.46, 127.16, 126.72, 126.47, 126.37, 126.28, 126.17, 126.12, 126.05, 125.63, 124.91, 124.86, 123.20, 122.50, 52.94, 52.38, 46.96, 45.94, 45.59, 45.32, 19.57

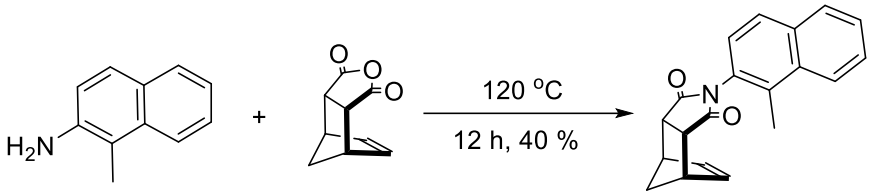

Scheme 4.4. Synthesis of rotor **11**

N-phenyl-*o*-phenylenediamine (113.4 mg, 0.62 mmol) and *cis*-5-norbornene-*endo*-2,3-dicarboxylic anhydride (112.3 mg, 0.68 mmol) were added to a 20-dram vial along with a magnetic stir bar. The vial was then capped and heated to 120 °C in a silicon oil bath for 15 hours while stirring. After letting the vial cool to room temperature, the crude material was purified by column chromatography (ethyl acetate/hexanes = 1:1, v/v) to give a brown solid **15** (198.3 mg, 97 %). ^{1}H NMR (500 MHz, 1,1,2,2-tetrachloroethane-d_2) δ 7.41 (dd, *J* = 7.5 and 7.6 Hz, 1 H), 7.34 (dd, *J* = 7.5 and 8.0 Hz, 1 H), 7.29 - 7.23 (m, 2 H), 7.09 - 6.91 (m, 5 H), 6.28 (s, 2 H major), 6.20 (s, 2 H minor), 5.60 (s, br, 1 H major), 5.38 (s, 1 H minor), 3.50 - 3.48 (m, 3 H), 3.35 - 3.34 (m, 1 H), 1.80 (dd, *J* = 9.3 and 9.2 Hz, 1 H), 1.60 - 1.58 (m, 1 H). ^{13}C NMR (100 MHz, $CDCl_3$) δ 177.10, 176.89, 143.20, 142.75, 139.98, 139.75, 135.23, 134.66, 130.11, 129.92, 129.51, 129.33, 129.26, 128.85, 123.55, 122.61, 122.39, 121.94, 121.43, 121.26, 121.11, 119.68, 118.17, 117.91, 77.53, 52.64, 52.35, 46.62, 45.86, 45.48, 45.37.

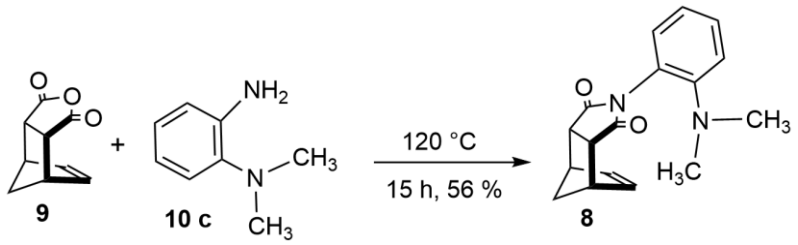

Scheme 4.5. Synthesis of rotor **15**

4.3.3. ^{1}H NMR and ^{13}C NMR Spectra

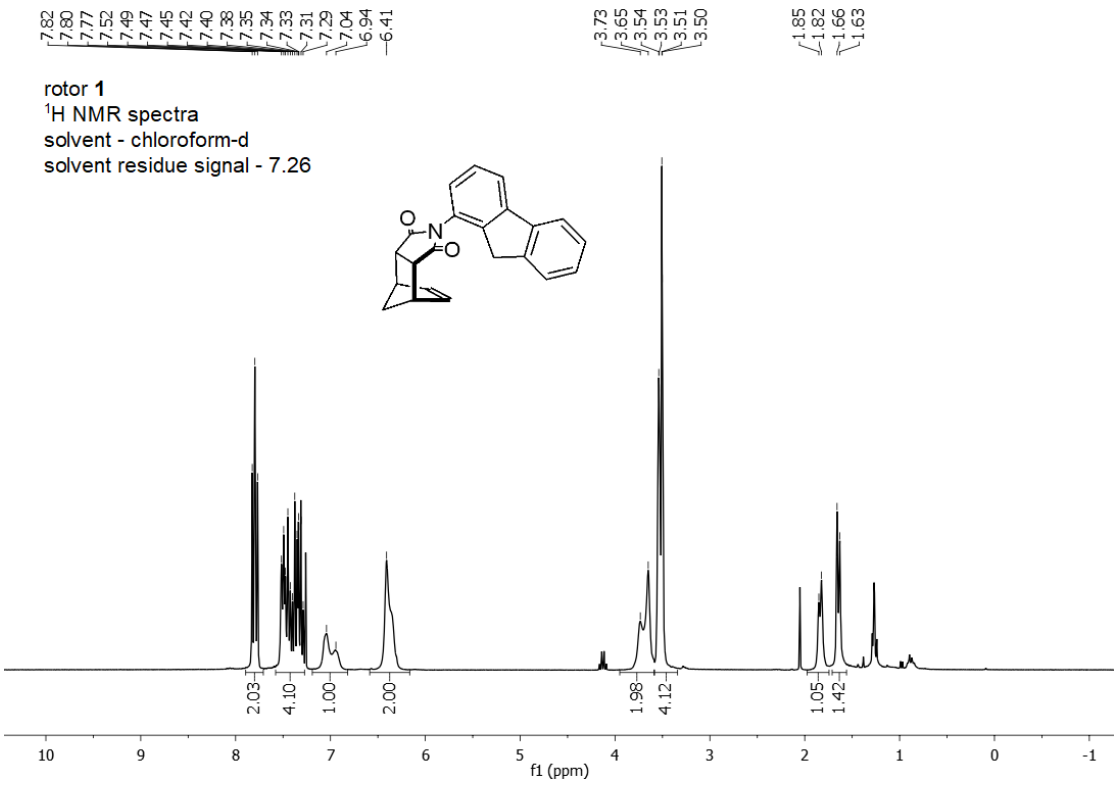

Figure 4.6. ^{1}H NMR spectra of rotor **1** (300 MHz, chloroform-d)

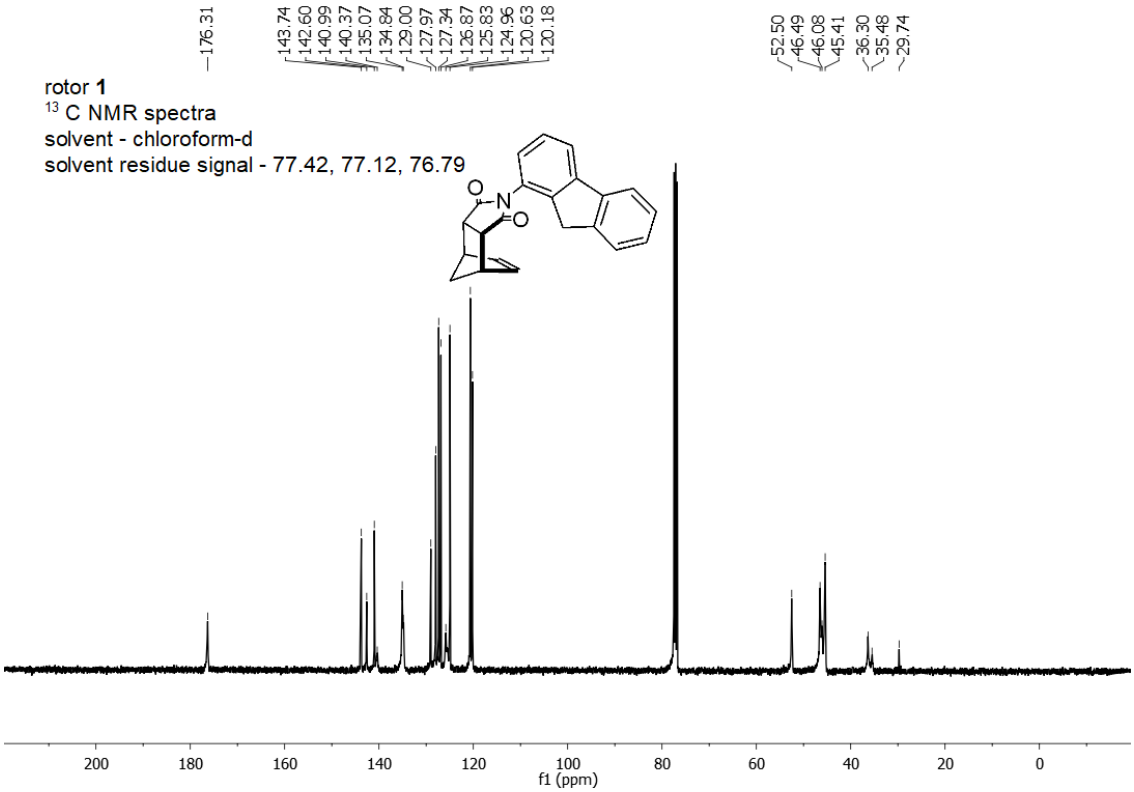

Figure 4.7. ^{1}H ^{13}C NMR spectra of rotor **1** (100 MHz, chloroform-d)

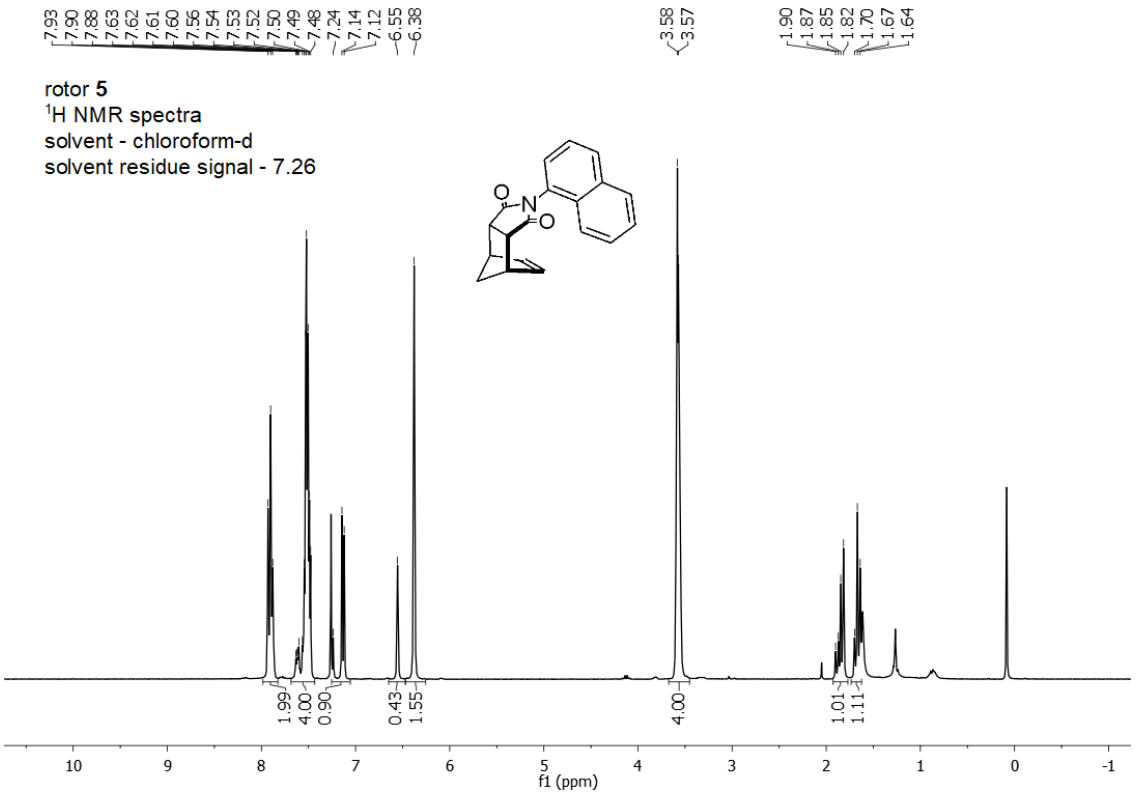

Figure 4.8. ^{1}H NMR spectra of rotor **5** (300 MHz, chloroform-d)

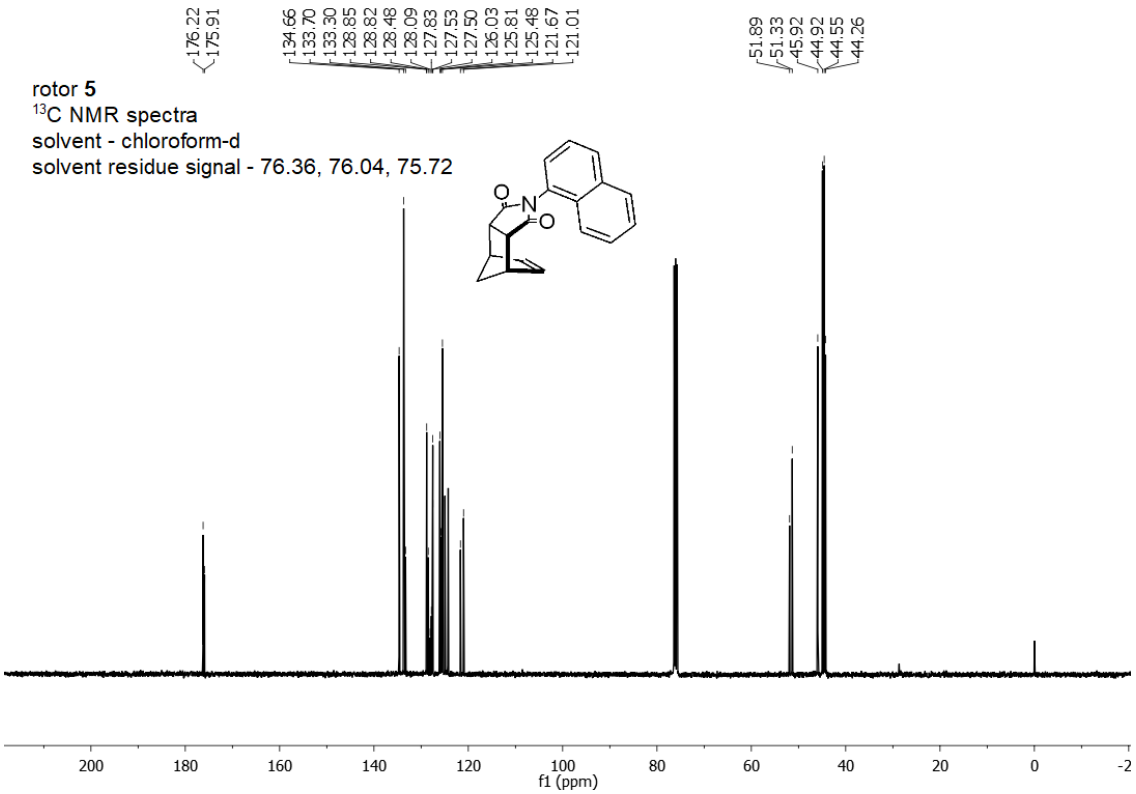

Figure 4.9. ^{13}C NMR spectra of rotor **5** (100 MHz, chloroform-d)

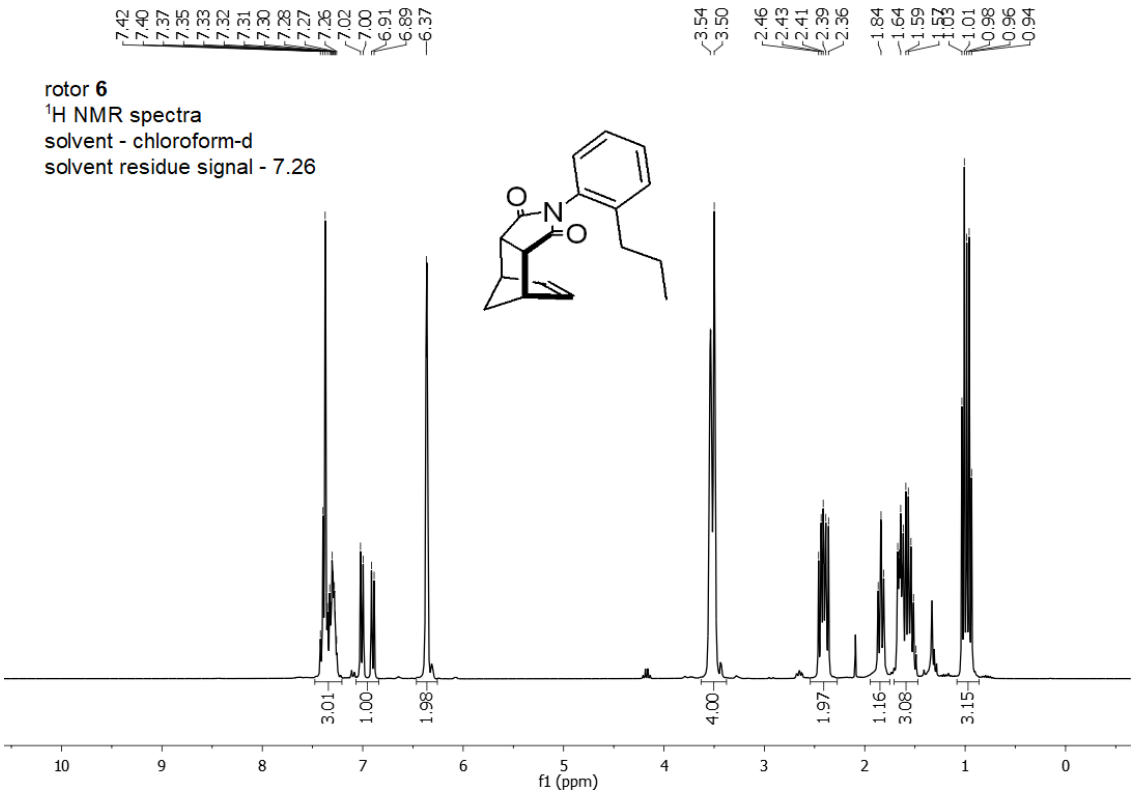

Figure 4.10. ^{1}H NMR spectra of rotor **6** (300 MHz, chloroform-d)

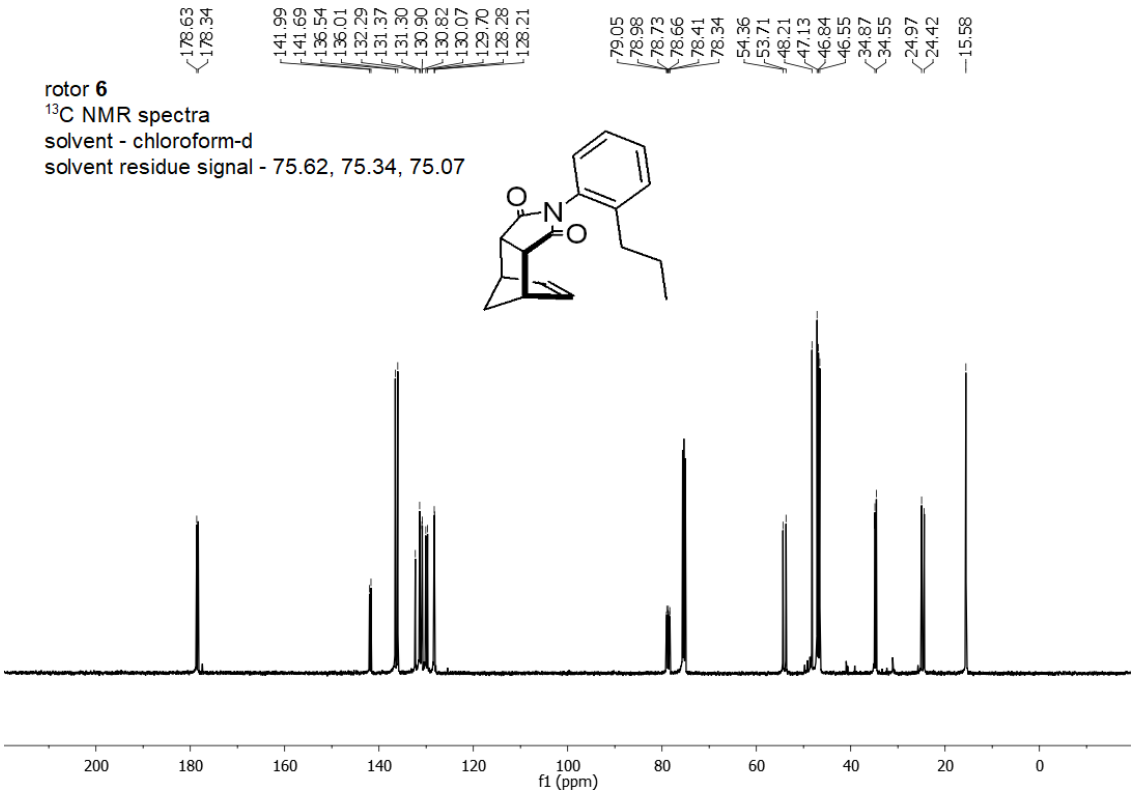

Figure 4.11. ^{13}C NMR spectra of rotor **6** (100 MHz, chloroform-d)

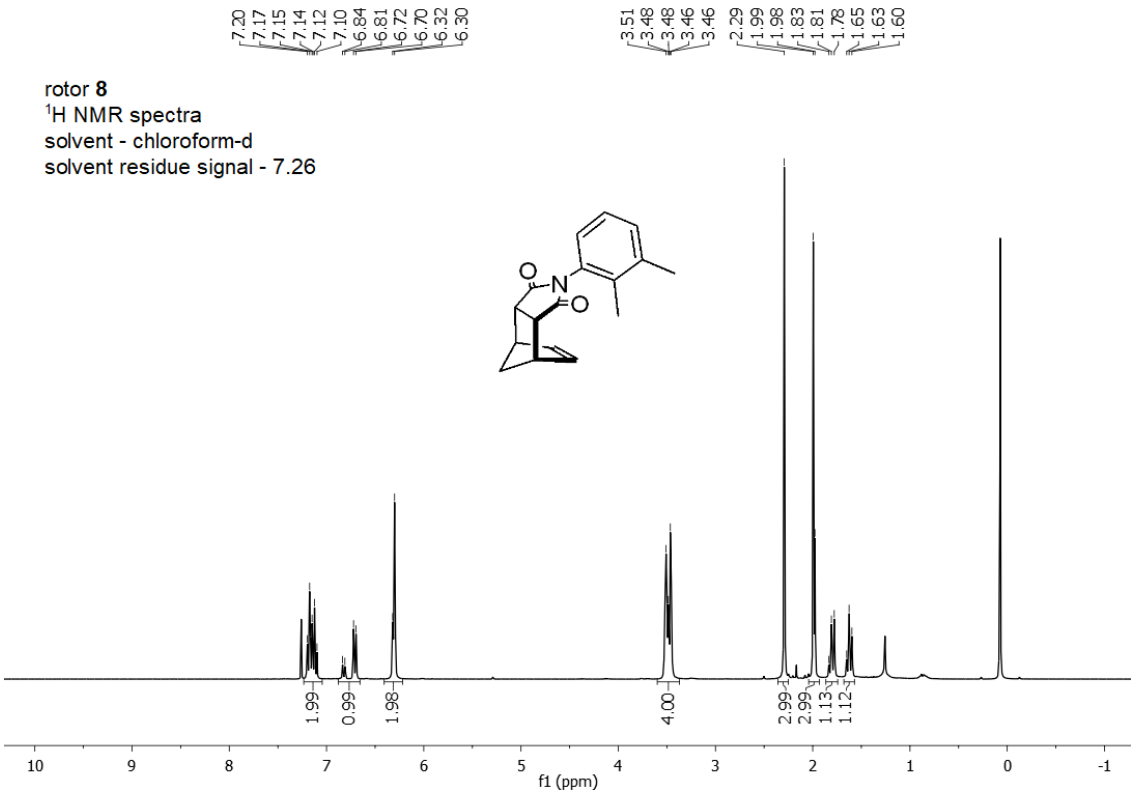

Figure 4.12. ^{1}H NMR spectra of rotor **8** (300 MHz, chloroform-d)

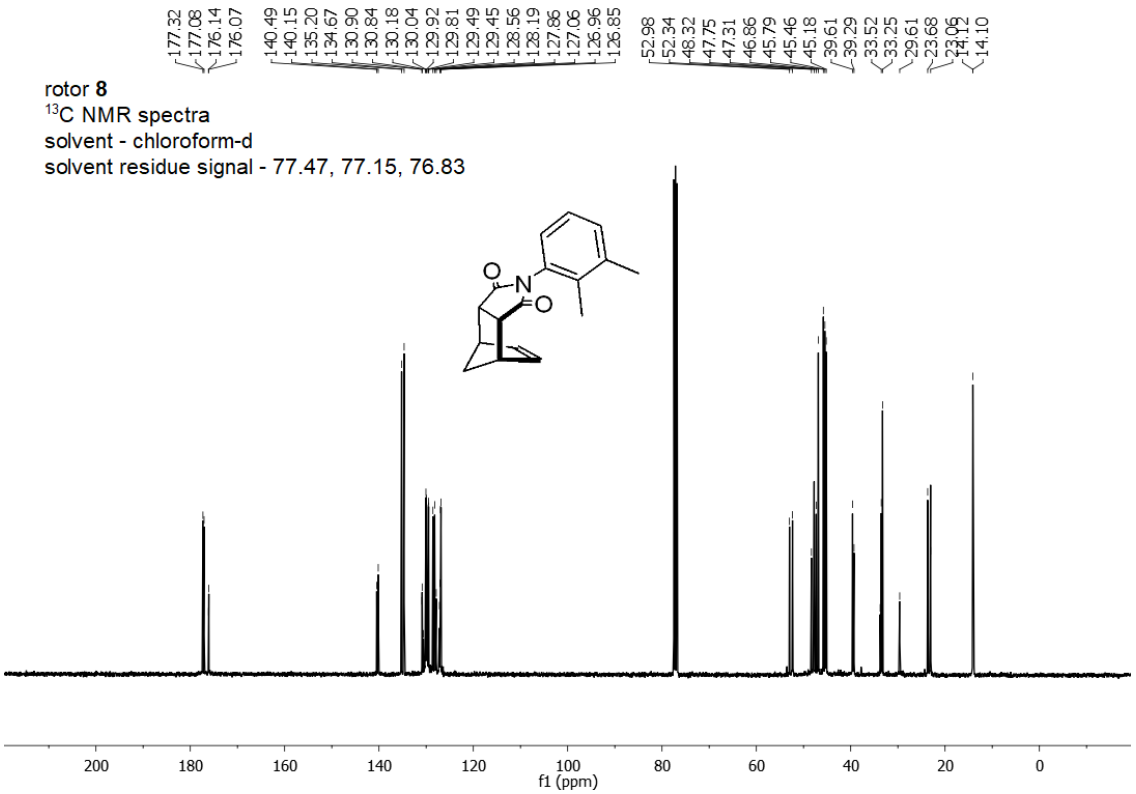

Figure 4.13. ^{13}C NMR spectra of rotor **8** (100 MHz, chloroform-d)

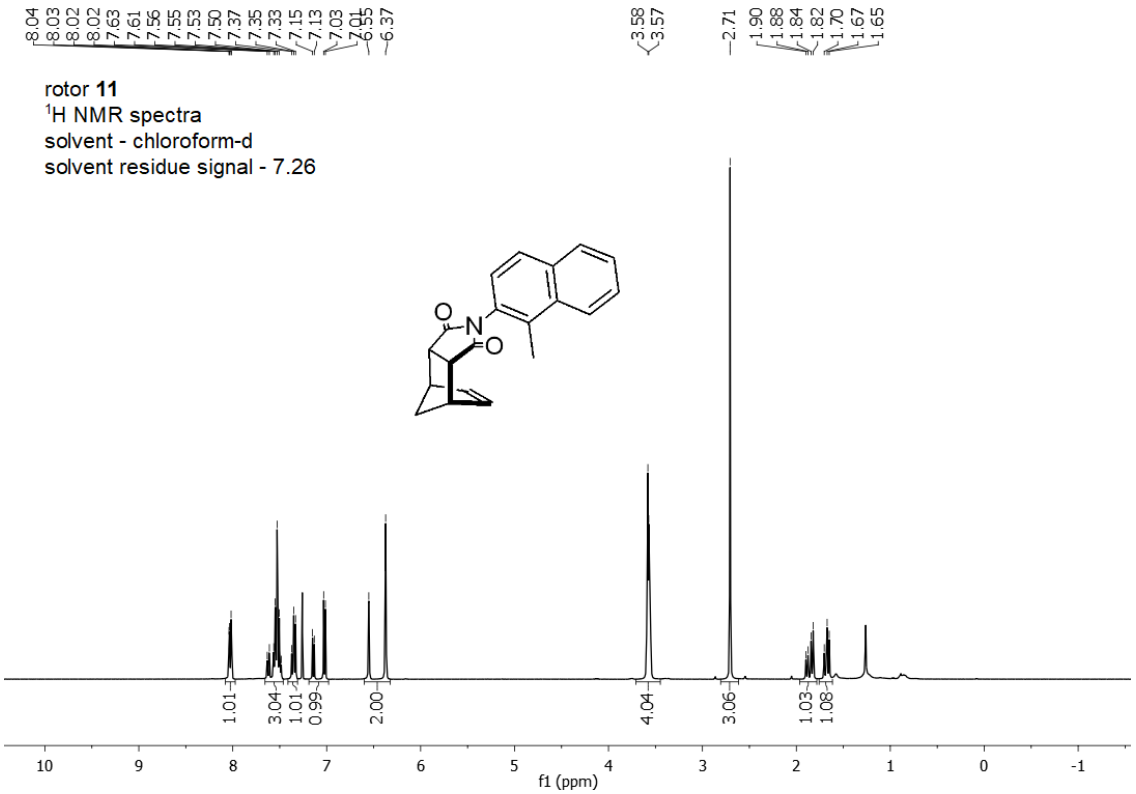

Figure 4.14. ^{1}H NMR spectra of rotor **11** (300 MHz, chloroform-d)

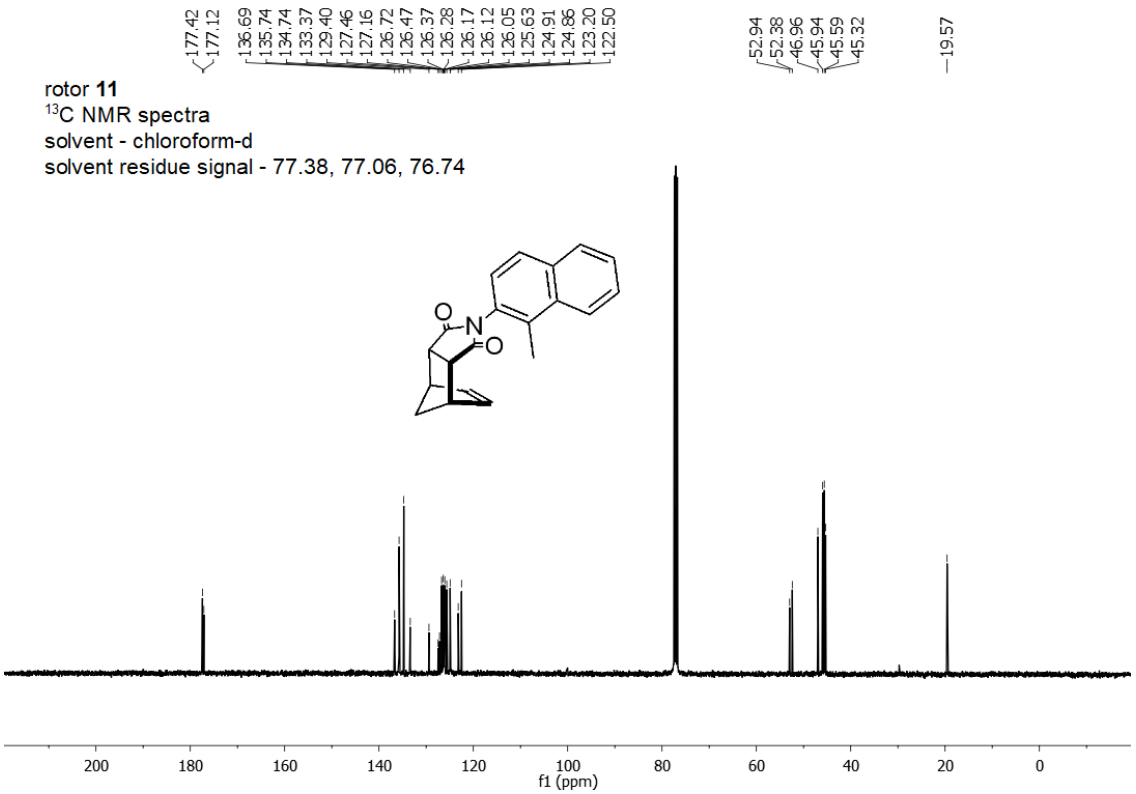

Figure 4.15. ^{13}C NMR spectra of rotor **11** (100 MHz, chloroform-d)

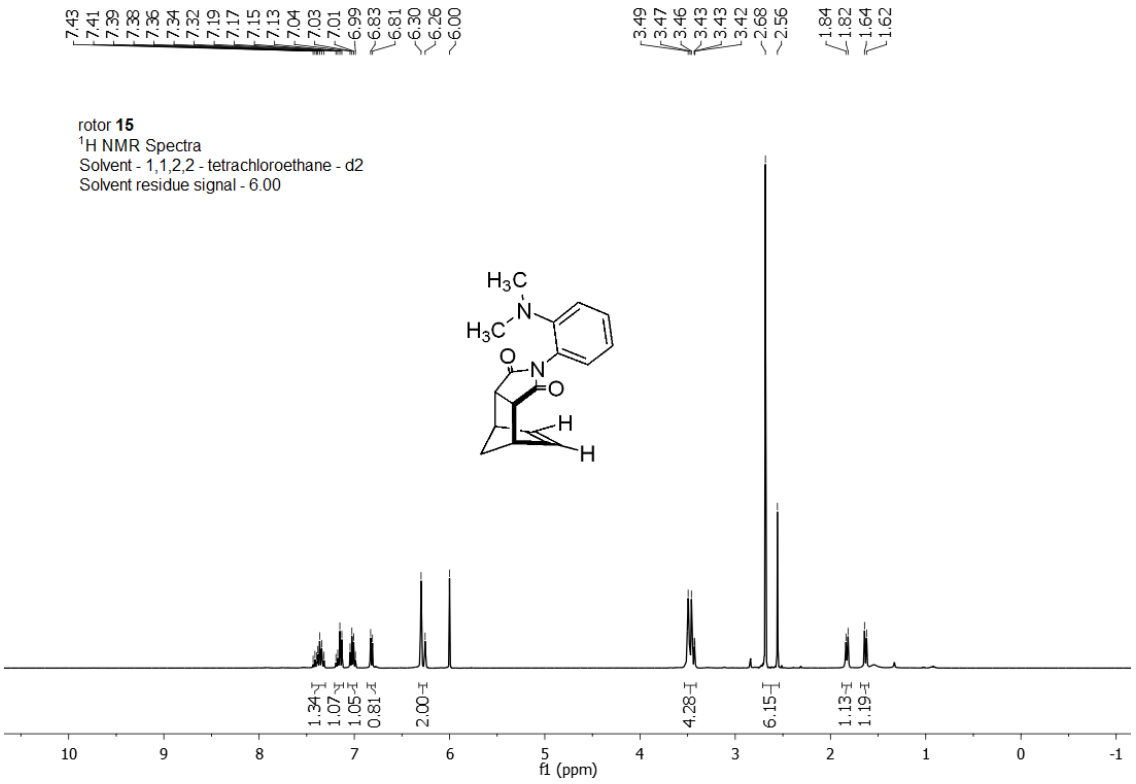

Figure 4.16. ^{1}H NMR spectra of rotor **15** (500 MHz, 1,1,2,2 - tetrachloroethane-d2)

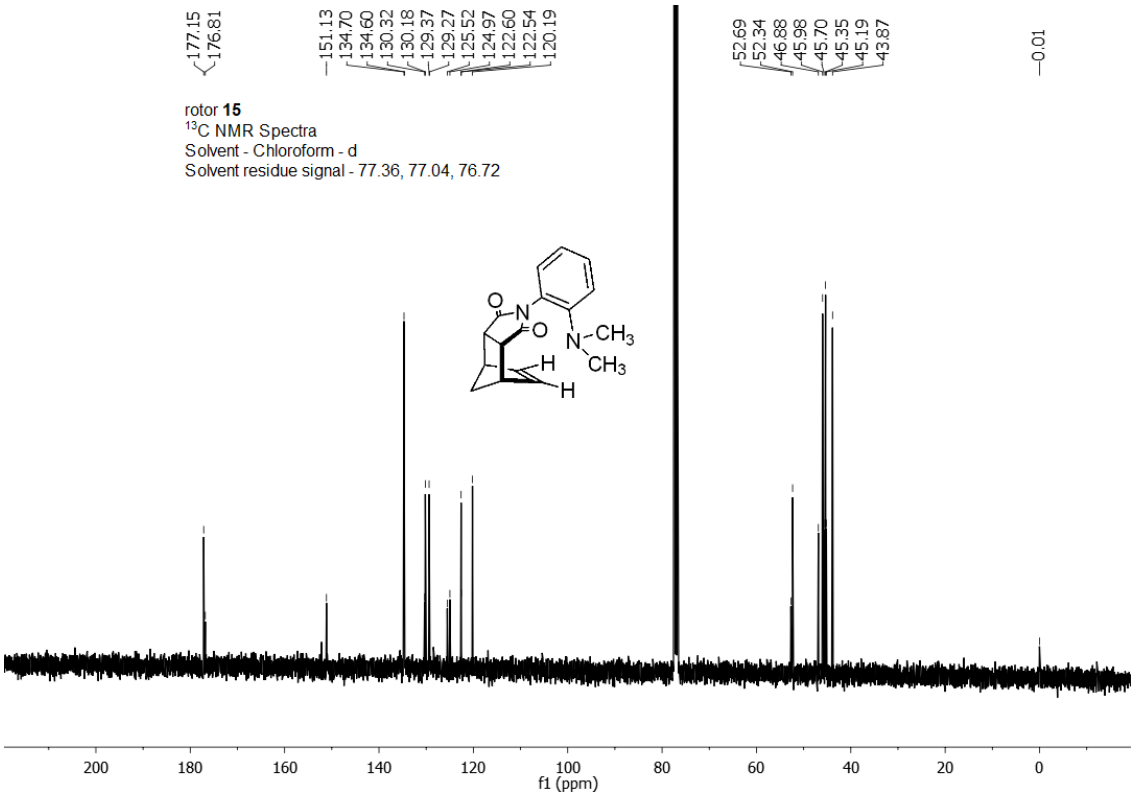

Figure 4.17. ^{13}C NMR spectra of rotor **15** (and 100 MHz, chloroform-d)

4.3.4. Table showing data for different rotors

Table 4.1. B-values, experimental and calculated rotational barriers of molecular rotors.

rotor number	substituent	$\Delta G^{\ddagger}_{expt}$ (kcal/mol)	$\Delta G\ddagger_{calc}$ (kcal/mol)	B-value (kcal/mol)
1	2-fluorenyl	15.43	13.32	4.34
2	-$(CH_2)_3$-	16.9	15.7	5.7
3	$(C=CH_2)CH_3$	19.54	19.63	7.11
4	Me	21.71	20.2	7.4
5	Ph	21.48	20.85	7.5
6	2-propyl	22.11	22.01	8.6
7	Et	21.96	22.4	8.7
8	2,3-diMe	24.02	23.38	9.6
9	-(CH_2)4-	24.2	23.1	10.5
10	iPr	23.66	24.4	11.1
11	1-naphthyl	22.41	22.22	11.65
12	F	15.6	15.41	4.4
13	OCF_3	18	16.58	5.5
14	OMe	20.2	19.5	5.6
15	$N(CH_3)_2$	22	22.21	6.9
16	Cl	22.1	22.5	7.7
17	Br	23.1	24.2	8.7
18	SMe	22.54	24.8	8.6
19	I	24.2	25.1	10
20	CF_3	23.7	25.6	10.5

Error in the EXSY rotational barriers was + 0.1 kcal/mol: B3LYP-D3/6-311G*

4.3.5. EXPERIMENTAL DETERMINATION OF ROTATIONAL BARRIERS

The rotational barriers (Table 4.1) were determined via exchange spectroscopy (EXSY) NMR experiments. (EXSY) NMR is observable by running nuclear Overhauser effect spectroscopy (NOESY) NMR experiments. In the spectra obtained from the NOESY experiments, out-of-phase signals off the diagonal of the 2D spectra originate from the nuclear Overhauser effect, while in-phase signals off the diagonal originate from exchange dynamics.[66] Integration of the signals were performed using MestreNova software, and rate

constants were obtained using the EXSYCalc software. The rotational barrier for each rotor was extrapolated to the room temperature for consistency. The TS enthalpy ($\Delta H^{\ddagger}$) and TS entropy ($\Delta S^{\ddagger}$) were obtained from the Eyring plots (Figure S1) following Equation S1. The rotation barriers were determined by plugging the TS enthalpy and entropy along with a temperature into Equation S2.

$$\ln\left(\frac{k_{ex}}{T}\right) = \frac{-\Delta H^{\ddagger}}{R} \times \frac{1}{T} + \ln\left(\frac{k_B}{h}\right) + \frac{-\Delta S^{\ddagger}}{R} \quad \textbf{(Eqn S1)}$$

$$\Delta G^{\ddagger} = \Delta H^{\ddagger} - T \times \Delta S^{\ddagger} \quad \textbf{(Eqn S2)}$$

$\Delta G^{\ddagger}$	= Gibb's free energy of the rotational barrier
R	= gas constant
T	= temperature
k_B	= Boltzmann's constant
k_{ex}	= exchange rate
$\Delta H^{\ddagger}$	= enthalpy change in the rotational barrier
$\Delta S^{\ddagger}$	= entropy change in the rotational barrier

Figure 4.18. Eyring and Gibb's Free Energy equations

Due to the wide temperature range needed for rotational barrier determination *two* solvents (dichloromethane and tetrachloroethane) with similar chemical properties but different melting/boiling temperatures were chosen. Dichloromethane-d2 (melting point = -95 °C, boiling point = 40 °C) is an appropriate choice for the rotors that requires a temperature range below 25 °C. Meanwhile, tetrachloroethane-d2 (melting point = -45 °C, boiling point = 145 °C) was an appropriate choice for the rotors that requires a temperature range above 25 °C.

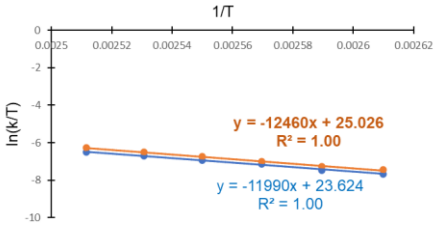

Figure 4.19. Eyring's plot for rotor **8**(2,3-diMe)

CHAPTER 5

FUTURE WORK

5.1. VALIDATION OF THE ACCURACY OF LP – LP INTERACTION STRENGTH

The objective of this chapter is to generate additional data to validate the quantification of the interaction between lone pairs, which was initiated in chapter 4 of this dissertation. Molecular rotors **21 - 23** have already been synthesized and characterized, and detailed information about these rotors can be found in the supplemental information section of this chapter. The next step involves experimentally measuring the rotational barriers of rotors **21 - 23**, while also synthesizing rotors **24** – **26** and measuring their barriers experimentally.

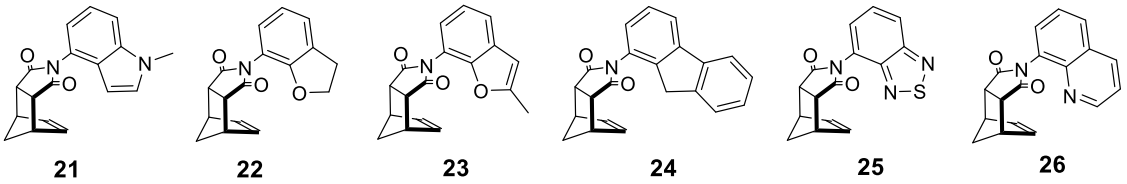

Figure 5.1. additional molecular rotors to be synthesized and used for the lone pair – lone pair measurement.

More molecular rotors need to be identified and their rotational barriers experimentally measured. The focus should be on identifying rotors with barriers below 15 kcal/mol since sufficient data points within the range of 15 – 25 kcal/mol have already been obtained. The method for experimentally measuring the barriers and quantifying the lone pair – lone pair interaction have been discussed in chapter 4 of this dissertation. Additionally, conducting experimental measurements for barriers below 6 kcal/mol would be challenging. Therefore, the strategy is to develop an effective theoretical method for calculating such barriers. This represents the next progression in the lone pair – lone pair project initiated in chapter 4 of this dissertation.

5.2 SUPPORTING INFORMATION

5.2.1 GENERAL EXPERIMENTAL INFORMATION

NMR spectra were recorded on Bruker 300 MHz spectrometer. Chemical shifts are reported in ppm (δ) referenced to the solvent residue. All spectra given for characterization purposes were taken at 25 ºC. All chemicals and solvents were purchased from commercial suppliers and used as received. Flash chromatography was performed using silica gel from Sorbent Technologies (60 Å, 200 – 400 mesh).

5.2.2 SYNTHESIS OF COMPOUNDS

1-Methyl-1H-indol-4-amine (92.7 mg, 0.63 mmol) and *cis*-5-norbornene-*endo*-2,3-dicarboxylic anhydride (86.5 mg, 0.53 mmol) were added to a 20-dram vial along with a magnetic stir bar. The vial was then capped and heated to 120 ºC in a silicon oil bath for 12 hours with mild stirring. After letting the vial cool to room temperature, the crude material was purified by column chromatography (ethyl acetate/hexanes = 1:1, v/v) to give a black crystalline solid **20** (135.9 mg, 89 %). ^{1}H NMR (300 MHz, $CDCl_3$) δ 7.39 – 7.26 (m, 2 H), 7.08 (d, J = 3.0 Hz, 1 H), 6.91 – 6.89 (m, 1 H), 3.78 (s, 3 H), 3.56 – 3.52 (m, 4 H), 1.86 – 1.83 (m, 1 H), 1.67 – 1.64 (m, 1 H). ^{13}C NMR (100 MHz, chloroform-d) δ 176.79, 137.94, 134.94, 129.73, 125.18, 124.12, 121.48, 118.56, 110.31, 88.91, 52.45, 46.24, 45.39, 33.06.

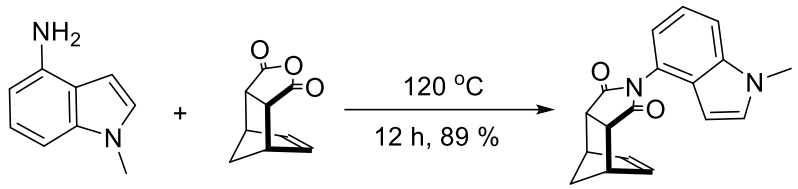

Scheme 5.1. Synthesis of rotor **21**

2,3-Dihydrobenzofuran-7-amine (115.7 mg, 0.86 mmol) and *cis*-5-norbornene-*endo*-2,3-dicarboxylic anhydride (119.6 mg, 0.73 mmol) were added to a 20-dram vial along with a magnetic stir bar. The vial was then capped and heated to 120 ºC in a silicon oil bath for 12 hours with mild stirring. After letting the vial cool to room temperature, the crude material was purified by column chromatography (ethyl acetate/hexanes = 3:4, v/v) to give an off-white solid **18** (145.0 mg, 71 %). ^{1}H NMR (300 MHz, $CDCl_3$) δ 7.20 – 7.17 (m, 1 H), 6.85 – 6.72 (m, 2 H), 6.26 (s, 2 H), 4.61 (t, J = 8.7 Hz, 2 H), 3.47 – 3.40 (m, 4 H), 3.23 (t, J = 8.7 Hz, 2 H), 1.77 – 1.75 (m, 1 H), 1.60 – 1.58 (m, 1 H). ^{13}C NMR (100 MHz, chloroform-d) δ 176.41, 155.48, 134.61, 129.23, 127.05, 126.81, 125.73, 120.69, 114.41, 72.06, 52.26, 51.80, 46.26, 46.01, 45.35, 39.47, 29.84

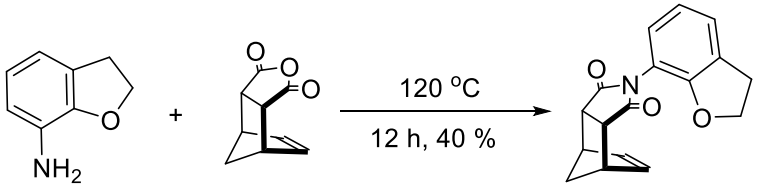

Scheme 5.2. Synthesis of rotor **22**

2-methylbenzofuran-7-amine (122.5 mg, 0.83 mmol) and *cis*-5-norbornene-*endo*-2,3-dicarboxylic anhydride (101.8 mg, 0.62 mmol) were added to a 20-dram vial along with a magnetic stir bar. The vial was then capped and heated to 120 ºC in a silicon oil bath for 12 hours with mild stirring. After letting the vial cool to room temperature, the crude material was purified by column chromatography (ethyl acetate/hexanes = 2:3, v/v) to give a brown powder **20** (146.4 mg, 80 %). ^{1}H NMR (300 MHz, $CDCl_3$) δ 7.47 (d, J = 7.8 Hz, 1 H), 7.19 (t, J = 7.8 Hz, 1 H), 6.92 – 6.91 (m, 1 H), 6.38 (s, 1 H), 6.33 (s, 2 H), 3.52 (s, 4 H), 2.42 (s, 3 H), 1.82 – 1.79 (m, 1 H), 1.65 – 1.62 (m, 1 H). ^{13}C NMR (100 MHz, chloroform-d) δ 176.40, 156.18, 149.29, 134.74, 131.10, 122.74, 122.18, 121.17, 115.53, 103.04, 52.10, 46.26, 45.50, 14.05.

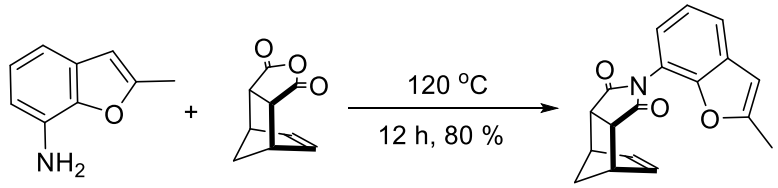

Scheme 5.3. Synthesis of rotor **23**

5.2.3 ^{1}H NMR and ^{13}C NMR Spectra

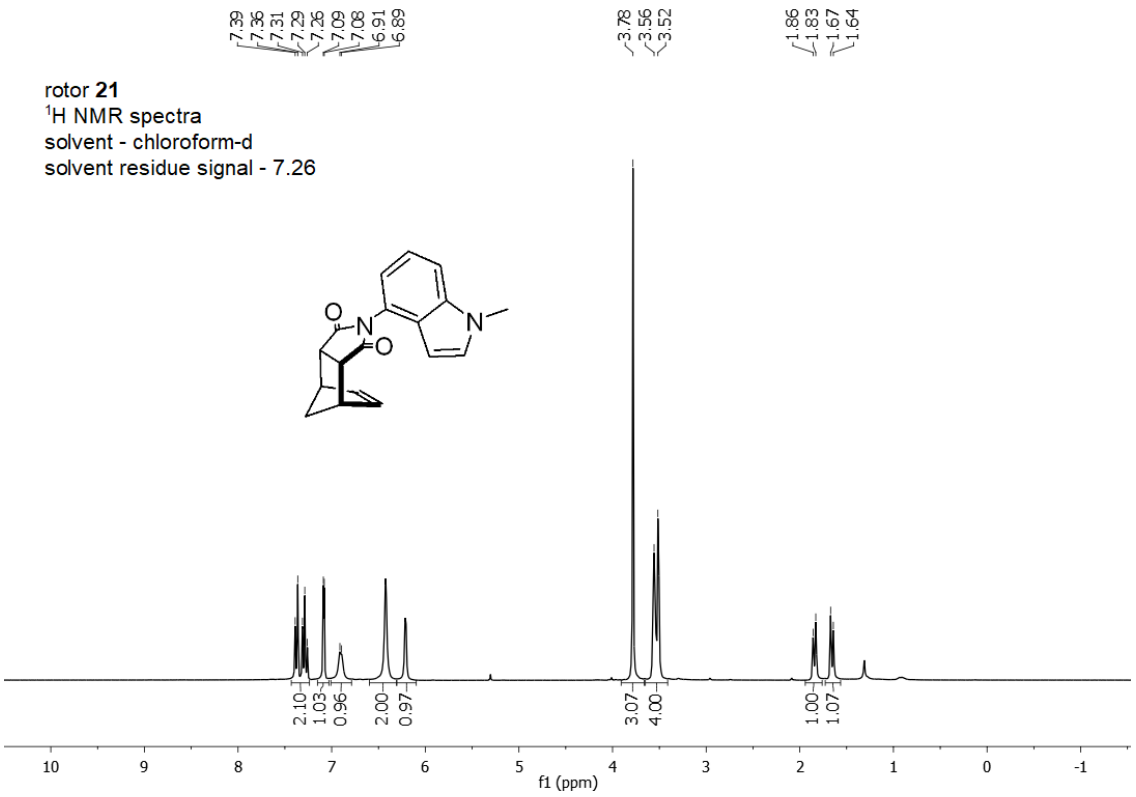

Figure 5.2. ^{1}H NMR spectra of rotor **21** (300 MHz, chloroform-d)

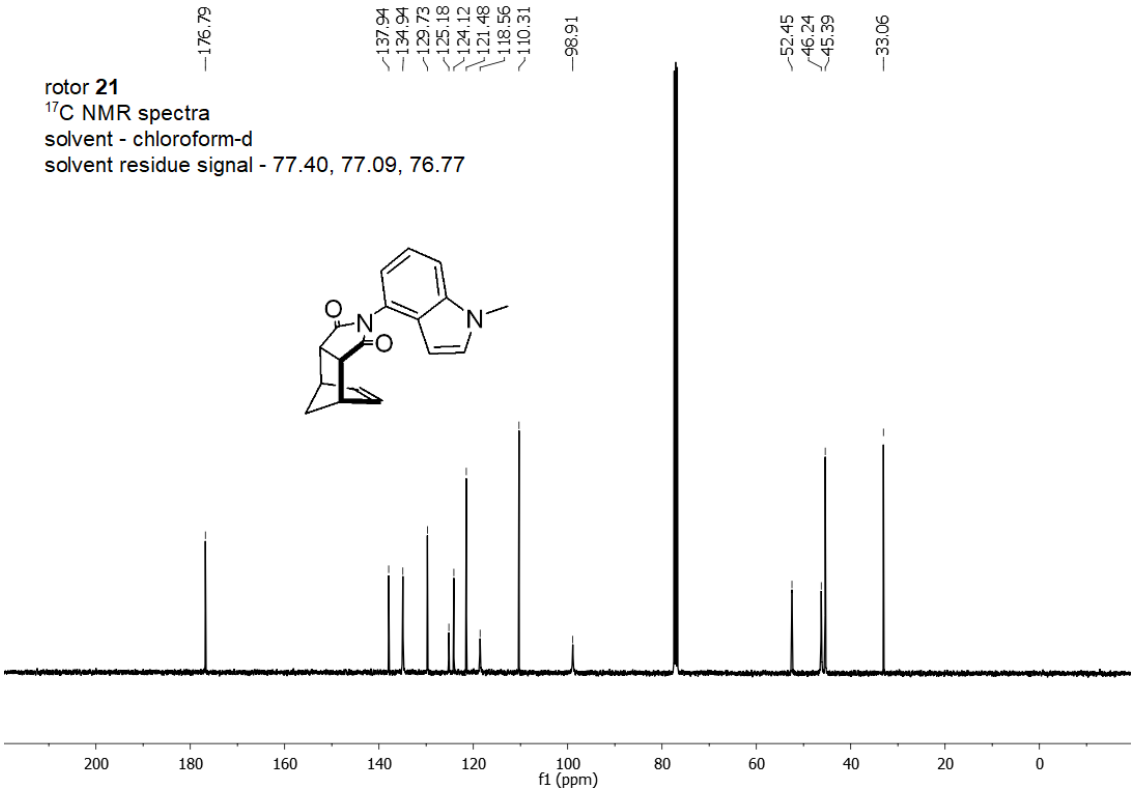

Figure 5.3. ^{13}C NMR spectra of rotor **21** (133 MHz, chloroform-d)

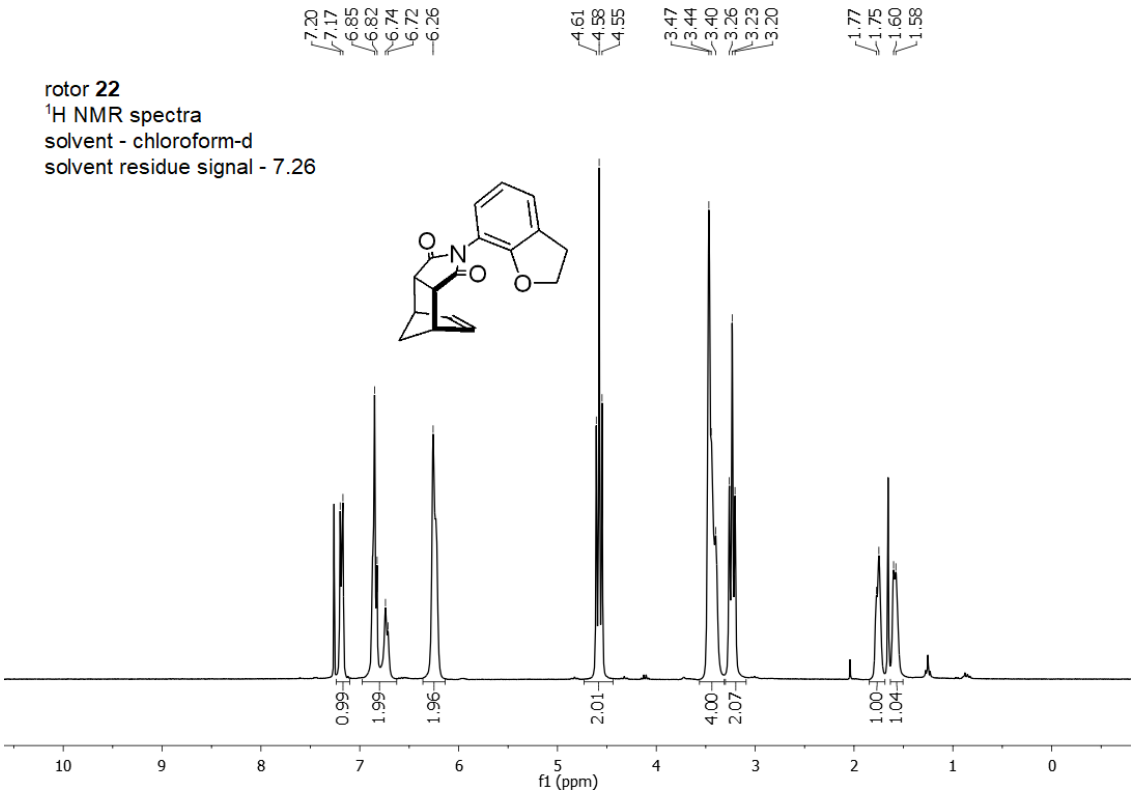

Figure 5.4. ^{1}H NMR spectra of rotor **22** (300 MHz, chloroform-d)

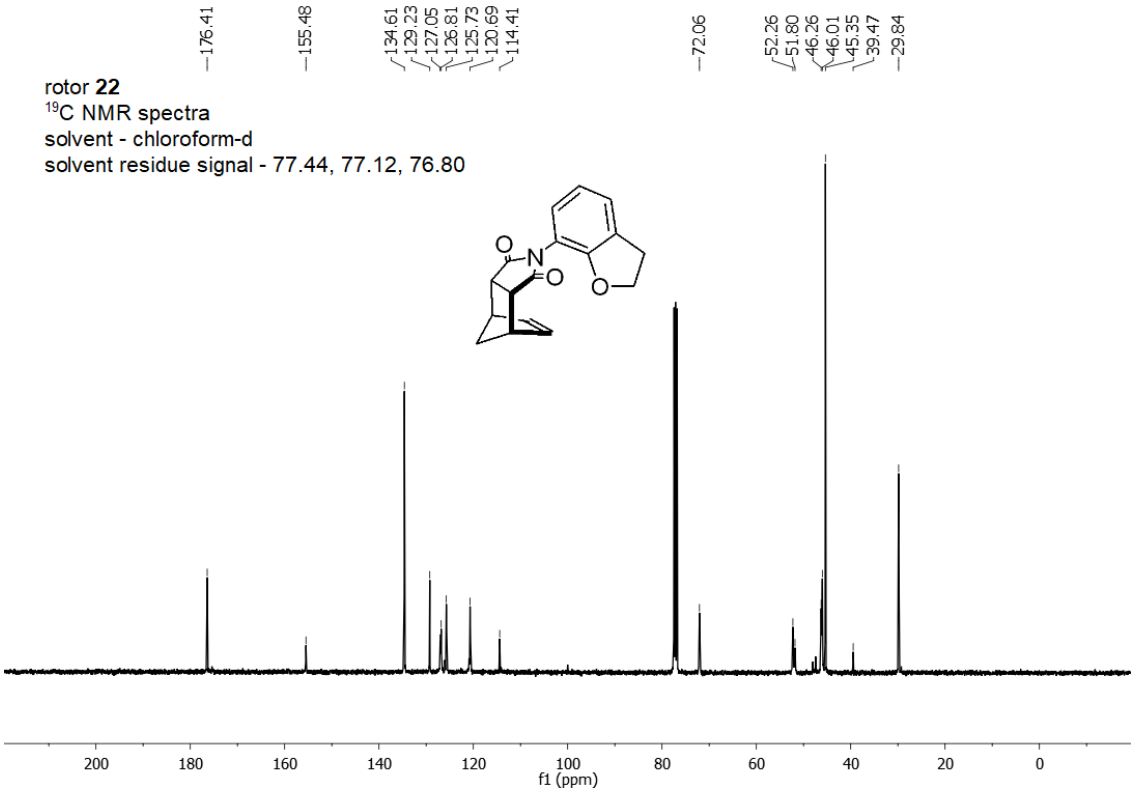

Figure 5.5. ^{13}C NMR spectra of rotor **22** (133 MHz, chloroform-d)

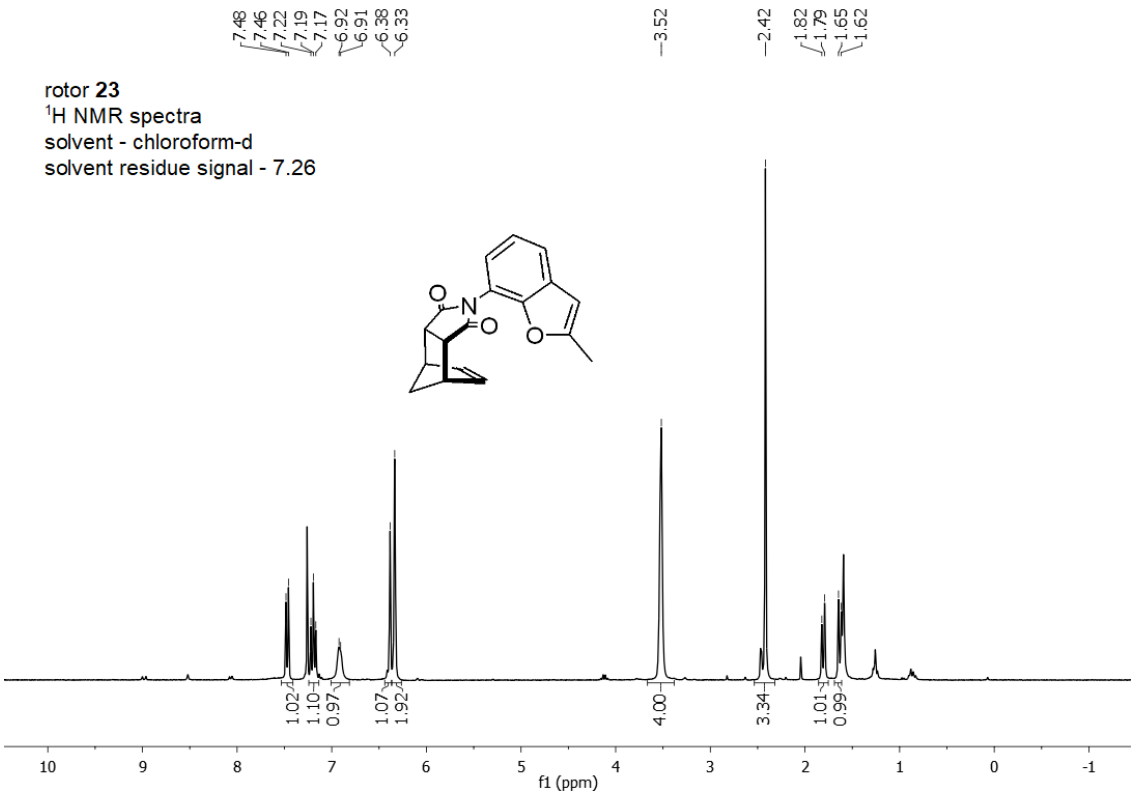

Figure 5.6. ^{1}H NMR spectra of rotor **23** (300 MHz, chloroform-d)

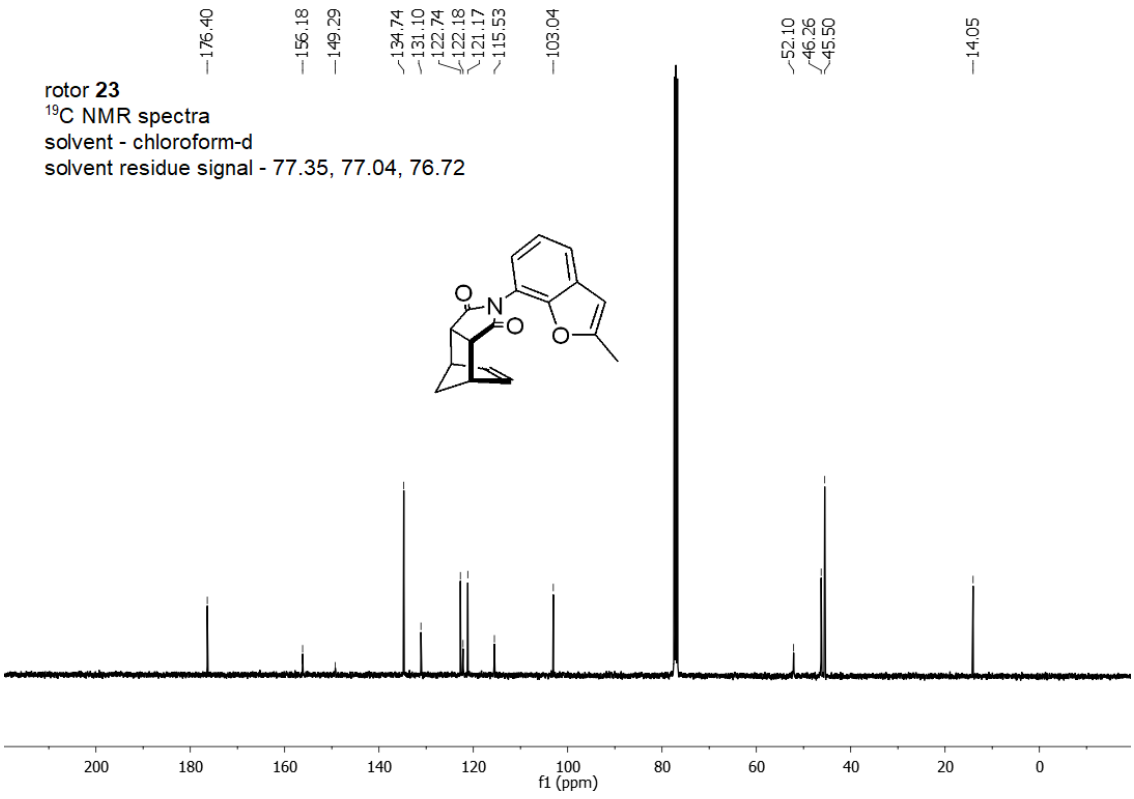

Figure 5.7. ^{13}C NMR spectra of rotor **23** (133 MHz, chloroform-d)

REFERENCES

(1) Hubbard, T. A.; Brown, A. J.; Bell, I. A. W. Cockroft, S. L. The Limit of Intramolecular H-Bonding. *J. Am. Chem. Soc.* **2016**, 138, 15114–15117. DOI: 10.1021/jacs.6b09130

(2) Desiraju, G.R. A Bond by Any Other Name. *Angew. Chem. Int. Ed*. **2011**, 50, 52-59. https://doi.org/10.1002/anie.201002960

(3) Wernet, P. et al. The structure of the first coordination shell in liquid water. *Science*. **2004**, 304, 995 - 999. doi: 10.1126/science.1096205.

(4) Cleland, W.W.; Kreevoy, M.M. Low-Barrier Hydrogen Bonds and Enzymic Catalysis. *Science.* **1994**, 264, 1887–1890. DOI:10.1126/science.8009219

(5) Jeffrey, G. A.; Saenger, W. Hydrogen Bonding in Biological Structures. *Springer-Verlag*, Berlin Heidelberg. **1991**, 15 – 54. doi:10.1007/978-3-642-85135-3

(6) Sessler, C. D.; Rahm, M.; Becker, S; Goldberg, J. M.; Wang, F; Lippard, S. J. CF_2H, a Hydrogen Bond Donor. *J. Am. Chem. Soc.* **2017**, 139, 9325–9332. doi: 10.1021/jacs.7b04457

(7) Pauling, L. The nature of the chemical bond. *J.Am. Chem Soc*. **1931**, 53, 1367-1400.

(8) Liu, K. et al., Water Clusters. *Science*. **1996**, 271, 929–933. DOI: 10.1126/science.271.5251.929

(9) Mukherjee, S.; Majumdar, S.; Bhattacharyya, D. Role of Hydrogen Bonds in Protein−DNA Recognition: Effect of Nonplanar Amino Groups. *J. Phys. Chem. B.* **2005**, 109, 10484–10492. https://doi.org/10.1021/jp0446231

(10) Kool, E. T.; Morales, J. C.; Guckian, K. M. Mimicking the structure and function of DNA: insights into DNA stability and replication. *Angew. Chem. Int. Ed*. **2000**, 39, 990-1009

(11) Mazmanian, K; Sargsyan, K; Lim, C. How the local environment of functional sites regulates protein function. *J. Am. Chem. Soc*. **2020**, 142, 9861–9871. https://doi.org/10.1021/jacs.0c02430

(12) Sigala, P. A.; Ruben, E. A.; Liu, C. W.; Piccoli, P.M.; Hohenstein, E. G. Martínez, T.J.; Schultz, A.J; Herschlag, D. Determination of hydrogen bond structure in water versus aprotic environments to test the relationship between length and stability. *J. Am. Chem. Soc*. **2015**, 137, 5730–5740. https://doi.org/10.1021/ja512980h

(13) Steiner, T.; Desiraju, G. R. Distinction between the weak hydrogen bond and the van der Waals interaction. *Chem. Commun.* **1998**, 891–892. doi:10.1039/a708099i

(14) Emamian, S.; Lu, T.; Kruse, H; Emamian, H. Exploring nature and predicting strength of hydrogen bonds: A correlation analysis between atoms-in-molecules descriptors, binding energies, and energy components of symmetry-adapted perturbation theory. *J. Comput. Chem*. **2019**, 40, 2868–2881. https://doi.org/10.1002/jcc.26068

(15) Adhikari, U; Scheiner, S. Sensitivity of pnicogen, chalcogen, halogen and H-bonds to angular distortions. *Chem. Phys. Lett*. **2012**, 532, 31– 35. https://doi.org/10.1016/j.cplett.2012.02.064

(16) Mao, Y.; Horn, P. R.; Head-Gordon, M. Energy decomposition analysis in an adiabatic picture. *Phys. Chem. Chem*. Phys. **2017**, 19, 5944– 5958. DOI: 10.1039/C6CP08039A

(17) Hill, J. G.; Legon, A. C. On the directionality and non-linearity of halogen and hydrogen bonds. *Phys. Chem. Chem. Phys*. **2015**, 17, 858-867. DOI: 10.1039/C4CP03376K

(18) Lommerse, J. P.; Price, S. L.; Taylor, R. Hydrogen bonding of carbonyl, ether, and ester oxygen atoms with alkanol hydroxyl groups. *J. Comput. Chem.* **1997**, 18, 757-774.

(19) Shahi, A.; Arunan, E. Why are hydrogen bonds directional? *J. Chem. Sci.* **2016**, 128, 1571–1577. https://doi.org/10.1007/s12039-016-1156-3

(20) Aakeröy, C. B.; Seddon, K. R.; The hydrogen bond and crystal engineering. *Chem. Soc. Rev.* **1993**, 22, 397-407. DOI: 10.1039/CS9932200397

(21) Hunter, C. A. Quantifying intermolecular interactions: guidelines for the molecular recognition toolbox. *Angew. Chem. Int. Ed*. **2004**, 43, 5310-5324. https://doi.org/10.1002/anie.200301739

(22) Legon, A. C. l.; Millen, D. J. Directional character, strength, and nature of the hydrogen bond in gas-phase dimers. *Acc. Chem. Res.* **1987**, 20, 39-46.

(23) Buckingham, A. D.; Fowler, P. W. A model for the geometries of van der Waals complexes. *Can. J. Chem.* **1985**, 63, 2018-2025. https://doi.org/10.1016/B978-044482596-4/50029-4

(24) Shimizu, K.D.; Li, Ping; Hwang, J. “Chapter 5: Solution-Phase Measurements of Aromatic Interactions.” In *Monographs in Supramol. Chem.* (eds. Johnson, D. W. Hof, F.) *RSC*. **2018**, 124 - 171. DOI:10.1039/9781782626626-0012411

(25) Fonseca, G. C.; van der Wijst, T.; Bickelhaupt, F. M. Supramolecular switches based on the guanine–cytosine (GC) Watson–Crick pair: effect of neutral and ionic substituents. *Chem. Eur. J.* **2006**, 12, 3032–3042. https://doi.org/10.1002/chem.200501301

(26) Umeyama, H.; Morokuma, K. The origin of hydrogen bonding. An energy decomposition study. *J. Am. Chem. Soc*. **1977**, 99, 1316–1332

(27) Fonseca G, C.; van der Wijst, T.; Bickelhaupt, F. M. Nanoswitches Based on DNA Base Pairs: Why Adenin–Thymine is Less Suitable than Guanine–Cytosine. *Chem. Phys. Chem*. **2006**, 7, 1971–1979. https://doi.org/10.1002/cphc.200600216

(28) Gilli, P.; Pretto, L.; Bertolasi, V.; Gilli, G. Predicting hydrogen-bond strengths from acid− base molecular properties. The p K a slide rule: toward the solution of a long-lasting problem. *Acc. Chem. Res*. **2009**, 42, 33-44. https://doi.org/10.1021/ar800001k

(29) Rackers, J. A.; Ponder, J. W. Classical Pauli repulsion: An anisotropic, atomic multipole model. *J. Chem. Phys.* **2019**, 150, 084104. https://doi.org/10.1063/1.5081060

(30) van der Lubbe, S. C.; Fonseca G, C. Hydrogen-bond strength of CC and GG pairs determined by steric repulsion: Electrostatics and charge transfer overruled. *Chem. Eur. J*. **2017**, 23, 10249– 10253. https://doi.org/10.1002/chem.201701821

(31) Grabowski, S. J. What is the covalency of hydrogen bonding? *Chem. Rev*. **2011**, 111, 2597– 2625. https://doi.org/10.1021/cr800346f

(32) Arunan, E.; Desiraju, G. R.; Klein, R. A.; Sadlej, J.; Scheiner, S.; Alkorta, I.; Nesbitt, D. J. Defining the hydrogen bond: An account (IUPAC Technical Report). *Pure Appl. Chem*. **2011**, 83, 1619– 1636. https://doi.org/10.1351/PAC-REP-10-01-01

(33) Strauss, M. A.; Wegner, H. A. Molecular systems for the quantification of London dispersion interactions. *Eur. J. Org. Chem*. **2019**, 2, 295-302. https://doi.org/10.1002/ejoc.201800970

(34) Hansen, P. E.; Kamounah, F. S.; Saeed, B. A.; MacLachlan, M. J.; Spanget-Larsen, J. Intramolecular Hydrogen Bonds in Normal and Sterically Compressed o-Hydroxy Aromatic Aldehydes. Isotope Effects on Chemical Shifts and Hydrogen Bond Strength. *Molecules.* **2019**, 24, 4533. https://doi.org/10.3390/molecules24244533

(35) Li, W.; Zhang, J. Recent developments in the synthesis and utilization of chiral β-aminophosphine derivatives as catalysts or ligands. *Chem. Soc. Rev*. **2016**, 45, 1657-1677. https://doi.org/10.1039/C5CS00469A

(36) Simón, L.; Goodman, J. M. Enzyme Catalysis by Hydrogen Bonds: The Balance between Transition State Binding and Substrate Binding in Oxyanion Holes. *J. Org. Chem.* **2010**, 75, 1831–1840. https://doi.org/10.1021/jo901503d

(37) Nagar, M.; Bearne, S. L.; An Additional Role for the Brønsted Acid–Base Catalysts of Mandelate Racemase in Transition State Stabilization. *Biochem.* **2015**, 54, 6743–6752. https://doi.org/10.1021/acs.biochem.5b00982

(38) Schreiner, P. R. Metal-free organocatalysis through explicit hydrogen bonding interactions. *Chem. Soc. Rev.* **2003**, 32, 289-296. https://doi.org/10.1039/B107298F

(39) Nishikawa, Y. Recent topics in dual hydrogen bonding catalysis. *Tetrahedron Lett*. **2018**, 59, 216-223. https://doi.org/10.1016/j.tetlet.2017.12.037

(40) Raynal, M.; Ballester, P.; Vidal-Ferran, A.; van Leeuwen, P. W. N. M. Supramolecular catalysis. Part 1: non-covalent interactions as a tool for building and modifying homogeneous catalysts. *Chem. Soc. Rev*. **2014**, 43, 1660–1733. https://doi.org/10.1039/C3CS60027K

(41) Doyle, A. G.; Jacobsen, E. N. Small-Molecule H-Bond Donors in Asymmetric Catalysis. *Chem. Rev.* **2007**, 107, 5713–5743. https://doi.org/10.1021/cr068373r

(42) Hansch, C.; Leo, A.; Taft, R. W. A survey of Hammett substituent constants and resonance and field parameters. *Chem. Rev.* **1991**, 91, 165–195. https://doi.org/10.1021/cr00002a004

(43) Bertrand, G. M. E. Electrostatics and Hydrogen Bonding. *Adv. in Mol. Cell Biol.* **1997**, 22, 109–132. doi:10.1016/s1569-2558(08)60108-3

(44) El-Mellouhi, F.; Bentria, E.; Marzouk, A. et al. Hydrogen bonding: a mechanism for tuning electronic and optical properties of hybrid organic–inorganic frameworks. *npj Comput. Mater. 2*. **2016**, 16035. https://doi.org/10.1038/npjcompumats.2016.35

(45) MacLeod, J. M.; Rosei, F. Directed Assembly of Nanostructures. *Comp. Nanosci. Technol.* **2011**, 13–68. doi:10.1016/b978-0-12-374396-1.00098-2

(46) Vik, E. C.; Li, P.; Maier, J. M.; Madukwe, D. O.; Rassolove, V. A.; Pellechia, P. J.; Masson, E.; Shimizu, K. D. Large transition state stabilization from a weak hydrogen bond. *Chem. Sci*. **2020**, 11, 7487-7494. DOI: https://doi.org/10.1039/D0SC02806A

(47) Pimentel, G. C.; McClellan, A. L. Hydrogen Bonding. *Annu. Rev. Phys. Chem.* **1971**, 22, 347–385. doi:10.1146/annurev.pc.22.100171.002023

(48) Biedermann, F.; Schneider, H. Experimental Binding Energies in Supramolecular Complexes. *Chem. Rev*. **2016**, 116, 5216–5300. https://doi.org/10.1021/acs.chemrev.5b00583

(49) Alkorta, I.; Rozas, I.; Elguero, J. Non-conventional hydrogen bonds. *Chem. Soc. Rev*. **1998,** 27, 163-170. https://doi.org/10.1039/A827163Z

(50) Hibbert, F.; Emsley, J. Hydrogen Bonding and Chemical Reactivity. *Adv. Phys. Org. Chem.* **1990**, 26, 255-379, https://doi.org/10.1016/S0065-3160(08)60047-7

(51) Alkorta, J.; Campillo, N.; Rozas, I.; Elguero, J. Ring Strain and Hydrogen Bond Acidity. *J. Org. Chem*. **1998**, 63, 7759–7763. https://doi.org/10.1021/jo980804l

(52) Raab, V. et al. 1,8-Bis(hexamethyltriaminophosphazenyl)naphthalene, HMPN: A Superbasic Bisphosphazene Proton Sponge. *J. Am. Chem. Soc*. **2005**, 127, 15738–15743. https://doi.org/10.1021/ja052647v

(53) Raab V.; Kipke, J.; Gschwind, R. M.; Sundermeyer, J. 1,8-Bis(tetramethylguanidino)naphthalene (TMGN): A New, Superbasic and Kinetically Active Proton Sponge. *Chem. Eur. J*. **2002**, 8, 1682–1693. doi:10.1002/1521-3765(20020402)8:7<1682::aid-chem1682>3.0.co;2-r

(54) Alder, R. W. Strain Effects on Amine Basicities. *Chem. Rev*. **1989**, 89, 1215–1223. https://doi.org/10.1021/cr00095a015

(55) Staab, H. A., Saupe, T. Proton Sponges and the Geometry of Hydrogen Bonds: Aromatic Nitrogen Bases with Exceptional Basicities. *Angew. Chem. Int. Ed.* **1988**, 27, 865–879. doi:10.1002/anie.198808653

(56) Perrin, C. L. Are Short, Low-Barrier Hydrogen Bonds Unusually Strong? *Acc. Chem. Res*. **2010**, 43, 1550–1557. https://doi.org/10.1021/ar100097j

(57) Taylor, R.; Kennard, O.; Versichel, W. The geometry of the N–H···O=C hydrogen bond. 3. Hydrogen-bond distances and angles. *Acta Cryst.* **1984,** B40, 280-288. DOI:10.1107/S010876818400210X

(58) Jeffrey, G. A.; Maluszynska, H. A survey of the geometry of hydrogen bonds in the crystal structures of barbiturates, purines and pyrimidines. *J. Mol. Struct*. **1986**, 147, 127–142. doi:10.1016/0022-2860(86)87064-8

(59) Bondi, A. van der Waals Volumes and Radii. *J. Phys. Chem*. **1964**, 68, 441–451. https://doi.org/10.1021/j100785a001

(60) Steiner, T. The Hydrogen Bond in the Solid State. *Angew. Chem. Int. Ed.* **2002**, 41, 48–76. doi:10.1002/1521-3773(20020104)41:1<48::aid-anie48>3.0.co;2-u

(61) Perrin, C. L.; Nielson, J. B. "Strong" hydrogen bonds in chemistry and biology. *Annu. Rev. Phys. Chem.* **1997**, 48, 511-44. doi: 10.1146/annurev.physchem.48.1.511. PMID: 9348662.

(62) Zhang, J.; Zhu, Q.; Li, S.; Tao, F. Prediction of aqueous pKa values of hydroxybenzoic acid using hydrogen-bonded complexes with ammonia. *Chem. Phys. Lett.* **2009**, 475, 15-18. https://doi.org/10.1016/j.cplett.2009.05.007.

(63) Peifeng S.; Chen, Z.; Wu, W. An energy decomposition analysis study for intramolecular non-covalent interaction. *Chem. Phys. Lett.* **2015,** 635, 250-256. https://doi.org/10.1016/j.cplett.2015.06.078.

(64) Pastorczak, E.; Prlj, A.; Gonthier, J. F.; Corminboeuf. C. Intramolecular symmetry-adapted perturbation theory with a single-determinant wavefunction. *J. Chem. Phys.* **2015**, 143, 224107. https://doi.org/10.1063/1.4936830

(65) Bordwell, F.G. Equilibrium Acidities in Dimethyl Sulfoxide Solution. *Acc. Chem. Res*. **1988**, 21, 456-463. DOI: 10.1021/ar00156a004

(66) Nikitin, K.; O'Gara, R. Mechanisms and beyond: elucidation of fluxional dynamics by exchange NMR spectroscopy. *Chem. Eur. J*. **2019**, 25, 4551–4589. DOI: 10.1002/chem.201804123

(67) Buckingham, A. D.; Fowler, P.; Hutson, J. M. Theoretical studies of van der Waals molecules and intermolecular forces. *Chem. Rev.* **1988**, 88, 963-988. DOI: https://pubs.acs.org/doi/pdf/10.1021/cr00088a008

(68) Chalasinski, G.; Szczesniak, M. M. State of the art and challenges of the ab initio theory of intermolecular interactions. *Chem. Rev.* **2000**, 100, 4227. https://doi.org/10.1021/cr990048z

(69) Meyer, E. A.; Castellano, R. K.; Diederich, F. Interactions with aromatic rings in chemical and biological recognition. *Angew. Chem. Int. Ed.* **2003**, 42, 1210. https://doi.org/10.1002/anie.200390319

(70) Kodama, Y.; Nishihata, K.; Nishio, M.; Nakagawa, N. Attractive interaction between aliphatic and aromatic systems. *Tetrahedron Lett.* **1977**, 18, 2105-2108. https://doi.org/10.1016/S0040-4039(01)83692-3

(71) Nishio, M.; Hirota, M.; Umezawa, Y. The CH/π Interaction. Evidence, Nature, and Consequences. *Wiley-VCH*, New York, **1998**

(72) Umezawa, Y.; Tsuboyama, S.; Takahashi, H.; Uzawa, J.; Nishio, M. CHπ interaction in the conformation of organic compounds. A database study. *Tetrahedron*. **1999**, 55, 10047-10056. https://doi.org/10.1016/S0040-4020(99)00539-6

(73) Matsumoto, A.; Tanaka, T.; Tsubouchi, T.; Tashiro, K.; Saragai, S.; Nakamoto, S. Crystal engineering for topochemical polymerization of muconic esters using halogen− halogen and CH/π interactions as weak intermolecular interactions., *J. Am. Chem. Soc.* **2002**, 124, 8891- 8902. https://doi.org/10.1021/ja0205333

(74) Nagahama, S.; Inoue, K.; Sada, K.; Miyata, M.; Matsumoto, A. Two-dimensional hydrogen bond networks supported by CH/π interaction leading to a molecular packing appropriate for topochemical polymerization of 1, 3-diene monomers. *Cryst. Growth Des*. **2003**, 3, 247-256. https://doi.org/10.1021/cg020070c

(75) Saigo, K.; Kobayashi, Y. The role of CH/π interaction in the stabilization of less-soluble diastereomeric salt crystals. *Chem. Rec.* **2007**, 7, 47-56. https://doi.org/10.1002/tcr.20100

(76) Clark, T. E.; Makha, M.; Sobolev, A. N.; Dalgarno, S. J.; Atwood, J. L.; Raston, C. L. Structural diversity of methyl-substituted inclusion complexes of calix [5] arene. *Cryst. Growth Des*. **2007**, 7, 2059-2065. https://doi.org/10.1021/cg0705658

(77) Quiocho, F. A.; Vyas, N. K. Novel stereospecificity of the L-arabinose-binding protein. *Nature.* **1984**, 310, 381-386. DO: Ihttps://doi.org/10.1038/310381a0

(78) Vyas, N. K.; Vyas, M. N.; Quiocho, F. A. A novel calcium binding site in the galactose-binding protein of bacterial transport and chemotaxis. *Nature*. **1987**, 327, 635-638. DOI: https://doi.org/10.1038/327635a0

(79) Tatko, C. D.; Waters, M. L. Comparison of C−H···π and Hydrophobic Interactions in a β-Hairpin Peptide: Impact on Stability and Specificity. *J. Am. Chem. Soc.* **2004**, 126, 2028-2034. https://doi.org/10.1021/ja038258n

(80) Kobayashi, K.; Asakawa, Y.; Kato, Y.; Aoyama, Y. Complexation of hydrophobic sugars and nucleosides in water with tetrasulfonate derivatives of resorcinol cyclic tetramer having a polyhydroxy aromatic cavity: importance of guest-host CH-π interaction. *J. Am. Chem. Soc.* **1992**, 114, 10307-10313. https://pubs.acs.org/doi/pdf/10.1021/ja00052a030

(81) Amabilino, D. B.; Ashton, P. R.; Brown, C. L.; Cordova, E.; Godinez, L. A.; Goodnow, T. T.; Pietraszkiewicz, M. Molecular meccano. 2. Self-assembly of [n] catenanes. *J. Am. Chem. Soc.* **1995**, 117, 1271-1293. https://pubs.acs.org/doi/pdf/10.1021/ja00109a011

(82) Frontera, A.; Garau, C.; Quiñonero, D.; Ballester, P.; Costa, A.; Deyà, P. M. Weak C− H/π interaction participates in the diastereoselectivity of a host− guest complex in the presence of six strong hydrogen bonds. *Org. Lett.* **2003**, 5, 1135-1138. https://doi.org/10.1021/ol034247n

(83) Sozzani, P.; Comotti, A.; Bracco, S.; Simonutti, R. Cooperation of multiple CH···π interactions to stabilize polymers in aromatic nanochannels as indicated by 2D solid state NMR. *Chem. Commun*. **2004**, 7, 768-769. https://doi.org/10.1039/B316855G

(84) Yamamoto, A.; Furuta, S. Y.; Horie, M.; Kodama, M.; Sato, W.; Iwasaki, F. Synthesis and Structure of 16 π Octaalkyltetraphenylporphyrins. *J. Am. Chem. Soc.* **2005**, 127, 14540-14541. https://doi.org/10.1021/ja052842+

(85) Lakshminarayanan, P. S.; Kumar, D. K.; Ghosh, P. solid state structural evidence of chloroform− benzene− chloroform adduct trapped in hexaanthryl octaaminocryptand channels. *J. Am. Chem. Soc.* **2006**, 128, 9600-9601. https://doi.org/10.1021/ja063228g

(86) Tarakeshwar, P.; Choi, H. S.; Kim, K. S. Olefinic vs aromatic π− h interaction: a theoretical investigation of the nature of interaction of first-row hydrides with ethene and benzene. *J. Am. Chem. Soc.* **2001**, 123, 3323-3331. https://doi.org/10.1021/ja0013531

(87) Ribas, J.; Cubero, E.; Luque, F. J.; Orozco, M. Theoretical study of alkyl-π and aryl-π interactions. Reconciling theory and experiment. *J. Am. Chem. Soc.* **2002**, 67, 7057-7065. https://doi.org/10.1021/jo0201225

(88) Kobayashi, Y.; Saigo, K. Periodic ab initio approach for the cooperative effect of ch/π interaction in crystals: relative energy of ch/π and hydrogen-bonding interactions. *J. Am. Chem. Soc.* **2005**, 127, 15054-15060. https://doi.org/10.1021/ja0434580

(89) Tsuzuki, K. Honda, T.; Uchimaru, M.; Mikami, M.; Tanabe, K. The Magnitude of the CH/π Interaction between Benzene and Some Model Hydrocarbons. *J. Am. Chem. Soc.* **2000**, 122, 3746 – 3753. https://doi.org/10.1021/ja993972j

(90) Shibasaki, K.; Fujii, A.; Mikami, N.; Tsuzuki, S. Magnitude of the CH/π Interaction in the Gas Phase: Experimental and Theoretical Determination of the

Accurate Interaction Energy in Benzene-methane. *J. Phys. Chem. A.* **2006**, 110, 4397–4404. https://doi.org/10.1021/jp0605909

(91) Shibasaki, K.; Fujii, A.; Mikami, N.; Tsuzuki, S. Magnitude and nature of interactions in benzene− X (X= Ethylene and Acetylene) in the gas phase: significantly different CH/π interaction of acetylene as compared with those of ethylene and methane. *J. Phys. Chem. A.* **2007**, 111, 753-758. https://doi.org/10.1021/jp065076h

(92) Mishra, B. K.; Deshmukh, M. M.; Venkatnarayan, R. C–H···π interactions and the nature of the donor carbon atom. *J. Org. Chem.* **2014**, 79, 8599 – 8606. https://doi.org/10.1021/jo501251s

(93) Tsuzuki, S. CH/π interactions. *Annu. Rep. Sect. C (Phys. Chem).* **2012**, 108, 69-95. https://doi.org/10.1039/C2PC90003C

(94) Wang, H.; Wang, W.; Jin, W. J. σ-Hole Bond vs π-Hole Bond: A Comparison Based on Halogen Bond. *Chem. Rev.* **2016**, 116, 5072–5104. https://doi.org/10.1021/acs.chemrev.5b00527

(95) Parrish, R. M.; Burns, L. A.; Smith, D. G.; Simmonett, A. C.; DePrince III, A. E.; Hohenstein, E. G.; Sherrill, C. D. Psi4 1.4: Open-Source Software for High-Throughput Quantum Chemistry. *J. Chem. Theory Comput.* **2017**, 13, 3185–3197. doi: 10.1021/acs.jctc.7b00174

(96) Kumar, A.; Gadre, S. R.; Mohan, N.; Suresh, C. H. Lone Pairs: An Electrostatic Viewpoint. *J. Phys. Chem. A.* **2014**, 118, 526–532. doi:10.1021/jp4117003

(97) Lee, J. D. Concise Inorganic Chemistry, 4 ed., *Wiley-Blackwell*, London, **1991**.

(98) Gillespie, R. J. The valence-shell electron-pair repulsion (VSEPR) theory of directed valency. *J. Chem. Educ*. **1963**, 40, 295.

(99) Gillespie, R. J. Fifty Years of the VSEPR Model. *Coord. Chem. Rev*. **2008**, 252, 1315−1327. https://doi.org/10.1016/j.ccr.2007.07.007

(100) Gillespie, R. J.; Nyholm, R. S. Inorganic Stereochemistry. *Q. Rev., Chem. Soc*. **1957**, 11, 339−380. https://doi.org/10.1039/QR9571100339

(101) Ruzziconi, R.; Spizzichino, S.; Lunazzi, L.; Mazzanti, A.; Schlosser, M. B. Values as a Sensitive Measure of Steric Effects. *Chem. - Eur. J*. **2009**, 15, 2645−2652. https://doi.org/10.1002/chem.200801963

(102) Vik, E. C.; Li, P.; Pellechia, P. J.; Shimizu, K. D. Transition State Stabilization by n→π* Interactions Measured Using Molecular Rotors. *J. Am. Chem. Soc*. **2019**, 141, 16579−16583. https://doi.org/10.1021/jacs.9b08542

(103) Vik, E. C.; Li, P.; Madukwe, D. O.; Karki, I.; Tibbetts, G. S.; Shimizu, K. D. Analysis of the Orbital and Electrostatic Contributions to the Lone Pair–Aromatic Interaction Using Molecular Rotors**.** *Org. Lett.* **2021**, 23, 8179–8182. doi.org/10.1021/acs.orglett.1c02878

APPENDIX A EMPIRICAL PARAMETERS

Empirical parameters used to model electrostatics for common substituents

R	σ_m	σ_p	F	R
CH_3	-0.07	-0.17	0.01	-0.18
$CH2CH_3$	-0.07	-0.15	0	-0.15
$CH(CH3)_2$	-0.04	-0.15	0.04	-0.19
$C(CH3)_3$	-0.1	-0.2	-0.02	-0.18
CCH	0.21	0.23	0.22	0.01
CN	0.56	0.66	0.51	0.15
Ph	0.06	-0.01	0.12	-0.13
Ph-F5	0.26	0.27	0.27	0
$CHCH_2$	0.06	-0.04	0.13	-0.17
CHO	0.35	0.42	0.33	0.09
$COCH_3$	0.38	0.5	0.33	0.17
COPh	0.34	0.43	0.31	0.12
COOH	0.37	0.45	0.34	0.11
$COOCH_3$	0.37	0.45	0.34	0.11
OH	0.12	-0.37	0.33	-0.7
OCH_3	0.12	-0.27	0.29	-0.56
OCF_3	0.38	0.35	0.39	-0.04
OPh	0.25	-0.03	0.37	0.4
SH	0.25	0.15	0.3	-0.15
SCH_3	0.15	0	0.23	-0.23
SCF_3	0.4	0.5	0.36	0.14
SPh	0.23	0.07	0.3	-0.23
NH_2	-0.16	-0.66	0.08	-0.74
$NHCH_3$	-0.21 -	-0.7	0.03	-0.73
NHPh	-0.02	-0.56	0.22	-0.78
$NHCOCH_3$	0.21	0	0.31	-0.31
$N(CH3)_2$	-0.16	-0.83	0.15	-0.98
$N(Ph)_2$	0	-0.22	0.12	-0.34
NO_2	0.71	0.78	0.65	0.13
F	0.34	0.06	0.45	-0.39
Cl	0.37	0.23	0.42	-0.29
Br	0.39	0.23	0.45	-0.22
I	0.35	0.18	0.42	-0.24
CF_3	0.43	0.54	0.38	0.16